Microparticle Manipulation using CW and Modulated Diode Laser

Yang Qian

Submitted in fulfilment of the requirements for the

Degree of Doctor of Philosophy

School of Engineering

College of Science and Engineering

University of Glasgow

September 2018

Abstract

Various platforms for microparticle manipulation have already been applied as useful tools for research in the life science field over recent decades. So far, several techniques have been investigated with their own advantages and limitations. For label-free approaches, such as acoustic tweezers, samples can be moved, controlled and separated in a gentle and precise manner. In order to achieve non-contact and remote control approaches, laser ultrasonics will be a potential technique for the acoustic tweezing field. In addition, using laser-induced thermal forces will be a novel and alternative tool for micromanipulation.

In this thesis, new platforms were developed for microparticle trapping and manipulation by either laser-induced surface acoustics based on a modulatable diode laser or laser-induced thermal forces without any absorbing coatings on the substrate.

For laser-induced surface acoustics, the intensity of generated surface acoustic waves (SAWs) based on our experimental setup was measured first. With inspiration from the literature, several attempts were made to generate and detect SAWs using a modulated laser beam from a diode laser by different combinations of generation methods and detection techniques, and improvements of the experimental system. However, none of the expected signals could be observed and measured. The factors that affected the amplitude of the SAWs were further investigated by numerical modelling. The results show that the surface displacement was enhanced significantly with a thin metal layer coated on the substrate, and by increasing the optical intensity within the illumination region at low modulation frequencies (~1 kHz). However, the displacement decreased greatly with frequency. At the high frequency (25 MHz) used in the experiments, it reduced to 2.95 fm, which was 5 orders of magnitude smaller than that at 1 kHz. It can be concluded that the generated SAWs were too weak to move particles under our experimental conditions.

For the laser-induced thermal forces technique, microparticles and biological samples were trapped and manipulated successfully in a thin fluidic chamber with a light absorber by the combined effect of laser-induced thermal convection flow and thermophoresis. From further characterisations of the two physical phenomena, it was demonstrated that the flow speed was proportional to the energy absorption, and the particle moving speed increased with particle size, which indicated that the particle suspension position affected the flow speed as well. Furthermore, the thermophoretic velocity increased with optical power absorption, and thermophoretic mobility (D_T) increased with the size and the lower thermal conductivity of particle. Moreover, numerical modelling based on the experiments was undertaken to further explain the phenomena and investigate the underlying mechanisms. In summary, this new platform opens up the possibility to develop a novel micromanipulation technique (optical-thermophoretic tweezers) with benefits of low cost, compact, biocompatible, modest optical power ($\leq$ 200 mW) and being easy to set up and operate, which provides significant advantage over large system usually used for micromanipulation.

Contents

List of tables

List of figures

Publication & conference

Publication

Shuailong Zhang, Yongpeng Liu, Yang Qian, Weizhen Li, Joan Juvert, Pengfei Tian, Jean-Claude Navarro, Alasdair W Clark, Erdan Gu, Martin D. Dawson, Jonathan M. Cooper, and Steven L. Neale, "Manufacturing with light - micro-assembly of opto-electronic microstructures," *Opt. Express* (2017), doi: 10.1364/OE.25.028838

Conference proceeding

Optics in the Life Sciences Congress, 2017, San Diego, USA, "Trapping and manipulation of microparticles using laser-induced optical and thermal forces", oral presentation, doi: 10.1364/OTA.2017.OtM3E.3

Acknowledgements

I would like to take this opportunity to express my sincere appreciation to my supervisors Professor John Marsh and Doctor Steven Neale for their efforts, guidance and supports. I am grateful for their advices and encouragements during my PhD studies. I would also like to thank them for giving me the opportunity to be the opportunity to carry out this research within their groups.

Special thanks to Dr. Andrew Glidle, Dr. Christian Witte, Dr. William Ward, Dr. Xiaofei Yuan and Mr. Nicholas J Scott for their patient and enthusiastic helps on microfluidics, acoustics, optics and electronics.

My acknowledgements also go to all the people who helped me in any technical aspects of this work, namely: Prof. Jonathan Cooper, Prof. Marc Sorel, Dr. Arslan Khalid, Dr. Julien Reboud, Dr. Robert Wilson, Dr. Scott Watson, Dr. Yangqing Song, Jason Bolderson, Laura Charlton, Pracha Yambangyang and all the technicians from the James Watt Nanofabrication Centre.

I also would like to thank my friends Dr. Juan Carlos Rodriguez Luna and Maab Al-Hafidh for providing any helps, advices and friendships during my stay in Glasgow.

Finally and most importantly, I would like to thank my parents for their infinite support in my whole life so far.

Author’s declaration

“I declare that, except where explicit reference is made to the contribution of others, this dissertation is the result of my own work and has not been submitted for any other degree at the University of Glasgow or any other institution.”

Yang Qian

Abbreviations

AG	Anode ground
Al	Aluminium
a-Si	Amorphous silicon
BAWs	Bulk acoustic waves
CNT	Carbon nanotube
CW	Continuous waveform
DI water	Deionized water
D_T	Thermophoretic mobility
EC	Electrical conductivity
EDL	Electrical double layer
EMI	Electromagnetic interference
FEA	Finite element analysis
fm	Femtometer
FNG	Function generator
FWHM	Full width at half maximum
IC	Integrated circuit
IDT	Interdigital transducer
IHP	Inner Helmholtz plane
IV	Current-voltage
LD	Laser diode
LDV	Laser Doppler vibrometer
$LiNbO_3$	Lithium niobate
Mo	Molybdenum
N.A. (/NA)	Numerical aperture
OHP	Outer Helmholtz plane
OP	Optical power
PDMS	Polydimethylsiloxane
PN	Pressure node
QCW	Quasi-continuous-wave
Ra	Rayleigh number
Re	Reynolds number
SAWs	Surface acoustic waves
SBAWs	Standing bulk acoustic waves

SDS	Sodium dodecyl sulfate
SMD	Surface-mount device
SMT	Surface-mount technology
SNR	Signal-to-noise ratio
SPICE	Simulation Program with Integrated Circuit E9mphasis
SSAWs	Standing surface acoustic waves
SWNT	Single-walled carbon nanotube
θ	Particle moving angle
θ_R	Rayleigh angle
∇T	Temperature gradient

Chapter 1

Introduction

In this chapter, an overview of several main techniques used for microparticle trapping and manipulation is briefly introduced, followed by the motivations and an outline of the thesis.

1.1 Background

The trapping and manipulation of microparticles have been widely used in life sciences study for many years. Several techniques have been investigated including electrokinetics [1], dielectrophoresis (DEP) [2], optical tweezers [3], optoelectronic tweezers [4], hydrodynamic flow [5], magnetic tweezers [6] and acoustic tweezers [7, 8]. For both the electrokinetics and dielectrophoresis techniques, particles are manipulated under an electric field established in the fluid. However, the electrokinetic phenomena occur when the electric field is uniform and the surfaces of particles are charged, which can be related to the concept of the diffusion layer of the electrical double layer (EDL). Dielectrophoresis requires a non-uniform electric field and polarizable particles that do not need to be charged. However, the strength of the dielectrophoretic force depends strongly on the electrical properties of the medium and the particles, the shapes and the sizes of particles, as well as on the frequency of the electric field. Therefore, the two techniques are limited by the buffer conductivity and require a low concentration of samples [1, 2, 9]. For optical tweezers, particles are trapped and moved by the optical gradient force induced by a focused laser beam. In order to achieve stable trapping, a tightly focused beam from a microscope objective with high numerical aperture (NA) is needed, leading to a high optical intensity within the illumination region, which may cause damage to the samples. Single particle manipulation can be achieved by this technique, but also multiple particle trapping by involving different light configurations, such as beam splitting, rapid laser beam movement and spatial light modulator (SLM) [10]. However, these extra configurations normally lead to a complex system setup and extra costs [11]. For optoelectronic tweezers, particles are trapped and manipulated by the DEP arising from a localised electric field gradient within a microfluidic chamber constructed from two indium tin oxide (ITO) coated glass plates, with one of them additionally being covered with a photoconductor such as amorphous silicon (a-Si). The localised electric field gradient is established by projecting light patterns with a certain wavelength on the a-Si coated ITO glass plate, meanwhile an alternating voltage is applied between the photoconductor and the ITO plate. The conductivity of the photoconductor increase linearly with the incident light intensity, which results in the voltage across the liquid being increased [4]. Although this technique requires lower light intensities than optical tweezers, specific electrical properties of the samples and devices are needed [12-14]. For hydrodynamic flow, particles are constrained in the middle of the channel by outer sheath flows. However, this approach requires a high sheath flow rate and high purity of the sample solution. The sheath solution may dilute and disperse the samples as well [9, 15]. For magnetic tweezers, particles with prelabelled magnetic materials are moved in a non-uniform magnetic field, where they experience a gradient force [16, 17]. However, for cell samples, the viability may be affected by pre-labelling materials [7, 18]. In terms of acoustic tweezers, particles can be focused, separated or patterned by standing acoustic waves within a microfluidic channel. The acoustic waves can be generated either by a bulk ultrasonic transducer to create bulk waves, or by interdigital transducers (IDTs) to create surface waves. The standing waves can be generated either by a single traveling wave with its reflections, or by two travelling waves with the same frequency but opposite directions. However, piezoelectric materials are required to create waves for either type of transducer, and waves with only a fixed frequency or narrow frequency range can be generated, which limits the applications of this technique [19].

Compared to other approaches, acoustic tweezers can offer significant advantages in terms of being non-invasive, low power consumption and label-free; so are suitable for all kinds of microparticles and cells. However, the drawbacks described above are still critical. To address these limitations, using laser ultrasonics to generate acoustic waves would be a better approach, due to the multiple choices for the substrate material, the flexible aperture size and the wider frequency range of the created waves. Because of its high sensitivity, this technique has already been used to characterize materials and inspect material's defect, such as cracks. According to the type of ultrasonic wave, laser ultrasonics can be classified as laser bulk acoustics or laser surface acoustics. Due to the fact that illumination in the thermoelastic region is non-destructive, both types of wave have been studied and applied to non-destructive testing (NDT) technology for many years. However, in terms of particle manipulation, only few papers have reported surface cleaning by the laser-induced surface acoustic waves [20, 21]. It is uncommon to find that this approach to ultrasonics has been used as acoustic tweezers for particle manipulation.

Apart from these well-developed techniques, using thermophoresis to manipulate particles in the liquid, which is still under investigation, is a novel approach that may become a new star in the particle manipulation field. Although no general physical model of particle thermophoresis in liquids has been developed so far, two features thermophobic and thermophilic thermophoresis, have been studied and shown that particles can be trapped and moved by either approach. For the thermophilic approach, researchers have reported by adjusting the ionic strength, PH and the temperature of the sample solution, particles can be diverted towards the warm region [22-31]. DNA and microparticles can be trapped and patterned by a light beam focused either on the liquid region [31] or on a substrate with a high absorption coating [32] based on the thermophilic feature, which demonstrates the potential capability of particle tweezing. In terms of the thermophobic approach, there is less research on particle trapping. However, it has been reported that microparticles accumulate around a hot region by a combination of laser-induced convection currents and thermo-photophoretic forces created by projecting a focused laser beam on a substrate with a high absorption coating [33].

Regarding the literature [34-37], researchers demonstrated the possibility of SAW generation using single modulated diode laser based on single spot illumination. However, the maximum magnitude of the generated wave measured was about 450 fm, which was too weak to move microparticles. In this project, in order to create stronger, stable and continuous SAWs, the multi-line illumination approach is applied with single modulated diode laser. With the design of the line array, enhanced SAWs with narrow frequency bandwidth can be generated under lower optical intensity, which increases the signal-to-noise ratio (SNR) for detection and increases the chance for successful micromanipulation. Furthermore, we successfully exploit laser-induced thermal convection flow and thermophoresis to achieve particle manipulation in a disposable fluidic chamber with non-treated substrate. With benefits of high optical absorption of SWNT cluster suspended in the sample solution and our biocompatible device, both microbeads and cells are trapped and confined within in a ring-shape region around the localized hot region (see Fig. 6-21 (a) and (b)), achieving the optical-thermophoretic tweezing. Although similar phenomena were reported by other research groups [33, 38-41], the substrates of their devices needed to be pre-treated by coating a thin layer of high optical absorber in many cases, and the biological samples had not been applied with their systems. In addition, our platform provides low optical intensity, and the sample device is cheap, easy to assemble and use. By involving current spatial light modulation techniques, our system will become a useful and versatile tool in life science field.

1.2 Aim of this work

The original aim of the project was to develop a new platform for particle trapping and manipulation using surface acoustic waves (SAWs) generated by an array of modulated semiconductor lasers. By looking into the amplitude of SAWs induced by single diode laser, the results showed the average surface displacement was nearly 150 fm. However, the minimum amplitude of SAWs for particle manipulation needs to be around 0.6 nm. This meant at least ten arrays containing 100 diode lasers for each were needed, which was challenging for the experimental configurations. Therefore, different physical mechanisms were investigated to achieve particle manipulation. Using an interdisciplinary approach, based on knowledge of laser ultrasonics, bioengineering and microfluidics, microparticle manipulation was implemented by laser-induced thermal forces (Stokes's drag and thermophoretic force based on thermophobic feature) without any coatings on the substrate. A physical understanding and related numerical modelling were then developed, demonstrating the potential capability of our device for optical-thermophoretic tweezers.

1.3 Thesis outline

The thesis is organised in eight chapters, which are structured as follows:

Chapter 2 presents some basic concepts and more detailed reviews of applications and related developments in particular fields that are covered in the work, including laser ultrasonics, acoustic tweezing, heat transfer and thermophoresis. The work described in the thesis is informed and inspired by the literature review.

Chapter 3 deals with the materials and the methods used in the entire research program. This comprises a description of the main experimental system setup, the sample device design and fabrication using either photolithography or microfluidic techniques, the preparation of colloidal solutions based on biochemical techniques, cell culture and a brief introduction to the software used in the study.

Chapter 4 describes SAWs generation in the thermoelastic region using a modulated diode laser with different illumination methods, and detection using different techniques as well. The test results are discussed and the limitations of our system are summarized.

Chapter 5 presents studies of the surface displacement arising from several factors through numerical modelling based on the work in Chapter 4. From the modelling, several potential improvements are proposed, which will probably enhance the SAWs induced by our system for particle manipulation in the future.

Chapter 6 introduces a new particle manipulation technique, which enables the successful trapping and manipulation of both microparticles and biological cells in a thin fluidic chamber through a combination of laser-induced thermal convection flow and thermophoresis arising from thermophobic behaviour based on continuous illumination. The characteristics of these two physical mechanisms are studied as well. Moreover, potential applications of the concept for continuous particle manipulation such as single particle trapping are outlined. In addition, microparticle manipulation under discontinuous illumination was described and discussed as well.

Chapter 7 presents numerical modelling of the work in Chapter 6. By looking into the statuses of the temperature and the fluid flow within the chamber, the results agree well with experimental results and extra findings are obtained. Furthermore, by linking the experimental and the numerical results, a deep understanding of the underlying physical phenomena is provided.

Chapter 8 ends this thesis by giving a summary of the findings obtained during the entire research program and indicates some potential directions for future work.

Chapter 2

Literature review

In this chapter, some basic concepts and detailed reviews of several techniques covered in the work presented in the thesis are described, which are laser ultrasonics, acoustic tweezing, heat transfer and thermophoresis. The characteristics, applications and relative development of each technique are reviewed as well, which provide inspiration for the later research in Chapters 4 and 6.

2.1 Ultrasonic waves

Acoustic waves can be defined as a kind of mechanical wave that can propagate through solids, liquids and gases. The frequency spectrum can be divided into three parts: infrasound, audible sound and ultrasound. For humans, the frequency range of the audible sound is from 50 Hz to 20 kHz. Below this range, the acoustic waves are called infrasound. Above this, the waves can be called ultrasound. According to the wave modes, acoustic waves can be classified into two main groups: bulk waves and surface waves.

2.1.1 Bulk waves

Bulk waves are acoustic waves that propagate internally through a medium. They can be used to detect the discontinuities of a material, such as cracks. There are two types of bulk waves: longitudinal waves and shear waves.

Longitudinal (compression) bulk wave

As is known, when an acoustic wave propagates through a medium, if the direction of the particle displacement is the same as the direction of the wave propagation, then the wave is called as longitudinal wave. In the meantime, the material is expanded and compressed in the same direction as well. Fig. 2-1 (a) shows the propagation of a longitudinal wave.

Shear (transverse) bulk wave

The property of shear wave is opposite to that of longitudinal wave. The direction of the particle displacement is perpendicular to the direction of the wave propagation. Fig. 2-1 (b) shows the propagation of a shear wave.

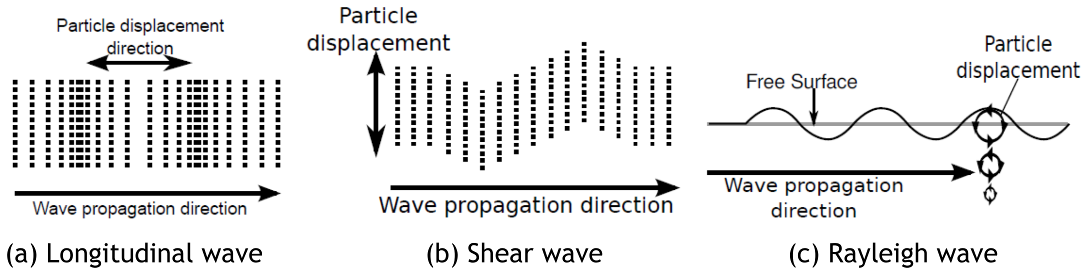

Fig. 2-1: The relations between particle displacement and wave propagation direction for three types of acoustic waves: (a) a longitudinal wave, (b) a shear wave and (c) a Rayleigh wave [42].

2.1.2 Surface acoustic waves (SAWs)

A surface acoustic wave is an acoustic wave that propagates on the surface of a medium. With increasing penetration depth, its amplitude will decay exponentially. The wave has been used in chemistry and biology commonly, such as for detecting the composition of a gas, detecting proteins and bacteria [43]. The two main types of this kind of waves are Rayleigh waves and Love waves.

Rayleigh waves

Rayleigh waves consist of longitudinal and shear components whose amplitude decreases exponentially with penetration depth. In isotropic solids, the particle displacement is in the form of an elliptical motion (see Fig. 2-1(c)). When the waves propagate along the surface of a solid from left to right, the movement of particles is counter clockwise. In the ideal situation, no dispersion occurs during the propagation. However, if the density of the solid varies with depth, the velocity of the wave will be dependent on its wavelength. As a result, the velocity for low frequencies is faster than that for high frequencies. Due to the fact that the maximum penetration depth is about two times the wavelength [44], it will be insensitive if detecting the cracks of which the depth is greater than two wavelengths from the surface. So they can be used to detect the microdefects along the surface of a material.

Rayleigh waves have been applied to many applications of material characterization such as surface-breaking fatigue cracks detection [45, 46], stress measurement of materials [47-50], surface roughness assessment [51, 52] and surface microstructure imaging [53-56]. In this thesis, Rayleigh waves will be used as an important part of the particle manipulation system.

Love waves

A Love wave is a transverse surface wave, which vibrates the surface horizontally perpendicular to the direction of the wave propagation. Unlike the Rayleigh wave, no vertical displacement particle motion is involved. The amplitude of the wave decreases exponentially with penetration depth. Generally, Love waves travel faster than Rayleigh waves. So far, it has been used as a sensing technique for chemical and biological sensors in gaseous and liquid environments, due to its high sensitivity [57-59].

Lamb waves

A Lamb wave is a bulk acoustic wave, which normally occurs when a Rayleigh wave propagates along a thin substrate. It is formed by the interaction of elastic waves generated along two parallel closed boundaries in a solid. Regarding the penetration depth of the Rayleigh wave, if the thickness of the sample is thin enough, normally equal or less than two times the wavelength, the wave will reach to the bottom surface with enough energy to cause elastic vibration on both two surfaces. According to the particle motions along the surfaces in phase or antiphase, the mode of Lamb wave can be classified as two types: antisymmetrical and symmetrical. Similarly, Lamb waves also contain a longitudinal component and a shear component. They can be used to inspect a range of defects such as delamination [60, 61] and cracks [62, 63]. Fig. 2-2 shows the propagation of Lamb waves with different modes.

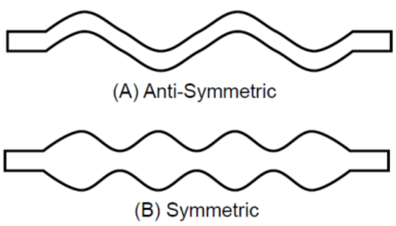

Fig. 2-2: Schematics of Lamb waves propagation with two different modes: (a) anti-symmetric mode and (b) symmetric mode [42].

2.2 Laser ultrasonics

2.2.1 Laser-launched bulk waves technology

In the thermoelastic region, in order to generate bulk acoustic waves (BAWs), a created thermoelastic source should be buried in the sample body, which can be achieved by choosing a certain wavelength of the laser beam allowed to penetrate significantly below the surface depending on the absorption coefficient of the sample. A typical generation method is using single spot illumination. The measurement is carried out by irradiating a pulsed beam from a Q-switched solid laser on a metallic disc (e.g. aluminium alloy or mild steel) of variable thickness. The pulse duration can be varied from 20 – 30 ns, and the pulse energy is typically below 100 mJ. A piezoelectric transducer is attached on the opposite surface to detect the generated acoustic waves [64]. With this concept, the bulk waves has already been used in the industry to inspect material and surface conditions. However, this configuration restricts BAWs only working in the solid material. In recent decades, several researchers reported generating BAWs in liquid using different methods. In 2014, Padilla-Martinez *et al.* [65] used a novel method of thermocavitation to generate acoustic shock waves by a modulated CW laser incident in a highly absorbing liquid. The liquid used was a saturated solution of copper nitrate ($CuNO_4$) filled in a glass cuvette. The thermocavitation was created by heating up a local area of liquid beyond its spinodal limit with a focused laser beam at 150 mW and 2 μm in diameter. The superheated water became unstable, producing a fast-expending vapour bubble. The acoustic shock waves were generated due to the thermocavitation collapse. The generated waves were then detected by a hydrophone, showing a series of pulse signals with maximum repetition rate of 4 kHz, due to the long-time process of cavitation from generation to collapse. This technique can be further studied in the particle manipulation field. However, due to the low pulse repetition rate and toxic operating solution, the applications for manipulation and biological samples will be restricted.

In the applications of cell therapy (e.g. gene therapy), the thermally generated acoustic cavitation should be avoided as cellular metabolism is easily transformed by a slight temperature change. To address it, Baac *et al.* [66] developed a new technique for focused ultrasound generation in liquid by a nano-composite optoacoustic transmitter. The transmitter was configured by a concave lens coated with a nano-composite film of gold, multi-walled carbon nanotubes (CNTs) and polydimethylsiloxane (PDMS). The ultrasound waves were created by irradiating a laser beam from a 6-ns pulsed laser on the lens. Due to the high optical absorption of the CNTs, the high coefficient of thermal expansion of the PDMS and the curvature of the lens, the high-amplitude focused shock waves were generated. The focused ultrasound region was 75 μm in lateral and 400 μm in axial directions. The repetition rate of laser pulse was 20 Hz and the pulse energy was 12 mJ. By looking into the detected signals from a fibre-optic hydrophone in the frequency domain, the results showed broadband frequency spectra with central frequency at 15 MHz. However, due to the nonflexible frequency variation of the generated wave, its applications in the particle manipulation field will be limited.

2.2.2 Laser-launched SAWs technology

Laser-launched SAWs is one of applications on the laser ultrasonics, which has already been used to investigate the mechanical properties of materials, and might be applied to the applications on chemical and biological sensors. In recent decades, both generation and detection techniques have been developed and improved. In the following section, the development of generation system will be introduced.

2.2.2.1 Single spot and single line illuminations

According to the principle of SAW generation by lasers, it can be classified into two physical regions: the ablation region and the thermal-elastic region. For the former, a sufficient optical intensity is needed from the laser to generate a plasma above the surface of the substrate. The ultrasound is then formed due to the contribution of the further expansion of the plasma. Normally, this method will cause damage on the surface of sample. For the latter, the surface of the substrate is heated up by a laser beam with lower intensity, and the resulting thermal expansion will generate SAWs without surface damage. In terms of single spot illumination, normally, the optical system consists of a spherical lens system, which can be used to control the size of the beam spot, and a pulsed laser system [67]. For single line illumination, a cylindrical lens system and a pulsed laser system are used [68-70]. In order to control the size of the light strip precisely, some papers suggest adding either a certain dimensional slit [71, 72] or a circular aperture with certain radius [73] before the cylinder lens system. However, for the SAWs generation in the thermal-elastic region, it is difficult to generate strong SAWs by either illumination method, due to the low optical intensity of laser beam and the broadband frequency spectrum of the generated SAWs, which reduces the signal-to-noise ratio (SNR) of the detection system. By narrowing down the bandwidth of the detection system [74], a stronger signal can be obtained. However, this can be challenging depending on the detection techniques used. Therefore, creating a SAW with narrower bandwidth would be a feasible way to increase the SNR.

2.2.2.2 Multi-line illumination

In order to form a narrow-band SAW, a multi-line illumination structure is studied and used as one of generation methods. For the ideal layout, the widths of lines should all be the same, and the lines should be distributed evenly with equal distance between two adjacent lines. As a result, a narrow bandwidth of frequency spectrum of created SAWs will be obtained at the desired frequency. There are two main groups of techniques used to achieve multi-line illumination: the line-projecting technique and the line-depositing technique.

To demonstrate the narrow-band signal generation by multi-line illumination, Huang *et al.* [74] reported using theoretical calculation approach based on the hypothesis of Gaussian incident beam to show the frequency spectra of the generated SAWs by single line and line array illumination, as shown in Fig. 2-3. The function *H(f)* is the Fourier transform of the single-line generated wave, and the function *S(f)* is the Fourier transform of the line-array generated wave based on the array containing 9 lines. A very broad spectrum of *H(f)* is obtained with the maximum amplitude at frequency $f_m = \sqrt{2}c / \pi d$, where c is the speed of the SAW and d is the beam radius of the Gaussian beam. In contrast, for the array function *S(f)*, several amplitude peaks with narrow bandwidth are obtained, which occur at frequencies $f_n = (n+1)f_0$, n = 0, 1, 2… , where $f_0 = 1/\Delta t$ is the fundamental frequency of *S(f)* and Δt is the travelling time for the wave to propagate between two adjacent lines. They also found that when the number (N) of lines in the array was large, the amplitudes of the subsidiary peaks of *S(f)* were much smaller. The signal bandwidth was determined by the number of lines, which was given by $2f_0/N$. Furthermore, regarding the travelling time Δt and the speed of the wave (c), the distance (δ) between two adjacent lines was calculated as

$$\delta = c \cdot \Delta t = \frac{c}{f}. \quad \text{(Eq. 2-1)}$$

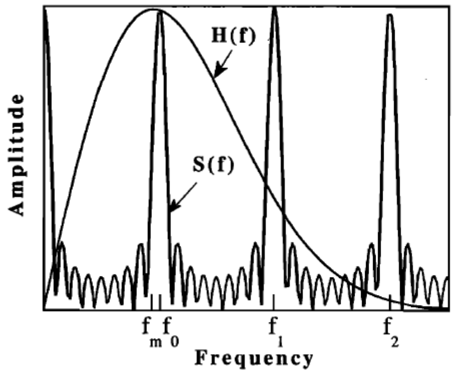

Fig. 2-3: Plots of theoretical frequency spectra of function *H*(*f*) and *S*(*f*) with an illuminating line array containing 9 strips [74].

Line-projecting technique

In this technique, the optical strips are transferred onto the substrate by projection, which is flexible by varying the line width and the line spacing on the same substrate. There are a few methods to choose: using a holographic diffraction grating [74], a periodic transmission mask [75], a lenticular array [76, 77], the beam interference from one laser [78-80] or two independent lasers [81] and a laser array [82]. However, for diffraction grating, transmission mask and lenticular arrays, it is easy to cause a non-uniform strength of the illumination lines and the line spacing. In addition, due to the low transmission efficiency of mask, it is possible that less than half of the optical intensity can be delivered to the sample.

Line-depositing technique

In order to generate stable SAWs, for the line-depositing technique, metal lines with high absorption coefficient are defined on the surface of a sample by photolithography. The cheap optical transducer (CHOT) [83] is one of the applications based on this technique. For the generation system (g-CHOT), a metal line array with certain interval is attached on the surface of substrate. The SAWs are created by heating up the strips with a pulsed laser, based on the thermoelastic effect. The properties of the generated wave are determined by the geometrical characteristics of the metal strips. For instance, the width and the spacing of lines are designed to match half the wavelength of the ultrasound [84]. Furthermore, straight parallel lines can generate plane wavefront SAWs while arc lines will focus the waves on a single point. The schematic of the g-CHOT is shown in Fig. 2-4.

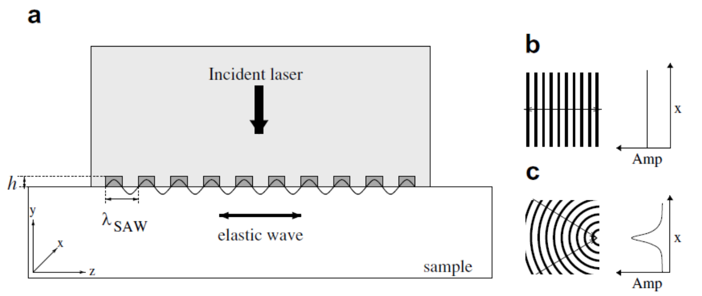

Fig. 2-4: (a) The structure of g-CHOT for the SAW generation, λ_{SAW} is the period of the metal lines, *h* is the height of lines; (b) and (c) show the straight lines and the arc lines generate the plan and the focused ultrasound waves, respectively [85].

2.3 Particle manipulation with standing ultrasonic waves

According to Section 2.1, standing ultrasonic waves can be classified as two types: standing bulk acoustic waves (SBAWs) and standing surface acoustic waves (SSAWs). Particle manipulation with each wave type requires different properties of microfluidic devices. In the following section, the features of typical standing waves and the detailed information of particle manipulation based on different wave types are introduced and discussed.

2.3.1 Standing waves

A standing wave is a stationary wave in which the amplitude of each point on the oscillation axis is constant. Normally, it is formed by the interference of two waves with same amplitude, wavelength and frequency but opposite directions. The two waves could be generated by one wave and its reflection or be generated by two individual sources. The point with minimum amplitude of the wave is called node. On the contrary, the point with maximum amplitude is called antinode. Due to the nature of a standing wave, it does not propagate through a medium and thus energy will not be transmitted.

Standing ultrasonic waves are therefore formed by the interference of two ultrasonic waves based on the mechanism of the normal standing wave. Particle manipulation with standing ultrasonic waves can therefore be investigated and developed.

2.3.2 Particle manipulation with standing bulk acoustic waves (SBAWs)

In this application, bulk acoustic waves (BAWs) are generated by a single bulk acoustic transducer attached on either the front surface [86-88] or the bottom surface [89-92] of a microfluidic chip with a glass-silicon structure (including a glass lid and a silicon channel). When the generated bulk acoustic waves penetrate into the channel, due to the superior reflection performance of silicon, standing BAWs are formed by the generated waves and related reflections. Thus, nodes and antinodes are created in the channel. In the meantime, lateral acoustic radiation forces are also generated by the SBAWs, which push particles towards either nodes or antinodes depending on the density and the compressibility of the medium and the particles.

2.3.3 Acoustic radiation force

When an acoustic wave propagates within the microfluidic channel, pressure fluctuations are generated, which result in an acoustic radiation force. In fact, particles experience four forces within the standing acoustic wave field: acoustic radiation force, viscous force, gravity force and buoyancy (shown in Fig. 2-5). The gravity force and the buoyancy are determined by the densities of the particle and the medium. Normally, the densities of the polystyrene beads and the cells used for manipulation are very similar to those of sample solutions, which results in the two forces being balanced. Thus, the motion of the particle is determined by the acoustic radiation force and the viscous force, which can be written as [7, 93]

$$F_r = \left(\pi p_0^2 V_c \beta_w / 2\lambda\right) \cdot \varphi(\beta, \rho) \cdot \sin\left(2k\vec{x}\right) \quad \textbf{(Eq. 2-2)}$$

$$\varphi(\beta, \rho) = \frac{5\rho_c - 2\rho_w}{2\rho_c + \rho_w} - \frac{\beta_c}{\beta_w} \quad \textbf{(Eq. 2-3)}$$

$$F_v = 6\pi\eta r\vec{v} \qquad \textbf{(Eq. 2-4)}$$

where F_r and F_v are the acoustic radiation force and the viscous force; p_0, λ, V_c, k, x are the amplitude of acoustic pressure, the wavelength of the acoustic wave, the volume of the particle, the wave vector, and the distance from a pressure node, respectively; and φ, ρ_c, ρ_w, β_c, β_w represent the acoustic contrast factor, the density of the particle, the density of the medium, the compressibility of the particle, and the compressibility of the medium, respectively; η, r and v are the medium viscosity, the particle radius, and the flow velocity relative to the particle, respectively. The direction of the acoustic radiation force is affected by the acoustic contrast factor φ. If $\varphi > 0$, the particle will be pushed to a pressure node whereas, if $\varphi < 0$, the particle will be pushed to an antinode.

Comparing Eq. 2-2 with Eq. 2-4, it can be seen that both forces are related to the size of particle. However, the acoustic radiation force is determined by the volume of the particle while the viscous force is controlled by the radius of particle. A large size particle will experience a larger net force, resulting in being moved faster towards either a pressure node or antinode than a smaller one. In addition, the acoustic radiation force is also related to the density and the compressibility between the particles and the medium.

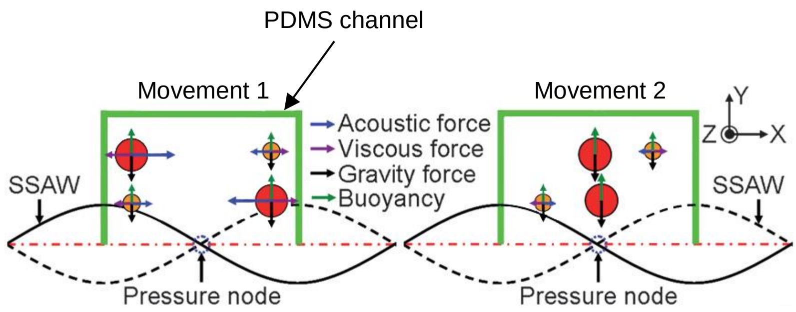

Fig. 2-5: Mechanism of particle separation with different sizes under the acoustic radiation force. Movement 1 shows the original positions of particles; movement 2 shows the process of the separation: larger particles experience larger net force and are moved to the pressure node faster than smaller ones [93].

2.3.4 Particle manipulation with standing surface acoustic waves (SSAWs)

As described in Subsection 2.3.2, the application of particle manipulation based on standing bulk acoustic waves (SBAWs) requires a high reflection property of the microfluidic chip, such as glass-silicon substrate. However, due to the complex fabrication processes and high power consumption, it can only be used in few parts of research field. Although the Polydimethylsiloxane (PDMS) polymer is commonly used for microfluidics, it cannot be used for SBAW-based particle manipulation due to the poor reflection performance.

In order to address above issues, in 2008, Shi *et al*. [15] investigated an novel method to manipulate particles by standing surface acoustic waves (SSAWs) within a PDMS channel. The SSAWs were created by two individual interdigital transducers (IDTs) with an array of parallel straight-fingers and equal finger spacing for each device. The interference of SAWs generated from IDTs resulted in the formation of the SSAW, meanwhile, pressure nodes and antinodes with a periodic distribution were created as well. When the SAWs encountered the liquid, a small amount of acoustic energy leaked into the liquid under the Rayleigh angle θ_R and propagated as a longitudinal pressure wave inside the channel, due to the refractive index difference between the substrate and the fluid. As a result, a pressure fluctuation was formed, causing the acoustic radiation force. Depending on the density and the compressibility of the medium and the particles, the particles were diverted towards either a pressure node or an antinode. The process of SSAWs generation is shown in Fig. 2-6. The IDTs were deposited on the lithium niobate ($LiNbO_3$) piezoelectric wafer by photolithography and the PDMS channel was fabricated by soft lithography. In addition, this technique is non-invasive, and offers a high sensitivity, low power consumption, low cost and easy fabrication.

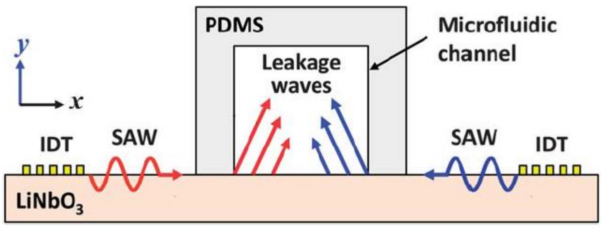

Fig. 2-6: Schematic of SSAWs generation with PDMS channel and IDTs [94].

Interdigital transducers (IDTs)

An interdigital transducer (IDT) is a device that converts electronic signals to mechanical surface waves or vice versa based on the piezoelectric effect. It consists of a sequence of interlocking metal electrodes, also called fingers, between two electrical bus bars. The transducer is usually defined on the piezoelectric substrate by photolithography. Normally, quartz or lithium niobate ($LiNbO_3$) are used as the deposition wafer. Lithium tantalite can be used as well. A typical SAW sensor includes two IDTs: one is for generation, which is driven by an input electronic signal, and the other is for detection, which is connected to a signal collection and analysis system. The schematic of a sensor system is shown in Fig. 2-7. For the particle manipulation system used in [15], both IDTs are generation devices in order to generate SSAWs. In addition, the wavelength (λ) and the frequency of generated SAW are determined by the width (d) of electrode and the spacing (D) between two adjacent electrodes of the IDT, which can be expressed as:

$$D = d = \lambda / 4 . \qquad \textbf{(Eq. 2-5)}$$

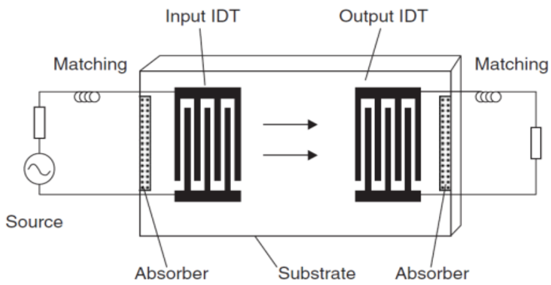

Fig. 2-7: Schematic of a typical SAW sensor [95].

Recent development

In the last seven years, several further investigations on SSAW-based particle manipulation have been reported by different research groups. They can be summarized as five parts: IDT development, parameter-affected acoustic radiation force, multi-dimensional manipulation, input signal study and other investigations. A review of each part follows:

IDT development

According to the design of a conventional IDT, the frequency of generated SAW is fixed as each electrode of the IDT is straight, which limits particle manipulation with different frequencies on one SSAW device. In early 2012, Ding *et al.* [8] designed a new IDT with slanted electrodes, which achieved the SAW generation with a range of frequencies on one device. The design method is the same as for conventional IDTs; however, the dimensions of the two different-size ends of each electrode are determined by the minimum and the maximum frequencies. The layout is shown in Fig. 2-8 (a). Furthermore, it is very difficult to implement miniaturization according to the short aperture of the SAW in a certain frequency. In order to solve this issue, at the end of that year, Ding *et al.* [96] improved the design by chirped IDT which integrates wider frequency range and aperture. In each IDT, the width and the distance between the straight electrodes increase linearly; as a result, it can generate a wide range of frequencies. By controlling the frequency of input signal, the position of the pressure node in the channel can be changed correspondingly. Thus, samples can be directed into different multi-channel sorters at the outlet region. The schematic is shown in Fig. 2-8 (b).

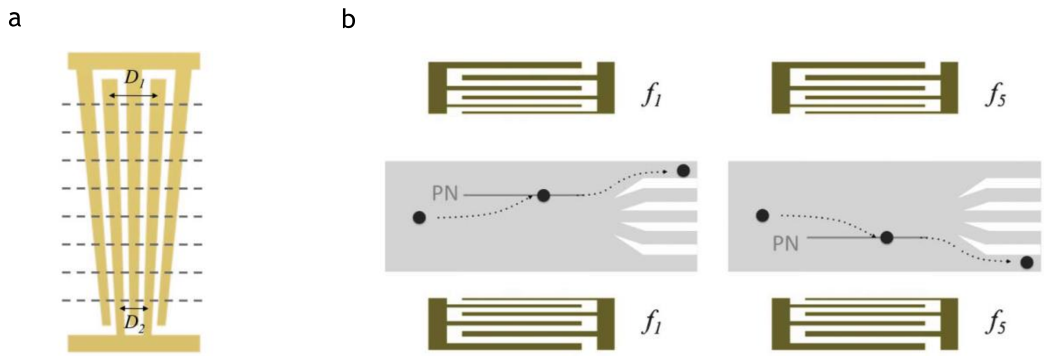

Fig. 2-8: (a) The layout of the slanted IDT; D_1 and D_2 are the period of slanted electrodes which are relative to the minimum and the maximum frequency, respectively [8]. (b) The schematic of chirped IDT; the solid lines represent the position of pressure node (PN) with relative frequency f_1 and f_5 [96].

Parameter-affected acoustic radiation force

As described in Subsection 2.3.3, the acoustic radiation force is affected by the size (volume) of particles, the density and the compressibility of the medium and the particles. Each parameter has been investigated in recent years. For the size of particles, researchers in [93] and [97] reported the separation of polystyrene beads with different particle sizes by two parallel IDTs with straight fingers. They also demonstrated that the larger particles experienced a larger acoustic radiation force, and could be moved faster towards to the pressure node than smaller particles. Moreover, platelets have been successfully separated from the human whole blood by SSAW in [9]. In terms of the density of particles, Nam *et al.* [98] separated alginate beads with three different densities, which contained different numbers of the P19 mouse embryonic carcinoma (EC) stem cells by cell encapsulation technology, and collected them from five outlets in a PDMS channel fluidic device. For the compressibility of particles, numerical modelling of MCF-7 cells and leukocytes separation with different sizes and compressibility was studied. From the results, they found that a small difference in compressibility can result in a significant increase of separation distance [99].

Multi-dimensional manipulation

For 2D particle manipulation, instead of using parallel IDTs, two orthogonal IDTs were used. The period of the generated pattern within PDMS channel was $\sqrt{2}/2$ times the SAW wavelength, which was reported in [7]. In addition, the shape of channel was changed from rectangle to square regarding the apertures and the positions of IDTs.

Input signal study

Most research about SSAW-based particle manipulation has been focused on concentrating particles or separating bulk target particles from flow stream in the channel. It has proved challenging to separate a single particle from main sample stream by SSAW, however Li *et al.* implemented it successfully in [100]. According to that paper, a single water-in-oil droplet was sorted from the main droplet stream and diverted into different micro-channel sorter by SSAW that was generated by two parallel chirped IDTs. The IDTs were designed with narrow apertures and driven by a pulsed input signal with a certain pulse duration at the desired repetition rate and relatively large voltage. They found that a higher input voltage was able to generate a stronger acoustic radiation force, which could push droplets faster in the y-direction (orthogonally to the flow direction).

Other investigations

Since 2014, Ding *et al.* [99] and Li *et al.* [19] successfully separated polystyrene beads with different sizes and cells, and white blood cells (WBCs) from debris by using tilted-angle SSAWs. Instead of placing the channel perpendicular to the oscillation axis of SSAWs, in this case it was placed with an angle of non-90 degree between the two IDTs to achieve tilted-angle SSAWs within the channel. Due to this arrangement, multi-pressure node lines with an angle inside the channel were generated without varying the driving frequency from fundamental to harmonics [101]. Benefiting from it, if target particles escaped from one pressure nodal line, they could be trapped again by the neighbouring nodal line and separated from the non-target particles. In addition, the SSAWs based cell culture was studied to achieve an organised cell co-culture within a single PDMS channel [102]. Moreover, the bacteria samples were also concentrated at a single pressure node by this technique [103].

2.4 Heat transfer

Heat transfer is a physical process of thermal energy being transferred from a high temperature subject to a low temperature subject. It occurs when there is a temperature difference between physical systems. There are four fundamental modes of heat transfer: advection, conduction, convection and radiation. More details about each mode are described in the following subsections.

2.4.1 Advection

Advection is the mechanical transport of a substance by bulk motion of fluid. The fluid can be either liquid or air, which contains thermal energy. The motion of fluid is formed due to heat transfer. More technically, advection should be the mass transfer by the velocity of the fluid, which is indirectly affected by the heat transfer occurring on the carrier. Advection happens when fluid currents are present, which indicates it cannot occur in rigid solids as molecular diffusion is not involved [104, 105].

2.4.2 Conduction

Conduction is heat transfer in the form of the transfer of microscopic kinetic and potential energy by the combination of vibrations and collisions of molecules, and movements of atoms and electrons within a body or between bodies in physical contact. It can take place in several states of substance including solids, liquids, gases and waves. Different from advection, there is no material moving from one place to another during conduction. It occurs when there is a temperature difference. The ability of a material to conduct heat is called thermal conductivity, which is measured in watts per meter-kelvin (W/(m·K)). Its value depends on the material and varies greatly from material to material [106-108].

2.4.3 Convection

Similar to advection, convection transfers heat energy by fluid flow from one place to another. It can occur in both liquids and gases. The moving fluid carries energy during the process. Convection can be considered as the combination of advection and conduction. The fluid motion can be generated by a temperature difference only or by extra mechanical methods. Therefore, there are two types of convection: natural convection and forced convection.

Natural convection

Natural convection is a type of fluid convection in which the fluid motion is generated without any external sources. It can occur when a temperature gradient established in the fluid. The density and the pressure of the fluid system vary with temperature distribution, resulting in the density of the fluid close to a high temperature region being less than that in a low temperature region. Regarding the principle of buoyancy, the less dense fluid moves towards the cool region, whereas the denser fluid moves towards the hot region due to gravity. This cooler fluid is then heated by the heat source and repeats the above fluid motion continuously, forming a convection current inside the system. The heat energy is transferred from the bottom of the convection cell to the top by the fluid. Therefore, natural convection can transfer mass as well. There is a special case in which the top and the bottom boundaries of the fluid system are cooled or heated uniformly; the convection generated under this situation is called Rayleigh-Bénard convection [106-110].

Forced convection

Forced convection takes place when the heated fluid is transferred physically by external sources, such as fans, pumps and other mechanisms. In this type of convection, a large amount of energy can be transferred efficiently [106-108].

2.4.4 Radiation

In this mode, heat energy is transferred through electromagnetic waves and radiated to surroundings in all directions. The radiation is generated by charge-acceleration or dipole oscillation due to particle motion in the heat source.

Differently from other three modes, no physical motions or interactions of matter are involved and no physical contacts are required between objects. The radiation rate of heat energy is proportional to the temperature of the object; as a result, the higher temperature of the source, the more energy is released [106-108].

2.5 Thermophoresis

Thermophoresis is a phenomenon in which a mixture of suspended particles migrate along the thermal gradient established in the system. Depending on the properties of the particles and the condition of the surroundings, particles can move either away from or towards the high temperature region. So far, several studies on the physical mechanisms and properties have been undertaken based on two conditions: gas and liquid conditions. In the gas condition, the physical mechanism of thermophoresis has been well understood and studied, whereas the studies are still controversial in the liquid condition. More details about each condition are described below.

2.5.1 Studies in gas condition

In the gas condition, generally, when a particle is near a high temperature region, it will experience a net force in the direction of decreasing temperature as hot gas molecules have greater momentum than cool molecules. The force the particle experiences is called the thermophretic force. However, it is determined by several factors, such as sample size, and the thermal conductivities of sample and surroundings. For small particles of which the diameters are smaller than the gas mean free path (which is 0.066 μm at 23 °C and 1 atm), the force can be expressed as [111]

$$F_{th} = -\frac{p\lambda d_p^2 \nabla T}{T} \qquad \textbf{(Eq. 2-6)}$$

where p is the pressure of surroundings, λ is the gas mean free path, d_p is the particle diameter, ∇T is the temperature gradient, and T is the absolute temperature of the particle. For large particles of which the diameters are larger than the gas mean free path, the temperature gradient within the particle needs to be considered, which will be determined by the thermal conductivity of the particle, k_p, and thermal conductivity of the surroundings, k_a. Therefore, the force can be modified as [111]

$$F_{th} = -\frac{9\pi d_p \eta^2 \nabla T k_a}{2\rho_g T k_p} \quad \textbf{(Eq. 2-7)}$$

where η is the viscosity of surroundings and ρ_g is the density of surroundings. From the equation, it can be seen that the thermophretic force is directly influenced by the thermal conductivities of particles and surroundings.

2.5.2 Studies in liquid condition

Thermophoresis can be considered as the combination of Brownian diffusion and an additional particle transport mechanism. For a colloidal sample with low concentration (c), in the presence of a thermal gradient (∇T), the total mass flux (J) can be written as [30, 112-116]

$$J = J_D + J_{TD} = (-D\nabla c) + (-cD_T \nabla T) \quad \textbf{(Eq. 2-8)}$$

where D is the Brownian diffusion coefficient, ∇c is the particle concentration gradient, D_T is the thermal diffusion coefficient (also termed thermophoretic mobility). The first term J_D arises from Brownian diffusion based on Fick's first law, and the second term J_{TD} arises from thermal diffusion [117, 118]. Since mass flux can also be expressed as the product of the velocity field of mass elements flowing and the mass concentration (c), the thermophoretic velocity (v_{th}) can be written as [31, 115, 116, 119]

$$v_{th} = -D_T \nabla T\ . \quad \textbf{(Eq. 2-9)}$$

In the steady state, thermophoretic transport and Brownian diffusion are balanced (J = 0), for small temperature differences (dT), we can obtain

$$\frac{dc}{c} = -S_T dT \quad \textbf{(Eq. 2-10)}$$

where S_T is Soret coefficient and $S_T = D_T/D$. The particle transport direction is determined by the sign of D_T. When D_T >0, particles will be moved towards the cold region with 'thermophobic' behaviour, whereas particles will be moved towards the warm region with 'thermophilic' behaviour when D_T is negative [30, 113-116, 119]. Therefore, by controlling D_T, particles can be either trapped by the heat source to achieve a tweezing application or moved away from the heat source. Unlike the theoretical studies under gas conditions, so far, there is no general physical model of particle thermophoresis in liquid and no general clear picture of the characteristic of D_T, which restricts the applications of thermophoresis in colloidal science. In the following subsections, several potential physical mechanisms and studies of the characteristics of D_T and S_T reported from literature are reviewed.

Physical mechanisms

Thermoosmosis in the electric double layer (EDL). When a particle is suspended in a liquid, normally an electric double layer is formed along the boundary between the particle surface and the aqueous surroundings. The particle movement is mainly affected by the excess hydrostatic pressure within the diffuse layer, which vanishes far beyond the Debye length. When a non-uniform temperature distribution is established within the liquid, the pressure gradually varies along the boundary, forming a relatively higher pressure at the cold side. Eventually, a flow moving towards the higher temperature region is created along the surface due to the combination of osmotic pressure and viscous forces. The flow velocity reaches the maximum at a distance beyond one Debye length. With further studies, it is found that the velocity can be affected by the salinity of solvent as well [120-123].

Thermoelectric effect. In an electrolyte solution, the positive and negative free ions can be driven along the temperature gradient due to the thermoelectric effect. In the steady state, an electrostatic field is formed between the hot and the cold regions, which affects the movements of suspended particles depending on their charge. The sign of particle velocity depends on the both the surface and thermoelectric potentials. Normally, most colloids are negatively charged with the surface potential ζ varying from -10 mV to -100 mV. However, both signs of the thermoelectric potential can be observed depending on the chemical components of the electrolytes [30, 122-124].

Thermally driven depletion forces. When colloidal samples are suspended in a polymer solution of a non-uniform concentration, particles migrate towards the low concentration region due to the depletion force. Similarly, when a temperature gradient establishes inside the solution, polymers accumulate in the low temperature region, which results in the particles being diverted to the warm region [125, 126].

Dispersion forces. For particles suspended in simple liquid, the van der Waals interaction is dominant. The thermoosmosis flow along a solid-liquid interface occurs in the presence of the solvent density gradient. Except for water under 5 °C, due to simple liquid expansion upon heating, the high density solute accumulates in the cold region, which results in particles being more likely attracted to the cold region rather than the hot region under the effect of the molecular dispersion force. Consequently, the solvent is driven towards the high temperature region, which leads to an opposite motion of suspended particles or macromolecules [122].

Key research findings

Ionic strength and PH dependence

Regarding the literature [30], in the cases of 26 nm carboxyl spheres dispersed in CAPS-NaCl and citric acid-NaCl buffers with a particle concentration of 2 wt%, D_T increases with ionic strength from a negative value to a positive value when the ionic strength is less than or equal to 5 mM. Differently, at high ionic strength (≥100 mM), the buffers have no significant influences on D_T. In terms of PH, at low ionic strength, the D_T values in the CAPS-NaCl buffer (PH=10.5) are higher than those in the citric acid-NaCl buffer (PH=3.3). Again, at high ionic strength, PH does not have any significant influence on D_T. Here, CAPS is 3-(cyclohexylamino)-1 propanesulfonic acid. In contrast, the S_T value in pure sodium dodecyl sulfate (SDS) surfactant decreases with solution concentration until 100 mM. Beyond this concentration, S_T is not affected. For cases of SDS solutions containing NaCl and NaOH separately with different concentrations, the S_T values decrease with solute concentration as well. In the NaCl-SDS solution, the sign of S_T is always positive, whereas it becomes negative in the NaOH-SDS solution when the solute concentration is higher than 50 mM [28]. Furthermore, D_T is also dependent on the composition of both the carrier liquid and the particle. For colloidal samples of polystyrene microbeads suspended in a 0.1% FL-70 plus 0.02% w/v NaN_3 carrier solution and a water solution containing 0.10 mM TBAP, D_T increases with particle size in the former case, whereas it shows a decreasing trend in the latter case. Here, FL-70 is a mixed anionic and nonionic surfactant and TBAP is tetrabutylammonium perchlorate, which is an electrolyte [24].

Temperature dependence

The effects of temperature on D_T and S_T have been studied and reported by several authors. For a general trend, both coefficients increase with temperature, varying from a negative value to a positive value based on studies in many aqueous and non-aqueous colloidal systems [22, 23, 25, 26, 28, 29, 31]. Normally, the sign changes to positive at around 4-6 °C for aqueous solutions. However, the sign-switching temperature point strongly depends on the composition of the carrier solution. For instance, the temperature points for unsalted and salted solutions are lower than those points in a NaOH solution. In addition, it is also solute concentration dependent. In a NaOH solution, the value increases with the NaOH concentration [28, 29]. However, not all of cases will follow the above trend; for a colloid containing a temperature-responsive polymer suspended in ethanol, D_T shows a decreasing trend with temperature and changes sign at around 30 °C [27].

Particle size dependence

Unlike the clear trend showing the effect of temperature, the findings on the particle size dependence are relatively controversial, especially for particles in the nanometre and micrometre size. Specifically, according to literature [22], studies of polystyrene (PS) spheres with a radius varying from 11 nm to 253 nm suspended in a solution containing DI water, heavy water (D_2O) and Triton X100 with ionic strength of 10 mM have been implemented. The results show that D_T is independent on particle size with temperature gradient of 0.1 K/μm. In contrast, under a higher temperature gradient (0.05 - 0.2 K/μm) and wider particle size range (R = 20 nm – 2 μm), the measurements show an increasing trend with bead size [31, 116]. This time, the colloidal samples were dispersed in DI water containing 1 mM Tris that restricts the PH of solution to 7.6. Surprisingly, the D_T value decreases with particle size, when the temperature gradient is reduced to

2E-4 K/μm and the particle size is narrowed down from 26 – 130 nm [30]. The potential reasons causing these three significant differences are due to the different order of magnitudes of thermal gradients and different compositions of the carrier liquid. However, this important issue still demands further investigations.

Collective effect

Furthermore, the effects of interparticle interactions on D_T also need to be considered. As summarized in [127], D_T significantly increases when the particle mass fraction of the sample solution increases from 0.01 to 0.3 g/g. When further increasing the mass fraction to 0.9 g/g, the value of D_T is not affected. The collective effect can be explained only by the thermoelectricity theory when the particle mass fraction is smaller than 0.08 g/g. Here, the sample solution is made by suspending silica beads with 70 nm diameter into an aqueous solution containing 0.03 mM Sulpho-Rhodamine B. In contrast, the D_T value varies from positive to negative with particle concentration increasing from 0.061-1.92 g/g when 100 nm and 500 nm PS beads are dispersed in DI water [128]. Differently, for the same solution containing particles with 1 μm diameter, D_T remains negative but slightly increases with mass fraction varying from 0.12–3.91 g/g. Both phenomena arise from the electrostatic repulsive force due to the thermal gradient. Therefore, the interparticle interaction has strong effects on small particles at a low mass fraction, whereas the weaker effects are seen for large particles.

Applications

Due to D_T being strongly dependent on temperature, ionic strength and PH of the sample solution, several applications focusing on particle accumulation and trapping have been undertaken by tuning the sign of D_T. As reported in [115], a large population of PS particles with 477 nm in diameter were successfully accumulated in the hot region of a microfluidic channel in a 100 mM NaOH solution with flow rate of 0.01 μL/min. In contrast, particles with the same size suspended in a 100 mM NaCl solution were accumulated at the cold region of the channel under the same flow rate. The thermal gradient was established by gluing a resistive Joule heater onto one side of the channel. In [119], the local concentration of 20 nm diameter PS particles with thermophilic property were controlled within a cuboidal fluid cell by a focused laser beam that was used as heat source. The two opposing sides of the cell were attached to thermoelectric coolers, in order to create a strong thermal gradient. Further, the thermophoretic tweezing was achieved by trapping and manipulating a single PS particle through heating a substrate coated with a nanoporous Au film with a focused laser beam. In this case, particles with a relatively high surface charge density were required for effective thermophoretic trapping. Therefore, by adjusting the surface charge density, particle separation could be achieved. The surface charge was modified by adding ionic/non-ionic surfactants into the sample solution. The laser beam was controlled by a digital micromirror device (DMD) to implement manipulation. Again, the application was undertaken based on a negative D_T [32]. In addition, crystal generation could be achieved by accumulating colloidal particles using thermophoresis as well. In terms of applications in biological studies, thermophoresis could be used to analyse protein functionality and the interactions of proteins or other molecules in biological liquids such as blood serum or cell lysate [127].

2.6 Beer–Lambert law

The Beer-Lambert law describes the properties of light attenuation for different materials in which the light is travelling. By definition, the internal transmittance (T) can be expressed as [129]

$$T = \frac{I}{I_0} = e^{-\alpha L} \qquad \textbf{(Eq. 2-11)}$$

where I and I_0 are the optical intensity of the transmitted and the incident light, α is the absorption coefficient of material, L is the distance that the light has travelled within the material. Here, the equation is obtained by neglecting the light reflection and light scattering at the surfaces of the material. Furthermore, the absorption coefficient is related to the wavelength of the incident light (λ_0) and the imaginary part of the refractive index of the material (κ), of which the general term can be expressed as [130]

$$\alpha' = \frac{4\pi\kappa}{\lambda_0}. \qquad \text{(Eq. 2-12)}$$

2.7 Summary

Regarding the literature review on acoustic tweezing based on interdigital transducers (IDTs), it can be concluded that although this approach can offer significant advantages in terms of being non-invasive, low power consumption and label-free, the choice of substrate is restricted by piezoelectric materials only. In addition, the waves are generated with only a fixed frequency or narrow frequency range, which limits the further applications. In contrast, laser ultrasonics would be a better approach, due to the multiple choices for the substrate material, the flexible aperture size and the wider frequency range of the created acoustic waves. With inspiration from the literature about laser ultrasonics and acoustic tweezers (see Sections 2.2 and 2.3), the laser-induced SAWs in the thermoelastic physical region using single modulated diode laser was performed by three different illumination methods, which were single spot, single line and multi-line illuminations. For the detection, several detection techniques were used, including visualisations of the fluid flow in a single droplet and particle movements in a thin chamber, measurement of the temperature variation on the surface of the substrate based on the thermal imaging technique, and surface vibration measurements by a fibre-optic hydrophone, laser Doppler vibrometer and slanted interdigital transducer (IDT). The detailed information will be described and discussed in Chapter 4.

With inspiration from the literature about heat transfer and thermophoresis (see Sections 2.4 and 2.5), we developed a new platform to achieve trapping and manipulation of microparticles and biological samples with a light absorber in a thin fluidic chamber by the combined effect of laser-induced thermal convection flow and thermophoresis. Through further studies, an intuitive theoretical model to identify the underlying physics was developed, and related physical characteristics were investigated, demonstrating the possibility of this new platform for the development of the optical-thermophoretic tweezing technique. The detailed information will be described and discussed in Chapter 6.

Chapter 3

Methods

In this chapter, the optical system setup for experiments of the laser-induced SAWs detection and the microparticle manipulation by laser-induced thermal forces is presented. Then, the designs and fabrication of the sample devices used in the experiments are described. Furthermore, the protocols for the preparation of colloidal solutions, biological sample mixtures and cell culture are introduced.

3.1 Optical system setup

The optical system setup used for most of the experiments in Chapters 4 and 6 is shown in Fig. 3-1. The whole setup comprised two systems: a microscope system and a laser system. For the microscope system, a cold white LED array was used as the illumination source. Two groups of aspheric condenser lenses with different focal lengths were used to collimate and adjust the size of the light beam, labelled ① and ③. The two irises ② were the condenser diaphragm and the field diaphragm, respectively. The beam after the condenser lens was reflected by a 50:50 beamsplitter ④ and projected into a 10x objective (NA = 0.25). Part ⑤ was a tube lens, which was followed by a CMOS camera with resolution of 1280 x 1024 and a colour sensor. In terms of the laser system, an aspheric collimation lens ⑥ with short focal length was used to collect and collimate the beam. Due to the fact that the objective was also used to focus the laser beam during the experiment, two bi-convex lenses (⑦ and ⑧) with different focal lengths were used to ensure the beam was focused on the sample plane. Furthermore, a short pass dichroic filter ⑨ was used to reflect the laser beam into the objective but be transparent to visible light. The particles were manipulated using a multimode CW laser diode at 808 nm with maximum optical power of 1 W. Here, the particular wavelength chosen was because the relatively larger absorption coefficient was obtained at that wavelength, regarding optical properties of the substrate. In Chapter 4, the laser-induced SAWs were generated by single spot and single line illumination methods. Regarding the working mechanisms of SAW generation based on the two methods (see Subsection 2.2.2), a substrate with large absorption coefficient is required to ensure the generation region is close to the surface. Moreover, according to the commercial market for laser diode, the highest optical power was delivered at that wavelength as well.

The diffraction-limit angular resolution of the microscope system is determined by following the Abbe diffraction limit expressed as [131]

$$d = \frac{\lambda}{2NA} \qquad \textbf{(Eq. 3-1)}$$

where *d* is the minimum resolvable distance that is the minimum distance between distinguishable objects in an image, λ is the light wavelength and *NA* is the numerical aperture. The system resolution can be increased by either shorter light wavelength or larger NA value. The diameter (Φ) of focused laser spot is determined by following the theory of Airy disk expressed as [131]

$$\phi = 1.22\frac{\lambda}{NA}. \qquad \textbf{(Eq. 3-2)}$$

The size of the focal spot can be reduced by either shorter light wavelength or larger NA value. Therefore, in order to increase the optical intensity of the laser illumination region, the rear aperture of the objective needs to be fully illuminated, which increases optical resolution as well.

a b

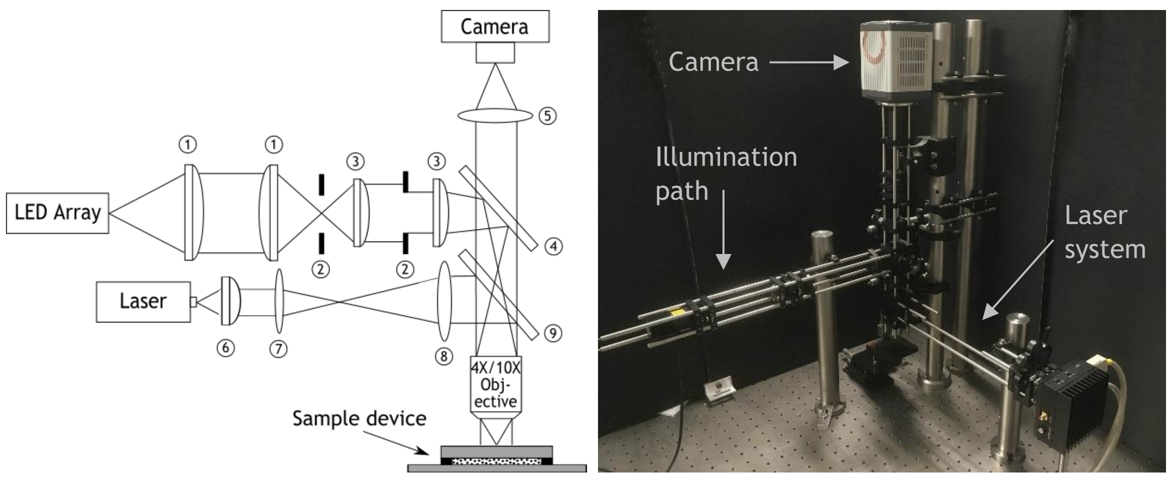

Fig. 3-1: (a) Schematic of the experimental setup; ① and ③: aspheric condenser lenses with different focal lengths, ②: condenser/field diaphragm, ④: 50:50 beamsplitter, ⑤: tube lens, ⑥: aspheric collimation lens, ⑦ and ⑧: bi-convex lenses with different focal lengths, ⑨: short pass dichroic filter. (b) Real system setup.

3.2 Sample device fabrication

3.2.1 Laser-induced SAW device fabrication

In Chapter 4, three illumination methods were used to generate SAWs using the laser beam, which were single spot illumination, single line illumination and multi-line illumination. Different SAW devices were designed and fabricated to match these illumination schemes.

For single spot and single line illumination, a silicon (Si) substrate with one third of the surface area coated with an aluminium (Al) thin layer was used as the SAW device and fabricated by standard photolithography. The dimensions (L x W x H) of the substrate were 3.5 cm x 2.6 cm x 0.5 mm and the thickness of the metal layer was 30 nm. Here, a Si substrate chosen was due to the property of high optical absorption and low cost. With benefits of even higher optical absorption of the thin Al coating, almost all of light energy could be absorbed within the thickness of a few tens of nanometres, resulting in the generation source being treated as on the surface of the substrate. Therefore, the SAWs was enhanced. The thickness of 30 nm chosen was to ensure the incident laser beam being fully absorbed by the Al layer.

The fabrication procedure is shown in Fig. 3-2 (a). The substrate was first purified by two-step solvent cleaning: acetone with ultrasonic cleaning for 5 mins, followed by isopropanol (IPA) with ultrasonic cleaning for another 5 mins. The substrate was then blow-dried by nitrogen. Here, the benefits of using solvent cleaning and ultrasonic cleaning were that the solvents could dissolve contaminates quickly and flow off the sample surface. Due to their high volatility, they often evaporated quickly and left much less residue than water cleaning. The purpose of using two solvents was to ensure that the sample was returned to a contaminant free state. Contaminates could include particulate matter on the surface as well as any traces of organic, ionic, and metallic impurities. During ultrasonic cleaning, microscopic cavitation was formed and collapsed by the sonic agitation, which created shock waves that loosened and detached contaminates. The dried substrate was then exposed to an oxygen plasma, with power of 100 W for 2.5 mins, in order to remove any stubborn debris remaining after solvent cleaning. Afterwards, metal deposition was performed using an electron beam evaporator (Plassys II, PLASSYS-BESTEK, France) to form the Al thin layer, with the non-deposition area covered by a cleaned glass slide. Fig. 3-2 (b) shows a SAW device after fabrication.

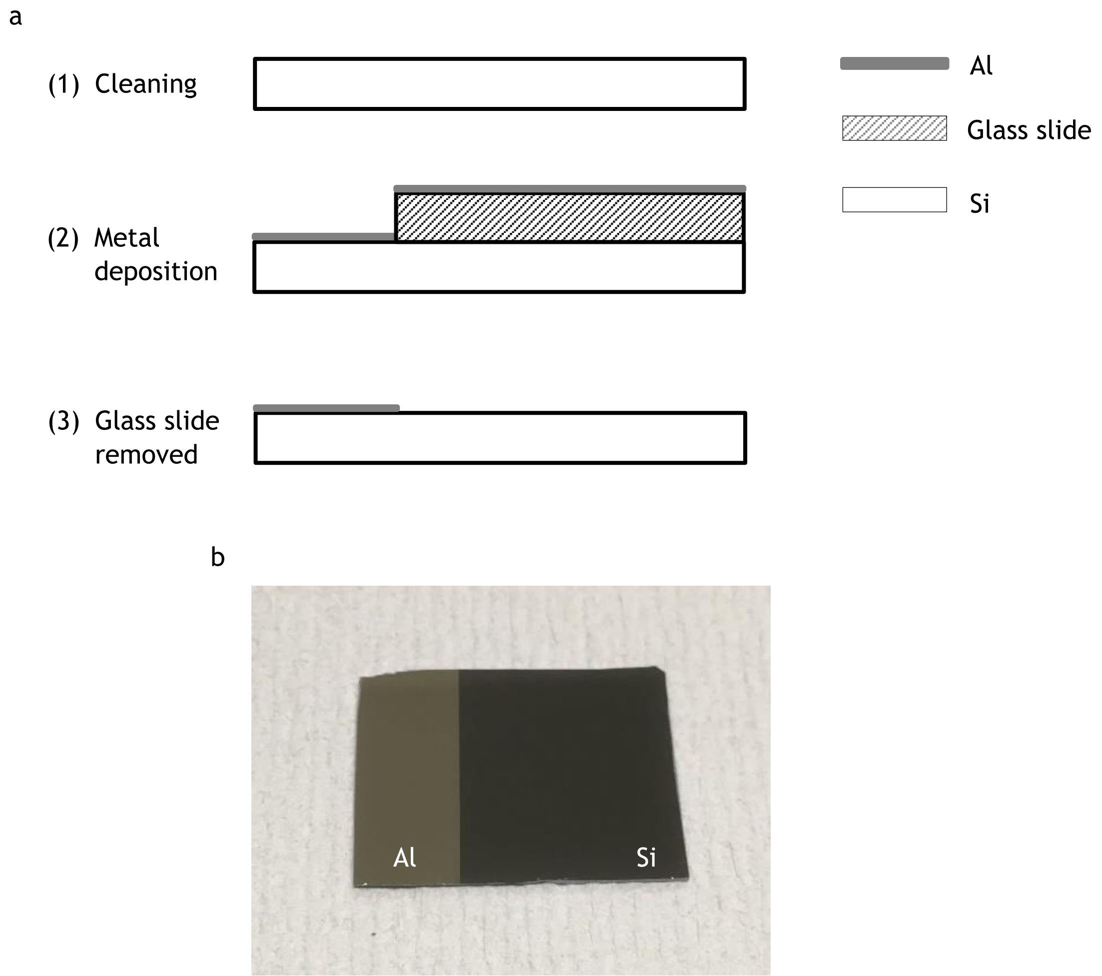

Fig. 3-2: (a) Fabrication process for SAW device based on single spot and single line illumination patterns. 1. Silicon substrate is cleaned by solvent cleaning combined with ultrasonic cleaning, and oxygen plasma; 2. Glass slide placed on part of sample and deposition of 30 nm Al layer; 3. Process finished by removing glass slide. (b) Real device after fabrication.

For multi-line illumination, a metal line array (1 cm x 1 cm) used as SAW device was fabricated on either a soda-lime glass slide (7.6 cm x 2.6 cm x 1 mm) or a lithium niobate ($LiNbO_3$) wafer (4 inch, 128° Y-cut, double-sided polished, Roditi, UK), depending on the SAW detection technique used (see Sections 4.6 and 4.7). The array patterns were transferred onto both substrates by standard photolithography using the procedure shown in Fig. 3-3 (a). Substrates were cleaned by following the same procedures of solvent cleaning, ultrasonic cleaning, and blow-dried by nitrogen as in Fig. 3-2. Next, the cleaned substrates were spin coated with MCC primer 80/20 at 4000 rpm for 30 s to help increase photoresist adhesion to the sample surface, followed by a second spin coating with S1818 positive photoresist at the same speed and time. The substrates were then soft baked on a hotplate at 95°C for 2.5 mins to remove any solvent residues and increase the density of the photoresist. The coated substrates were exposed under UV light through a photomask containing the pre-designed patterns by a mask aligner (Mask aligner MA 6, SÜSS MicroTec AG, Germany) for 5 s (for glass slide) and 6 s (for $LiNbO_3$ wafer), respectively. The exposed resists were developed in Microdev developer (Microposit, Shipley, UK), which was prepared by diluting the original stock solution in pure deionised water with ratio of 1:1, for 1 min 25 s. Afterwards, critical cleaning was performed by exposure of the patterned substrates to an oxygen plasma with power of 100 W for 2.5 mins, which was followed by metal deposition of 100 nm molybdenum (Mo) to form the line array. Here, the Mo layer chosen was due to its relatively low reflectance comparing to other common metals (see Table 5-1), in order to reduce the loss of the incident optical power caused by reflection. The thickness of 100 nm chosen was to ensure the optical energy being fully absorbed by the metal lines, in order to enhance the SAWs, regarding the working mechanisms of SAW generation by the multi-line illumination (see Subsection 2.2.2). A metal lift-off step was performed by soaking the devices in acetone at 50°C overnight. Fig. 3-3 (b) and (c) show the finished SAW devices with related detection parts. Here, the metal dots on the $LiNbO_3$ wafer in image (c) are fabricated unintentionally, and are the patterns created by holes in the mask holder due to the wafer size being larger than the mask. Luckily, these dots neither contact the array and the detector (slanted IDT) nor lie within the gap between the two devices. Therefore, the experiment should not be affected by them. Fig. 3-3 (d) and (e) show microscope images of the fabricated metal strips of the array and the electrodes of the slanted IDT under 4x magnification. Please note, as transmitted light microscopy was used when taking the images, both features are represented as the dark-colour patterns.

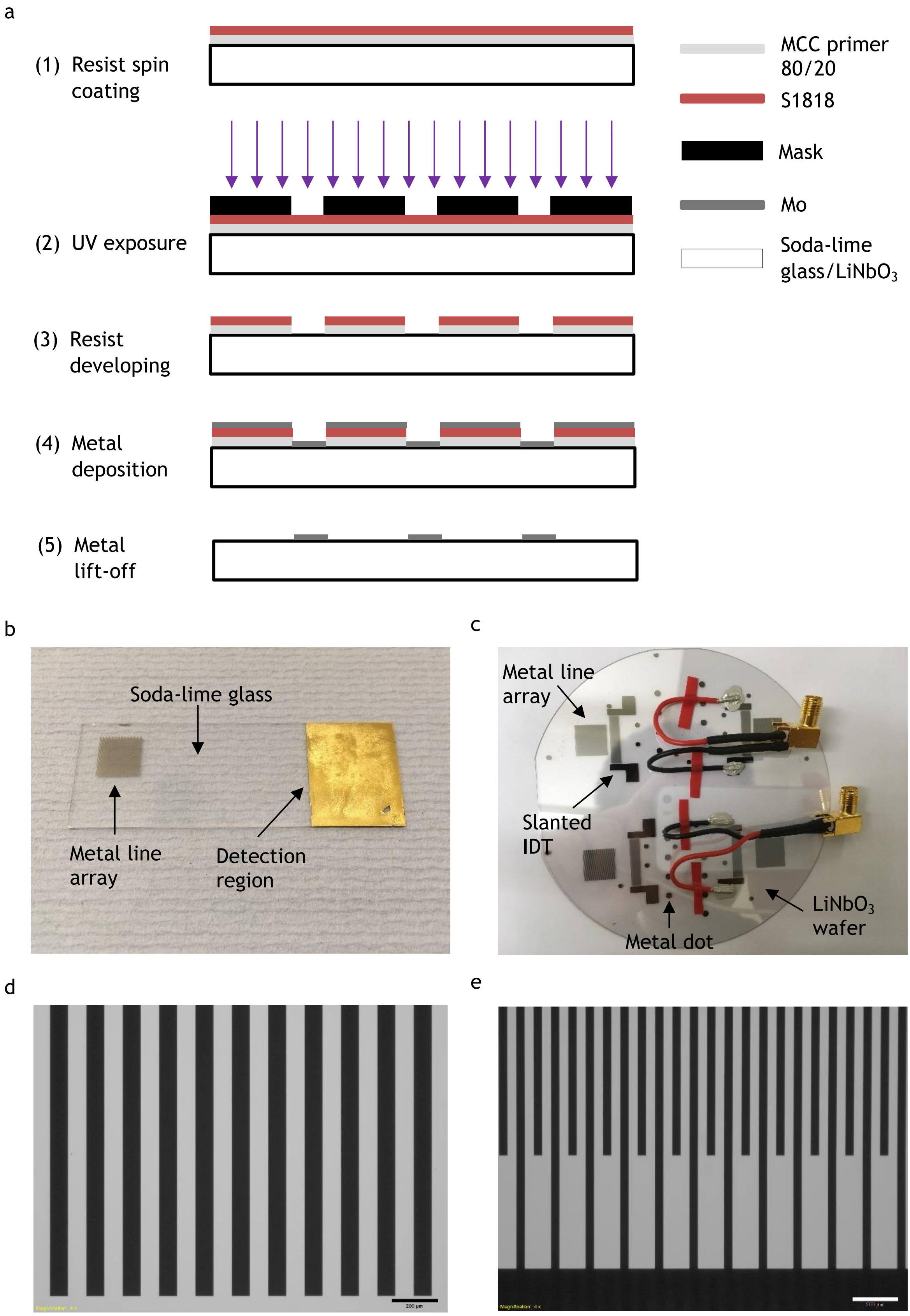

Fig. 3-3: (a) Fabrication process for SAW devices based on multi-line illumination. 1. The substrate is cleaned and spin coated with MCC primer 80/20 and S1818 resist followed by soft baking at 95°C for 2.5 mins; 2. Transfer of array pattern by UV exposure for 5-6 s; 3. Development of exposed resist; 4. Deposition of 100 nm Mo layer; 5. Metal lift-off in acetone at 50°C for overnight. (b) Actual device based on a glass slide after fabrication. (c) Actual device based on a $LiNbO_3$ wafer after fabrication (the metal dots being fabricated unintentionally). (d) and (e) are microscope images of part of the metal line array and the slanted IDT under 4x magnification. Scale bar: 200 μm.

In terms of the photomask design, the array patterns were drawn by an IC (integrated circuit) mask layout editor L-Edit (v2015.4, Mentor Graphics Ltd) and fabricated by Compugraphics International Ltd with a minimum feature size of 10 μm. According to Eq. 2-1, the line width was designed to be half that of the generated SAW wavelength. For the experiments based on the soda-lime glass slide, two SAWs with different frequencies were generated, 10 and 15 MHz. Because the speed of sound in soda-lime glass is 3127 m/s, the strip widths were 156.4 and 104.2 μm, respectively. For the experiments based on the $LiNbO_3$ wafer, waves with 25 MHz were generated. Because the speed of sound is 3980 m/s in the y-direction, the strip width was 79.6 μm.

3.2.2 SAW detection device

In terms of detection techniques, for the single spot and single line illumination schemes, no any further device fabrication was required. However, for the multi-line illumination, further fabrication was needed for both types of devices. For the device based on soda-lime glass slide, a light-reflected detection region located 4.5 cm away from the metal array was required, as a laser Doppler vibrometer (LDV) was used for SAW detection. To fabricate the detection region, after the last step of metal lift-off, the substrate surface was coated with S1818 resist using a pipette except for the detection area, followed by soft baking on a hotplate at 95°C for 5 mins. Afterwards, the resist region was covered by a cleaned glass slide and a gold (Au) layer with thickness of 100 nm was deposited on both the detection area and the glass slide. Finally, the resist was lifted-off, by soaking the device in acetone at 50°C for 10 mins. The fabrication procedure is shown in Fig. 3-4 and the device after fabrication is shown in Fig. 3-3 (b). Please note the image shown in Fig. 3-3 (b) was taken 2 years after the fabrication being completed. Due to its poor surface adhesion, some parts of the gold layer in the detection region have fallen off, which does not reflect the quality of the fabrication.

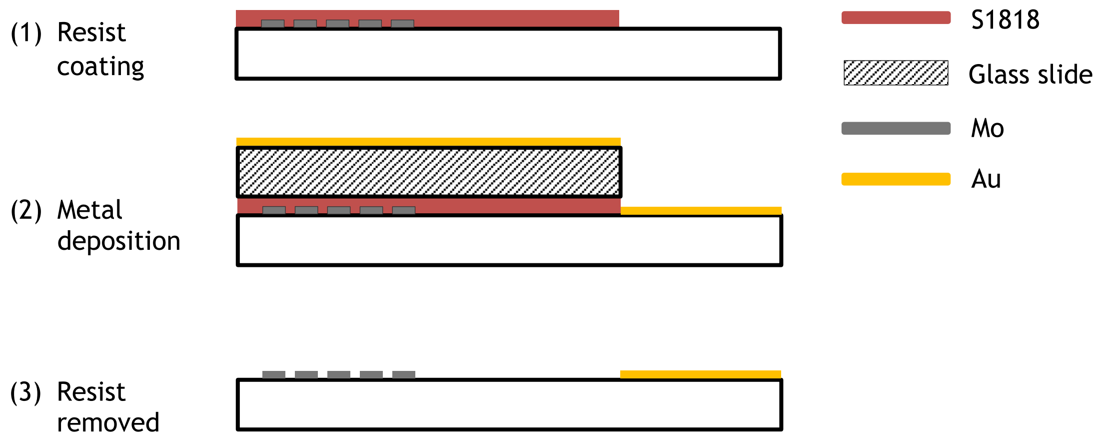

Fig. 3-4: Fabrication process for SAW detection device based on soda-lime glass substrate. (1) The glass substrate with metal line array is coated with S1818 resist by pipetting and soft baking at 95°C for 5 mins; (2) Deposition of 100 nm Au layer with resist region covered by a cleaned glass slide; (3) Resist is removed in acetone at 50°C for 10 mins.

For the device based on the $LiNbO_3$ wafer, a slanted IDT was used as a detector, which was fabricated at the same time as the line array and followed exactly the same procedure (see Fig. 3-3 (a)). According to Eq. 2-5, the width of fingers should be one quarter of the generated SAW wavelength. As the detection frequency range was designed from 24 to 26 MHz, the widths of the two ends of the electrodes were 41.46 and 38.27 μm, respectively. Finally, the wires were connected to the device with silver paint applied to the connection pad of the interdigitated electrodes. The device after fabrication is shown in Fig. 3-3 (c). As mentioned in Subsection 2.3.4, the IDT could be used for either SAW generation or SAW detection. Therefore, after fabrication, the performance of the slanted IDT was assessed by monitoring the vibrations of several 5 μL water droplets under different SAW frequencies within the detection frequency range. These droplets were placed in front of the electrodes and along the aperture of the device. The IDT was actuated by connecting a signal generator (TG5011, Aim-TTi Ltd.) combined with an amplifier (ZHL-5W-1, Mini-Circuits, Inc.) via SMA connectors.

3.2.3 Fluidic device

The device used in the experiments in Chapter 6 was a thin fluidic chamber that was constructed by attaching a glass cover slide, cut to appropriate dimensions, onto a substrate separated by a thin spacer frame (see Fig. 3-5 (b)). Depending on the experimental conditions, the substrate could be either a silicon substrate or a normal microscope slide. Two holes, with diameter of 2 mm, drilled diagonally and close to diagonally opposite corners of the cover slide were used as inlet and outlet. After injecting the sample solution into the chamber, the inlet and the outlet were sealed by tape. The exterior edges of the chamber were sealed by a tiny amount of petroleum jelly to prevent any perturbations from liquid evaporation. The thickness of the chamber was around 100 μm. The dimensions (L x W x H) of the microscope slide and glass cover slide were 7.6 cm x 2.6 cm x 1 mm and 1.9 cm x 2.6 cm x 1 mm, respectively. Fig. 3-5 shows schematics of the device and real devices constructed on a microscope slide.

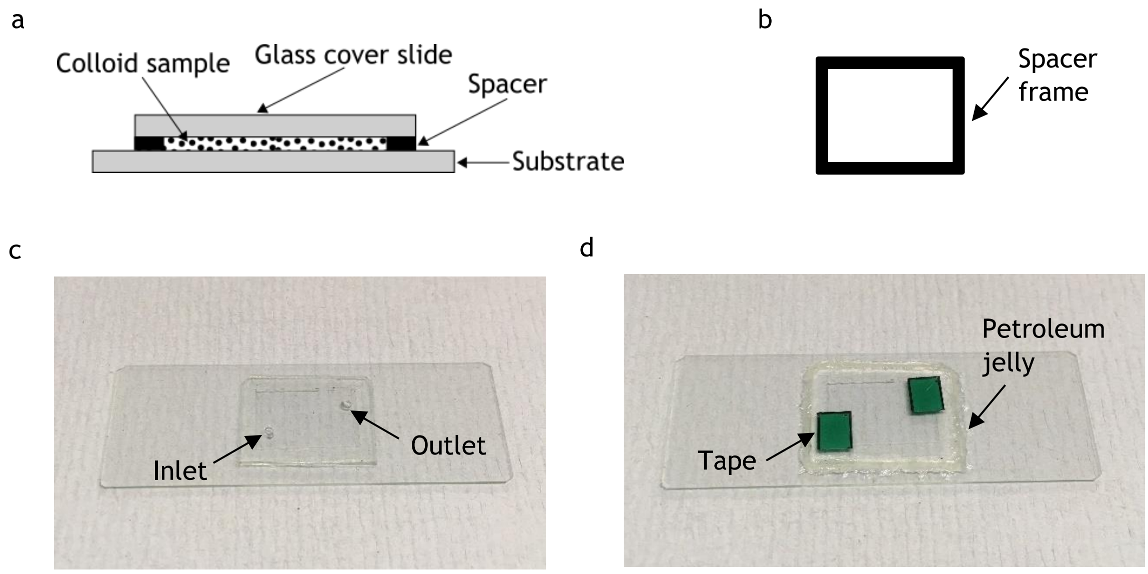

Fig. 3-5: (a) and (b) are schematics of the fluidic device and the spacer frame, respectively. (c) and (d) are the real devices based on a normal microscope slide without/with sealants, respectively.

3.3 Sample solution preparation

3.3.1 Colloidal sample of microbead suspension

The colloidal solutions were prepared by suspending the as-supplied polystyrene microbead stock solutions with different bead sizes (10%w/w, 1.0 μm, 4.95 μm and 20 μm in diameter, Bangs Laboratories, Inc.) in deionised water with a dilution ratio of 1:100, following by vortex mixing in order to obtain a homogeneous suspension. The prepared colloidal solutions were then injected into the sample device manually through the inlet using a pipette. The colloidal samples will be used in Subsections 6.1.1 and 6.2.1.

3.3.2 Colloidal mixture of microbead and SWNT cluster

The colloidal mixture of microbeads and single-walled carbon nanotube (SWNT) clusters was prepared in two main steps. In the first main step, in order to prepare the SWNT cluster suspension, an SWNT conductive ink (1 mg/mL, Sigma-Aldrich Co. LLC) was dispersed into ultra-pure deionised water at ratio of 140 mg : 1 mL followed by vortex mixing. Because the conductive ink was solvent-based, in order to remove any solvent effects on the experimental results, the mixture was then washed at least three times before moving to the next step. In the washing step, the mixture was centrifuged at 4000 rpm for 10 minutes, followed by removal of the supernatant. Then, the sample pellet was refilled with fresh cell culture medium RPMI1640 followed by vortex mixing. Here, the RPMI1640 was chosen, as the final purpose of the experiment is to manipulate biological samples using our device. To form appropriate clusters, the suspension was then sonicated for 2 hours in a beaker cooled with ice cubes.

In the second main step, the as-supplied polystyrene microbead stock solutions with different bead sizes (1.54 μm, 2.88 μm, 4.95 μm, 7.79 μm and 9.97 μm in diameter) were suspended in the SWNT cluster suspension with dilution ratios of 0.5 μL : 1 mL, 3 μL : 1 mL, 0.5 μL : 1 mL, 20 μL : 1 mL and 60 μL : 1 mL, followed by vortex mixing. The prepared colloidal solutions were then injected into the sample chamber manually by pipetting. The colloidal samples will be used in Subsection 6.2.3 and Section 6.3.

3.3.3 Biological mixture of microbead and SWNT cluster and Jurkat cells

The biological mixture was prepared in three main steps. In the first two steps, a colloidal mixture of microbeads and SWNT clusters was prepared following the same procedure as in the last Subsection, with extra two steps after the washing step. The mixture was sterilized under UV light for 1 hour, followed by washing one more time before the 2-hour sonication. The purpose of adding the extra steps is to maintain good cell viability during the experiments. In the final step, a Jurkat cell solution with pre-adjusted concentration (Jurkat, Clone E6-1 (ATCC® TIB-152™), 9.15×10^7 cells/mL) was added into the colloidal mixture with a dilution ratio of 20 μL : 1 mL.

Please note that once the sample solution was sterilized, the rest of the preparation was performed in a cell culture hood. The prepared biological mixture will be used in Subsection 6.3.4.

3.3.4 Jurkat cell subculturing

Jurkat cells (Jurkat, Clone E6-1 (ATCC® TIB-152™)) were cultured in a 25 cm^2 culture flask containing the RPMI1640 cell culture medium (Gibco, Thermo Fisher Scientific Inc.) with a supplement of 10% fetal bovine serum (Gibco, Thermo Fisher Scientific Inc.), 1% penicillin–streptomycin (Gibco, Thermo Fisher Scientific Inc.) and 1% L-Glutamine (Gibco, Thermo Fisher Scientific Inc.). An incubator with constant temperature of 37°C and 5% CO_2 was used during the culture. The cells were passaged once the cell density reaching to roughly $1x10^6$ cells/mL (normally, every 2-3 days) in order to maintain the standard growing rate. During the subculturing, the cell solution was centrifuged at 4000 rpm for 4 minutes, followed by removal of the supernatant. Then, the cell pellet was refilled with the same volume of fresh cell culture medium as before. Finally, the cell density was diluted to $1x10^5$ cells/mL by transferring a proper volume of undiluted cell solution to a new culture flask containing fresh cell culture medium.

3.4 Software

3.4.1 COMSOL Multiphysics

COMSOL Multiphysics is a simulation software package, which can perform single or multiple physics modelling by finite element analysis. In Chapter 5, the heat transfer model coupled with the solid mechanics model will be used for modelling the temperature differences and relative displacements on the surface of a device illuminated by a modulated laser beam. In Chapter 7, the heat transfer model coupled with the laminar flow model will be used for modelling the thermal distribution across the device and the fluid flow within the thin chamber.

3.4.2 Tracker v4.11.0

Tracker is a free video analysis software, which is built on the open source physics Java framework and written by Douglas Brown. It is mainly used to monitor the single bead movement over time by analysing video frames. With its built-in particle tracking function, after defining dimensions and coordinates, objects can be easily tracked manually or automatically with real-time display of position, velocity and acceleration overlays. The software will be used in Chapters 6 and 7 to analyse the trajectories and speeds of colloidal samples.

3.4.3 OrCAD Capture and PSpice

OrCAD Capture is a schematic capture software, which is mainly used to draw the schematic outline of an electric circuit on the screen. Most commercial components can be easily found in its built-in library. Once a component is added to the schematic drawing, related information, such as electric characteristics, physical dimensions and footprint are added automatically to enable PCB design.

OrCAD PSpice is a SPICE (Simulation Program with Integrated Circuit Emphasis) circuit simulator, which is used for modelling analogue and mixed-signal circuits to provide complete signal analysis and verification. The simulator is integrated into OrCAD Capture, which is convenient for circuit design. However, not all components can be found in the built-in library. In particular, for the laser diode, the electric characteristics had to be built from scratch or modified manually from a built-in component with similar characteristics, using SPICE commands. In Chapter 4, these two programmes will be used to assess the performance of the transient total drive current of the modified laser modulation circuit.

3.4.4 Altium Designer

Altium Designer is PCB design software, which integrates schematic capture, 2D/3D PCB design, FPGA development and release/data management. One of the benefits of using this software is the online component library. The library is built on a huge online database that includes electric characteristics, physical dimensions and footprint layouts of almost every component on the market, making the software very convenient to use for beginners. In addition, the online library is updated frequently. Another benefit is its 3D PCB layout viewing function. With this function, the designed PCB with virtual components can be easily rotated and zoomed in/out, which is very useful for examining whether the footprint matches with the pins of the component, and the spacing between two adjacent components. In Chapter 4, the PCBs of the frequency-mixer circuit, which would be used in the laser-induced SAWs detection, were designed and fabricated by this software.

Chapter 4

Laser-induced SAWs detection

Back to the 1990s, researchers had demonstrated the feasibility of using modulated CW semiconductor lasers for acoustic wave generation in the kilohertz to low megahertz (below 2 MHz) frequency range on either metal substrate or metal-film coated substrate by single spot illumination, showing the magnitude of the wave could go up to 60 pm [36, 37]. For the generation in the higher megahertz frequency range (1-200 MHz), in 2004, researchers reported the maximum magnitude of the wave was approximately 450 fm at 50 MHz and 87 MHz using the same illumination method and modulated beam from a diode laser [34, 35]. Compared to the minimum magnitude (around 0.6 nm) of the surface acoustic wave for particle manipulation measured in Chapter 5, the results from above literature were not sufficient. Therefore, before achieving microparticle manipulation by laser-induced SAWs, it was necessary to check whether SAWs could be created under our experimental conditions, and to measure the amplitude of the SAWs.

In this part of the thesis, firstly, laser-induced SAWs were created by following the methods used in the previous literature, which were single spot and single line illuminations. Specifically, a modulated laser beam emitted from a single diode laser was focused on a silicon substrate partially coated with a thin metal layer. Secondly, in order to enhance the SAWs, a different approach was used by the multi-line illumination with a modulated single diode laser. Specifically, a modulated laser beam was loosely focused on a metal line array that was previously fabricated on a transparent substrate. Benefiting from the design of the line array, the SAWs with narrow frequency bandwidth was enhanced under low optical intensity of the illumination, which increased the signal-to-noise ratio (SNR) for detection. Theoretically, the more lines being illuminated, the stronger waves should be obtained. However, large beam size was required in order to illuminate multiple lines, which significantly reduced optical intensity, resulting in the generated SAWs being even weaker than previous approaches. Therefore, this approach was limited by the balance between the optical intensity of the illumination and the number of illuminated line.

For the detection, several methods were used, including visualisations of the fluid flow in a single droplet and particle movements in a thin chamber, measurement of the temperature variation on the surface of the substrate based on the thermal imaging technique, and surface vibration measurements by a fibre-optic hydrophone, laser Doppler vibrometer and slanted interdigital transducer (IDT). However, due to the low signal-to-noise ratio (SNR) of the system setup, the low optical intensity of the illumination and the shallow optical modulation depth, the extremely weak waves were generated resulting in none of the expected signals being observed. Therefore, in order to investigate the amplitude of the waves, numerical modelling based on our experimental conditions was performed. The detailed information will be described and discussed in Chapter 5.

4.1 Laser-induced SAWs test by fluid streaming generation in single droplet

In this Section, it was attempted to observe laser-induced SAWs by visualising microparticle behaviours inside a single water droplet. The method of SAW generation was chosen as a single line illumination on a silicon substrate with a thin metal coating. By placing the droplet at different positions relative to the SAW irradiation, different phenomena should be observed as reported in the literature. However, through several attempts by varying the droplet size, beam size, modulation signal type and frequency, no obvious phenomena could be seen. Therefore, the optical system and alternative detection method were updated in an attempt to overcome the limitations of the current system setup.

4.1.1 Experimental method

Optical system setup

According to the literature in Section 2.3, in order to achieve particle manipulation by SAWs, a stream of SAWs with proper aperture should be generated, which can be created by the single line illumination method. Different from the experimental system setup in Section 3.1, in this experiment, the whole system included two separate optical systems: the laser system and the microscope system. The laser system was used for SAW generation and the microscope system was used for SAW detection that was in the form of particle behaviour visualisation. For the laser system, the schematic layout is shown in Fig.

4-1. As can be seen from the Figure, the system consists of six parts. For the laser diode (LD) system (part ①), a single mode CW laser diode with wavelength of 788 nm and optical power of 400 mW was chosen. The laser diode was placed into a laser diode mount with an extra function of frequency modulation function that could go up to 500 MHz. For the beam collimation and circularization system (part ②), two plano-convex cylindrical lenses with different focal lengths were included, to collimate the divergent beam of the laser diode. Each lens would collimate and control the size of beam in one direction by being placed horizontally or vertically. In terms of the beam size controlling system (part ③ and ④), two bi-convex lenses with different focal lengths were used to control the length (aperture) of the beam. Part ⑤ contained two broadband dielectric mirrors that were used to adjust the beam direction. Following to the literature [68-72], a plano-convex cylindrical lens (part ⑥) was used to focus the beam into a single line.

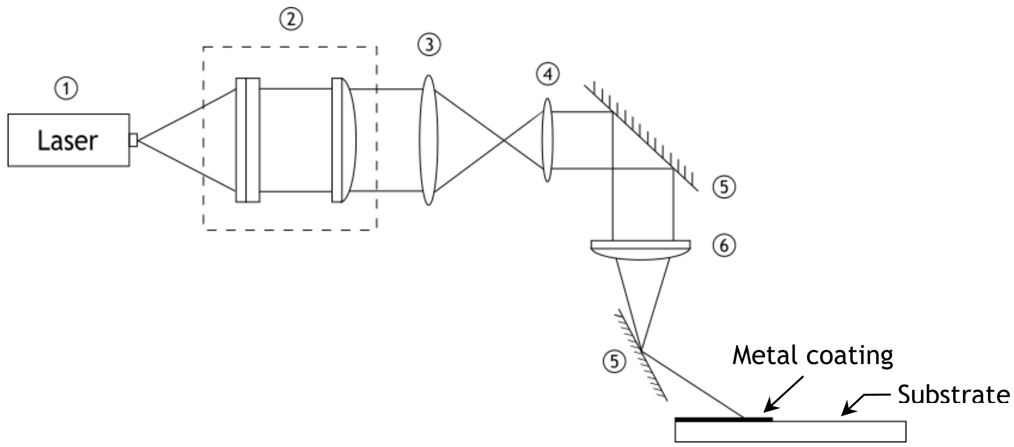

Fig. 4-1: The schematic layout of the laser system; ①: laser diode system, ②: beam collimation and circularization system, ③ and ④: bi-convex lenses, ⑤: broadband dielectric mirror, ⑥: plano-convex cylindrical lens.

For the microscope system, a simple brightfield reflection microscope based on the Köhler illumination technique was designed and assembled. As is well known, the Köhler illumination technique should create a smooth and uniform illumination background, which reduces image artefacts and provides high sample contrast. Normally, there are two diaphragms in the system: the condenser diaphragm, by which the image contrast is controlled, and the field diaphragm, by which the size of the illumination background is determined [132-134]. Fig. 4-2 shows the schematic layout of the microscope system used in the experiment. The whole system includes eight parts. Part ① is a cold white LED array that was used as the illumination source. Parts ② and ④ are aspheric condenser lenses with different focal lengths to collimate and adjust the size of the light beam. Part ③ is the condenser/field diaphragm. Part ⑤ is a 50:50 beamsplitter. Part ⑥ is a 4x objective (NA = 0.1). Parts ⑦ and ⑧ are the tube lens and a CMOS camera with resolution of 1280 x 1024 and a colour sensor. In order to obtain a clear background, the smallest illumination area should be in the centre of the image. Fig. 4-3 shows images of the smallest field aperture and the colloid sample of polystyrene beads with 45 μm in diameter. As shown in the Figure, only the image within the field aperture can be seen through the camera, which means the field diaphragm is working well. The positions of the reflected background light from the bead surfaces in the focal plane of the objective, which appear as focused light spots, are almost in the centre of the particle surfaces, which indicates the system is well aligned.

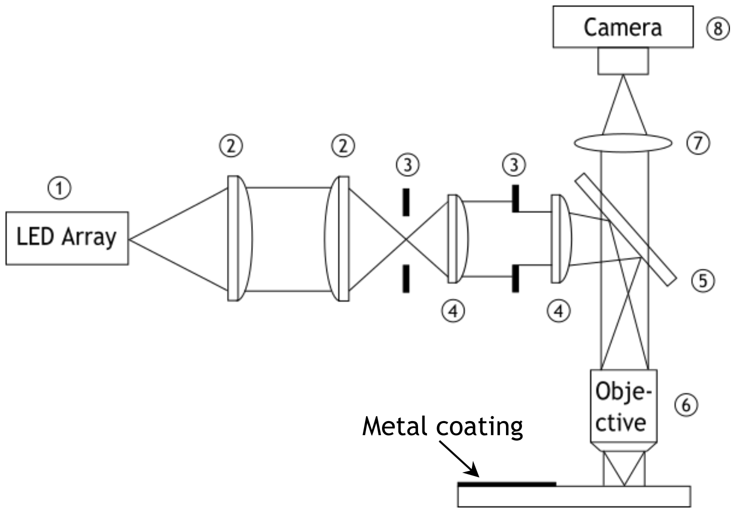

Fig. 4-2: Schematic of the microscope system; ①: LED array, ② and ④: aspheric condenser lenses with different focal length, ③: condenser/field diaphragm, ⑤: 50:50 beamsplitter, ⑥: 4x objective (NA = 0.1), ⑦: tube lens, ⑧: CMOS camera.

a

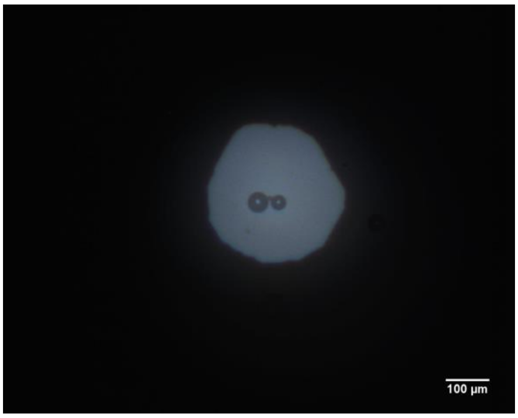

b

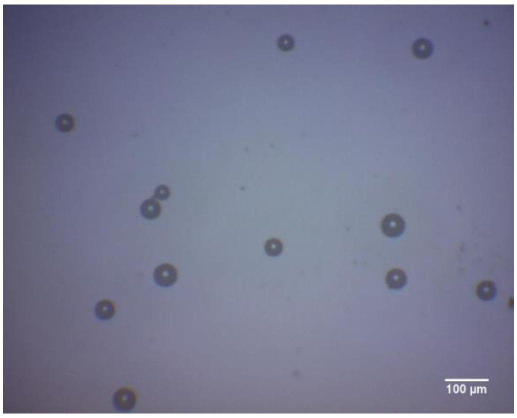

Fig. 4-3: (a) The image of the smallest illumination background area; (b) the image of the colloid sample with 45 µm polystyrene beads.

LD modulation

According to the specifications of the laser diode (LD) mount, a Bias-T circuit was integrated into the LD driving board, which was used to supply the high frequency modulation. The input impedance of the circuit was 50 Ω. In order to modulate the LD successfully, an external AC signal was required. In the following experiment, a function generator (TG5011, Aim-TTi Ltd.) was used as the external modulation source. Due to the maximum input power of the modulation circuit being 200 mW RMS, the modulation depth was limited. In order to operate the mount safely, calculations showed the peak voltage of the signal should not exceed around 3 V for a square wave. The performance of the modulation was assessed by a fast photodetector (HSA-X-S-1G4-SI, Laser Components (UK) Ltd.) and an oscilloscope (RTO1022, Rohde & Schwarz UK Ltd.). To avoid saturating the photodetector, an ND filter with transmission of 1.304% was placed after the laser diode, which was followed by a 10x objective (NA = 0.25) to focus light onto the detector. Fig. 4-4 shows the modulation results from the oscilloscope for a square wave with frequency of 20 MHz. As shown in the Figure, a square wave with period of 50 ns is captured by the oscilloscope, which demonstrates successful LD modulation. However, signal ringing occurs when the optical power is at upper bound, which may be caused by the Bias-T.

a

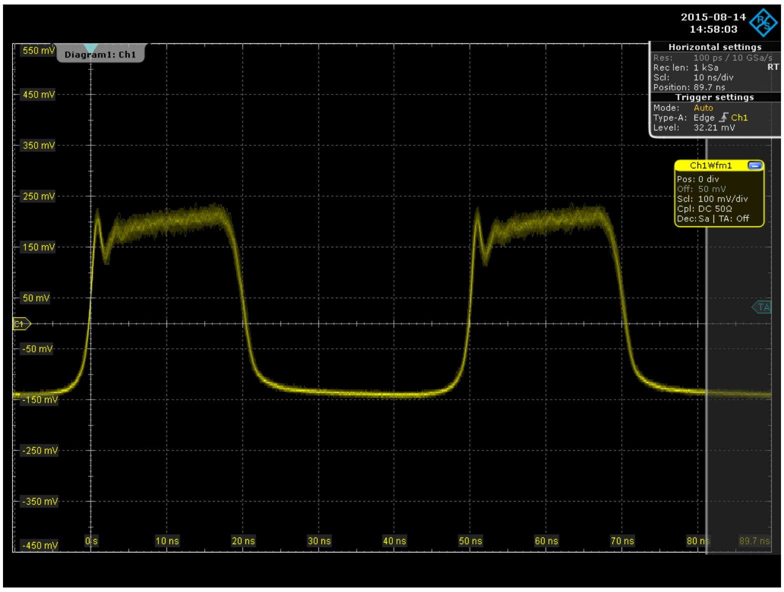

b

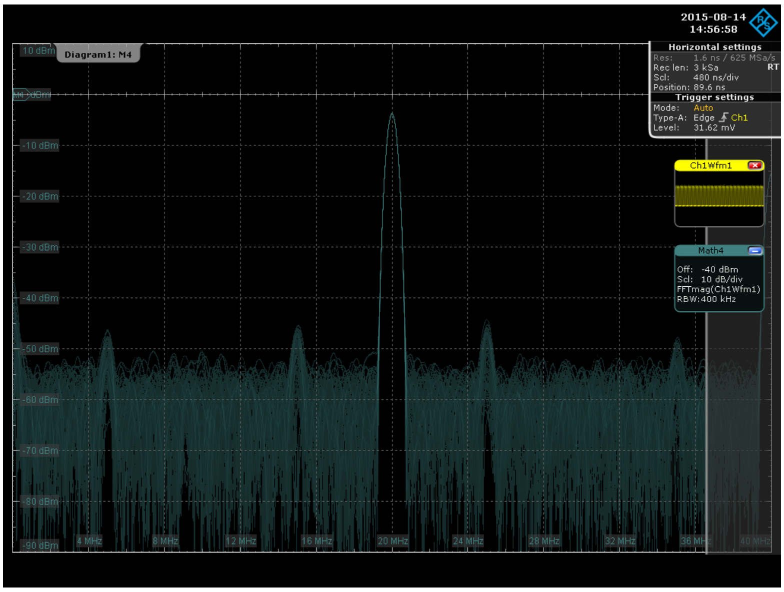

Fig. 4-4: (a) Modulated optical waveform detected by the photodetector (Input signal: square wave at 20 MHz & Time scale: 10 ns/div); (b) the corresponding frequency spectrum (FFT function).

Experiment overview

As reported in the literature [135-139], it is possible to generate fluid streaming inside single droplets using SAWs. Because of the difference between the velocity of sound in the fluid and the substrate, when SAWs encounter a droplet, a small amount of acoustic energy leaks into the liquid at an angle θ_R and propagates as a longitudinal pressure wave inside the droplet. Here, the angle is known as the Rayleigh angle, which obeying Snell's law of refraction [94, 140]

$$\sin(\theta_R) = \frac{v_{fluid}}{v_{solid}} = \frac{n_{solid}}{n_{fluid}}, \quad \textbf{(Eq. 4-1)}$$

where v_{fluid} and v_{solid} are the speeds of sound in the liquid and the substrate, n_{fluid} and n_{solid} are the corresponding refractive indices. Therefore, pressure fluctuations are formed which causes an acoustic radiation force, resulting in the fluid streaming being generated. By placing the droplet at different positions relative to the propagation of the SAW radiation, different phenomena should be observed. When the SAWs propagate through the centre of the droplet, if the amplitudes of the waves are strong enough, symmetrical fluid streaming and convection related to the radiation direction can be observed. However, if the amplitude of the wave is relatively low, then several concentric rings are created inside the droplet due to the generation of standing waves. When the droplet is placed along one side of the radiation propagation, because only the part of the volume interacts with the waves, the droplet experiences an asymmetric distribution of SAW radiation, which causes a single fluid streaming to be generated. As a result, the particles inside the droplet are rotated and concentrated at the centre of the droplet by the flow. Here, particles inside the liquid should experience two forces: Stokes's drag force and the acoustic radiation force. The above three phenomena are observed under the situation of Stokes's drag force dominating. For the case of the acoustic radiation force dominating, if the particle size is larger than 15 μm in diameter and the frequency of SAW is higher than 20 MHz, samples will be concentrated at the periphery rather than at the centre of the droplet, when the liquid partially encounters with the wave radiation. Fig. 4-5 shows schematic layouts of the fluid streaming patterns inside the droplet with different placing positions when Stokes's drag force plays the domination role.

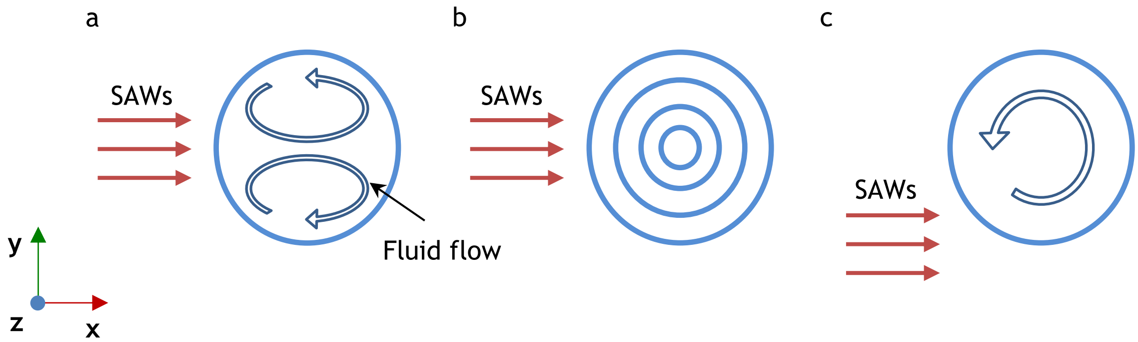

Fig. 4-5: Schematics (top view) of fluid flow patterns when droplet encounters SAW radiation at different positions: (a) the centre of the radiation propagation with high wave amplitude, (b) the centre of the radiation propagation with relatively low wave amplitude, (c) one side of the radiation propagation.

According to the above findings, it is possible to detect SAWs by visualising the particle behaviours in a single droplet. In this work, a silicon substrate, partially coated with an aluminium thin layer of thickness 30 nm, was used to generate the SAWs. The laser beam illuminated the coated region and a droplet containing a colloidal sample was placed on the non-coated region by pipetting, but close to the beam. The colloidal sample was prepared following the method described in Subsection 3.3.1. In this experiment, polystyrene beads with 10 μm in diameter were dispersed into DI water. Here, the aluminium thin layer was used because a stronger surface displacement could be obtained, based on the numerical modelling results in Subsection 5.2.2. During the experiment, droplets with three different volumes were tested separately, which were 2.5 μL, 5 μL and 10 μL. With reference to the literature, three positions were chosen for placing the droplets: the centre of the SAWs radiation, one side of the SAW radiation with half and less than half of the droplet interacting with waves. The LD was modulated with two types of input signals: square wave and pulse wave with pulse durations of 20 ns and 30 ns. The repetition rates of both signal types were swept from 200 kHz to 20 MHz. In addition, laser beams with two different sizes were projected onto the substrate: around 250 μm and 83 μm in the x-direction, and 5 mm and 3 mm in the y-direction, respectively. Fig. 4-6 shows the schematic layout of the experiment.

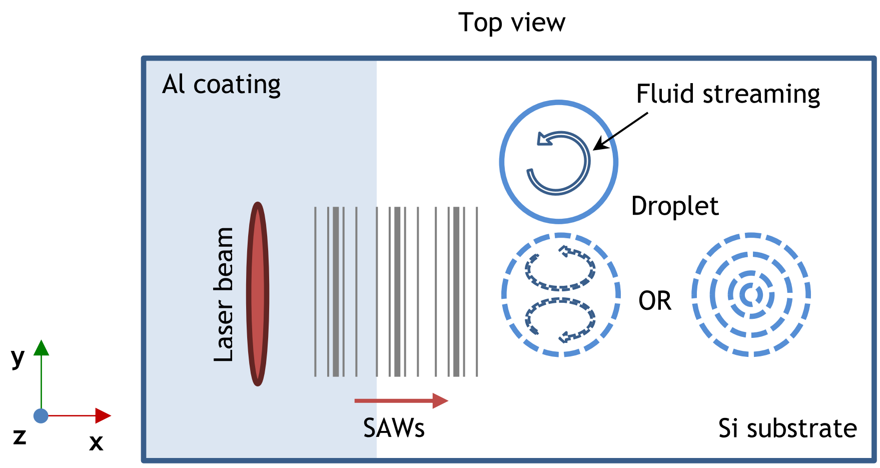

Fig. 4-6: The schematic layout of the SAW-induced fluid streaming experiment.

4.1.2 Results and discussion

Based on the experimental methods, the behaviour of particles inside the droplet should be expected to be similar to the phenomena reported in the literature under the situation of Stokes's drag force dominating. The experimental results were grouped and summarized based on the droplet-placing positions with different parameter combinations, and are listed in Table 4-1. From the Table, it can be seen that no obvious fluid streaming is generated inside the droplet, due to the strong Brownian motion of the particles. However, it is too early to conclude that no SAWs were created. Further, we measured the optical power of the laser beam reaching the sample; nearly 32.75% of total energy was lost in the system. Moreover, we also realised that the generated waves may have been too weak to create fluid streaming inside the droplet. Therefore, we tried to improve the optical system and use an alternative detection method, which will be discussed in Section 4.2.

Droplet position	Beam width	Metal layer	Signal type	Signal frequency	Droplet size	Results
Centre of the SAW radiation propagation	250 μm, 83 μm	Al (TH[1]: 30 nm)	Square wave, Pulse wave (PW[2]: 20 ns, 30 ns)	200 kHz-20 MHz	2.5 μL, 5 μL, 10 μL	No fluid streaming (Only random movement rather than concentric rings)
Half of the droplet encountered SAWs	250 μm, 83 μm	Al (TH: 30 nm)	Square wave, Pulse wave (PW: 20 ns, 30 ns)	200 kHz-20 MHz	2.5 μL, 5 μL, 10 μL	No fluid streaming (Only random movement rather than one directional rotation)
Less than half of droplet encountered SAWs	250 μm, 83 μm	Al (TH: 30 nm)	Square wave, Pulse wave (PW: 20 ns, 30 ns)	200 kHz-20 MHz	2.5 μL, 5 μL, 10 μL	No fluid streaming (Only random movement rather than one directional rotation)

Table 4-1: Experimental results of the laser-launched SAWs test by fluid streaming generation in single droplet.

4.2 Laser-induced SAWs test by particle movement visualization

In this Section, it was attempted to detect the laser-induced SAWs by monitoring the particle movements in a thin chamber. Because of the system limitations identified in the last Section, this time a single spot illumination method was chosen. In order to reduce the effect of liquid evaporation, a thin chamber was used rather than a droplet. After varying several experimental parameters, the expected particle movement still could not be observed. Therefore, it was necessary to figure out the best solution to improve either the SAW generation system or the detection system.

[1] Thickness of metal layer

[2] Pulse width of the input modulation signal

4.2.1 Experimental method

As discussed in Section 4.1, the generated SAWs may have been too weak to create fluid streaming inside the droplet. In order to strengthen the waves, the optical intensity in the illumination area was increased by reducing the beam size through adjusting the optical path of the laser system. Eventually, instead of using a line-shape light source, a single beam spot with a minimum diameter of 1 mm was obtained on the substrate. Moreover, a thin chamber filled with colloidal samples was used rather than a droplet, as the aim of the experiment was to visualise particle movements under the radiation of SAWs. According to the literature [141, 142], colloidal samples should be pushed away from the SAW generation source in the direction of the wave propagation due to the acoustic radiation force. Therefore, if the laser-induced SAWs were strong enough under our experimental conditions, similar phenomena should be expected.

Similar to the experiment in Section 4.1, here the laser spot was illuminated on the metal coating as well. The thin chamber with thickness of 100 μm was placed on the silicon substrate with 1-1.5 cm away from the light spot. The chamber was fabricated following the method described in Subsection 3.2.3, except the sidewall of the chamber, which faced the beam, was opened, after considering amplitude damping as the waves passed through the closed sidewall. The colloidal sample used was very similar to the one in the last Section except the sample concentration was doubled, and was then injected into the chamber by pipetting. In terms of the LD modulation, three types of the input signal were chosen: sine wave, square wave and pulse wave with pulse duration of 20 ns, 50 ns, 100 ns and 200 ns. The modulation frequency of all of signals was also swept from 200 kHz to 20 MHz.

4.2.2 Results and discussion

During the experiment, both the line-shape and the single spot light source were used to try to generate SAWs. The experimental results were summarized based on the signal type with different parameter combinations, and are listed in Table 4-2. As can be seen from the Table, only Brownian motion of the samples without any directional movements are observed, no matter the type of input signal and the different frequencies. Combining the experimental results in the current and the last sections, the potential reasons causing the issue were summarized as: 1. SAWs were created, but were too weak to move particles; 2. The optical intensity at the illumination area was still not strong enough to generate SAWs or stronger SAWs; 3. SAWs could not be formed under our experimental method and conditions. Therefore, a final attempt was made to detect SAWs by using a thermal imager, which will be discussed in the next Section.

Signal type	Signal frequency	Beam width	Metal layer	Results
Sine wave	200 kHz- 20 MHz	Line: 250 μm, 83 μm Spot: Φ1 mm	Al (TH: 30 nm)	No single directional movement (Only Brownian motion)
Square wave	200 kHz- 20 MHz	Line: 250 μm, 83 μm Spot: Φ1 mm	Al (TH: 30 nm)	No single directional movement (Only Brownian motion)
Pulse wave (PW: 20 ns, 50 ns, 100 ns & 200 ns)	200 kHz- 20 MHz	Line: 250 μm, 83 μm Spot: Φ1 mm	Al (TH: 30 nm)	No single directional movement (Only Brownian motion)

Table 4-2: Experimental results of the laser-launched SAWs test by visualising particle movements in a thin fluid chamber.

4.3 Laser-induced SAWs test by thermal imaging detection

4.3.1 Experimental method

In this experiment, a thermal imager (Ti25, Fluke UK Ltd.) was used to detect the laser-launched SAWs. SAWs can be treated as one type of mechanical elastic waves. During wave propagation, the surface of the substrate is deformed and the relative temperature changed due to the surface vibration. Therefore, it is possible to visualise the SAWs through detecting the heat radiation from the surface using a thermal imager, as reported in the literature [143]. In this experiment, the substrate without metal coating was used, as the thermal emissivity of the aluminium thin film was too low to be measured accurately by the imager. For the LD modulation, the settings and the frequencies of input singles were kept the same as those in Section 4.2.

4.3.2 Results and discussion

During the test, either the thinnest line (83 μm) light source or the smallest light spot (*Φ*1 μm) were applied in the substrate. Fig. 4-7 shows some typical thermal images with single light spot illumination under different conditions. The positions of the laser spots are obvious and easily found in most cases, and are pointed out by the target-dot reticule with the relative temperature reading. However, SAWs are not observed.

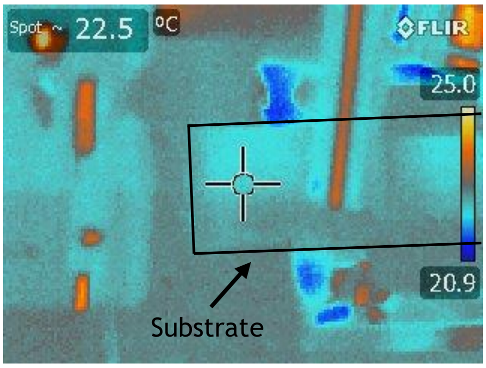

(a) Modulation off, low optical power under CW mode

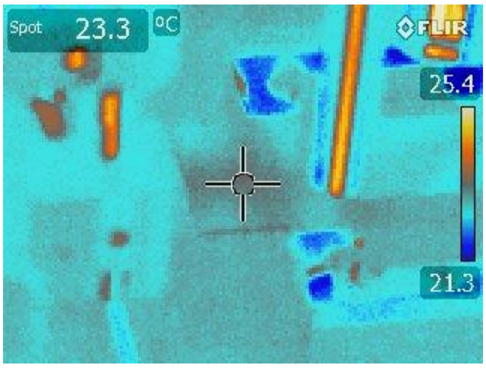

(b) Modulation on, pulse signal with duration of 200 ns at 300 kHz

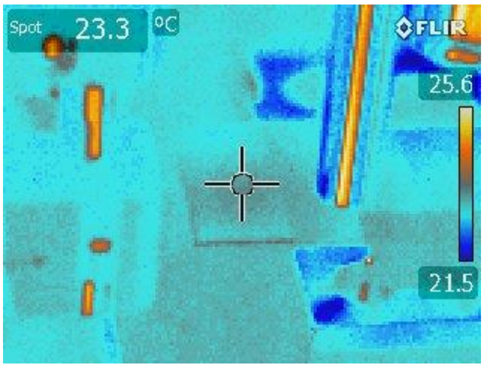

(c) Modulation on, pulse signal with duration of 50 ns at 300 kHz

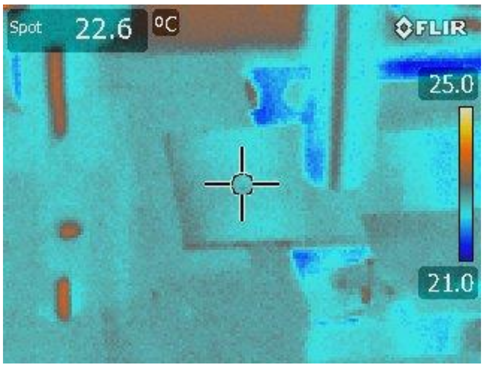

(d) Modulation on, pulse signal with duration of 100 ns at 300 kHz.

(e) Modulation on, pulse signal with duration of 200 ns at 300 kHz.

Fig. 4-7: Thermal images with/without modulated laser spot illumination at different pulse durations and frequencies. The black lines shown in the figure are to emphasize the outline and the position of the substrate. The target-dot reticules indicate the positions of the laser spot with the relative temperature readings.

Above all, through making several attempts to detect SAWs, two important points were realised: firstly, the modulation depth of the laser beam was restricted to a narrow range due to the limited working performance of the LD system. This reduced the temperature difference between the maximum and the minimum temperatures on the surface of the illumination area in the steady state. As a result, the corresponding thermal expansion in the vertical direction was reduced. Secondly, the optical intensity of the illumination area was still not strong enough due to the large size of the spot. Therefore, it was necessary to improve the modulation depth of the LD system to be as deep as possible, which will be discussed in Section 4.4, and to reduce the laser spot size as small as possible, which will be discussed in Section 4.5. In the meantime, it was also worth considering using the line array with light-absorptive material to generate SAWs. If the frequency of the modulated laser beam matched with the frequency of SAWs generated by the metal strips, the amplitudes of the waves should be enhanced (see Sections 4.6 and 4.7).

4.4 Laser diode system modification

In this Section, the laser modulation circuit was modified to support a nearly full modulation depth of 400 mA. In order to understand the output signal behaviour from the circuit under our experimental conditions, related circuit modelling was performed, which showed different transient responses under different types of signals and repetition rates. In terms of real performance tests, the behaviour of the detected modulated light matched well with the modelling results. In addition, the modulation depth was assessed, with the measurements showing that almost 10-30 mW was less than the ideal situation in most cases, which was acceptable.

4.4.1 Method

In our experiment, the CW laser diode needs to be driven in the Quasi-continuous-wave (QCW) operation mode. According to the specifications of the LD system, for high frequency modulation above 200 kHz, an integrated Bias-T circuit needs to be used. In this case, the LD controller only provides the DC operation current for the diode and the modulation signal is supplied by an external signal generator. The simple Bias-T includes one inductor and one capacitor in parallel. The inductor allows DC signal to pass through but blocks the AC signal, whereas the capacitor allows the AC passing through but blocks DC; as a result, the output signal from the circuit looks like an AC signal with DC bias. The structure of a simple Bias-T is shown in Fig. 4-8. In order to drive the laser safely, the upper bound of the modulated output current should not exceed the typical operating current of the LD and the lower bound should not be lower than the lasing threshold. According to the data sheet of our LD, the typical operating current was about 550 mA and the lasing threshold was about 120 mA. The maximum modulation depth should therefore not exceed 430 mA. As mentioned in Section 4.3, the maximum modulation depth of a square wave that the Bias-T could support was restricted to around 63 mA, due to the power rating of the terminal resistor. Therefore, it was necessary to replace the terminal resistor with the one with a higher power rating, in order to generate stronger SAWs. Eventually, the LD mount was disassembled. The main driving circuit and the Bias-T are shown in Fig. 4-9. As can be seen, the circuits are designed and fabricated based on surface-mount technology (SMT). The layout of the Bias-T is very similar to that shown in Fig. 4-8. The inductance of the inductor was measured by a RLC meter (RLC100, Digimess Instruments Ltd), to be around 2 μH. For the capacitor, the capacitance was around 220 nF. The terminal component was replaced by a resistor with resistance of 51 Ω and maximum power rating of 2 W, after considering the physical size-fitting issue of the component on the PCB. Therefore, the modulation depth of the total driving current passing though the diode should reach 400 mA.

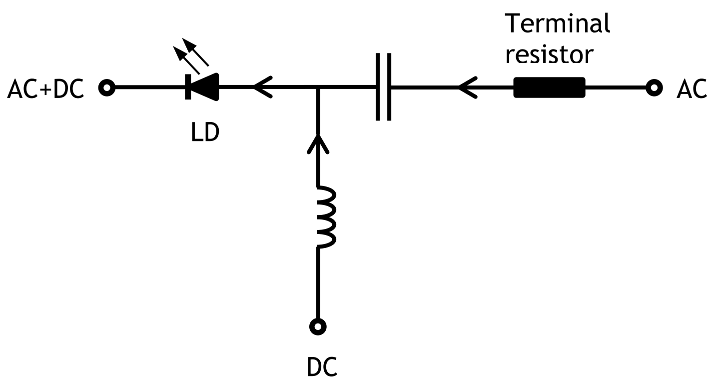

Fig. 4-8: The schematic layout of a simple Bias-T circuit.

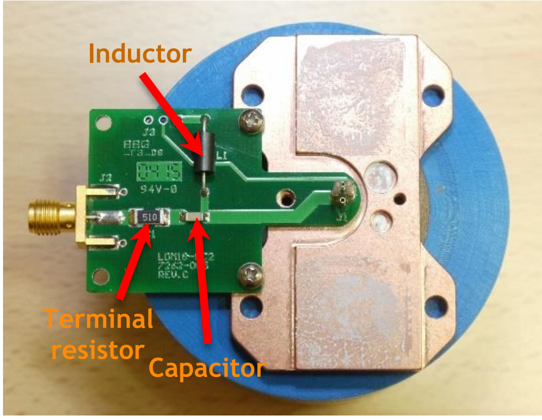

(a) Bias-T

(b) Main driving circuit

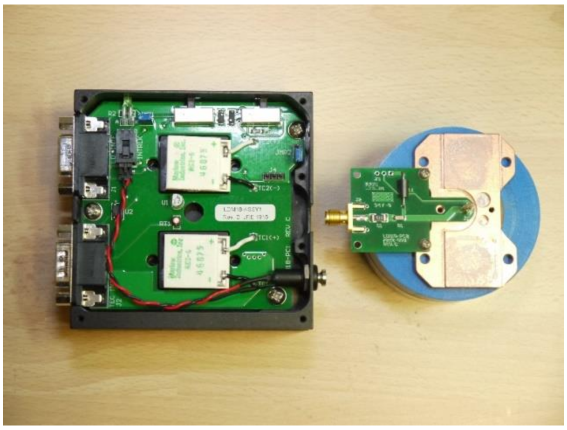

(c) Bias-T and main circuit

Fig. 4-9: Photographs of the Bias-T and the main driving circuit of the LD mount before modification.

4.4.2 Results and discussion

Simulation of LD modulation

Before assessing the performance of the modified modulation circuit, it was necessary to predict the behaviour of the total driving current and to determine the safe way to drive the LD; in this case, a reverse current and forward current overdrive should be avoided during the modulation. Therefore, the Bias-T circuit was modelled using the OrCAD PSpice simulation software. The schematic layout of the circuit in the simulation is shown in Fig. 4-10. The characteristics and the parameter values of each component were set based on the real parts. In the simulation, the modulation depth of the current was set as 400 mA. Regarding the resistance of the terminal resistor, the AC signal branch should be applied with a modulation signal with voltage of 20 Vpp, which was supplied by a programmable AC voltage source with piecewise linear function. In order to know the transient status of the current during the modulation, the value of the output signal from the voltage source was set as 4 Vpp for the first 200 periods and 20 Vpp for the further 100 periods. The inductor was connected to a DC current source of 350 mA. The polarity of the DC current source matched the polarity of the LD, being anode ground (AG). In order to match with the current-voltage (IV) characteristics of the real LD, the corresponding PSpice part model needed to be configured. Unfortunately, no preconfigured model was available in the default part library of the software. In order to obtain accurate results, a new PSpice model based on a general LD model was created. The model was written using the Spice command in which a normal diode was created, following by a lookup table based on the real current-voltage (IV) characteristics. The current was treated as the input and the output was the corresponding voltage [144-146]. The new LD model was tested by connecting it to a DC current source. The current was swept from 0 mA to 600 mA according to the datasheet of the IV curve of the LD, and the voltage across the LD was measured. Fig. 4-11 shows a comparison between the datasheet and the simulation results. It can be seen that the performance of the part model matches well with the real device.

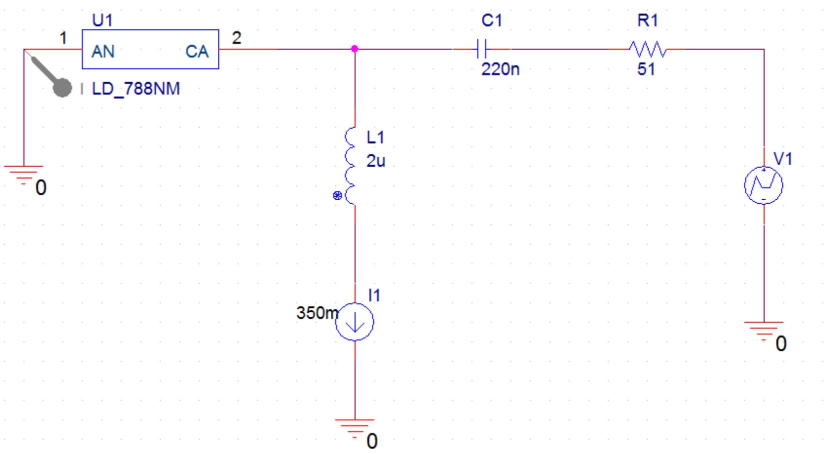

Fig. 4-10: Schematic of the Bias-T in the OrCAD PSpice software. I1 is the DC current source, V1 is the AC voltage source and U1 is the PSpice model for the LD.

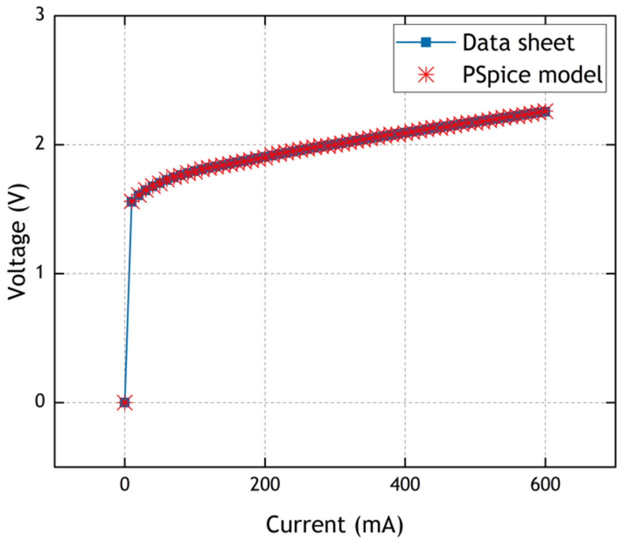

Fig. 4-11: The comparison between the measured data of the real LD and the modelling data of the created PSpice model in terms of the IV characteristics.

As for the experiment, in the simulation a square wave and a pulse wave were chosen as the input modulation signal. The repetition rates of both types of signals were swept from 200 kHz to 20 MHz. In terms of the pulse wave, three pulse durations were chosen of 25 ns, 50 ns and 100 ns. Based on the simulation results, it could be summarised that, for both types of signals, compared to the kilohertz frequency range, the current required more oscillation cycles to reach steady state in the megahertz range. No reverse current was seen with the DC current bias set to 350 mA. For the square wave, all signals oscillated around 330-350 mA. For the signal at 200 kHz, the modulation depth was 20 mA higher than the expected value (which was 400 mA). However, the depth gradually reduced with increasing frequency. At 20 MHz, it was approximately 20 mA lower than the expected value. For signals with frequencies below 500 kHz, the peak current was always close the absolute maximum operating current of 600mA, when the AC voltage was changed from 4 Vpp to 20 Vpp; this meant it was very easy to overdrive the LD at low frequencies. After that, the trace went back to the steady state with the maximum current being close to the typical operating current of 550 mA. Unlike the square wave, for the pulse signal, all signals below 1 MHz started oscillation at the lower pulse bound ranging from 310 mA to 340 mA in the steady state, which meant the LD would probably be overdriven. In contrast, the current levels of the lower pulse bounds of the oscillations reduced gradually and was close to 150 mA for the repetition rates above 5 MHz. Moreover, at the same frequency, when a longer pulse width was chosen, a relatively lower level of the oscillation lower pulse bound was obtained. Furthermore, for the signals with repetition rates below 5 MHz, once the AC voltage was changed to the high value, the traces continually increased until reaching the steady state. Therefore, it was necessary to use a lower DC bias current for the input modulation signal at low frequencies. Due to the large volume of the traces, only four graphs with typical traces were chosen in this work. Fig. 4-12 shows the transient traces of the drive current through the laser diode with a square wave at (a) 200 kHz and (b) 10 MHz. Fig. 4-13 shows the traces for a pulse wave at (a) 500 kHz with pulse duration of 25 ns and (b) 9 MHz with pulse duration of 50 ns.

a

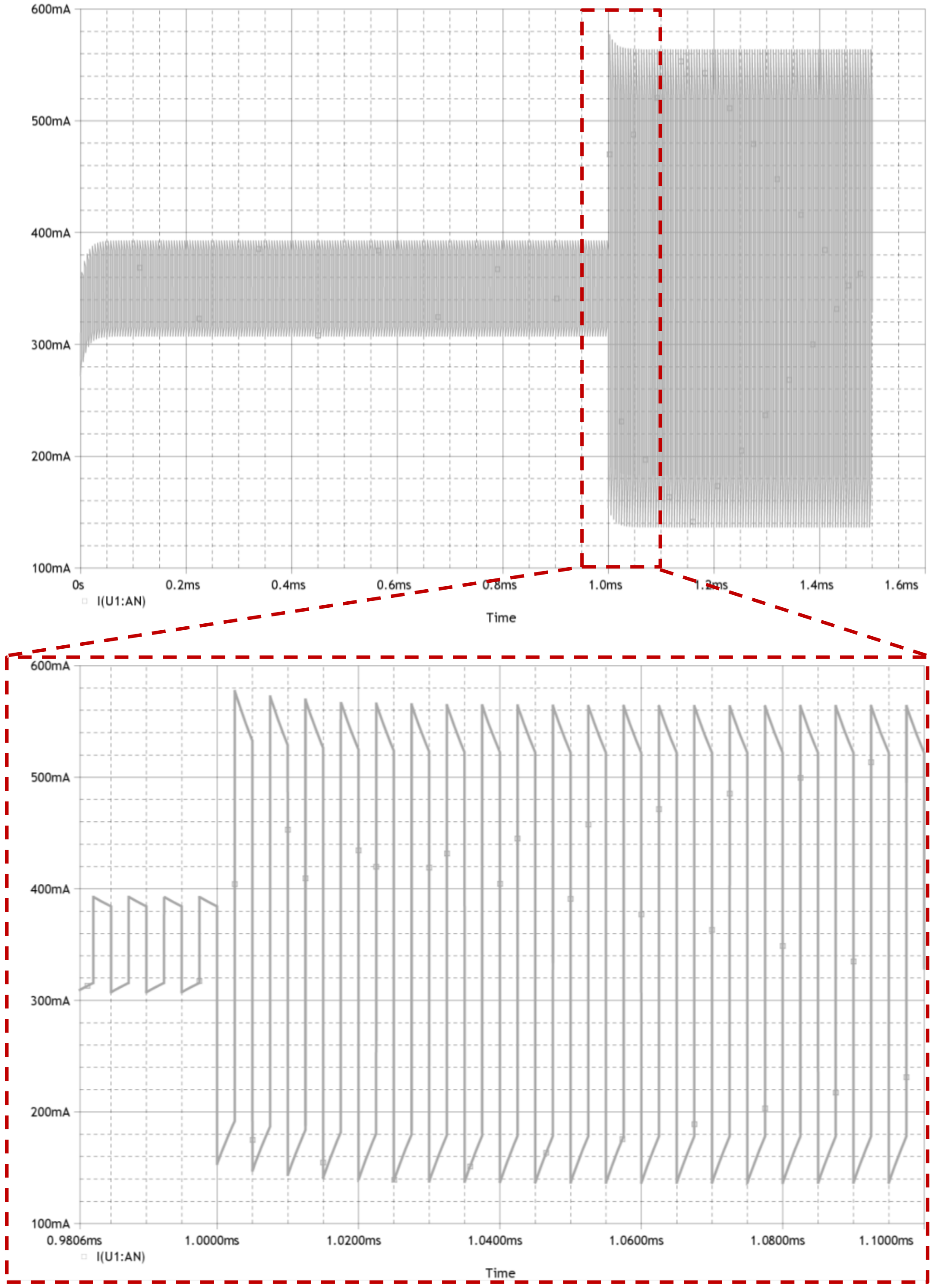
600mA
500mA
400mA
300mA
200mA
100mA
0s
0.2ms
0.4ms
0.6ms
0.8ms
1.0ms
1.2ms
1.4ms
1.6ms
I(U1:AN)
Time
0.9806ms
1.0000ms
1.0200ms
1.0400ms
1.0600ms
1.0800ms
1.1000ms

b

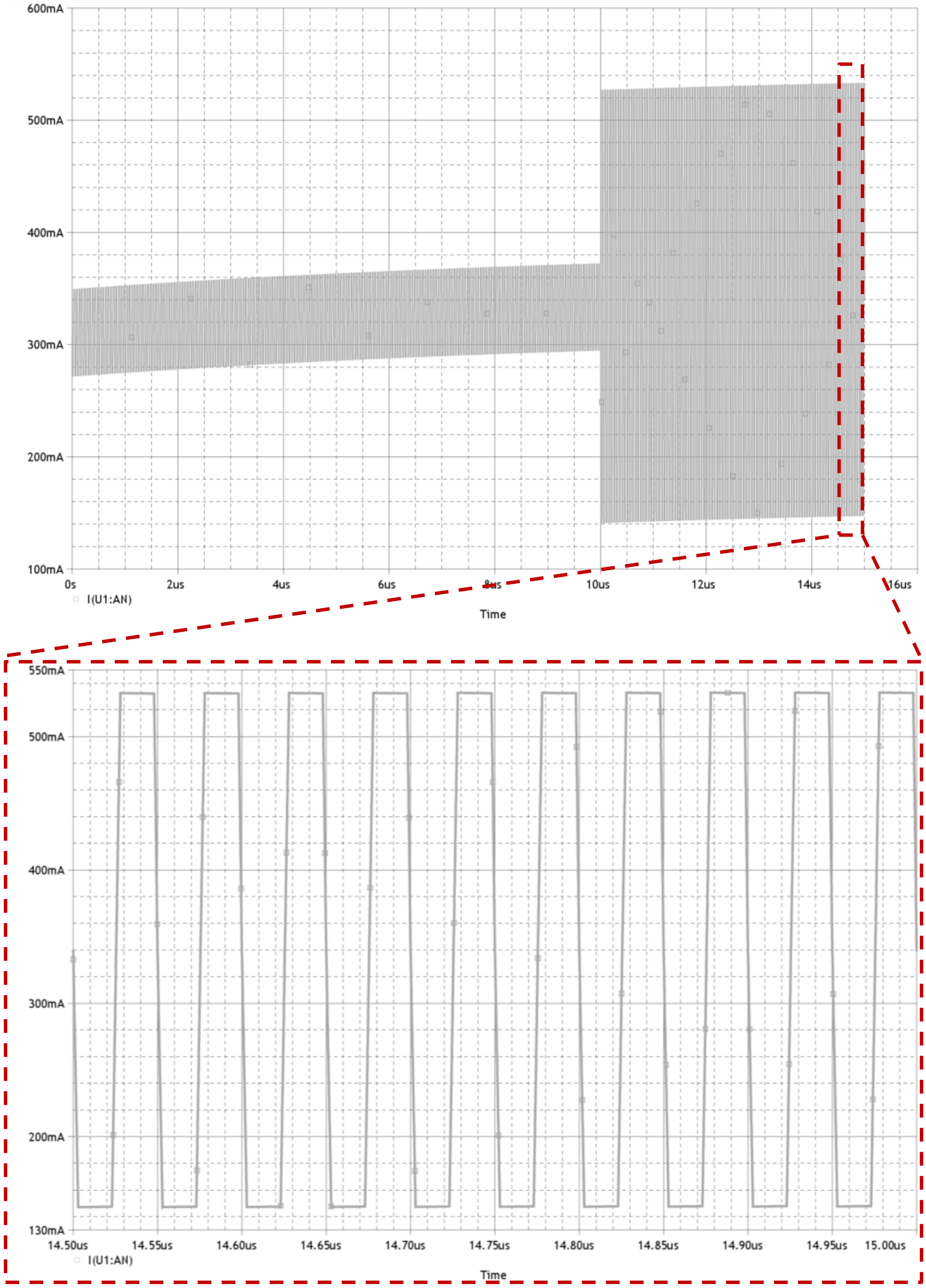

Fig. 4-12: Transient traces of the current passing through the laser diode with a square wave at (a) 200 kHz and (b) 20 MHz.

a

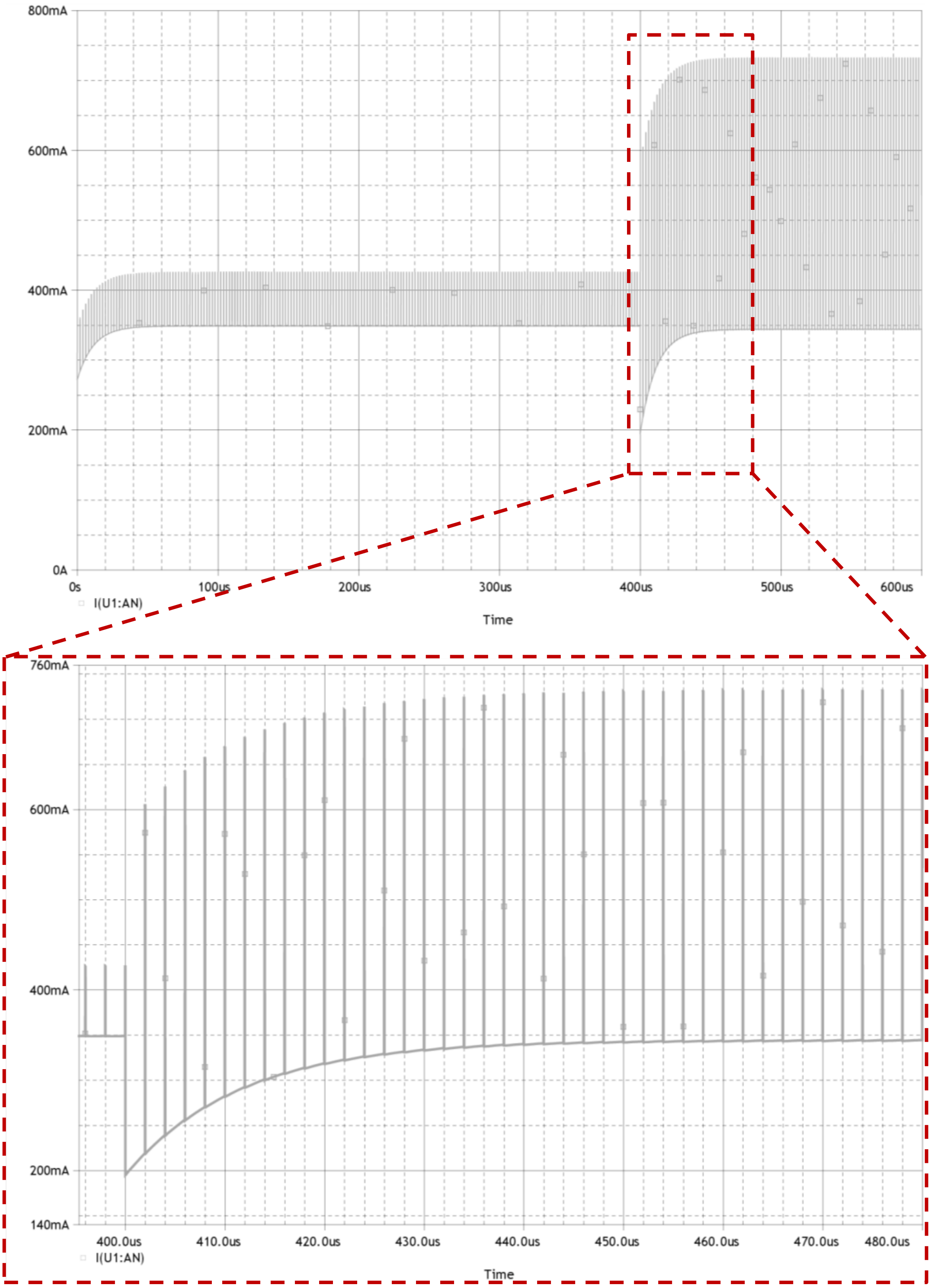
800mA
600mA
400mA
200mA
0A
0s
100us
200us
300us
400us
500us
600us
I(U1:AN)
Time
760mA
600mA
400mA
200mA
140mA
400.0us
410.0us
420.0us
430.0us
440.0us
450.0us
460.0us
470.0us
480.0us
I(U1:AN)
Time

b

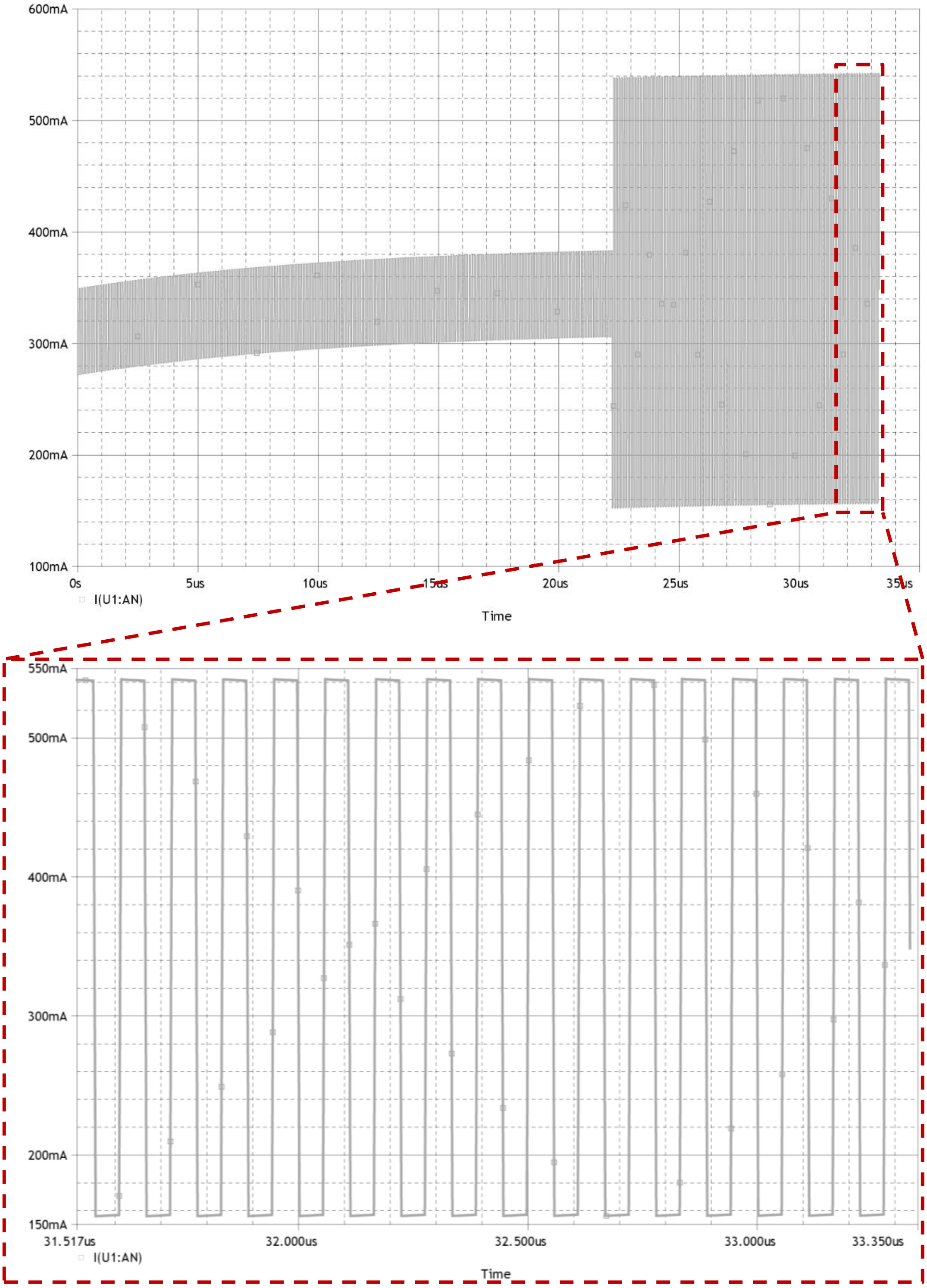

Fig. 4-13: Transient traces of the current passing through the laser diode with a pulse signal at (a) 500 kHz with pulse duration of 25 ns and (b) 9 MHz with pulse duration of 50 ns.

Real LD modulation

After completing the simulation, the real performance of the modified circuit was assessed. The measurement setup was the same as that described in Subsection 4.1.1. However, this time, the photodetector was replaced with DET200 from

Thorlabs Inc., as the previous detector was not available. The photocurrent was measured in the form of the voltage across a 50 Ω terminal resister that was connected to the detector in series. The LD mount was connected to a high power pulse generator (8114A, Hewlett-Packard Inc.) instead of the function generator. The frequency of the signal was swept from 200 kHz to 15 MHz. The types and the parameters of the input signals were kept the same as those in the simulation. With no modulation, the measured voltage was around 17.8 mV with DC bias current setting at 350 mA. Fig. 4-14 and Fig. 4-15 show the oscilloscope traces for a square wave at 5 MHz and a pulse wave at 1 MHz with pulse duration of 25 ns. For the square wave, the voltage level that the modulated light oscillates around is close to 17.8 mV, which matches with the simulation result. The waveforms at the upper bound and the lower bound are quite flat, which demonstrates that the modified circuit is working well. For the pulsed signal, the voltage level at the oscillation lower bound increases compared to the square wave, which also matches with the simulation results. Furthermore, the optical modulation depth was also assessed. The results was plotted as a function of repetition rate for different types of signals, and are shown in Fig. 4-16. In the graph, the modulation depth is shown in the form of optical power, which was calculated based on the following equations [147]:

$$\Delta P_{in} = \frac{\Delta V_{LOAD}}{R_{LOAD} \cdot R(\lambda)} \qquad \textbf{(Eq. 4-2)}$$

$$R(\lambda) = \frac{I_{PD}}{P_{in}} \text{ and } I_{PD} = \frac{V_{LOAD}}{R_{LOAD}}$$

where ΔP_{in} is the modulation depth in Watt, ΔV_{LOAD} is the voltage difference between the upper bound and the lower bound of the received signal, R_{LOAD} is the terminal resistance, $R(\lambda)$ is the responsivity of the photodetector at a wavelength of 788 nm, I_{PD} is the photocurrent. After statistical analysis based on the plotted data, the depths were 10-30 mW less than the ideal situation (356 mW) in most cases, which were acceptable. Here, the ideal modulation depth was the power difference between the measured optical powers at DC currents of 150 mA and 550 mA under the naked beam condition.

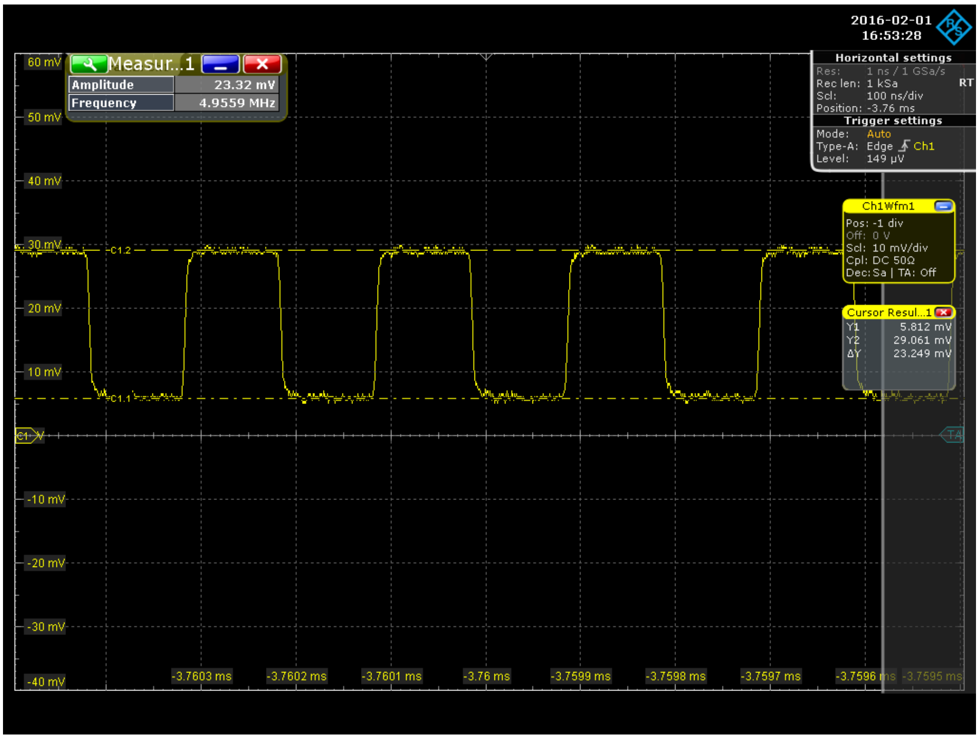

Fig. 4-14: The waveform of the modulated laser beam detected by the photodetector in the form of voltage (input signal: square wave at 5 MHz). Time scale: 100 ns/div.

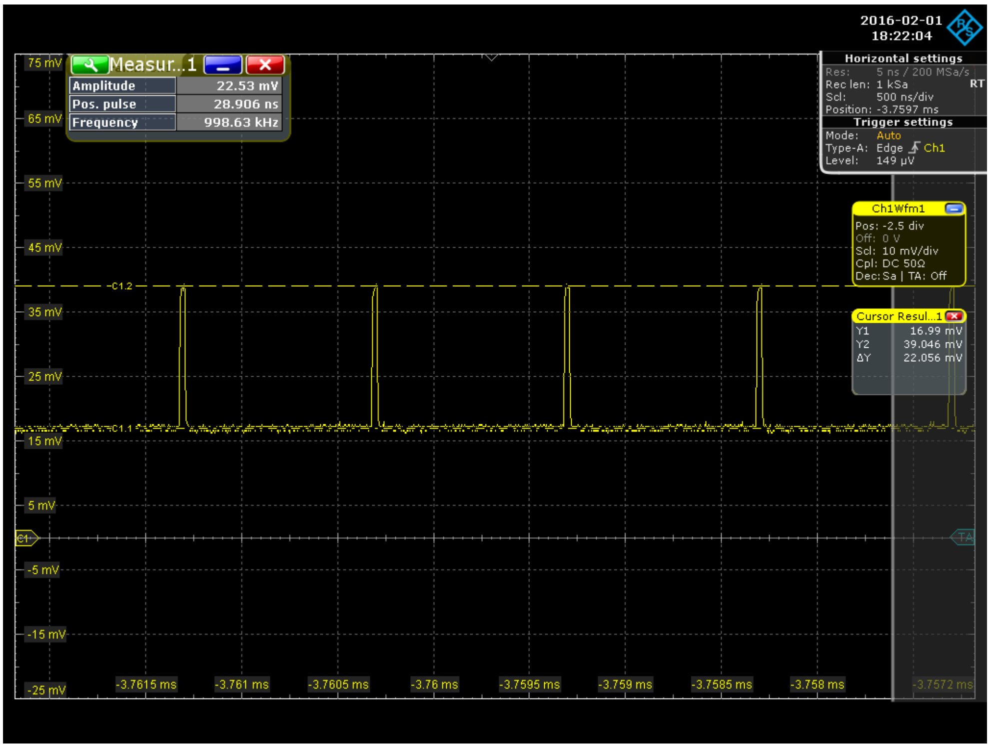

Fig. 4-15: The waveform of the modulated laser beam detected by the photodetector in the form of voltage (input signal: pulse wave at 1MHz with pulse duration of 25ns). Time scale: 500 ns/div.

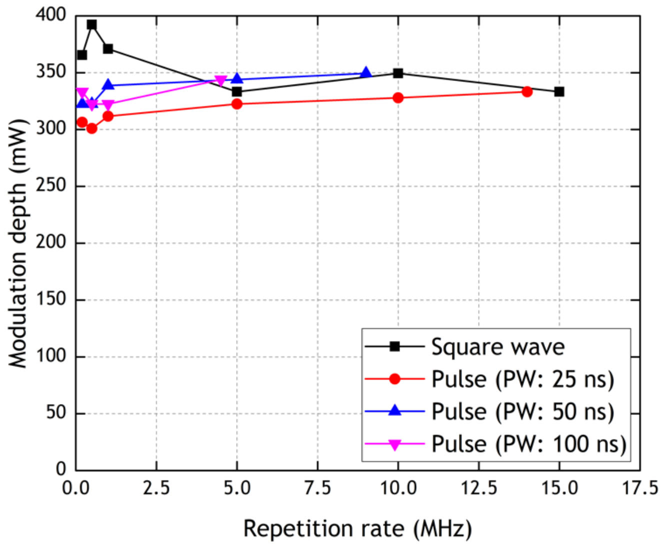

Fig. 4-16: The optical modulation depth for different input signals. The ideal modulation depth was 356 mW. (PW: pulse width).

4.5 Laser-induced SAWs test by fibre-optic hydrophone

As described in Section 4.3, the optical intensity on the illumination area should be increased in order to obtain stronger SAWs. In this section, the previous experimental system setup was updated to achieve an even smaller laser beam size. With the deeper modulation depth and the higher optical intensity, laser-induced SAWs were detected by a more sensitive device, namely a fibre-optic hydrophone.

4.5.1 Experimental method

In this experiment, a fibre-optic hydrophone (Precision Acoustics Ltd.) with high sensitivity was used for the SAWs detection. A hydrophone is a device, which can be used to detect underwater sound waves. However, unlike the convectional device, the sound-detection technique used by the fibre-optic hydrophone is based on interferometry rather than piezoelectricity, so weak sound waves can be detected with high sensitivity. In this particular device, a detachable fibre-optic sensor with a single transverse mode is used. The main part of the sensor is the tip of the fibre, which comprises two parallel metal mirrors, formed by thin gold coatings, with a polymer film between them to form a Fabry-Pérot interferometer. The sensor controller transfers laser light though the fibre to the tip. The reflected light is detected by a photodiode, of which the output electrical signal is used as the reference signal. When the acoustic wave encounters the front mirror of the fibre tip, due to the sound pressure, the optical thickness and the reflectance between the two mirrors are changed, resulting in an optical phase variation in the interferometer. In order to obtain the best results, the fibre tip should be placed facing the propagation of the waves [148-152]. The schematic layout of a typical fibre tip is shown in Fig. 4-17. In the experiment, an optical fibre with outer diameter of 125 µm was used. In order to increase the sensitivity of the detection, a thin chamber containing DI water with a thickness of approximately 150 µm was used rather than a droplet. The chamber was fabricated on the silicon substrate following the method introduced in Subsection 3.2.3, except the two sidewalls facing the propagation of the SAW radiations were opened. It was then filled with DI water by pipetting, which was followed by inserting the fibre-optic hydrophone carefully through one of the sidewalls. The sensor was then stabilized by fixing the fibre outside the chamber with “Blu Tack”. In addition, two substrates were tested separately: a silicon substrate with Al coating and a silicon substrate without Al coating. In the former case, the chamber was placed next to the metal coating. For both cases, the laser beam was illuminated on the silicon or the coating close to the chamber. As for the experiment in Section 4.2, in terms of the LD modulation, three types of the input signal were used: sine wave, square wave and pulse waves with pulse durations of 25 ns, 50 ns and 100 ns. The modulation frequencies of all signals were swept from 200 kHz to 20 MHz again. This time, a function generator (TGP3151, Aim-TTi Ltd.) was used as the modulation signal generator, which produced signals with 20 Vpp and was connected directly to the Bias-T circuit. The LD was driven by a DC current of 850 mA. The received signals from the hydrophone were measured by an oscilloscope with the laser modulation signal as trigger signal. Fig. 4-18 shows the schematic layout of the experiment setup.

For the optical system, the updated setup was used the same as that presented in Section 3.1, which used an objective to focus the laser beam. In this case, a 4x objective (NA = 0.1) was used, which projected a laser spot on the substrate with size of Φ8.63 µm in the x-direction and Φ122.81 µm in the y-direction. Moreover, compared to the previous experiments, the laser diode was replaced by a multimode one with more optical power as the previous diode was not available any more.

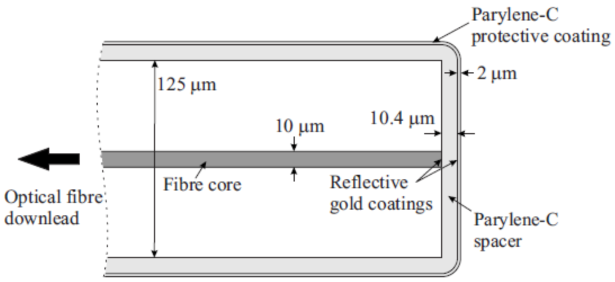

Fig. 4-17: The schematic layout of the structure of the Fabry-Pérot cavity at the tip of the optical fibre [151].

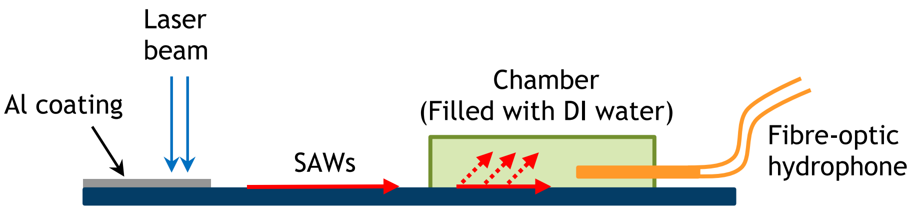

Fig. 4-18: The schematic layout of the experiment of laser-induced SAWs test by fibre-optic hydrophone.

4.5.2 Results and discussion

IDT-induced SAWs test by hydrophone

Before implementing the measurement, it was necessary to figure out the waveform of the detected signal that should be expected from the hydrophone. Therefore, a simple pre-test was performed using the hydrophone to detect SAWs created by a slanted interdigital transducer (IDT). As described in Section 2.3, the mechanism of SAWs generated by IDT is based on piezoelectricity. Therefore, the transducer used in the test was fabricated on a lithium niobate ($LiNbO_3$) wafer by photolithography. As for the experimental setup in Subsection 4.5.1, the same chamber was placed next to the IDT with the fibre sensor inside. The resonance frequency of the IDT was 3.62 MHz and the electrical power of the supply sine signal was around 35 dBm. The received sound signal was then captured by an oscilloscope. Fig. 4-19 shows a screenshot of the scope. The transient signal shown in yellow is the detected wave and the green-colour curve is the trigger signal from the supply signal generator. Obviously, the signal received by the hydrophone should be a sinusoidal wave.

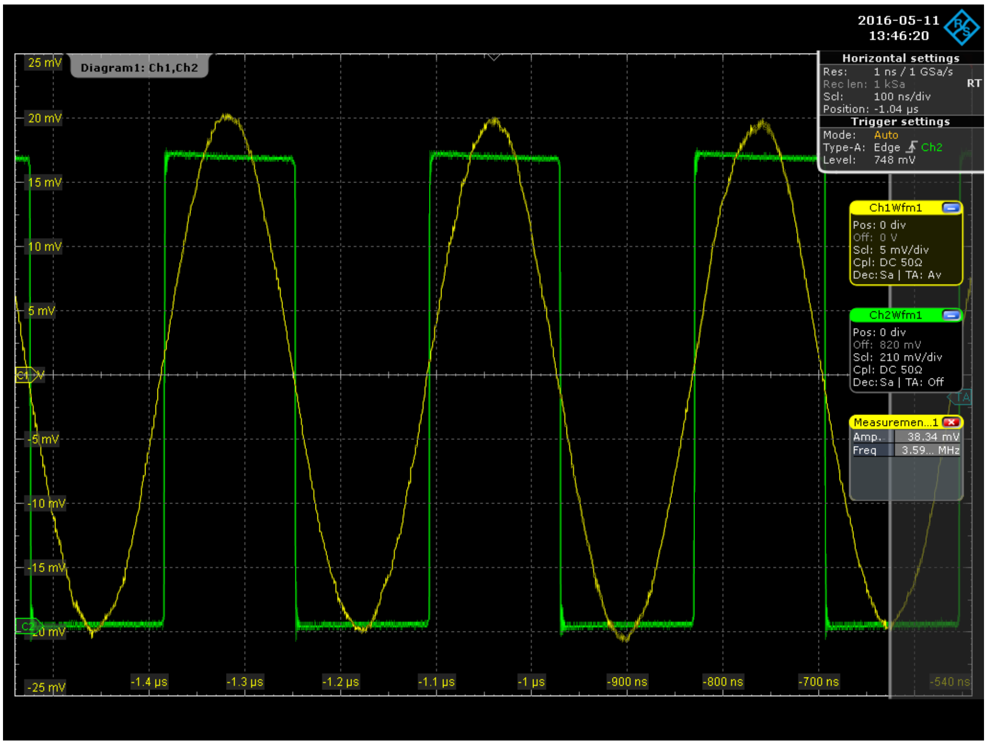

Fig. 4-19: The oscilloscope screenshot of the detected sound wave (shown in yellow) by the hydrophone in the form of voltage with relative trigger signal (shown in green) from the supply signal generator, showing the received signal with a sinusoidal waveform. (Supply signal: sine wave at 3.62 MHz). Time scale: 100 ns/div.

Laser-induced SAWs test by hydrophone

After determining the features of the signal received by the hydrophone, the experiment to detect the laser-induced SAWs was performed. The experiment results were grouped based on the type of the modulation signal with different parameter combinations, and are summarized in Table 4-3. During the experiment, only random noise signals without any obvious sinusoidal waveform were seen on the oscilloscope no matter the type of the input signal and the frequencies. Potential causes of this issue include: firstly, the longitudinal acoustic pressure wave was detected only by the hydrophone rather than the main SAWs. As described in Section 4.1, once the SAWs encounter fluid, only small amounts of acoustic energy leaks into liquid under the Rayleigh angle and propagates as longitudinal pressure waves inside the fluid, due to the refractive index difference between the substrate and the fluid. Therefore, it was possible that the pressure waves were too weak to be detected. Secondly, the SAWs may have been not strong enough. Therefore, regarding the literature [83-85], another experiment based on the different SAWs generation technique with more sensitive detection device was implemented, which will be described in the next Section.

Signal type	Signal frequency	Substrate	Results
Sine wave	200 kHz- 20 MHz	With & without Al coating (30 nm)	Random noise signal only
Square wave	200 kHz– 20 MHz	With & without Al coating (30 nm)	Random noise signal only
Pulse wave (PW: 25 ns, 50 ns & 100 ns)	200 kHz- 20 MHz	With & without Al coating (30 nm)	Random noise signal only

Table 4-3: Experimental results of the laser-launched SAWs test by the fibre-optic hydrophone in a thin fluid chamber.

4.6 Laser-induced SAWs test by laser Doppler vibrometer (LDV)

So far, several SAW detection techniques with the single line and single spot illumination were attempted. However, no obvious signals were detected. Therefore, it was worth trying to improve the signal-to-noise ratio (SNR), in order to enhance the sensitivity of the measurement system. In Section 2.2, it was shown that compared to the single line and single spot illumination methods, a much narrower bandwidth and higher amplitude of SAWs could be generated by multiline array illumination. This could improve the SNR without challenging the detection system by further reducing the detection bandwidth. In this section, laser-induced SAWs based on the multiline array illumination technique were detected by a laser Doppler vibrometer (LDV). Compared to the fibre-optic hydrophone used in the last section, the LDV detects the entire surface displacement rather than the partial acoustic energy.

4.6.1 Experimental method

Laser Doppler vibrometer (LDV)

Similar to the fibre-optic hydrophone, a laser Doppler vibrometer is a device for the non-contact displacement measurement of the surface vibration based on interferometry. In fact, the main part of the vibrometer can be viewed as an interferometer. Generally, a single laser beam is split into two optical paths with one of them being used as an internal reference beam and the other being used as a test beam. The test beam is directed onto the target and the related reflected beam is collected. The collected beam is then redirected through an internal optical system and interfered with the reference beam on a photodetector. Due to the surface vibration of the target, there is a phase difference between the two beams, which manifests as the optical intensity variations of the interference patterns on the photodetector. Finally, the photocurrent change is measured in the form of voltage by an oscilloscope. For different types of LDV, there are some differences in the configurations between each optical system. Fig. 4-20 shows the optical configuration of the vibrometer (OFV-534, Polytec GmbH) used in the experiment. The laser beam from a helium-neon laser is split into the reference beam and the object beam by a beam splitter BS1. The object beam passes through a polarizing BS2 beam splitter and a λ/4 plate, and is then focused by the lens on the object. The scattered beam from the sample is reflected back along the same optical path with the polarizing BS2 beam splitter functioning as an optical directional coupler together with the λ/4 plate, which deflects the reflected object beam to the BS3 beam splitter. An interference signal is then created due to the optical path difference between the reference and the object beams. In order to determine the sign of the signal, an additional frequency offset is added by including the Bragg cell in the reference optical path of the vibrometer [153].

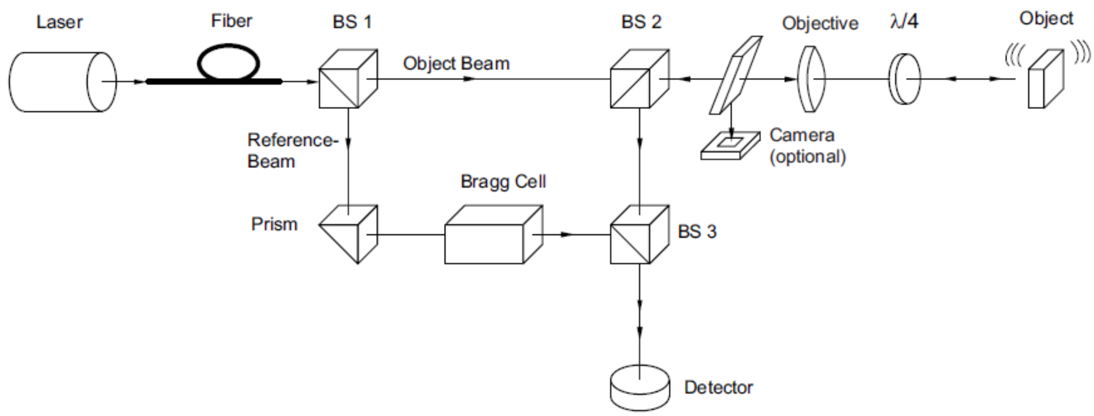

Fig. 4-20: The optical configuration of the laser Doppler vibrometer (OFV-534, Polytec GmbH) [153].

Experiment overview

In this experiment, laser-induced SAWs based on the multiline array illumination were generated by the same method reported in the literature [83-85] (see Subsection 2.2.2), in which the laser beam was projected on a pre-fabricated metal line array with a high light-absorption coefficient based on a soda-lime glass slide. Here, the soda-lime glass slide was used as substrate due to its high transmission at the beam wavelength of 808 nm. Two line arrays were used in the experiment, which were designed to create SAWs at 10 MHz and 15 MHz, respectively. Both arrays were fabricated using photolithography. Due to the fact that the measurement of the laser vibrometer mainly relies on surface reflection, the detection region in the substrate was coated with a thin gold layer of thickness 100 nm, in order to enhance the sensitivity of the measurement and the amplitude of the detected signal. The shortest distance between the array and the detection region was around 4.5 cm due to the limitation of the physical configurations of the optical system and the vibrometer system. In addition, the optical system setup was kept the same as that used in Section 3.1. Fig. 4-21 shows the main experiment overview.

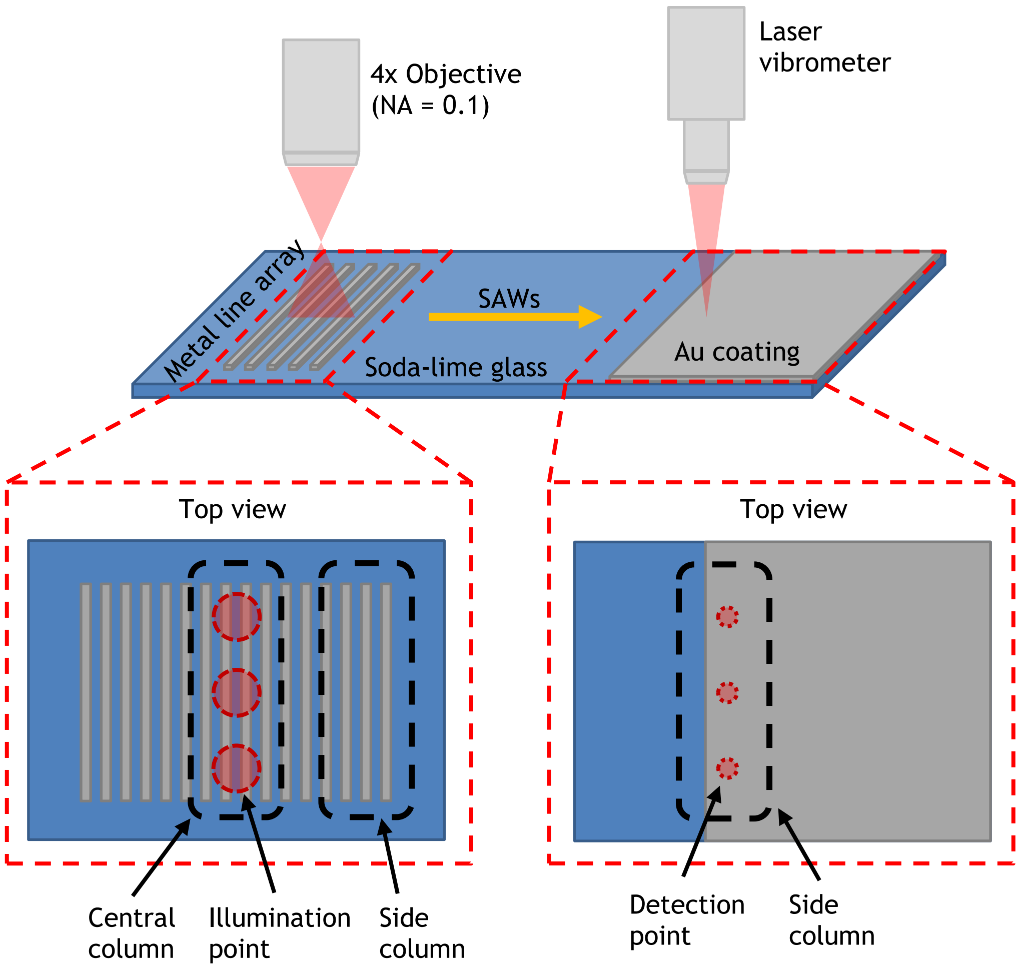

Fig. 4-21: The schematic layout of the experiment of laser-induced SAWs test by the laser Doppler vibrometer.

In terms of SAW generation, laser spots with different sizes were projected through the 4x objective (NA = 0.1) onto the array by simply adjusting the height of the substrate. For each size of light spot, two illumination regions were chosen:

the central column and the side column of the line array (see Fig. 4-21). For each illumination region, three illumination points were chosen: the top, the middle and the bottom of the region. In terms of detection, only the side column of the metal coating was used as the detection region. Inside the side-column region, three detection points were chosen, of which positions were relative to the illumination points. Again, considering the physical sizes of the two systems, the distance between the illumination point and the detection point was restricted to 4.6 - 4.8 cm. In terms of the LD modulation, modulated signals with 20 Vpp were produced from the same function generator used in Section 4.5. Two types of modulation signal were used: sine wave and square wave. For each signal type, frequencies of 10 MHz and 15 MHz were applied to match with the designed frequencies of the line arrays. In addition, two signal modes were also used: continuous signal mode and burst mode. In the burst mode, for the two modulation frequencies, the signal cycles of both sine and square waves were set as 1000 cycles. The periods of the bursts were set as 5 ms for square wave and 1 ms for sine wave. In terms of the detection system configuration, the vibrometer was connected to an amplifier with gain of 40 dB and a high pass filter with cutoff frequency of 3 MHz, followed by an oscilloscope (RTO1022, Rohde & Schwarz UK Ltd.). In terms of signal analysis, 2000 waveforms were averaged and a digital low pass filter with cutoff frequency of 20 MHz or 30 MHz (depending on the designed SAW frequency) was applied in the oscilloscope, in order to minimise the noise as much as possible.

For the design of the line array, both the strip widths and the intervals between strips were designed to be half of the SAW wavelength, regarding to the mechanism of the wave generation (see Subsection 2.2.2). According to the literature [154], the speed of sound waves in soda-lime glass is around 3127 m/s. By considering the thickness of the substrate and the fabrication technique used, the designed frequencies of the SAWs were chosen as 10 MHz and 15 MHz to avoid generation of a Lamb wave. After calculation, the strip widths were 156.4 μm for 10 MHz and 104.2 μm for 15 MHz waves. For the line array material, molybdenum (Mo) was selected as it has lower reflectance than other common metals. The height of the strips was designed as 100 nm so the transmittance was around 0.005 according to the Beer-Lambert law. The size of the array was 1 cm x 1 cm.

4.6.2 Results and discussion

LD performance test with burst mode

According to the simulations presented in Subsection 4.4.2, for a square wave modulation signal, a number of time periods are needed before the modulation reaches a steady state. Therefore, before implementing the measurement, it was necessary to assess the performance of the LD modulated in the burst mode to make sure there were sufficient signal cycles for the modulation to reach the steady state. The system setup was the same as that in Subsection 4.4.2, except the external modulation source was replaced by the function generator used in Section 4.5. Fig. 4-22 (a) and (b) show oscilloscope screenshots of the detected light for square waves at 10 MHz and 15 MHz, respectively. It can be seen that the results are similar to the modelling. The modulations reach steady state after approximately 470 signal cycles for 10 MHz and 650 cycles for 15 MHz respectively, which means the 1000 cycle criteria set in Subsection 4.6.1 is sufficient. Fig. 4-22 (c) and (d) respectively show the light modulation for a sine wave at the same two frequencies. Here, the modulation reaches steady state immediately once the burst starts without any waiting time in both cases, which means the number of signal cycles set in Subsection 4.6.1 for sine waves is also sufficient. Here, the yellow curves represent the trigger signals and the blue curves represent the detected light signals.

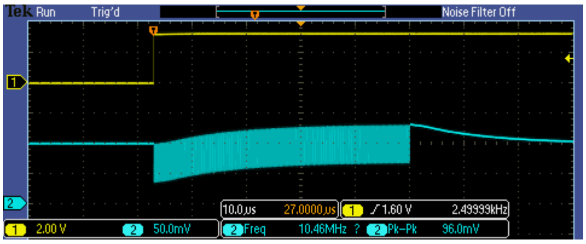

(a) Square wave, 10 MHz, 470 cycles

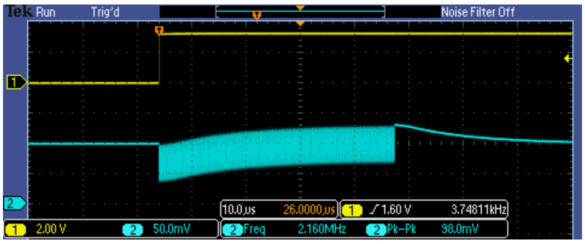

(b) Square wave, 15 MHz, 650 cycles

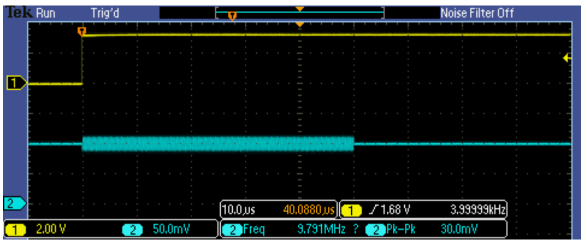

(c) Sine wave, 10 MHz, 500 cycles

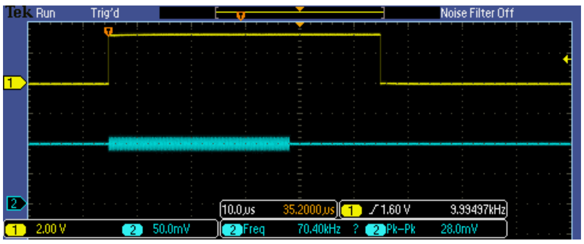

(d) Sine wave, 15 MHz, 500 cycles

Fig. 4-22: The oscilloscope screenshots of the LD modulation under burst mode (shown in yellow) and related trigger signals (shown in blue) for different types, frequencies and number of cycles of the modulation signals. (Time scale: 10 µs/div).

IDT-induced SAWs test by laser Doppler vibrometer

As in the previous experiment (Subsection 4.5.2), it was necessary to figure out the expected waveform of the detected signal from the vibrometer. In this experiment, the same IDT as that used in Subsection 4.5.2 was applied to create SAWs. The laser beam from the vibrometer was focused on a region that along the propagation of the SAW radiation and was close to the transducer. The transducer was activated with a sine wave signal under the continuous and burst mode, respectively. In the burst mode, the number of signal cycles was set as 100 with a burst period of 1 ms. Again, the frequency and the electrical power of the activation signal were 3.62 MHz and 35 dBm. Fig. 4-23 shows an oscilloscope screenshot of the detected SAWs under burst mode. The signals appear as soon as the burst starts. In each burst period, there is always a second series of pulses, which arises from the waves reflected from the edge of the substrate. In the continuous signal mode, as in the hydrophone experiment, signals with a sinusoidal waveform were obtained.

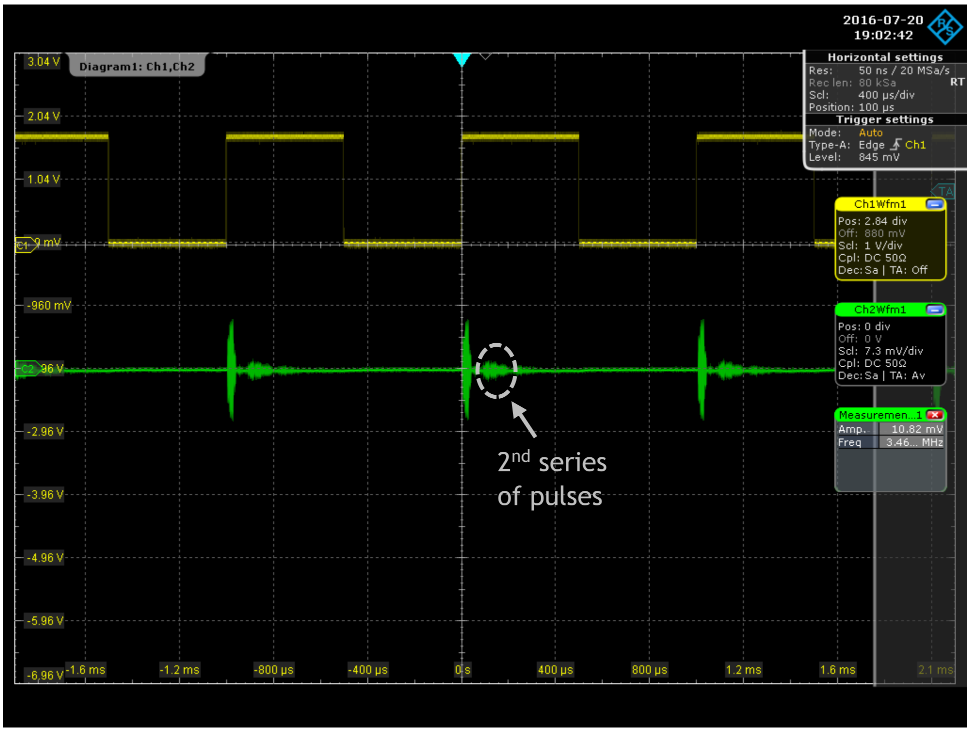

Fig. 4-23: The oscilloscope screenshot of the IDT-induced SAWs (shown in green) detected by the laser Doppler vibrometer under the burst mode with relative trigger signals (shown in yellow). (Supply signal: sine wave at 3.62 MHz; burst mode: 100 signal cycles with burst period of 1 ms). Time scale: 400 µs/div.

Laser-induced SAWs test by laser Doppler vibrometer

After determining the waveforms of the signals that should be expected from the vibrometer, detection of laser-induced SAWs was attempted. The measured results are summarized based on the signal mode with different parameter combinations in Table 4-4. During the experiments, none of the expected waveforms were seen. Only the random noise was captured under both continuous and burst modes. The potential causes of this issue were: firstly, the laser-induced SAWs were generated. However, they were too weak to be detected. Secondly, the distance between the generation point and the detection point may have been too long, especially when the waves were weak. Considering the attenuation after traveling that such a long distance, it is possible that the amplitude of waves was far below the detection limit of the device. Thirdly, the noise level of the vibrometer varied from 0.2 nm to 0.5 nm, which meant that the minimum displacement that the device could measure should be above 0.5 nm. Therefore, it is likely that the created SAWs were hidden by noise.

Signal mode	Signal type	Signal frequency	Results
Continuous	Square & sine wave	10 & 15 MHz	Random noise signal only
Burst (signal cycles: 1000, period: 1 & 5 ms)	Square & sine wave	10 & 15 MHz	Random noise signal only

Table 4-4: Summary of experimental results of the laser-launched SAWs test by the laser vibrometer.

4.7 Laser-induced SAWs test by IDT

Given the conclusions from the previous experiment, in this section, the experimental conditions were improved by using a higher magnification objective (20x, NA = 0.4) to increase the optical intensity in the illumination region, a lock-in amplifier to increase the SNR of the system and a new sample device, which was designed with shorter distance between the SAW generation region and the detection region.

4.7.1 Experimental method

Device design and fabrication

Instead of using the laser Doppler vibrometer, an interdigital transducer (IDT) with slanted fingers was used as the SAW sensor. The detection frequency range of the IDT was designed to be 24 MHz – 26 MHz. The particular frequency range was chosen to match the thickness of the device substrate and the fabrication techniques. A metal line array was again used as the SAW generator. However, the designed generation frequency was changed to 25 MHz in order to match the central detection frequency of the IDT. The line array and the IDT were fabricated on a lithium niobate ($LiNbO_3$) wafer separated by 1 mm and 5 mm. More detailed information about the design and fabrication can be found in Subsections 3.2.1 and 3.2.2.

Frequency-mixer circuit design and fabrication

The working frequency range of the lock-in amplifier (SR830, Stanford Research Systems) used in this experiment was from 1 mHz to 100 kHz, which is substantially lower than the SAW frequency. In order to solve this issue, a frequency mixer (AD835, Analog Devices, Inc.) was used in the connection between the IDT and the amplifier. In fact, the frequency mixer was a signal multiplier that multiplied the two input signals to produce a signal containing the sum and the difference frequencies of the input signals. These two frequencies could be isolated by filtering with either a high pass filter or low pass filter. Here, a sine wave at 24.95 MHz was used as one of the input signals of the mixer and the output signal was filtered by a low pass filter, in order to generate a signal at 50 kHz. With the help from one of the electronics technicians, a frequency-mixer circuit was designed and is shown in Fig. 4-24. The circuit was designed to generate two sinusoidal signals at 50 kHz that were used as the reference signal and the input signal of the lock-in amplifier, respectively. Thus, the circuit was divided into two blocks: the reference block and the signal block. The reference block included three units: a square-to-sine unit with additional function of voltage dividing, a frequency-mixer unit and a low pass filter unit. In this work, a 25 MHz square wave with 20 Vpp was used as both the LD modulation signal and one of the input signals to the mixer. The square-to-sine unit converted the square wave into a sine wave and reduced the voltage to 2 Vpp before being sent to the mixer. The signal block also included three units: a frequency-mixer unit, a low pass filter unit and an amplification unit with gain of 10x. In this block, no waveform conversion unit was needed, as the detected signal from the IDT was sinusoidal. The output signal from the sensor was used as one of the input signals of the mixer. As mentioned earlier, a 24.95 MHz sine wave with 2 Vpp was used as the second input signal of the mixers to both blocks.

In order to avoid electromagnetic interference (EMI) effects from the internal and external circuits, the PCB layouts of the two blocks were designed as two separate circuit boards using surface mount technology by commercial software (Altium Designer v18.0.12, Altium LLC). The boards were then isolated by individual metal cases. Fig. 4-25 shows the final version of the designs. Routing was performed on both sides of the board. The signal tracks and the footprint of the SMD components were mainly kept on the top side, whereas the power tracks and the ground plane were on the bottom. The purpose of the arrangement was to avoid any influence between the signals and the power supplies. The top copper layer and the bottom layer were connected through vias. The signal nets were designed to be as short as possible, and the power and the ground nets were kept much wider (normally 1-2 mm) than the signal tracks, in order to reduce parasitic inductance and capacitance. To avoid unwanted noise and distortion, power supply decoupling units were placed on the same side of the board as the mixer and the amplifier, and as close as possible to them. In addition, a Schottky diode with low forward voltage of 260 mV and a power inductor with inductance of 10 μH were added into each power track to provide reverse polarity protection and protection from reflected AC noise. Furthermore, the areas beneath the pins of the amplifiers on the bottom of the board were kept clear of any tracks to minimize the formation of parasitic capacitors, which would degrade the phase margin. The components J1-J4 and J6 were BNC connectors. The component J5 was a SMA connector. The components P1 and P2 were PCB terminal blocks that provided three pins for the positive and the negative power supply connections, and the ground connection between the board and the DC power supply.

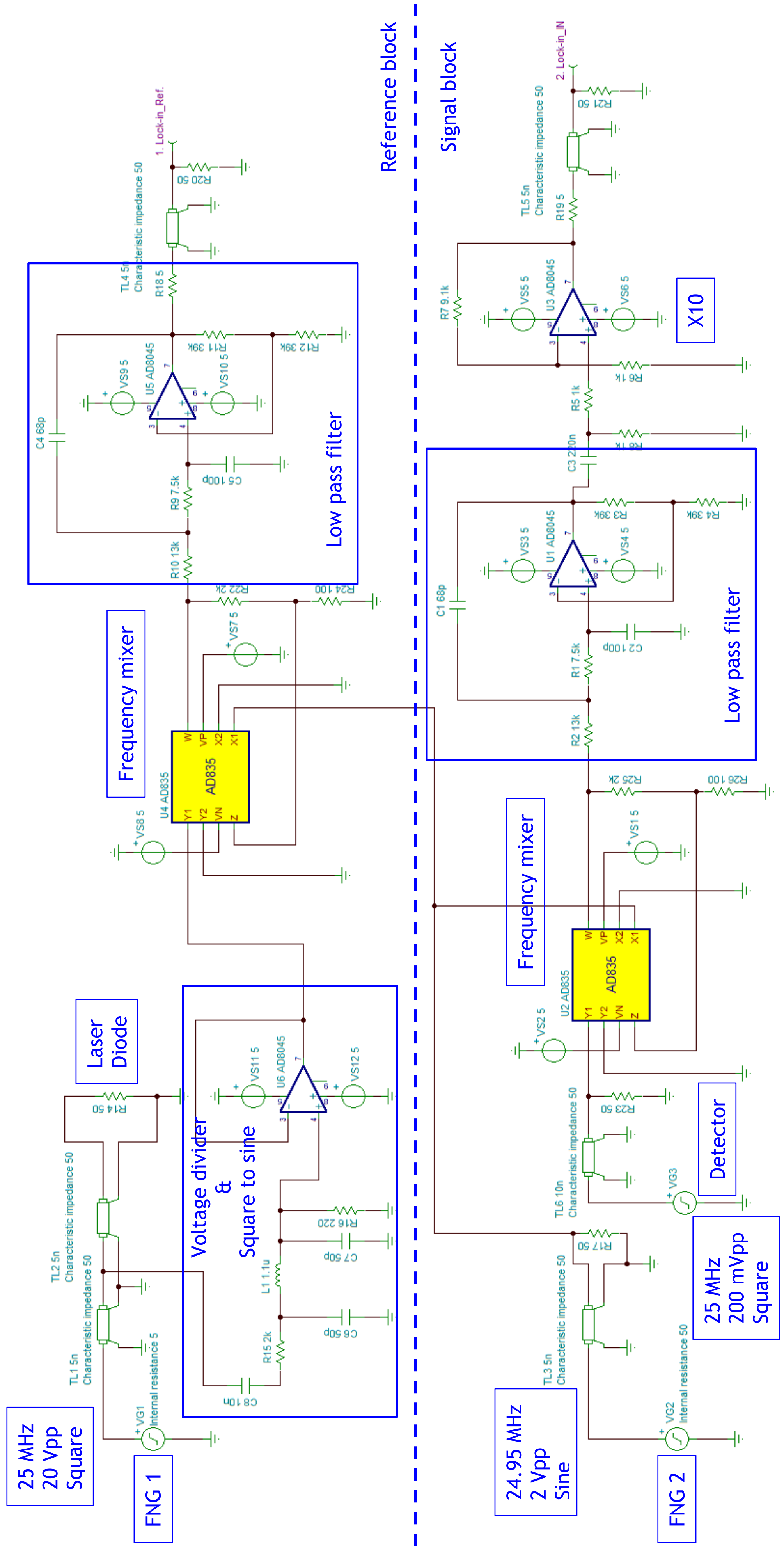

Fig. 4-24: Schematic of the design of the frequency-mixer circuit. (FNG: function generator).

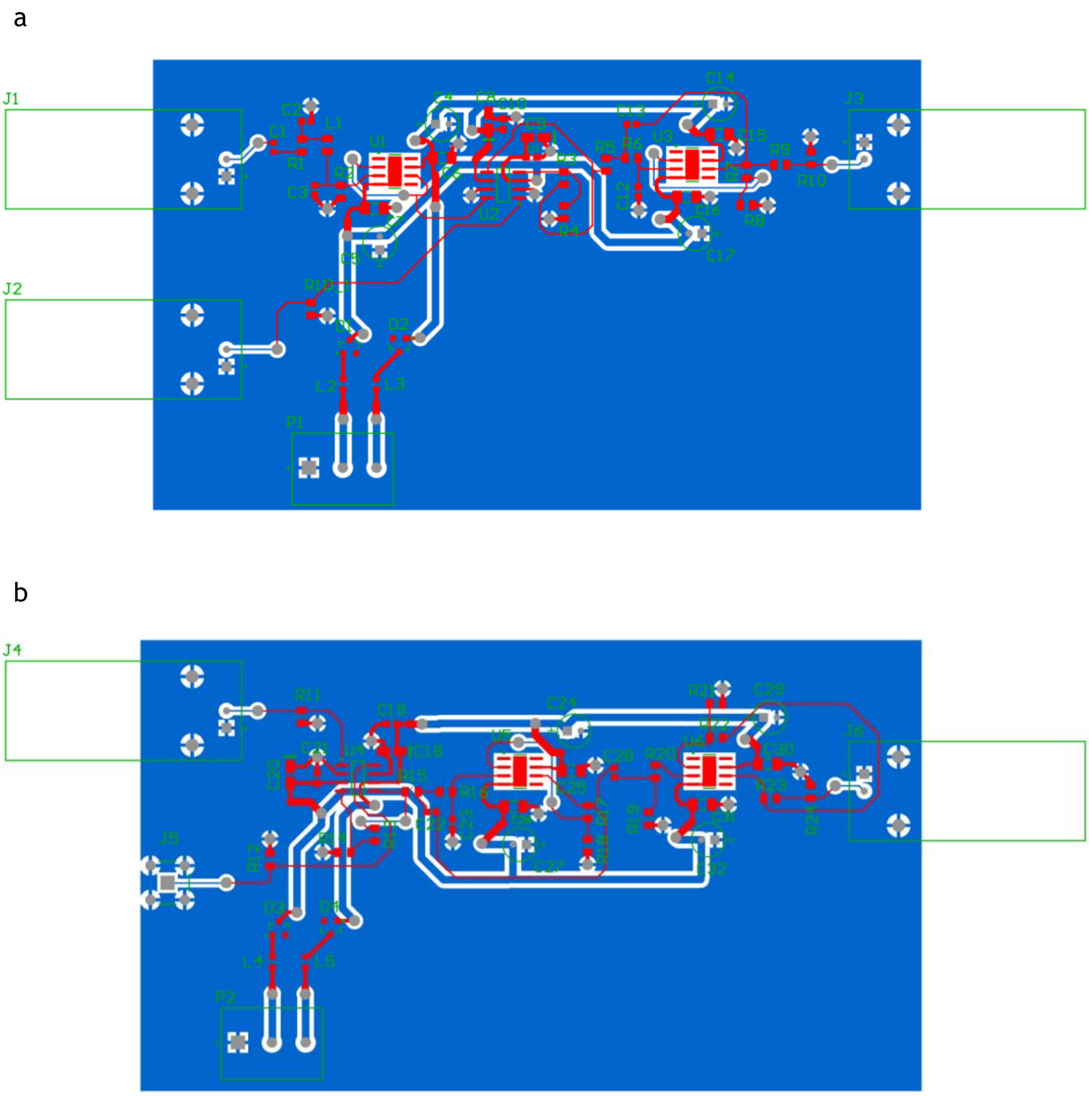

Fig. 4-25: The PCB layouts of the frequency-mixer circuit for (a) the reference block and (b) the signal block.

To assemble the components onto the PCB, the fabricated boards were coated with a solder paste layer. The SMD components were then placed on the solder paste carefully and aligned with the appropriated copper pin pads using tweezers. After that, the boards were transferred to a reflow soldering oven to complete the component mounting process. Photos in Fig. 4-26 show the two individual PCBs with assembled components sitting in their metal cases.

a

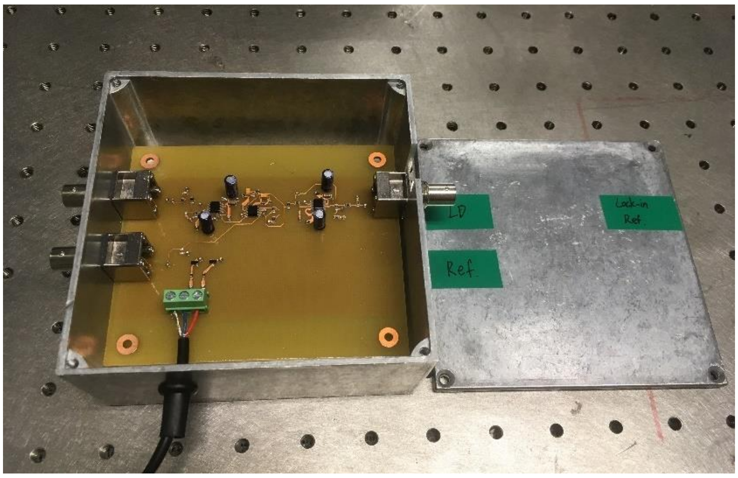

b

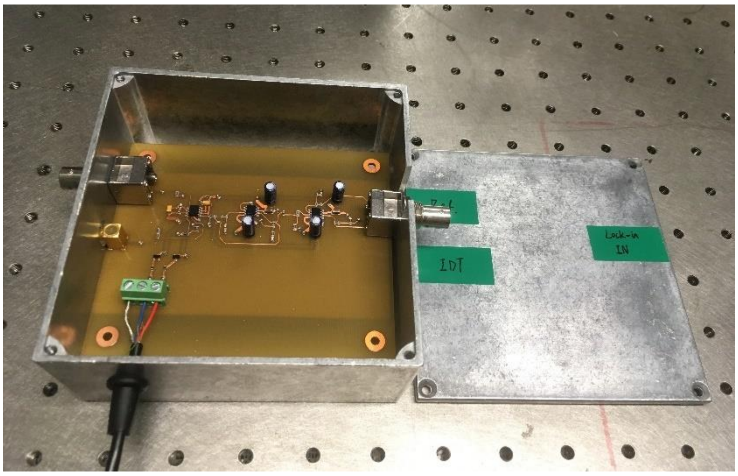

Fig. 4-26: The completed PCBs and component assembling with aluminium metal cases for (a) the reference block and (b) the signal block.

Experiment overview

In this experiment, two methods were chosen to create SAWs. In the first method, similar to that shown in Fig. 4-21, the line array was illuminated by the laser beam with different spot sizes. Because of the designed generation frequency of the metal line array being 25 MHz, the detection region was fixed to match the corresponding central detection frequency of the IDT, resulting in the illumination region being constrained to a row of the array, which was in the same line of the detection region. Again, in this region, there were three illumination points chosen: the left, the middle and the right of the row. In the second method, a single spot illumination was used. This time, an objective with magnification of 20x (NA = 0.4) was used to focus the beam tightly on a single metal strip of the array (laser spot size: x - Φ2.4 μm, y – Φ18.2 μm). The illumination position was also in the same line of the detection region. The devices with two different gaps between the array and the IDT were tested separately for each generation method. The detected signal was pre-processed by the frequency-mixer board before being inputted to the lock-in amplifier. The connections between the equipment used in the detection system are shown as a flow chart in Fig. 4-27. The connector J1 in the reference block was connected to the function generator 1 (FNG 1), which shared the same modulation signal (square wave at 25 MHz) as the laser diode (LD). The connector J5 in the signal block was connected to the IDT. Both connectors J2 and J4 were connected to the function generator 2 (FNG 2), sharing the same signal of sine wave at 24.95 MHz. The connectors J3 and J6 were connected to the lock-in amplifier to provide the reference and the input signals for the equipment, respectively. The LD modulation signal oscillated around a DC current of 850 mA in the first method, whereas it oscillated around 500 mA in the second method, in order to avoid ablation of the sample surface.

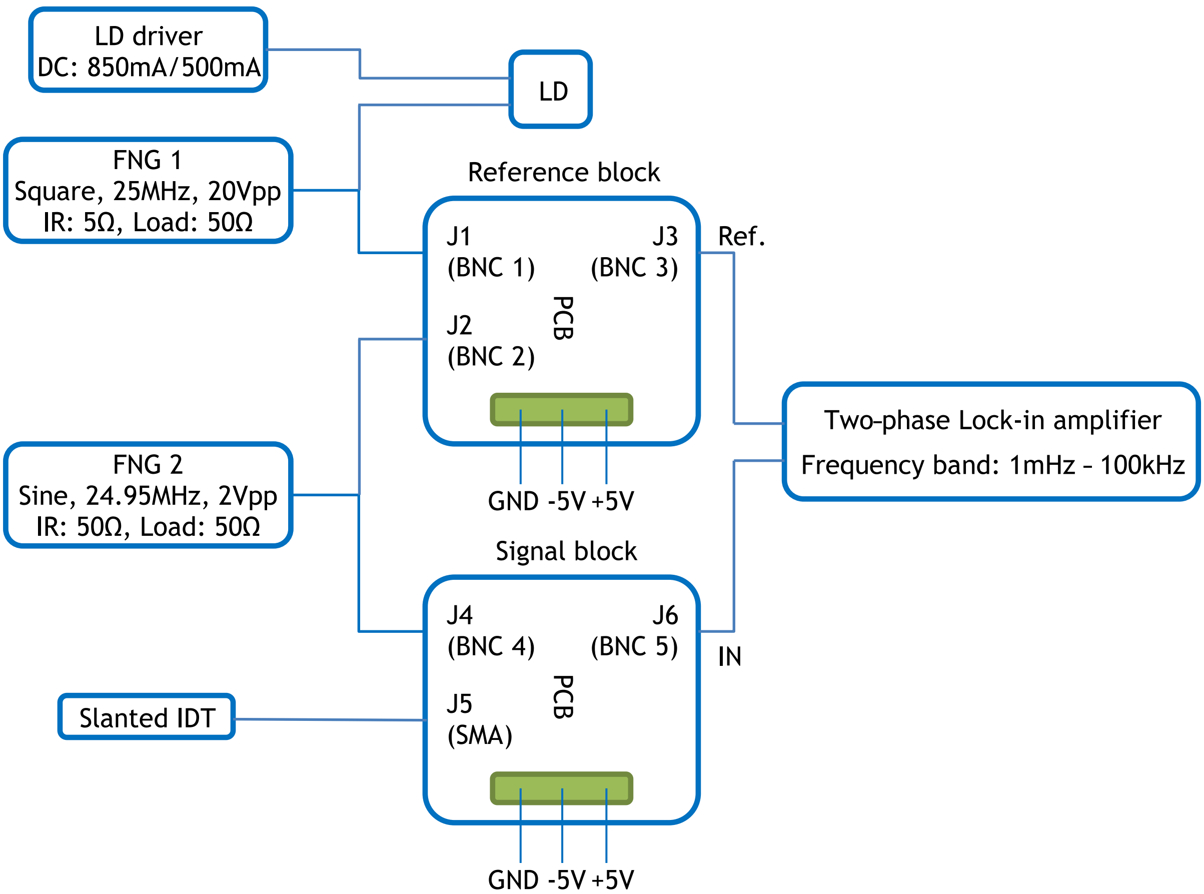

Fig. 4-27: Schematic of the connections between equipment and the frequency-mixer PCBs in the detection system.

4.7.2 Results and discussion

Frequency-mixer PCBs performance test

The performance of the two frequency-mixer PCBs was assessed before the experiment. In order to simulate the real experimental conditions as close as possible, the equipment setup followed that shown in Fig. 4-27, except the IDT was replaced by a function generator with three attenuators connected in series, which provided a sine wave with amplitude of 0.5 mVpp and frequency of 25 MHz at the board connector. The output signals from the two boards were connected to an oscilloscope, and are plotted in Fig. 4-28. It can be seen that, both signals are sinusoidal wave with the same frequency of 50 kHz, as expected from the design. The reference signal from the reference block had an average peak-to-peak voltage of 3.44 V, which is acceptable as the reference input of the lock-in amplifier. For the input signal coming from the signal block, the average peak-to-peak voltage value was about 4 mV. Although the input signal is not as expected that the value should be 10 times larger than the unprocessed signal (see Fig. 4-24), it is still acceptable as the signal input of the lock-in amplifier. In addition, there is a phase shift between the two signals, which arises from the phase shift between the original laser modulation signal and the original sensor signal. Therefore, according to the test results, it can be concluded that the two PCBs are working well, and are ready to be used.

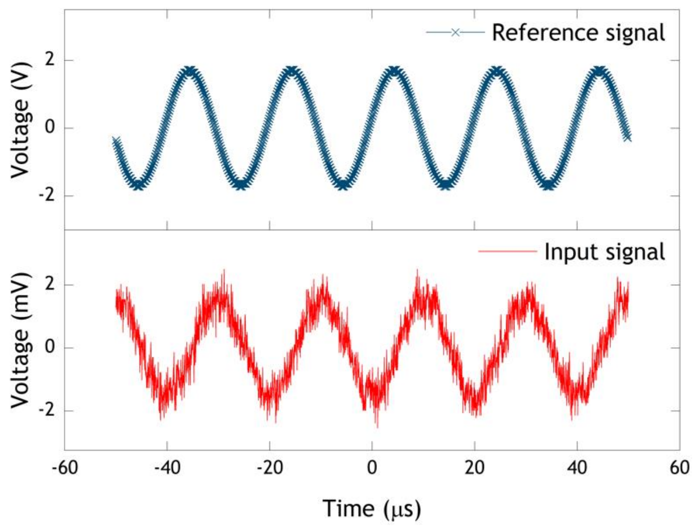

Fig. 4-28: The captured signals from the two PCBs by the oscilloscope are plotted as a function of time, which demonstrates good performance of the boards.

Laser-induced SAWs test by IDT

After assessing the performance of the PCBs, the signal noise level of the detection system was measured. The equipment setup followed that shown in Fig. 4-27, except the modulated laser beam was blocked before illuminating the line array. A signal varying from 6 mV to 20 mV RMS was displayed on the lock-in amplifier. Meanwhile, the phase difference between the detected signal and the reference signal was stable, which meant the input signal from the signal PCB was phase-locked. An oscilloscope confirmed both signals were sinusoidal waves with a frequency of 50 kHz. When disconnecting the IDT from the PCB, the voltage reading decreased to 60 μV, suggesting that the IDT was behaving as an antenna that received the modulation signal from the surroundings. Therefore, it was necessary to reduce the EMI by putting the sample device into a Faraday cage. The cage was made of aluminium mesh sheet with hole size of 1.13 mm x 1.31 mm. Two holes with diameter of 2.3 cm were cut in the top of the cage, in order to prevent the laser beam from being blocked by the mesh. After that, the signal noise level was measured again and the results are shown in Table 4-5. The noise level varied from 85 μV to 5 mV RMS, which was at least 4 times smaller than before.

Using this improved system, the laser-induced SAW detection was attempted. The results were summarized based on the illumination method with different parameter combinations, and are listed in Table 4-5. During the experiment, only noise was observed, with no obvious change in the signal value whether the laser beam was opened or blocked. After making several attempts to increase the modulation depth, the optical intensity of the sample, the SNR of the detection system, and use different illumination methods and detection equipment, it was still hard to determine whether the SAWs were generated under our experimental conditions. According to the literature [34, 35], a similar illumination method (single spot), modulated laser beam, optical system setup and incident optical power to ours were used previously. The detection system used was a Michelson interferometer with a detection point only 256 μm away from the generation point. They observed SAWs with a magnitude of approximately 350 fm at 25 MHz, which confirmed that extremely weak SAWs were created. By looking into the optical modulation depth and the beam size in our second experiment, the measured values of the two factors were 144.45 mW, *Φ*2.4 μm in the x-direction and *Φ*18 μm in the y-direction. Compared with the values used by [34, 35], which were 400 mW and *Φ*1.9 μm, our modulation depth was around 6.8 times smaller and the light spot was larger, meaning the amplitude of SAWs would be even weaker than 350 fm. It suggested that the IDT may not have been suitable for detecting such weak waves as it was strongly affected by EMI, reducing the SNR. In addition, the low optical intensity in the illumination region is the one of main reasons that would cause extremely weak waves to be generated. Further reducing the size of the light spot or changing the wavelength of the beam to increase absorption in the substrate are feasible ways to increase the optical intensity, and should be investigated in the future. Although the laser diode used in the experiment can produce more optical power than the previous one used in Sections 4.1-4.3, the difference between the lasing threshold and the typical operating current of the current diode is increased to 850 mA. However, the current laser modulation depth is only 400 mA. Therefore, there is a potential way to increase the modulation depth by modifying the modulation circuit, which can be investigated in the future. Last but not least, in order to reduce the distance between the generation and the detection regions while keeping the SNR as high as possible, a fibre-optic interferometer could be investigated to detect sound waves. This can be investigated in the future as well.

Illumination method	**Modulation signal**	**Sample device**	**Signal noise level**	**Results**
Metal line array	Square wave (DC: 850 mA AC: 20 Vpp)	Gap between generation and detection: 1 & 5mm	0.2 – 5.0 mV	Random noise signal only
Focused single light spot	Square wave (DC: 500 mA AC: 20 Vpp)	Gap between generation and detection: 1 & 5mm	0.085 – 4.0 mV	Random noise signal only

Table 4-5: Summary of experimental results of the laser-launched SAWs test by IDT that was isolated from the EMI effect by a Faraday cage.

4.8 Summary

In this Chapter, several attempts were made to generate and detect SAWs using a modulated laser beam. In the early stage of this work, it was attempted to create SAWs by the single line and the single spot illumination methods, and detect them by visualising the fluid flow in a single droplet and particle movements in a thin chamber, and by measuring the temperature variation on the surface of the substrate. However, according to the experimental results we obtained, none of these experiments showed the expected phenomena previously reported in the literature. After investigating potential reasons causing the issue, the laser diode mount was modified to achieve a deeper modulation depth, which should enhance the amplitude of SAWs by increasing the temperature difference between the upper bound and the lower bound of the modulated beam. By improving the optical system, the laser beam was focused tightly using an objective (4x, NA = 0.1) to increase the optical intensity in the illumination region. Following these two 'big' improvements of the system, it was attempted to create laser-induced SAWs by the single spot illumination method and detect with a fibre-optic hydrophone with high sensitivity. However, due to the working mechanisms of the device and the physics when the SAWs propagate along the liquid-solid boundary, only small amount of acoustic energy, which was transferred inside the liquid in the form of longitudinal pressure wave, could be received by the hydrophone. As a result, no obvious signals were obtained. In order to increase the SNR of the system, the line array illumination method was used to generate SAWs. For detection, both a laser Doppler vibrometer with higher sensitivity, and a slanted IDT with a lock-in amplifier were used as sensors. However, due to the long distance between the generation point and the detection point, and with extremely weak SAWs being created, neither systems could detect such weak waves against the noise background. In a similar experiment reported in the literature, the amplitude of SAWs was measured to be around 350 fm, which was far below the minimum displacement that could be detected by our current equipment. Furthermore, in order to confirm the amplitude of the surface displacement that could be expected, numerical modelling based on our experimental conditions was performed, and will be described in the next Chapter.

Chapter 5

Simulation of laser-induced surface acoustic waves (SAWs)

In this chapter, the surface displacement of the substrate due to several factors was studied through numerical modelling based on the experiments in Chapter 4. Through modelling the transient laser heating and the relative thermal expansion in the vertical direction of the top surface of a silicon substrate in the steady state, it showed that elastic waves were generated under modulated laser illumination at low modulation repetition rates. By introducing a thin metal layer with higher absorption coefficient on the substrate surface and increasing the optical intensity in the illumination region, the surface displacement was increased significantly. However, as the modulation repetition rate was increased, the displacement was greatly reduced. For instance, at 25 MHz, the displacement was 4.75 orders of magnitude smaller than the value at 1 kHz (which was 0.026 nm without metal coating). This indicates that the created waves would be too weak to move particles and difficult to be detected based on our current setup of the detection system.

Before performing any modelling, it was necessary to find out the weakest SAWs that could move particles. The study was performed in the following two steps: the experiment of particle manipulation and the amplitude measurement of SAWs. In the first step, an interdigital transducer (IDT) fabricated on a piezoelectric substrate was used as the SAW generator. Due to the working mechanisms of the transducer (see Section 2.3), the amplitude of the waves was controlled by the supplied electric power. The experiment was performed by placing a square glass capillary, containing colloidal samples of polystyrene beads with size of Φ9.95 μm, on the substrate at a distance about 1.2 cm away from the IDT. The generated SAWs penetrated into the capillary and then established bulk standing waves inside the capillary due to the multi-reflections from the sidewalls, which resulted in the beads being moved into pressure nodes. In order to obtain a better penetration effect, a water-based coupling layer was created between the capillary and the substrate by pipetting. At the resonant frequency of the IDT, the weakest acoustic pressure force was obtained by reducing the supplied electric power until bead movements could no longer be observed. Here, the lowest supply power was around 30 dBm. In the second step, the amplitudes of the 'weakest' SAWs were measured by a laser Doppler vibrometer (UHF-120, Polytec GmbH). The detection region was chosen to be the same area where the capillary had been placed. Through data analysis, the average amplitude was found to be 0.6±0.3 nm.

5.1 Method and parameter settings

In this simulation, 3D modelling based on the experiment in Section 4.1 was performed using COMSOL Multiphysics modelling software, which was developed based on finite element analysis (FEA). Considering the aperture of the generated SAWs and the spatial profile of the laser beam, a 2D elliptical Gaussian beam was created as shown in Fig. 5-1 (a). The diameter of the beam was set at 245.9 μm in the x-direction and 5 mm in the y-direction for the case of SAWs with a frequency of 20 MHz and the speed of 4918 m/s in silicon. Here, the diameter in the x-direction was the wavelength of the waves as the SAWs were created by combining several laser-launched single SAW pulses without intervals. To model the modulated laser beam, a square waveform that was a function of time was used, following by multiplying with the Gaussian beam profile. Here, a square waveform was chosen based on the real modulation signal used in the experiment in Section 4.1. The amplitudes of the created Gaussian beam and the waveform were normalised between 0 and 1. The frequency of the waveform was set as 1 kHz. Fig. 5-1 (b) shows five periods of the square wave with normalized value. It should be noticed that the modulation repetition rate was set as 1 kHz rather than 20 MHz as the simulation was mainly focused on the surface behaviour under the steady state. According to the simulation results in the CW mode, the temperature almost reaches steady state after 5 ms (see Fig. 5-3 (a)), which means that to study the thermal expansion in the vertical direction at 20 MHz under the steady state, the simulation time should be longer than 5 ms. Furthermore, considering the accuracy of the transient results, the simulation time step was set as one quarter of the signal duration. Due to the limitation of the computer memory, no results could be obtained, therefore, the modulation repetition rate was reduced to the low frequency in order to continue further analysis. In addition, the simulation time was set as 30 signal periods. Fig. 5-1 (c) shows a 3D geometric structure created in the model with the dimension (W x L x H) of 5 mm x 35 mm x 0.5 mm, which represents the silicon substrate. Here, an ellipse is drawn on the top surface of the substrate, which represents the laser heating area and finer meshing is used within the area in order to model the Gaussian beam profile properly. The dimensions of the ellipse were set to be the same as the laser beam.

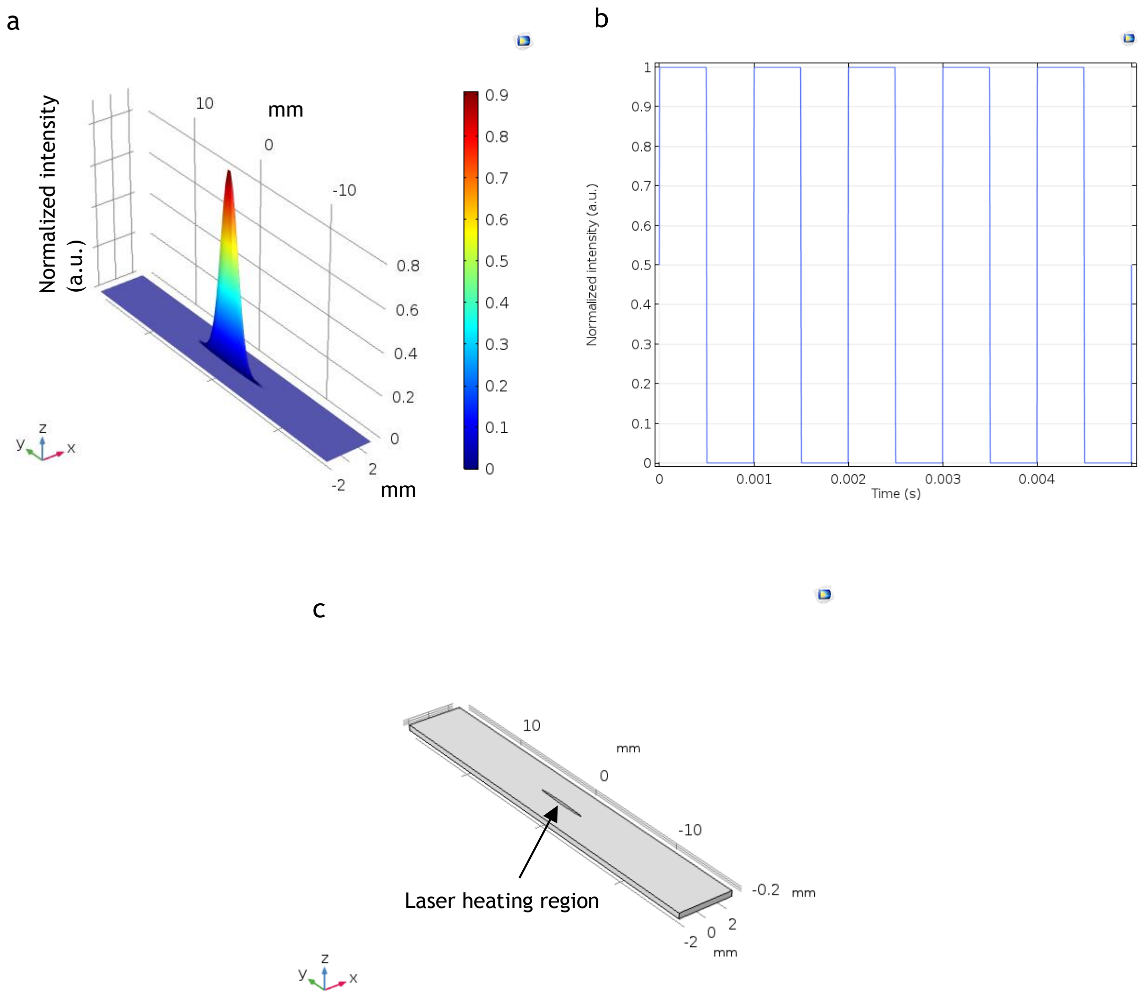

Fig. 5-1: (a) The elliptical Gaussian beam spatial profile; (b) five periods of the square waves with normalized values; (c) the 3D geometric structure, which represented as a silicon substrate with an elliptical laser heating area.

In this work, the transient temperature and the relative physical deformation due to the thermal expansion of the top surface of the substrate were the two main factors that we looked into. Therefore, there were two physical models chosen and coupled in the simulation: a heat transfer model and a solid mechanics model. In the heat transfer model, the heat transfer was calculated according to the heat equation

$$\rho C_p \frac{\partial T}{\partial t} + \rho C_p u \cdot \nabla T + \nabla \cdot q = Q$$
$$q = -k \nabla T \qquad \textbf{(Eq. 5-1)}$$

where ρ is the density, C_p is the specific heat capacity at constant pressure, T is the absolute temperature, u is the velocity field, k is the thermal conductivity and Q is the heat source. In order to apply the modulated beam profile into the modelling, the type of the heat source was set as a domain heat source that was expressed as [155-158]:

$$Q(x,y,z) = Q_0\left(1 - R_c\right) \cdot \frac{A_c}{4\pi\sigma_x\sigma_y} e^{-\left[\frac{(x-x_0)^2}{2\sigma_x^2} + \frac{(y-y_0)^2}{2\sigma_y^2}\right]} \cdot e^{-A_c z} \cdot \text{waveform} \quad \textbf{(Eq. 5-2)}$$

where Q_0 is the average power of the laser beam; R_c and A_c are the reflectance and the absorption coefficient of silicon at 790 nm; σ_x and σ_y are the standard deviations of the Gaussian beam in the x- and y-direction, which are one quarter of the beam diameter, according to the relation between the beam radius (at $1/e^2$ of maximum optical intensity) and them. For the boundary conditions, the diffuse surface and the convective heat flux were applied on all boundary surfaces except the bottom surface, in order to model the heat dissipation from the substrate to the ambient air and natural air-cooling. A constant temperature of 20°C was applied on the bottom surface of the substrate, in order to model the ideal cooling effect of the heat sink. The initial temperature of the domain was set to 20°C. In terms of the solid mechanics model, the relevant mechanical parameters were kept as the default values in the software for silicon. For the boundary conditions, all of domain surfaces were set as free to deform except the bottom surface that was set as a fixed constraint, resulting zero deformations in all directions. Fig. 5-2 shows the main boundary conditions of the two physical models added on the domain. For the meshing, a physics-controlled mesh with extremely fine element size was chosen. Additional details about the values of the main parameters used in the simulation are listed in Appendix III.

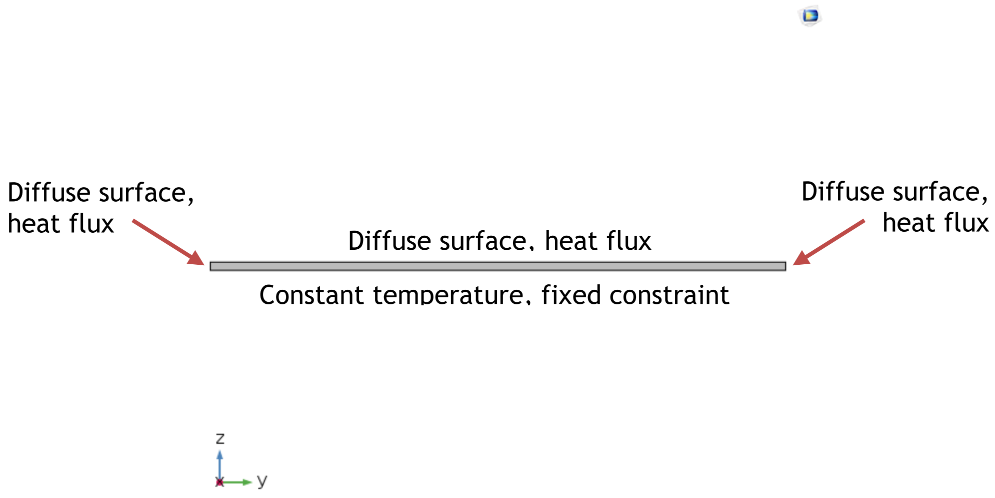

Fig. 5-2: The boundary conditions of both the heat transfer model and the solid mechanics model applied on the domain.

5.2 Results and discussion

5.2.1 Transient temperature and thermal expansion

As described above, the transient temperature and the relative thermal expansion of the central point, which absorbed the maximum energy from the laser beam on the top surface of the substrate, were analysed and are shown as a function of time in Fig. 5-3. Fig. 5-3 (a) and (b) show the surface temperature under the laser operation modes of CW and quasi-continuous-wave (QCW) with a modulation repetition rate of 1 kHz and a modulation depth of 269 mW. Fig. 5-3 (c) shows the relative surface displacement in the vertical direction under the QCW mode. As shown in the graphs, under the CW mode, the temperature reaches steady state after approximately 5 ms. Compared to the situation without illumination, the temperature increase is around 0.094 °C. Under the QCW mode, the repetition rate of the temperature fluctuation matches well with the laser modulation frequency, which means the ability of silicon to dissipate heat is efficient at a low modulation frequency. As for the CW mode, the temperature variations become steady after 5 ms. The maximum temperature increase in the steady state is around 0.074 °C, which is 0.02 °C less than that in the CW mode. In terms of the vertical thermal expansion, the variations of the surface displacements also match well with the temperature variations, which indicates good deformability of the substrate at low variation rate. The surface displacements were obtained by calculating the difference between the maximum and the minimum displacements in each repetition period. The average value was then calculated, which was around 0.026 nm. Compared with the weakest SAWs generated by the IDT for particle manipulation, of which the amplitude was 0.6 nm; this was 22 times smaller. Considering the absorption coefficient of the material, the surface displacement could be increased by shortening the thickness of the light energy absorption region within the material, which could be achieved by coating an additional thin metal layer with higher light absorption on the top of the substrate. The detailed information and the simulation results are discussed in the next Subsection 5.2.2.

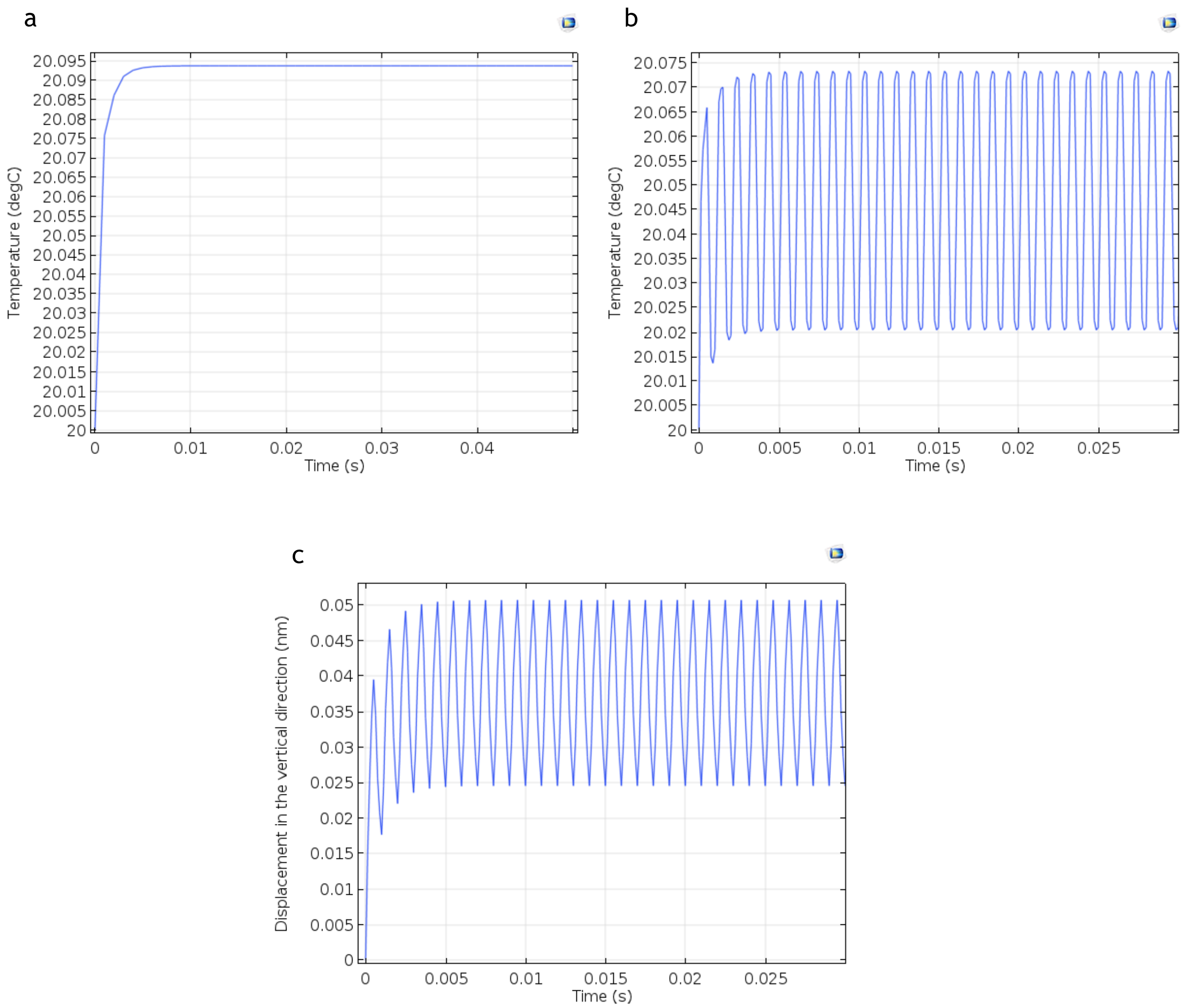

Fig. 5-3: (a) The temperature distribution under the CW operation mode at central point on the top surface; (b) the temperature distribution under the QCW mode with modulation frequency of 1 kHz at the same point; (c) the relative thermal expansion in vertical direction.

5.2.2 Effects of extra metal layers

In this Subsection, the effects on the surface displacement with metal thin layers coated on the substrate were investigated through modelling. Table 5-1 shows a comparison of the characteristics of several common metals used for metal deposition. It can be seen that the absorption coefficients of metals are much higher than silicon, although the reflectance of silicon is relatively lower. Due to the low absorption coefficient of silicon, almost all of the energy is absorbed within a thickness of 38 μm, according to the Beer-Lambert law. In this case, the thermoelastic source can be treated as being buried in the sample body, resulting in bulk acoustic waves being generated (see Subsection 2.2.1). In order to reduce the energy dissipation during the waves propagating from the generation point to the sample surface, it would be better to generate SAWs by constraining the light absorption within nanometre scale from the surface. By introducing a thin metal layer deposited on the sample surface, the total incidence light energy can be absorbed within the thickness of a few tens of nanometres and then transferred to the surface of the silicon substrate to create stronger SAWs. In addition, the transmittance in Table 5-1 was calculated based on the Beer-Lambert law [64, 159]. Following the above considerations, two metals (aluminium and molybdenum) with relatively low reflectance and high absorption coefficient were selected, in order to study the effects on the surface displacement. In the simulation, the parameter settings were kept the same as those used in Section 5.1. Only the reflectance and the absorption coefficient were adjusted to match with the relative materials, and the domain heat source was replaced by a thin layer heat source. The thicknesses of the two metals were determined based on Table 5-1. The average power of the laser beam, the modulation frequency and the simulation time were also kept as 269 mW, 1 kHz and 30 modulation periods.

Material	Reflectance (at 788 nm)	Absorption coefficient (at 788 nm)	Thermal conductivity (at 788 nm)	Transmittance
Sliver (Ag)	0.99551	8.7397e+5 cm^{-1}	429 [W/(m*K)]	NA
Gold (Au)	0.97548	7.6673e+5 cm^{-1}	317 [W/(m*K)]	NA
Copper (Cu)	0.96119	7.8431e+5 cm^{-1}	400 [W/(m*K)]	NA
Aluminium (Al)	0.87232	1.3312e+6 cm^{-1}	237 [W/(m*K)]	0.018436 (TH: 30 nm)
Molybdenum (Mo)	0.55914	5.4042e+5 cm^{-1}	138 [W/(m*K)]	0.004498 (TH: 100 nm)
Silicon (Si)	0.33039	1154.6 cm^{-1}	130 [W/(m*K)]	0.012434 (TH: 38 μm)

Table 5-1: Characteristic of several common metals used for metal deposition and silicon. (TH: thickness of material)

Table 5-2 lists the simulation results for the average temperature difference and the average thermal expansion in the vertical direction at the central point of the top surface of the silicon substrate with/without different metal layers. Similar to the method of obtaining the surface displacement in the last subsection, the average temperature differences were obtained by calculating the difference between the maximum and the minimum temperatures in each repetition period under the steady state, followed by data averaging. Comparing the results, we can conclude that the effects of involving metal thin layers are obvious. The temperature differences at the point of interest were higher in the case of a substrate with coatings than for pure silicon only, which results in stronger thermal expansions. The highest surface displacement (around 0.166 nm) was obtained for a substrate with a molybdenum layer. Thus, the displacement was increased to 6.4 times the value for a non-coated substrate. However, compared with the target value of 0.6 nm, there still was a difference of 0.414 nm, which could be reduced further by either increasing the laser power or reducing the size of the illumination area. Here, the displacement was obtained at a modulation repetition rate of 1 kHz. In order to investigate the effects on the displacement with different modulation frequencies, the corresponding modelling was performed as well, which will be discussed in the next Section.

Material	Temperature difference (°C)	Surface displacement (nm)
Si	0.053	0.026
Si & Al (TH:30 nm)	0.088	0.036
Si & Mo (TH: 100 nm)	0.412	0.166

Table 5-2: The simulation results of the temperature difference and the relative thermal expansion in the vertical direction at the central point of the top surface of the silicon substrate with/without different metal layers.

5.2.3 Effects of laser modulation frequencies

So far, the studies have mainly focused on the steady state for low modulation frequencies. However, according to the real experiments in the last Chapter, the laser beam was modulated from 200 kHz to 20 MHz. As mentioned before, the modelling could not be completed in the steady state with high modulation frequencies due to the limitation of the computer memory capacity. Therefore, in this part, the effects on the surface displacement from different modulation frequencies were studied indirectly by looking into the surface temperature differences in the steady state at low frequencies and in the transient state at high frequencies. Specifically, the modelling was based on the pure silicon substrate without any coatings. Similar to Section 5.1, the parameter settings were kept the same. However, in order to apply different frequencies into the simulation, the 'Parametric Sweep' function was activated with the modulation frequency being swept from 1 kHz to 50 MHz. This time, the simulation time was increased to 100 modulation periods. At both low and high frequencies, the temperature differences at the central point of the top surface of the substrate were calculated and averaged by the same method used in the last Subsection. The only difference between the two groups was that 100 temperature difference points were counted for the high frequencies. The temperature difference was plotted as a function of modulation frequency, and is shown in Fig. 5-4. Both the x-axis and the y-axis are presented on a log10 scale. The temperature difference decreases with the frequency increasing. At 25 MHz, the temperature difference is 4.75 orders of magnitude smaller than that at 1 kHz. As the thermal expansion is proportional to the temperature difference, the surface displacement at 25 MHz could be predicted to be 0.46 fm without a metal coating and 2.95 fm with a Mo layer. Compared to the target value of 0.6 nm for the weakest SAWs of particle manipulation, the modelling results are much smaller, and the created waves are far too weak to move particles.

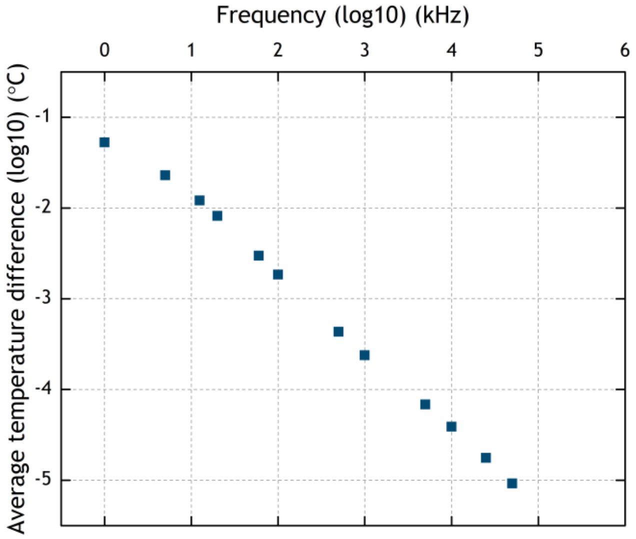

Fig. 5-4: Simulation results of the temperature difference plotted as a function of modulation frequency at the central point of the top surface of the substrate.

5.2.4 Effects of beam sizes

In this Subsection, the effect on the surface displacement with smaller beam size under the same optical power is studied. The modelling was performed based on the experimental conditions described in Section 4.5. In the simulation, a model representing a silicon substrate without any coatings was built. Similar to the settings in Section 5.1, the beam shape on the sample surface was still kept as elliptical, but the size of it was reduced to *Φ*8.63 μm in the x-direction and *Φ*122.81 μm in the y-direction, representing the size measured for a focused beam through a 4x objective (NA = 0.1). Due to the fact that the laser was replaced by a multimode diode with higher optical power, the reflectance and the absorption coefficient of silicon were adjusted to match with the new wavelength, which was 808 nm. The average optical power Q_0 in Eq. 5-2 was changed from 269 mW to 378 mW based on real measurements. The modulation frequency and the simulation time were also kept as 1 kHz and 30 modulation periods. The physical models and the relative boundary condition settings were kept the same as those described in Section 5.1. In terms of the data analysis, the surface temperature difference and the relative displacement were calculated and averaged following the same methods used in Subsections 5.2.1 and 5.2.2. The average surface displacement in the vertical direction at central point of the top surface of the substrate was found to be around 1.19 nm, which was nearly 46 times higher than the value (0.026 nm) with a larger beam size. Thus, it could be predicted that the surface displacement increased with decreasing beam size. However, according to Fig. 5-4, the value would be reduced to 21.16 fm at modulation frequency of 25 MHz. By using a molybdenum absorption layer, the value could be increased to approximately 135 fm, which was in the same displacement scale as the values reported from the literature in the last Chapter (see Subsection 4.7.2). The surface displacement could be increased further under higher magnification objective. However, the sample surface would ablate easily.

Therefore, based on the modelling results, it can be concluded that the SAWs can be created by a modulated laser beam based on our experimental conditions. However, due to the extremely weak amplitudes of the waves, they are far below the minimum displacements that our current devices can measure. In addition, it is worth mentioning that the above models were based on the full modulation depths, which means the incident light power was modulated starting from 0 mW. However, in the real experiments, considering the safe operation of the LD, the lower bounds of the modulation current were set above the lasing threshold. Therefore, the real modulation depths for modelling in Subsections 5.2.1 - 5.2.3 and Subsections 5.2.4 were 11% and 51% smaller than those used in the modelling, which meant the amplitudes of the real SAWs were smaller than the simulation results.

5.3 Summary

In this Chapter, several numerical studies were implemented based on the experiments on laser-induced SAWs described in Chapter 4. Specifically, the transient nature of the temperature and the relative thermal expansions in the vertical direction at the central point of the top surface of the silicon substrate were investigated. At a light modulation repetition rate of 1 kHz, both the temperature and the displacement variations matched well with the modulation periods, which indicate the ability of heat dissipation and the deformability of the silicon substrate were sufficient. By involving metal thin coatings with higher absorption coefficients, the surface displacement was increased. For a molybdenum (Mo) layer, the displacement was increased to 6.4 times the value for a non-coated substrate. Through varying the modulation repetition rate from

1 kHz to 50 MHz, the relative temperature differences shown a decreasing trend with frequency. At 25 MHz, the amplitude of the surface displacement was reduced to 2.95 fm with a Mo layer, which was about 5 orders of magnitude smaller than that at 1 kHz. Furthermore, the SAWs could be enhanced by reducing the beam size. For instance, by using a 4x objective (NA = 0.1) and a Mo layer, the surface displacement could be increased to approximately 135 fm at modulation frequency of 25 MHz. Unfortunately, the created waves were still not strong enough to move particles even by a tightly focused beam using a higher magnification objective (20x, NA = 0.4, see Section 4.7). Regarding the literature in Subsection 2.2.1, instead of using SAWs, the laser-induced acoustic shock waves could be used to move particles as well. However, due to the toxic operating solution, low pulse repetition rate and nonflexible frequency variation, it was impossible to achieve either biological sample manipulation or advanced particle trapping based on standing ultrasound waves, which did not meet the aim of the project.

As reported in Chapter 4, acoustic waves could be strengthened by either increasing the optical intensity of the illumination area further or increasing the modulation depth. However, for the former solution, the sample surface would ablate easily, which could not achieve continuous particle manipulation. For the latter solution, the LD modulation circuit needed to be modified to allow deeper modulation depth. In addition, the optical power could be increased by an array of diode lasers. However, in order to achieve the target displacement of 0.6 nm, at least ten arrays containing 100 diode lasers for each were needed, which was challenging for the experimental configurations. Therefore, compared to above methods, using an extra light absorber with higher absorption coefficient would increase the possibility of particle manipulation by the modulated laser beam. The more details about this will be described in Chapter 6.

Chapter 6

Microparticle manipulation by laser-induced optical and thermal forces

This chapter discusses the manipulation of microbeads and biological samples using laser-induced forces based on several different physical mechanisms in a fluid chamber by a diode laser. By focusing the laser beam onto a silicon-based substrate, large microbeads (Φ20 μm) were trapped and manipulated by the optical gradient force. Smaller particles (Φ4.95 μm), however, were pushed away from the beam by laser-induced thermophoresis. By varying the incident optical power and the material of samples, the particle speeds were analysed, showing an increase with optical power and a decrease with thermal conductivity of the materials. By involving an extra light energy absorber – single-walled carbon nanotube (SWNT) clusters into sample solution, the symmetrical laser-induced thermal convection flows were observed and a ring shaped particle-stopping region was formed. As expected, similar phenomena were found when the material of the substrate was changed to glass. By varying the optical power absorbed by the clusters and the size of the particles, the average particle speeds were analysed showing a directly proportional trend with energy absorption and an increase with particle size. The ring diameter of the particle-stopping region also increased with particle size. For the biological samples of Jurkat cells, similar movements were observed. Regarding the above findings, we were able to develop a model of the physical process underpinning the motion of particles. Furthermore, the SWNT clusters were illuminated by a modulated laser beam. Instead of acoustic pulses being generated, some interesting particle behaviours were observed. Based on the previous studies, several physical mechanisms were predicted and one of them was investigated through analysis of particle trajectories. Last but not least, by increasing the incident optical power further, gas bubbles were generated. The water-displacement method was used to try to collect the bubbles.

6.1 Theory

In this Section, some important definitions and equations used in the later sections are listed and described. These theories could help us to understand the physical mechanisms of the results based on our experimental conditions.

6.1.1 Reynolds number

In fluid dynamics, Reynolds number (Re) is a numerical expression of the ratio of inertial (due to mass) forces to viscous (due to friction) forces. It is a useful tool to predict the flow situation in fluid systems. At low Re numbers (typically less than 2000), the flow is mainly dominated by the viscous force, which often results in laminar flow. In contrast, for cases of high Re numbers, the flow is mainly dominated by the inertial force, which results in turbulent flow [160, 161]. The Re number is defined as [162]:

$$\mathrm{Re} = \frac{\rho u L}{\eta} = \frac{uL}{\nu}$$
$$\nu = \frac{\eta}{\rho} \qquad \text{(Eq. 6-1)}$$

where ρ is the density of the fluid, u is the velocity of the fluid with respect to the object, L is the characteristic linear dimension, η is the dynamic viscosity of the fluid and v is kinematic viscosity of the fluid. In the following sections, the experiments were performed within water-based solutions. Therefore, to predict the flow situation based on our experimental conditions, the value of the kinematic viscosity (v) in above equation could be determined based on the case of water, which was around 1.01E-6 m^2/s. The fluid velocity (u) was assumed to be the same as the measured particle velocities, due to the densities of most of particles (polystyrene, 1.05 g/cm^3) being close to the water density. Regarding the data plotted in Fig. 6-17, the maximum fluid velocity was about 1.7E-6 m/s. The characteristic dimension (L) would be the particle size, of which the maximum was around 1.0E-5 m. After calculation, the Re number was around 1.7E-5, which is much smaller than 1.

6.1.2 Laminar flow and Stokes flow

Laminar flow is a kind of flow when the flow motion can be treated as several parallel fluid layers without any disturbances between each other. As mentioned above, it occurs when the Re number is low. Particles which follow the flow will move in straight lines and parallel to the solid-fluid interface [163].

Stokes flow is one type of laminar flow under the situation of the Re number being much smaller than 1. This kind of flow normally occurs under different typical situations, such as very low flow velocities, very large viscosities of fluids or very small length-scales of flows [164, 165]. The movement of particles inside the Stokes flow will be dominated by the viscous force that can be described as a drag force exerted by the surrounding fluid. The drag force is also known as Stokes's drag force, which can be expressed as [163]

$$F_d = 6\pi\eta R\vec{v} \qquad \textbf{(Eq. 6-2)}$$

where η is the dynamic viscosity of the fluid, R is the radius of the particle, v is the flow velocity. Based on the calculation in the previous section, it can be inferred that the fluid flows generated in the later experiments were Stokes flows. The movements of particles were determined by the flows and one of the forces the particles experienced was the Stokes's drag force.

6.1.3 Electrical double layer (EDL)

An electrical double layer (EDL) composed of two parallel layers of charge along the solid-liquid interface appears when an object encounters a fluid. The first layer is called Stern layer, in which the solid-liquid interface is mainly occupied by solvent molecules mixed with a small amount of specifically adsorbed ions, followed by some solvated/hydrated ions. Due to the intrinsic charge of the solid, the layer of the solvent molecules mixture displays a strong electrical orientation. The plane passing through the centres of the specifically adsorbed ions is called the inner Helmholtz plane (IHP). The plane passing through the centres of the solvated ions is called the outer Helmholtz plane (OHP). The second layer, called as diffuse layer, is the region just beyond the OHP. This layer is mainly composed of free solvated ions of which the concentration decreases exponentially with the distance from the object surface [166-169]. The schematic structure of the EDL is shown in Fig. 6-1.

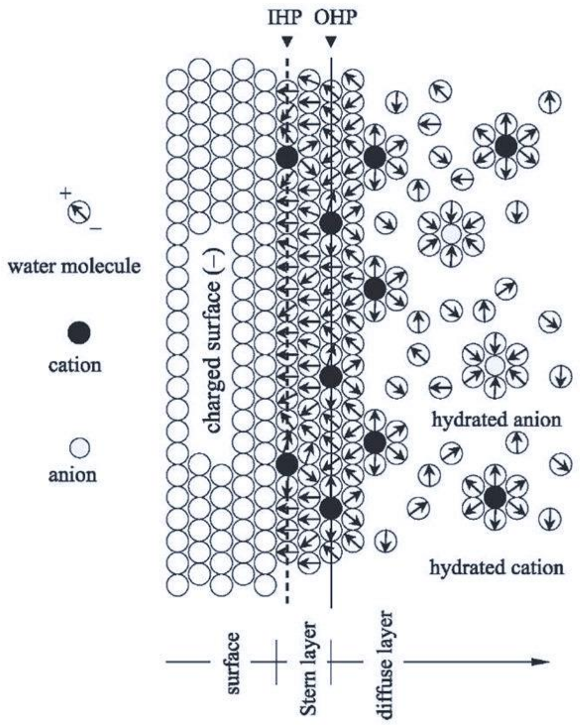

Fig. 6-1: The schematic structure of the electrical double layer (EDL) [166].

In an electrolytic solution, the characteristic thickness of the EDL can be approximated as 1-1.5x Debye length. The Debye length (κ^{-1}) can be expressed as [167, 169]

$$\kappa^{-1} = \sqrt{\frac{\varepsilon_r \varepsilon_0 k_B T}{2 N_A e^2 I}} \qquad \textbf{(Eq. 6-3)}$$

where ε_r is the dielectric constant of the solvent, ε_0 is the permittivity of free space, k_B is the Boltzmann constant, T is the absolute temperature in Kelvins, N_A is the Avogadro constant, e is the elementary charge and I is the ionic strength of the electrolyte.

6.2 Microbead manipulation with laser-induced optical force

In this Section, experiments with sample solutions containing different sizes of polystyrene microbeads are described. According to the experimental results, only the largest particles (*Φ*20 μm) could be trapped and manipulated by the laser-induced optical force. In contrast, for the particles with smaller sizes, instead of being trapped, the different particle reactions were observed and described in Section 6.3, which implied other types of forces being generated based on our experimental conditions.

6.2.1 Experimental methods

In this experiment, colloidal solutions were prepared by following the method described in Subsection 3.3.1 and injected into the sample device with substrate material of silicon (see Subsection 3.2.3) by pipetting. The experimental system setup was the same as the one described in Section 3.1 except a 10x objective (NA = 0.25) was used. The samples were then illuminated by the laser diode operated CW with full optical power (OP) on the sample of 378 mW at 1.1 A and a spot size of *Φ*2.5 μm in the x- and *Φ*52.9 μm in the y-direction. During the experiments, three colloidal solutions containing microbeads with different sizes (*Φ*1 μm, *Φ*4.95 μm and *Φ*20 μm) were tested. The experimental phenomena were recorded at a frame rate of 15 fps and the recording time was 57 s.

6.2.2 Results and discussion

For the sample solution containing polystyrene beads with 20 μm in diameter, we observed that up to three beads could be trapped and moved simultaneously in 2D by the laser line. We also noticed that particles only experienced the force within a short distance from the beam centre, which indicated that the particles mainly experienced optical gradient force. In contrast, neither of the smaller size beads (1 μm and 4.95 μm in diameter) could be manipulated under the same experimental conditions. Fig. 6-2 (a) and (b) show the original positions of the laser spot and the three beads of interest (*Φ*20 μm, highlighted by red dashed circles), and one of the video frames during trapping and manipulation, respectively.

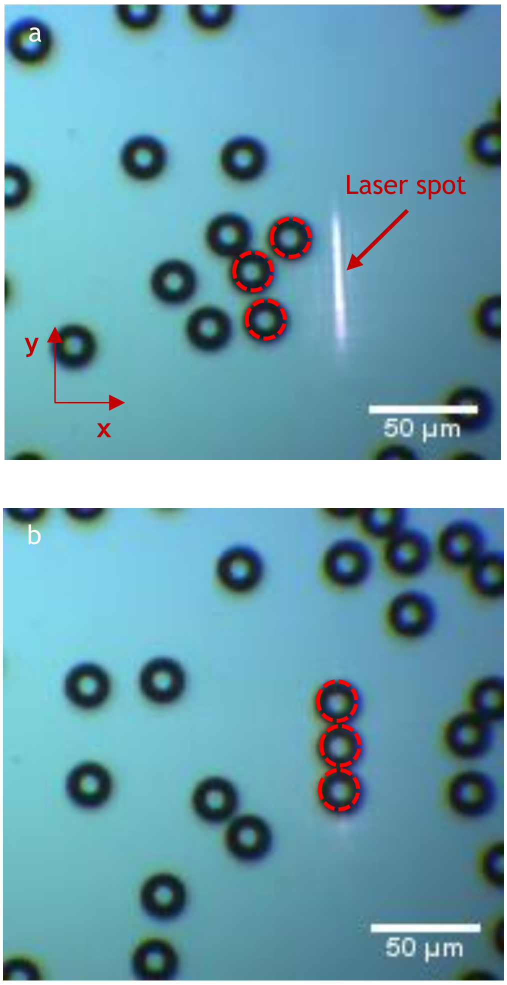

Fig. 6-2: (a) The original positions of the laser spot and the polystyrene beads of interest (Φ20 μm, highlighted by the red dashed circles). (b) One of the video frames during the trapping and manipulation. Laser spot size: Φ2.5 μm in the *x*-direction, Φ52.9 μm in the *y*-direction.

The experimental phenomena show that it is possible to move a few large beads with the laser beam focused through a low N.A. lens, but to move more and small particles simultaneously, we went on to investigate laser-induced thermal forces.

6.3 Microbead manipulation with laser-induced thermal forces on a silicon substrate

Instead of particle trapping, in this section, microbeads with smaller size were moved away from the illumination region without moving the laser beam, which was caused by laser-induced thermal forces. Through further studies, characteristics of one of the forces in our system were revealed. By involving an extra light absorber and reducing particle size further, stronger movement was observed and some extra interesting findings were gained. Based on the studies, more clues were obtained which improved our understanding about the physical mechanisms of the experimental phenomena.

6.3.1 Experimental method

The experimental setup and conditions in this experiment were the same as the previous experiment, except polystyrene beads with 4.95 μm diameter were used. Instead of moving the laser spot, a static laser beam was focused on the silicon substrate rather than on the particles. The responses of five particles of interest were analysed by particle tracking software (See Subsection 3.4.2).

6.3.2 Results and discussion

During the experiment, we found that most beads around the laser spot moved continuously away from the illuminated region under continuous irradiation condition, which we believe was caused by thermophoresis due to the thermal gradient arising from the absorbed light power. However, two beads were trapped by the beam, which may have been the contributions of the gradient of the light intensity profile and thermal convection flow. The relevant results are shown in Fig. 6-3. The positions of the five beads of interest without and with laser irradiation at the very beginning of the video are shown in Fig. 6-3 (a) and (b), respectively. In Fig. 6-3 (c), the colour curves show the relevant trajectories of the particles at the last video frame; the longest distance of one bead movement is around 100 μm. The two trapped beads are identified by the red arrows.

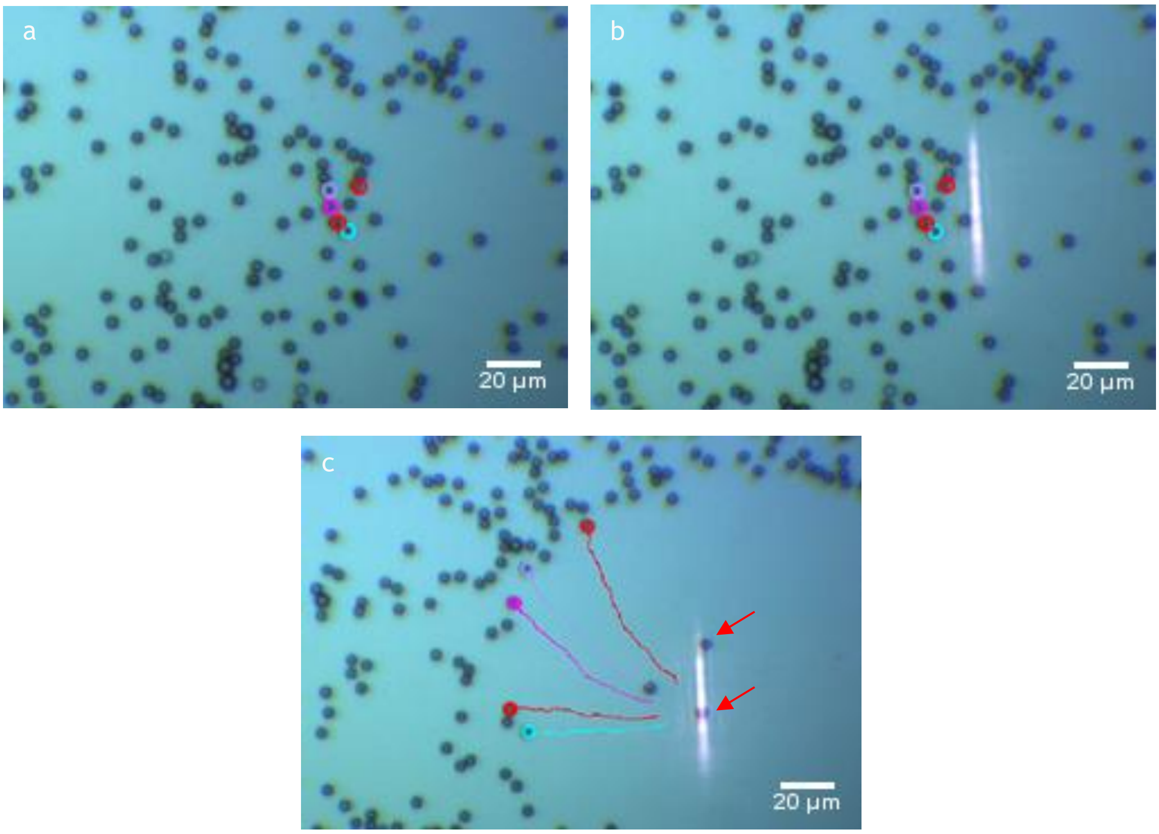

Fig. 6-3: The movement analysis of the 4.95 µm polystyrene beads (a) without laser illumination, (b) with laser beam at the very beginning, (c) with laser beam at the last frame by software Tracker. Laser line size: *Φ*2.5 µm in the x-direction, *Φ*52.9 µm in the y-direction.

In order to support the conclusions from the experimental phenomenon, another experiment was performed based on a non-absorbing substrate, which was a normal glass slide, under the same experimental conditions. The results showed that none of beads could be moved. Therefore, the effect of the optical scattering force could be neglected. Besides, particles can only experience the optical scattering force close to the light beam. In our case, the beads moved up to 100 µm away from the laser spot.

6.3.3 Further studies

As mentioned in Chapter 2, although the principle of thermophoresis in gases is well studied, there is no general physical model of particle thermophoresis in liquids. So far, several mathematical models and experimental findings have been reported by researchers [22-27, 29, 30, 32, 116, 120, 127, 128]. However, these conclusions appear to depend strongly on their specific experimental conditions. Even some conclusions from different authors are contradictory. Therefore, in order to understand the physical mechanisms responsible for our observations, it is necessary to investigate laser-induced thermophoresis and thermal convection flow by looking into the particle behaviours under different experimental conditions, such as using different sample materials with similar particle size (silica, Φ5.20 μm, and polystyrene, Φ4.95 μm) and the same incident optical power, or using different incident optical power (OP) with the same bead material and size.

Different sample materials, similar particle size and same incident optical power

Under this condition, the experiment was repeated seven times. Fig. 6-4 (a) and (b) show the real particle trajectories with different sample materials but similar bead size and the same incident optical power (OP). As shown in the graphs, both silica and polystyrene beads spread out, moving away from the laser beam in radial directions. However, these trajectories are not symmetrical based on either x-axis or y-axis, which is unexpected regarding the modelling results in Section 7.2. Furthermore, the bead moving speeds were compared for the two sample materials as well, of which the results are shown in Fig. 6-4 (c). The particle speed was obtained by dividing the distance between the original and the final positions of the bead, by the corresponding time period. This was done by analysing the bead movement using the particle tracking software. The results were then plotted as a function of particle starting angle (θ). The starting angle was determined based on the coordinate of the bead initial position relative to positive x-axis (see Fig. 6-4 (d)). As shown in the Figure, the polystyrene beads move faster than the silica beads. The thermal conductivity of polystyrene (around 0.033 W/(m·K)) is lower than silica (around 1.1-1.4 W/(m·K)), which may affect the thermophoretic mobility, D_T (See Subsection 2.5.2). Interestingly, the potential relation was also revealed through the theoretical studies of D_T in the literature [170-172].

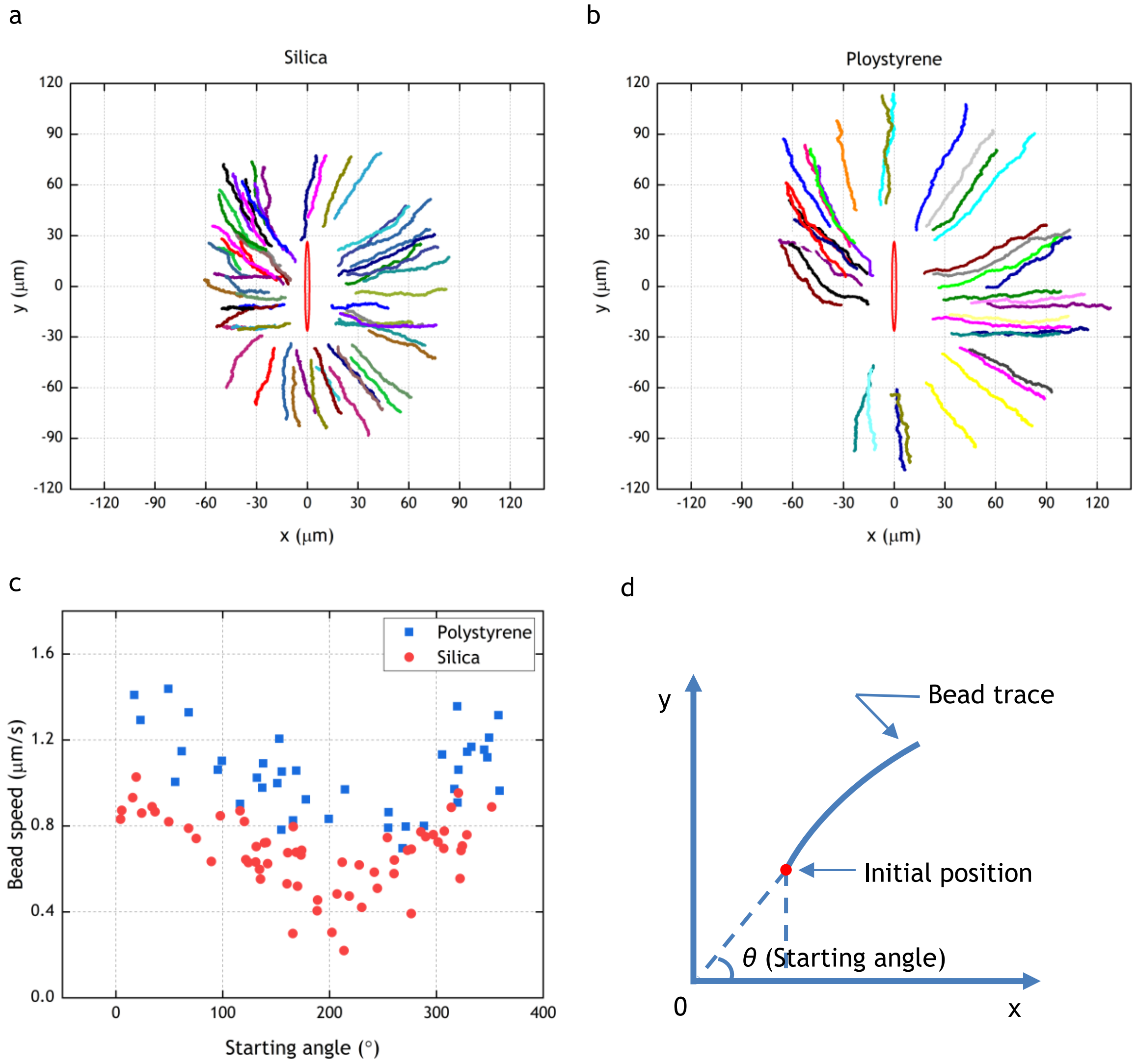

Fig. 6-4: Multiple plots of real bead trajectories with same incident optical power (378 mW, 100% OP) but different materials: (a) silica (Φ5.20 µm) and (b) polystyrene (Φ4.95 µm). (c) is the related bead speed plot as a function of starting angle. (d) is the definition of starting angle (θ). The red oval represents as the laser spot.

Different incident optical power with the same bead material and size

Similar to previous case, under this condition, the experiment was repeated seven times as well. Fig. 6-5 shows the comparison of bead speeds with different input optical powers. By comparing graph (a) to (d), the bead speed tends to increase with the incident optical power, indicating that the effect of thermophoresis increases with the light absorption. The trend is demonstrated as well in graph (e) showing the relation between the average bead speed and the incident optical power represented as the percentage of the full optical power.

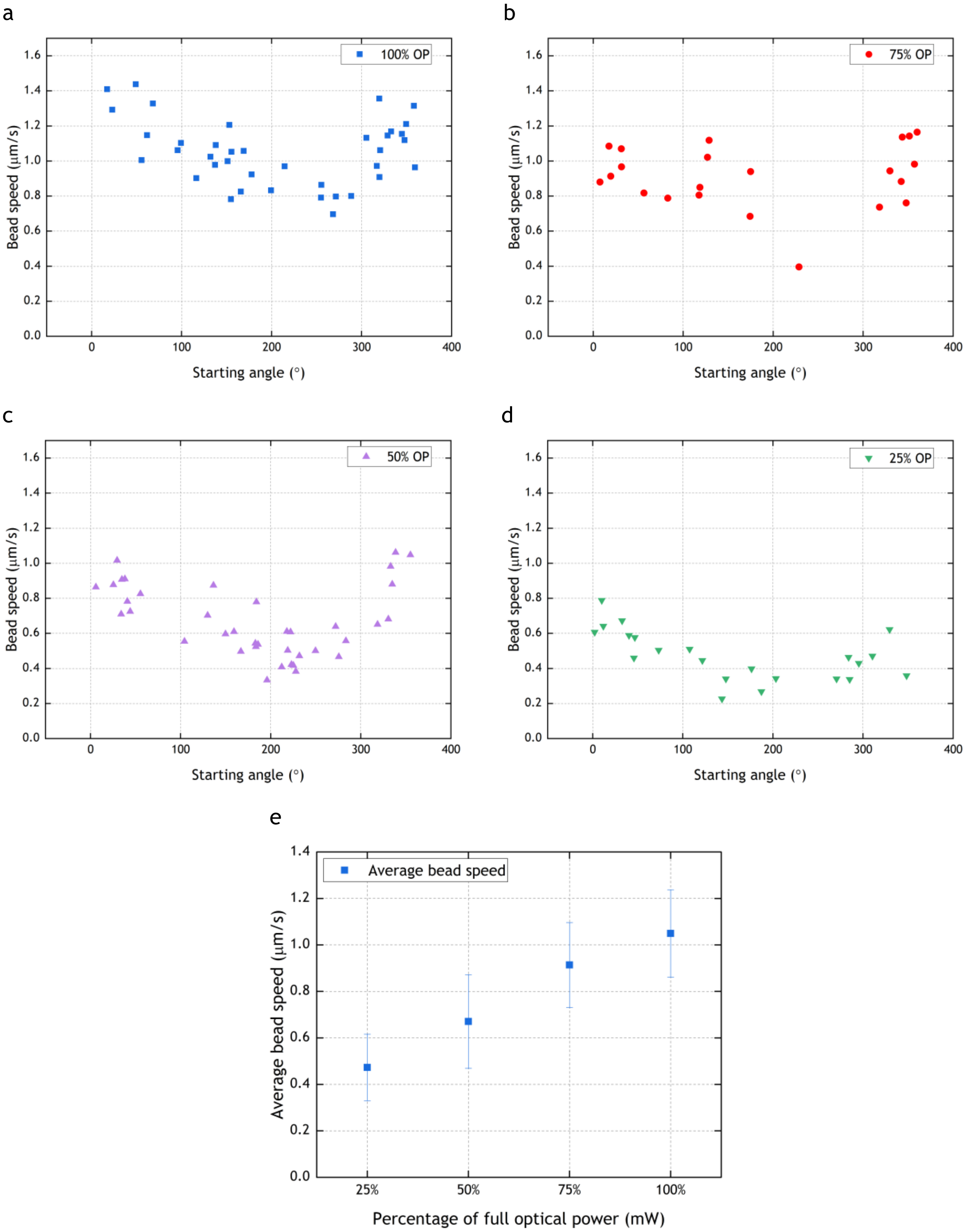

Fig. 6-5: (a - d) are the plots of bead speed as a function of starting angle under different incident optical powers with same bead material (polystyrene) and size (Φ4.95 μm). (e) is the plot of average bead speed as a function of incident optical power.

Effect of particle initial position

It is worth mentioning that according to the graphs in Fig. 6-5, the bead speed decreased with starting angle until reaching to around 200° and then increased, seen as the asymmetrical particle trajectories shown in Fig. 6-4. In order to investigate this trend, after checking the experimental recordings carefully, a slow fluid flow with direction from the left side to the right side of the light spot was found in most cases, which may have been caused by solution evaporation due to poor sealing of the sample chamber. Therefore, this unexpected slow fluid flow should be the main reason causing the asymmetry. The relation between bead speed and particle initial position was also investigated by examining the data in the high-speed regions (with starting angle range from 0° to 50° and from 300° to 360° approximately) and low-speed regions (with starting angle range from 100° to 300° approximately) based on the speed-angle plots in Fig. 6-5. In the low-speed regions, the data was divided into two groups based on the distance from the beam. Fig. 6-6 shows the two typical cases found during the study. Specifically, Fig. 6-6 (a) and (b) show the speed-angle plot of silica beads with data points highlighting based on the speed region and the position, and relative bead initial positon plots, respectively. As shown in the graphs, in the high-speed region, as we expected, the starting positons of most beads are close to the beam. In the low-speed region, there appears to be a trend that the bead speed decreases with distance relative to the beam. Similarly, Fig. 6-6 (c) and (d) show the speed-angle plot of polystyrene beads at 50% of the full incident optical power, and relative bead positon plots, respectively. Similar to the silica beads, in the high-speed region, the initial positons of most beads are close to the beam. However, in the low-speed region, similar speed ranges are seen for both particles close to the beam and far from the beam, which is potentially caused by the weak fluid flow. Therefore, the bead position is another factor affecting the trend shown in Fig. 6-5.

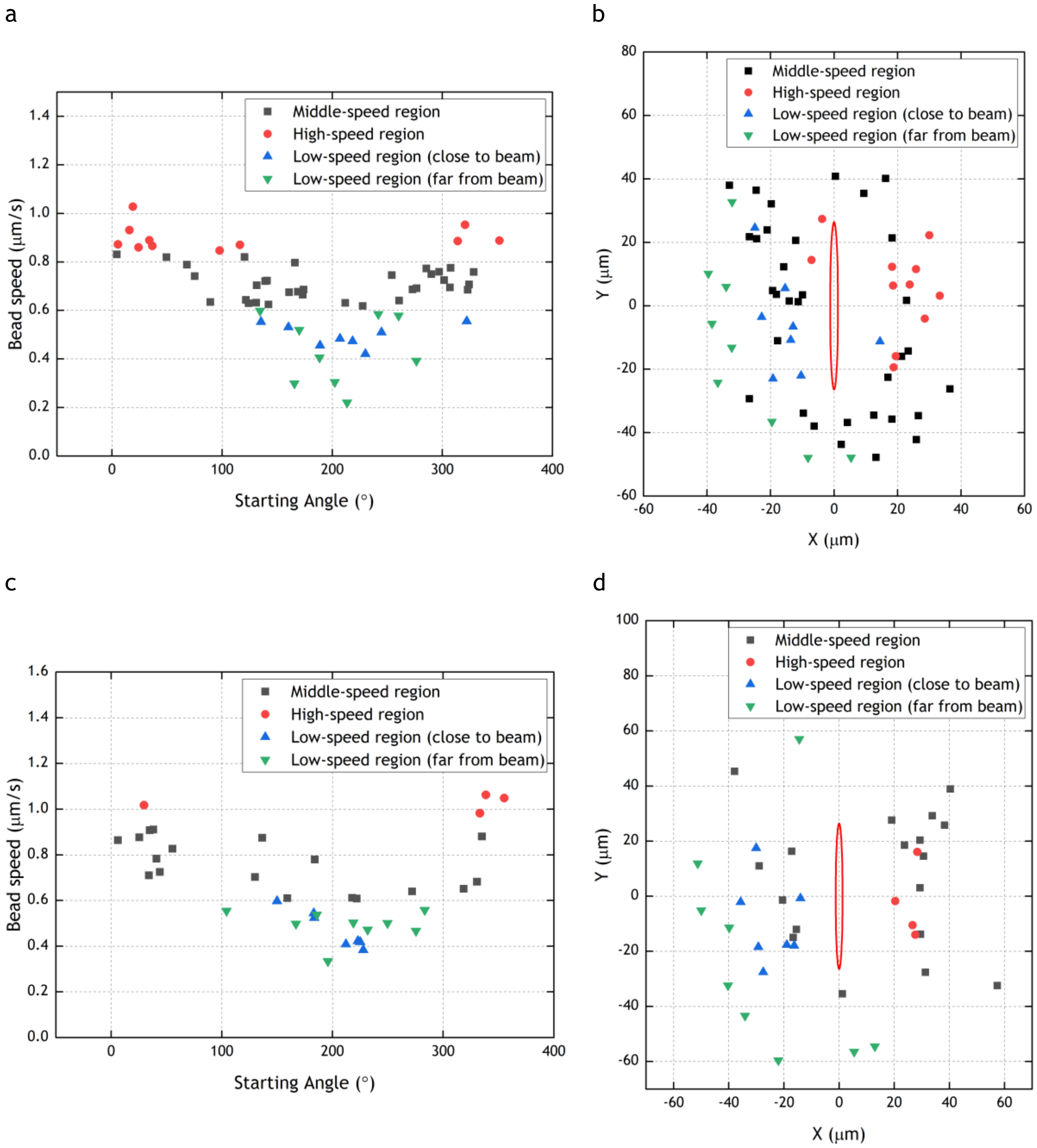

Fig. 6-6: The bead speed-starting angle plots of silica beads with 100% OP based on the different speed region (a) and relevant initial bead position plots (b); the bead speed-starting angle plots of polystyrene beads with 50% OP based on the different speed region (c) and relevant initial bead position plots (d). The red oval represented as the laser spot.

So far, only laser-induced thermophoresis has been discussed. For thermal convection flow, no evidence of any fluid flows or streaming was observed during the experiments. Therefore, from the above findings, it can be concluded that the experimental phenomena are mainly due to thermophoresis. A more detailed analysis of thermal convection flow using a multiphysics numerical simulation will be presented in the next Chapter.

Effects of SWNT cluster and particle size

According to Chapter 4, the amplitudes of laser-induced SAWs were too weak to be detected due to the weak thermal expansion of the sample surface. Therefore, it is necessary to update our experiment by involving an extra light energy absorber – single-walled carbon nanotube (SWNT) clusters into the colloidal solution, in order to increase the absorption. In addition, under the CW laser-operation mode, the existence of laser-induced thermal convection flow in the sample chamber can be investigated as well by involving the extra absorber. For a better explanation, let us consider that if the convection flow was generated, according to the type of convection introduced in Subsection 2.4.3, the convection flow should be natural convection, as there was no extra force added into the chamber. Natural convection is generated by fluid density differences due to the temperature gradient established inside the liquid. Therefore, in order to enhance the convection flow, the temperature gradient can be increased by increasing the energy absorption. The SWNTs are a good choice for this purpose, due to the property of high optical absorption. In order to observe the flow more easily, the particle size was reduced to Φ1.54 μm (purchased from Polysciences, Inc.) because larger size beads tended to sediment at the substrate surface within a short period after injecting into the sample chamber. By choosing beads with smaller sizes, particles are more likely to remain suspended in the liquid for a longer time due to the reduced mass of the beads themselves. Therefore, stronger phenomena for smaller beads should be expected. However, in order to keep the experimental conditions as consistent as possible, the 10x objective (NA = 0.25) had to be used. Therefore, the smallest size of particles, which could be visualized easily and tracked stably by the analysing software, was around 1.5 μm diameter.

The sample solution was prepared by following the method described in Subsection 3.3.2. The laser was operated CW with the incident optical power reduced to 180 mW at 650 mA, in order to avoid strong thermal expansion effects (see Section 6.6). For the camera settings, the frame rate was changed to around 20 frames/second and the recording time was varied to 30 s. During the experiment, the symmetrical laser-induced thermal convection flow was clearly seen by observing different particle movements through varying the height of the focal plane: particles close to the substrate moved towards the SWNT cluster and were then redirected upwards as they approached the cluster, and then moved away from the cluster. After travelling for a certain distance, the microbeads moved down towards the substrate and repeated the above patterns continuously. Fig. 6-7 shows some interesting experimental phenomena found during the experiment. In Fig. 6-7 (a), most of beads could not follow the fluid flow entirely; particles and SWNT debris (which means clusters with much smaller sizes compared to the cluster of interest) started moving towards the hot region as soon as the laser beam illuminated to the cluster. As the beads and the debris approached the cluster, they started to attach to it and continued to accumulate throughout the lasing period, which was unexpected. Eventually, after 30 s, a mixture of beads and SWNT debris distributed around the main cluster. Fig. 6-7 (b – d) show a control experiment, in which the laser beam was focused on the silicon substrate directly with no SWNT clusters. Interestingly, the results we obtained were similar to the findings reported in a published journal from a research group in Mexico [33]. In our control experiment, particles started moving towards the beam with much lower speed than 2 μm/s reported in the journal paper, and a much weaker fluid convection flow was observed. After illumination for 1-2 mins at roughly 50% of full optical power (180 mW), more and more particles stopped at a certain distance from the light spot and started to accumulate at that position, leaving a clear region around the beam. Therefore, an obvious ring shape was formed by the cloud of particles. After increasing the laser to full power following a further 1-2 mins, the beads did not move away from the illumination region. Based on the above phenomena, it was suggested a laser-induced thermal convection flow moved particles towards the beam, and thermophoresis pushed particles away from the hot region due to the thermal gradient formed by the energy absorption in the substrate. Bead stopping was caused by particles experiencing two balanced forces with opposite directions.

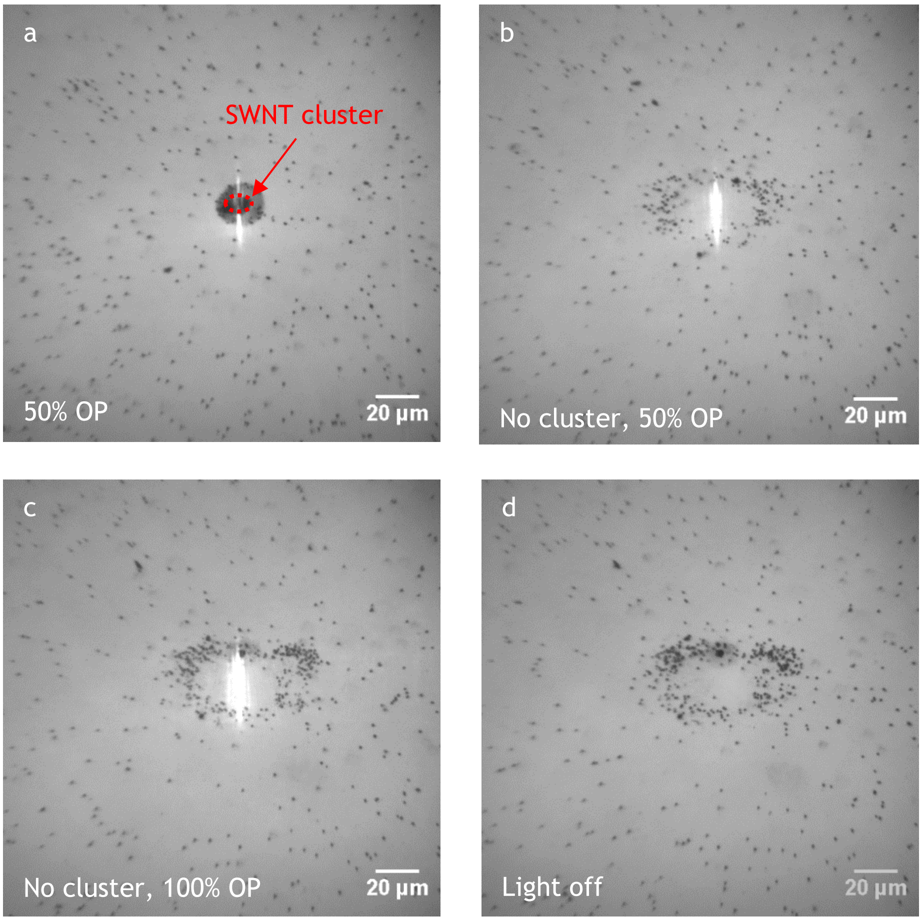

Fig. 6-7: Experimental phenomenon (a) with SWNT cluster and *Φ*1.54 μm polystyrene beads under the illumination with nearly 50% OP (180 mW); (b) without SWNT cluster and with *Φ*1.54 μm polystyrene beads under the illumination with the same OP as graph (a); (c) without SWNT cluster and with *Φ*1.54 μm polystyrene beads under full-power illumination; (d) without SWNT cluster and with *Φ*1.54 μm polystyrene beads under the condition of light-off.

Furthermore, by comparing Fig. 6-3 (c) and Fig. 6-7 (c), we can see that the experimental system setup and most of the experimental conditions are the same, except for the particle size (*Φ*4.95 μm in Fig. 6-3 and *Φ*1.54 μm in Fig. 6-7), the video frame rate and the recording time (15 fps & 57 s in Fig. 6-3, and 20 fps & 30 s in Fig. 6-7). Interestingly, the phenomena observed in the two experiments were also different. As shown in Fig. 6-3 (c), after 57 s particles tended to move further away from the hot region, while in Fig. 6-7 (c), particles formed a stopping area with a ring shape that was close to the cluster within 30 s. This difference may imply that, unlike convection flow, the thermophoretic velocity is not only dependent on temperature gradient, but particle size as well.

6.4 Microbead manipulation with laser-induced thermal forces on a glass substrate

According to the findings from Subsection 6.3.3, it was decided to repeat the experiment using glass substrate after considering the potential applications for biological sample. In the following sections, the SWNT energy absorber was used, and more detailed studies were undertaken to verify the conclusions of Section 6.3. During these investigations, both expected and unexpected results were obtained. Through appropriate data analysis, more characteristics of the forces were revealed, which provided more detailed information about the experimental phenomena. These new findings are also fundamental to the simulations reported in Chapter 7. In addition, in terms of biological applications, we demonstrate that the cells can be collected as well.

6.4.1 Experimental method

In this experiment, the colloidal mixture of SWNT clusters and beads used in Subsection 6.3.3 was chosen as the sample solution. The substrate was replaced by a normal glass microscope slide with thickness of 1 mm. The clusters of interest were illuminated through a 10x objective (NA = 0.25) by the laser diode operated CW with an optical power of 180 mW at 650mA and spot size of Φ2.5 μm in the x- and Φ52.9 μm in the y-directions. The experimental phenomena were recorded at a frame rate of 20 fps and the recording time was 30 s. The movements of particles were analysed by particle tracking software.

6.4.2 Results and discussion

During the experiment, similar particle behaviour was seen to that in Subsection 6.3.3. Fig. 6-8 (a) and (b) show the results from the first and the last frame of the image stack. Due to the high optical absorption of the SWNT cluster and low reflection of glass, the position of the laser spot is highlighted by a red dashed oval. Comparing the two images, it can be clearly seen that most of beads are dragged towards the beam, stop at a certain distance from the cluster and start accumulating at that position, leaving a clear region and forming an obvious ring shape around the cluster. Again, as discussed before, this phenomenon was caused by the particles experiencing two balanced forces with opposite directions. The two forces induced by laser heating were thermophoresis, which pushed particles away from the hot region, and thermal convection flow, which moved particles towards the SWNT cluster. It is also worth mentioning that during the experiment, in most cases, once the beads stopped moving, they always stayed at the same position and remained in focus, which demonstrated the vertical component of Stokes's drag force was weaker than gravity force. In addition, photophoresis was not involved in this experiment, because almost none of beads were illuminated by the laser beam, as seen in Fig. 6-8 (a). Here, photophoresis was defined as a phenomenon that suspended particles started to migrate when being illuminated by a sufficiently intense beam of light.

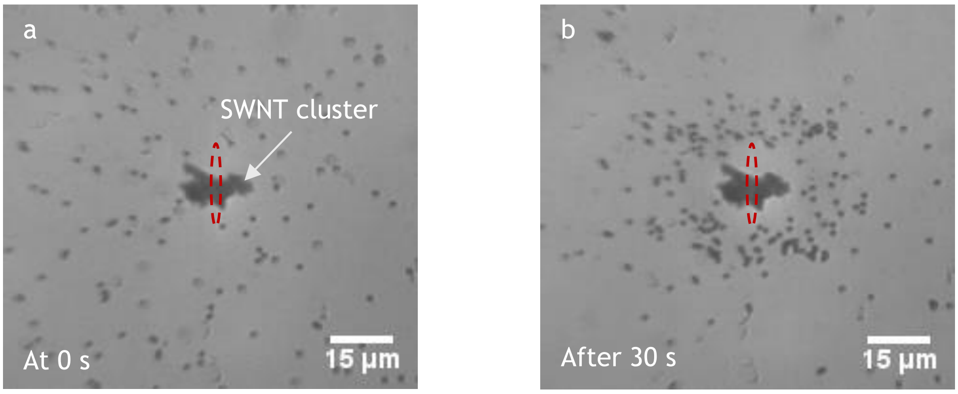

Fig. 6-8: Particle manipulation of 1.54 μm polystyrene beads with SWNT cluster on glass substrate (a) at t=0 s, (b) at t=30 s. Laser spot size (highlighted by the red dashed ovals): Φ2.5 μm in the x-direction, Φ52.9 μm in the y-direction.

Based on above results, a control experiment without SWNT clusters was also implemented. The relevant results are shown in Fig. 6-9. As shown in the figure, particles still move towards the light spot but with a much lower speed under the same recording time, tending to form a stopping area with a ring shape. In order to investigate the reason for this, the light energy absorption within the water and the glass substrate domain were calculated. Fig. 6-10 shows a schematic plot of part of sample device. In the graph, I represents the optical intensity after the beam passes through the cover slide; I_1 is the optical intensity after the light passes through the glass-water interface; I_2 is the intensity where the beam reaches the water-glass interface and I_3 is the intensity after the light passes through the boundary between the two domains. R is the reflectance at the glass-water interface, which can be calculated by Fresnel reflection at normal incidence:

$$R = \left| \frac{n_1 - n_2}{n_1 + n_2} \right|^2 \qquad \textbf{(Eq. 6-4)}$$

where n_1 and n_2 are the refractive indices of the two media, respectively. After substitution, R = 4.364E-3 at wavelength of 808 nm. The energy absorption in each domain and I_2 were calculated based on the Beer-Lambert law (See Section 2.6) with the travelling path length set as the thickness of the water domain, which was 100 μm. After calculation, the light energy absorbed in the water domain was 2.22E-4*I, while for the glass substrate, it was 3.98E-3*I. This suggests the above phenomena in the control experiment were caused by the combination of the effects of the thermal convection flow and the thermophoresis mainly generated by the light absorption in the glass substrate.

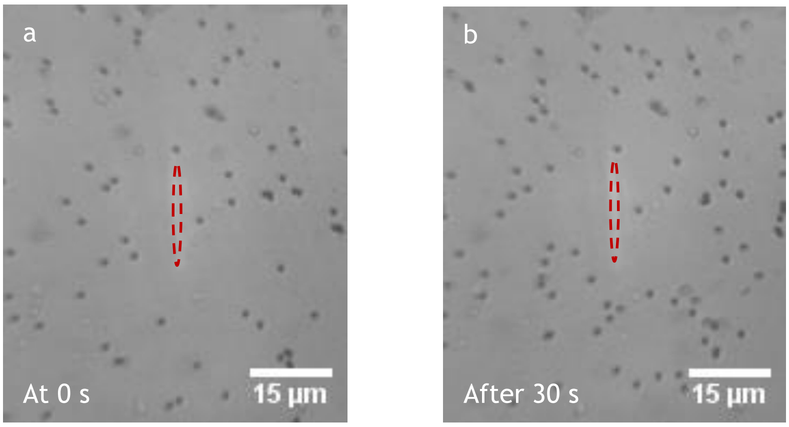

Fig. 6-9: Control experiment on particle manipulation of 1.54 μm polystyrene beads without SWNT cluster on glass substrate (a) at t=0 s, (b) at t=30 s. Laser spot was highlighted by the red dashed ovals.

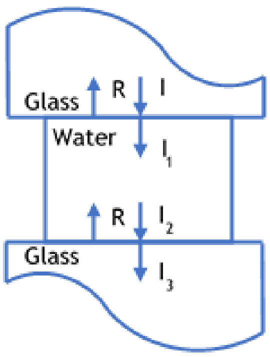

Fig. 6-10: Schematic plot of part of sample device (cross section along the central body).

In addition, according to the further experiment described in Subsection 6.3.2, no movement was seen under the conditions of full optical power, polystyrene beads

4.95 μm in diameter and a glass substrate. However, compared with results shown in Fig. 6-9, it can be suggested that the difference arises from the particle suspension position relative to the surface of the substrate and the particle size. As described before, larger size beads tended to sediment at the substrate surface within a short period, whereas smaller sizes particles were more likely to remain suspended in the liquid for a longer time due to the reduced mass of the beads themselves, which resulted in particles suspending in the different vertical positions. Regarding the modelling results in Fig. 7-13 (c) and Fig. 7-14, both laser-induced thermal convection flow and thermophoresis increase with particle suspension position. Therefore, polystyrene beads with Φ1.54 μm experienced stronger thermal forces than those with Φ4.95 μm. No movement being seen for the 4.95 μm beads was due to the thermal forces being too weak to compete with Brownian motion.

6.4.3 Further studies

Although further investigations were undertaken as reported in Subsection 6.3.3, there still was not enough information to reveal the physical mechanisms of the experimental phenomena fully. Therefore, some extra studies were implemented to try to elucidate the characteristics of the convection flow and thermophoresis through further data analysis and a further set of tests. The details are described below.

Effect of cluster shape on particle-stopping position

Firstly, we investigated the relation between the bead-stopping position and the shape of the SWNT cluster, for which the results are shown in Fig. 6-11. Fig. 6-11 (a) shows position plots of the bead final positions and the edge of the cluster. Fig. 6-11 (b) plots the distance between the particles and the cluster edge as a function of the directional angle. Here, each position point on the edge of the cluster was determined by the cross point between a line, which was drawn from the beam centre to the bead of interest, and the cluster edge. The beam centre was represented as (0, 0) in both two graphs. The related directional angle was calculated based on the position of the bead of interest and the positive x-axis. Note that the data points are randomly distributed within a range between 6 μm and 12 μm, which indicates that the bead-stopping positions are not affected by the shape of the laser spot. Therefore, according to both graphs, it can be concluded that the absorbed light energy was converted into heat that was conducted through the cluster and dispersed into the adjacent liquid resulting in a temperature gradient. In this case, the cluster can be treated as a bulk heat source with its shape determining the particle stopping positions.

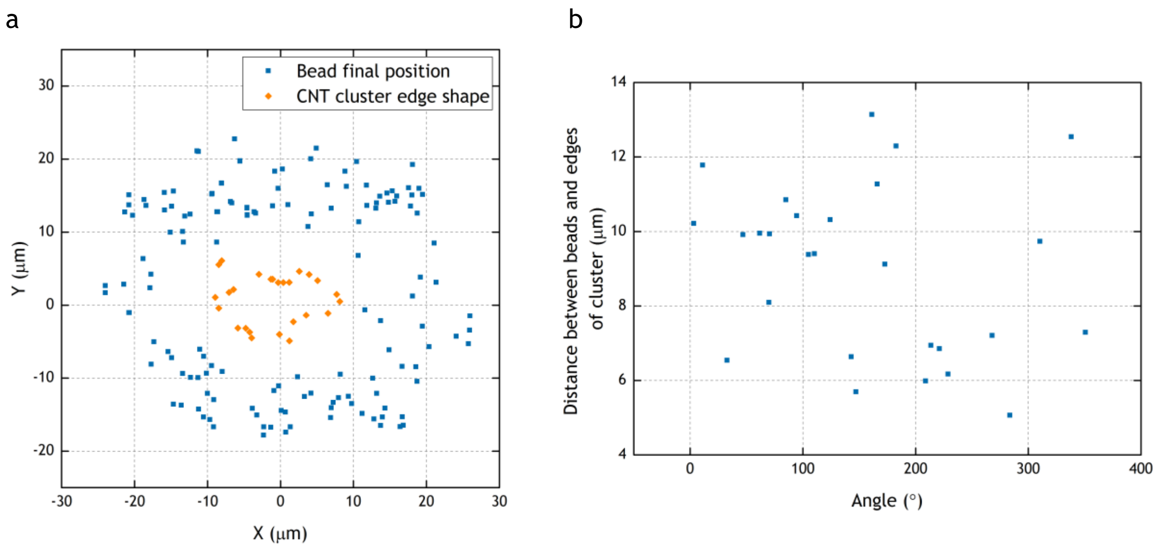

Fig. 6-11: The 'ring shape' investigations: (a) position plots of the bead final positions and the SWNT cluster edge points, (b) distance plot between the beads and the cluster edge points.

Theoretical model of the working mechanisms

Secondly, to explain the working mechanisms of our system, we first developed an intuitive model to identify the underlying physics for the glass substrate system with SWNTs. Having identified the underlying physics, we could then apply a sophisticated numerical model (COMSOL) to more complex geometries. For the glass substrate system with SWNTs, the key observation that requires explanation is as follows: at long distances from the illuminated SWNT cluster particles move towards the cluster. As they approach the cluster, they slow down and stop at a characteristic distance that depends on the particle size. This suggests that forces associated with two distinct physical phenomena are acting on the particles and that they have different dependencies on distance. We conclude that the movements of particles are determined by the combined effect of laser-induced thermal convection flow and thermophoresis.

The analysis is as follows. We propose that the particle velocity $v(r)$ as a function of distance (r) relative to the beam center can be expressed by two terms, one arising from convection and the other from thermophoresis. For the first term, the convection is taking place in a chamber only ~100 μm high, but around 20 mm (L) × 13 mm (W) in chamber area was used in the experiment. Other than in the immediate area of illumination and at the edges of the chamber, the situation can be simplified as laminar fluid flow in 2D, with the flow dropping to zero in the middle of the chamber, i.e. at a height of approximately 50 μm. The physical model can be visualized as thin layers of fluid with a circular shape moving towards the cluster, which is shown in Fig. 6-12 (a) and (b). At time t, consider the fluid at a radius r_1 from the cluster. In a time dt, the fluid moves a distance dr_1, and the volume of fluid crossing r_1 is $2\pi r_1 dr_1 \cdot \delta d$, where δd is the thickness of the fluid laminate. At a radius r_2 closer to the heated region, the fluid moves a distance dr_2 in dt with a volume of $2\pi r_2 dr_2 \cdot \delta d$. From conservation of mass, these two volumes are equal. If both areas are divided by dt, we obtain

$$2\pi r_1 \cdot \frac{dr_1}{dt} = 2\pi r_2 \cdot \frac{dr_2}{dt}$$

$$r_1 \cdot v_1(r) = r_2 \cdot v_2(r) = -a$$

$$v_{FLOW}(r) = -\frac{a}{r}. \qquad \textbf{(Eq. 6-5)}$$

Here, a is a constant and the flow velocity is proportional to $1/r$, with the negative sign indicating the flow is towards the heat source.

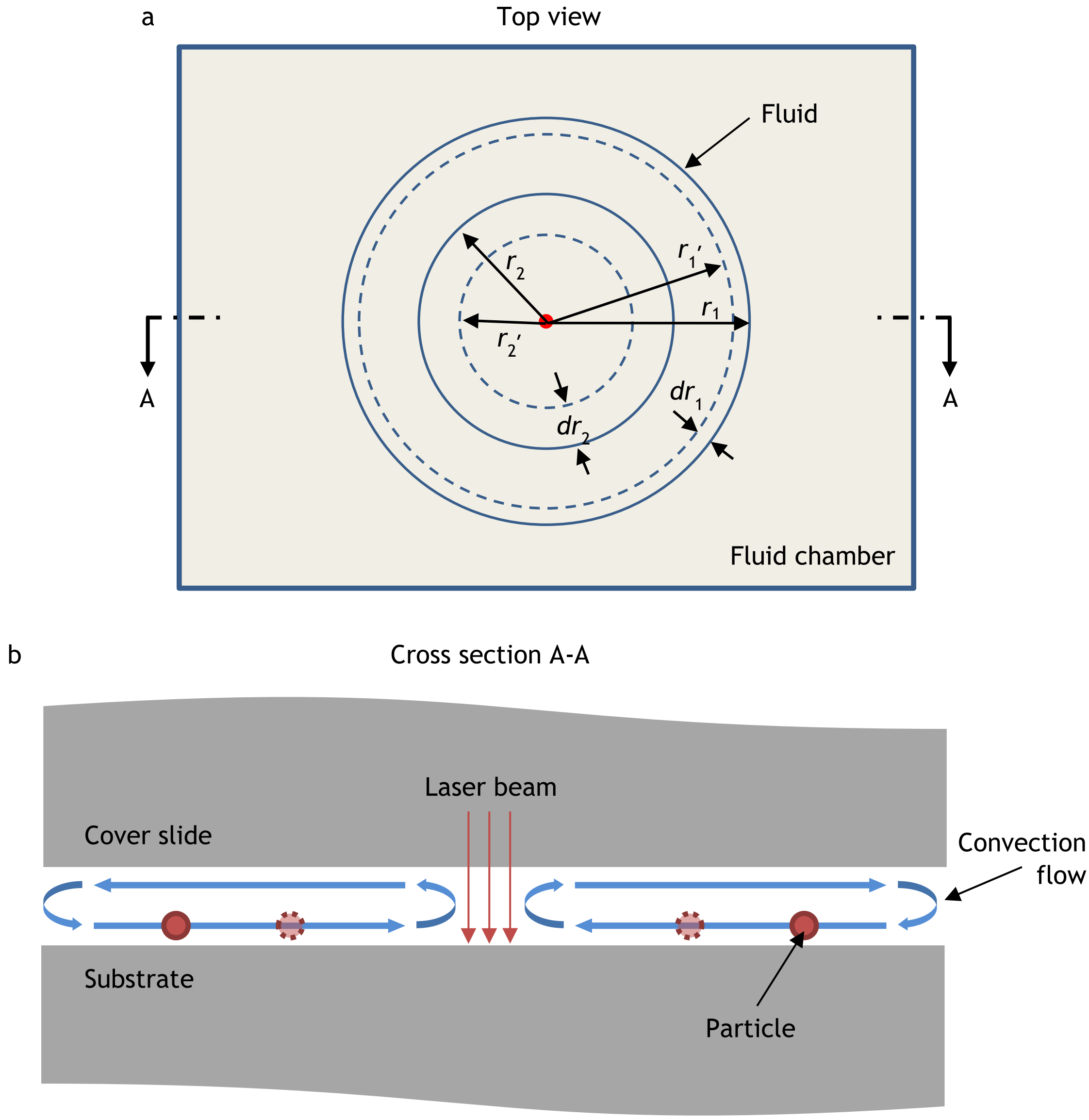

Fig. 6-12: The simplified physical model of 2D fluid flow in the fluid chamber from (a) the top view and (b) cross section view.

The velocity due to the thermophoresis force is given by Eq. 2-9. To calculate the thermal gradient, the cluster can be treated as point heat source, with heat transferred to its surroundings predominantly by conduction (see Section 7.1) even in the water domain because of the low Rayleigh number. Because the thermal conductivities of glass (0.8 W m^{-1} K^{-1}) and water (0.6 W m^{-1} K^{-1}) are similar and the glass substrate and cover are relatively thick, the isotherms are essentially spherical and centered on the heat source, as shown in Fig. 6-13. Referring to the Fourier's law [173], we obtain

$$q = -k\nabla T \qquad \textbf{(Eq. 6-6)}$$

where q is the heat flux, k is the thermal conductivity, ∇T is the temperature gradient and the negative sign represents the direction of heat transfer. Because the isotherms are spherically symmetric, the total heat flow (Q) across an isotherm is given by

$$Q = 4\pi r^2 q$$

and so

$$\nabla T = -\frac{Q}{4\pi k}\cdot\frac{1}{r^2} = -\frac{b'}{r^2}$$

where b' is a parameter proportional to Q , and r is the radius of a spherical isotherm. Substituting into Eq. 2-9 and assuming D_T is constant, the thermophoretic velocity is given by

$$v_{TH}\left(r\right) = \frac{b}{r^2} \qquad \text{(Eq. 6-7)}$$

where $b = D_T \cdot b'$, v_{TH} is proportional to $1/r^2$. Therefore, the particle velocity, v_p, can be expressed as a function of distance as:

$$\frac{dr}{dt} = v_p = v_{FLOW}\left(r\right) + v_{TH}\left(r\right) = -\frac{a}{r} + \frac{b}{r^2}. \qquad \text{(Eq. 6-8)}$$

The directions of the two flows have already been considered, so a and b should be positive numbers. If both sides of the equation are multiplied by dt, we obtain

$$dt = \frac{r^2}{b - ar}\cdot dr \qquad \text{(Eq. 6-9)}$$

The relationship between position and time can be found by integrating Eq. 6-9, which can be expressed as

$$\int dt = \int \frac{r^2}{b - ar} dr$$

$$t = -\frac{2b^2 \ln\left(b - ar\right) + ar\left(ar + 2b\right)}{2a^3} + c \qquad \textbf{(Eq. 6-10)}$$

where c is an integration constant.

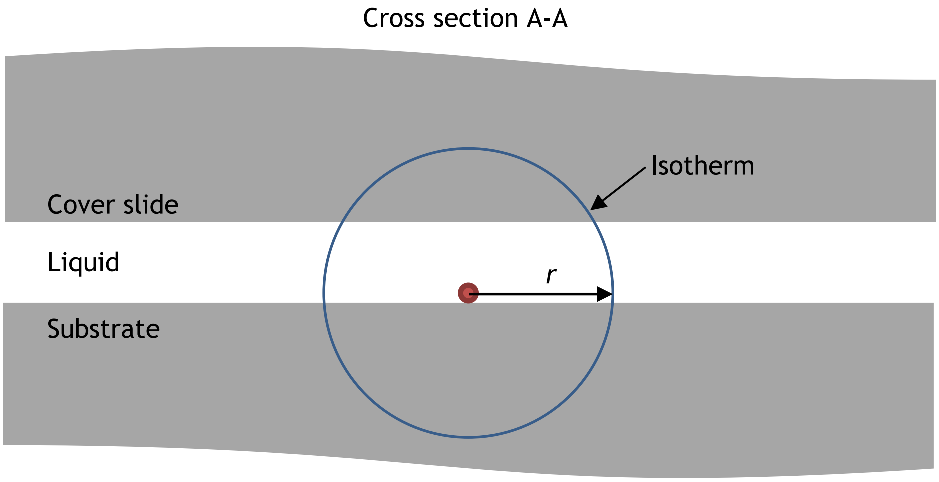

Fig. 6-13: The theoretical model of heat transfer within the sample device from the cross section view relative to Fig. 6-12.

In order to assess our theory, the movements of particles from several recordings were analysed by particle tracking software (Tracker; v4.95, Douglas Brown, USA). Fig. 6-14 shows three typical bead trajectories with different initial positions being plotted as a function of time, and the related particle positons calculated from Eq. 6-10 being plotted as fitted curves. As shown in the figure, the closed curve fitting indicates that our theoretical model is reasonable. At the beginning, the beads start moving towards the cluster due to the Stokes's drag force dominating. As the particles approach the hot region, the thermophoretic force increases more quickly than the drag force. As a result, the net force experienced by the particles decreases, and eventually the beads stop because the forces balance. Also note that bead A and bead B stopped at different distances from the cluster as the initial position of bead A was closer to the beam than bead B. Bead A probably stopped at the interior edge of the ring shape and the bead B probably stopped at the exterior edge of the ring shape due to particle accumulation. Bead C did not get close enough to stop, which was an artefact arising from the limited recording time.

After analysing 83 particle trajectories, the speed of the particles could reach an average of 3.2 μm/s. The average values of parameters a and b were 246 ± 141 and 4842 ± 4533, respectively. The real values of the two parameters were plotted as a function of particle original position relative to the beam centre, and are shown in Fig. 6-15. As shown in the figure, there are two cases, which are labelled as bead 1 and 2, appearing to be far from typical results, which result in the huge variations on both parameters. By checking the real movements of the two particles, any unexpected behaviours were not found. Therefore, it can be concluded that the variations arise because each curve is fitted to individual trajectories, which by their nature showing significant variations. However, the conclusion that the dominant forces are Stokes's drag associated with convection flow and thermophoresis holds. We will see in Chapter 7 that numerical modelling based on these two forces allows us to predict particle trajectories.

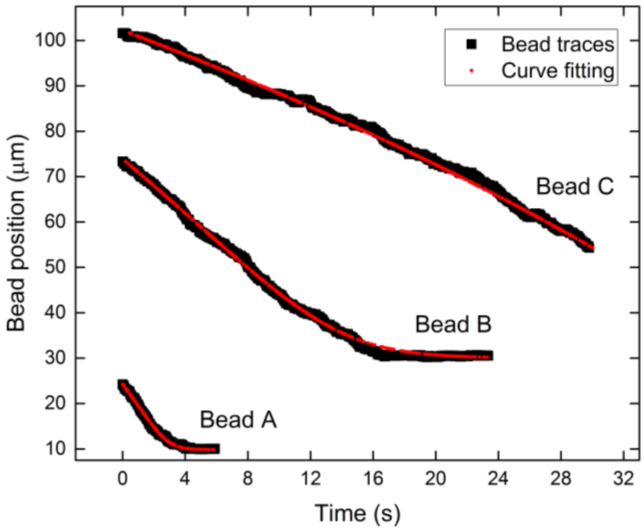

Fig. 6-14: Individual bead position plots as a function of time, and related curve fittings.

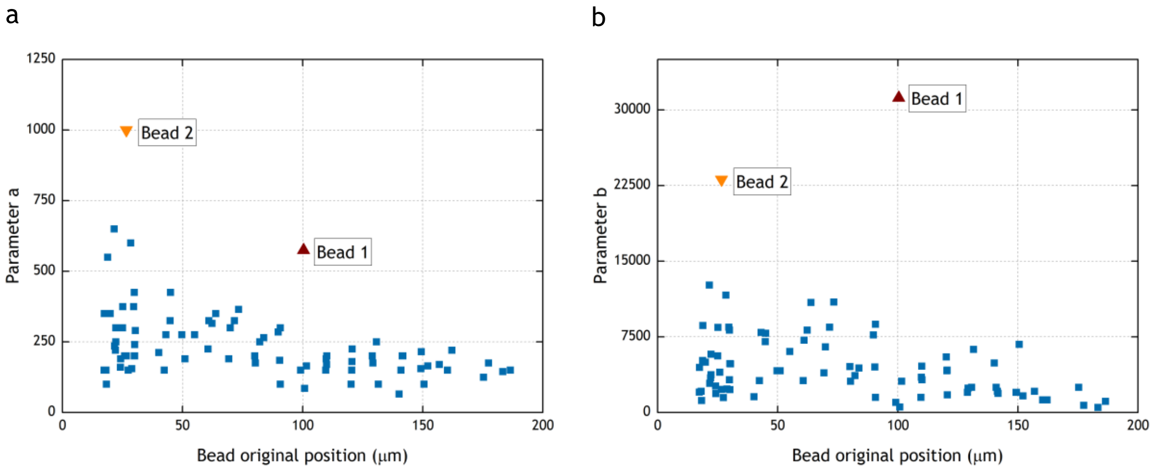

Fig. 6-15: Plots of curve fitting parameters as a function of bead original position relative to the beam centre for (a) parameter a and (b) parameter b. Bead 1 and bead 2 are exceptional cases, leading huge variations on both parameters.

Effect of absorbed optical power on particle speed

Thirdly, some further tests with the same sample solution but different incident optical powers were implemented. This time, in order to monitor the energy absorption by the SWNT clusters, the sample device was placed on top of an optical power sensor (S130C, Thorlabs, Inc.). For each test, the laser beam illuminated in two different areas: a cluster and an area without any clusters. The related power readings were recorded in order to calculate the power absorption. The other parameters were the same as for the previous experiment. Moreover, clusters of similar shape and thickness were chosen for each measurement in order to keep the experimental conditions consistent. The incident optical power was controlled by varying the supply current, and five different current levels were used in these tests. The values of the currents and related power absorption are summarized in Table 6-1. From the Table, it can be seen that all the tested clusters absorbed only a small amount of the incident light, with most of the light passing through. This suggests the SWNT clusters are formed by low density SWNTs with large gaps between each nanotube.

In the tests, we focused on the behaviours of particles under different conditions. Based on the curve fitting results from the last study, particles were tracked and each bead trajectory was curve fitted by adjusting parameters a and b (see Eq. 6-10). The two parameters were then used to calculate the bead speed at a certain distance from the beam centre. Fig. 6-16 shows the plot of average bead speed as a function of absorbed optical power (OP). From the graph, it can be clearly seen that the bead speed at 75 μm away from the beam centre is proportional to the power absorption, which indicates the dominated Stokes's drag linearly increasing with light absorption. The distance of 75 μm was chosen because at a supply current of 350 mA, the movements of particles were much slower compared to other cases, which limited the moving distances. The data under all of these five cases were grouped based on the particle positions and related trajectories. We found that the number of trajectories that covered the position point of 75 μm was the highest. It also needs to be noted that, when there is no power absorption happening in the SWNT cluster, particles should be static. However, due to the effects of Brownian motion, random particle movements were seen during the experiment. In this case, the single error bar shown in the plot was the speed of Brownian motion that was obtained by averaging the particle moving speeds measured from 10 beads in total. For each bead, the particle moving speed was measured in several equivalent time periods of one experimental video, and then averaging the data. The rest error bars shown in the plot represent as the standard deviations of the measurements under different absorbed optical powers. Here, the number of particles measured in each case could be summarized as 4 beads for OP absorption of 2.99 mW, 9 beads for OP absorption of 4.40 mW, 10 beads for OP absorption of 6.40 mW, and 8 beads for OP absorption of 9.60 mW. In addition, some large standard deviations in the plot are due to the wide variations of the parameters a and b used to analyse the bead speed (see Eq. 6-8) during the curve fitting. As explained before, the wide variations arise from the nature of bead trajectories showing significant variations.

Supply current (mA)	OP without SWNT cluster (mW)	OP with SWNT cluster (mW)	OP absorption by SWNT cluster (mW)
0	0	0	0
350	35.50	32.51	2.99
450	73.40	69.00	4.40
550	110.40	104.00	6.40
650	145.40	135.80	9.60

Table 6-1: Energy absorption test of SWNT clusters under different incident optical power (represented by supply current).

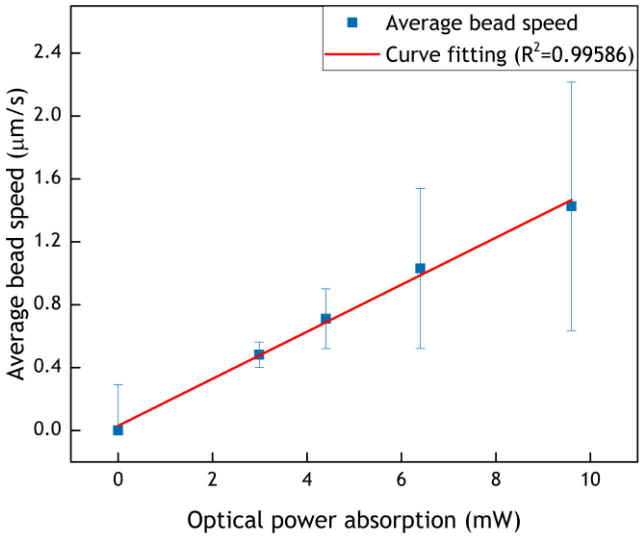

Fig. 6-16: Average speed of polystyrene beads (*Φ*1.54 μm) under different light absorption by SWNT clusters at the distance from the beam centre of 75 μm.

Effect of particle size on particle speed

Tests with four different particle sizes (*Φ*2.88 μm, *Φ*4.95 μm, *Φ*7.79 μm and *Φ*9.97 μm) were also carried out. The first two bead stock solutions were purchased from Bangs Laboratories, Inc., the rest were purchased from Kisker Biotech GmbH & Co. KG. All of the particles were made of polystyrene. The sample solutions were prepared following the method described in Subsection 3.3.2, except 0.5% (w/w) sodium dodecyl sulfate (SDS) was added to each solution in order to prevent aggregation of beads and unspecific binding to the substrate surface. As for previous tests, the sample device was placed on the optical power meter sensor, in order to track the power absorption. Again, similar shapes and thicknesses of clusters were chosen under each test. The remaining parameters were kept as same as for the previous study and the laser diode was operated CW with an optical power of 180 mW at 650mA. The movements of particles were analysed by the particle tracking software and related speeds were calculated by following the same method as before through curve fitting. Finally, the average bead speeds were plotted as a function of bead size in Fig. 6-17. As shown in the graph, the average bead speed increases with the particle size except for the case of particles with *Φ*1.54 μm, for which the data comes from Fig. 6-16. Here, a distance of 75 μm was again chosen due to the fact that the comparison should be undertaken under the same experimental conditions. In order to investigate the reason for the data in the case of *Φ*1.54 μm not following the trend, the differences between the two studies are summarized and listed in Table 6-2.

According to the literature [24, 28, 30, 167, 169, 174], thermophoresis and the thickness of the electrical double layer (EDL) generated along solid-liquid interface are related to the ionic strength of the solution. Therefore, it was necessary to measure the electrical conductivities of our sample solutions. The tests were simply performed by an electrical conductivity meter (B-771, Horiba, Ltd.) and the average results were 14.60 mS/cm for beads with *Φ*1.54 μm and 14.38 mS/cm for the other cases. The two values are very close, which means the effect of the ionic strength on thermophoresis is not significant so can be ignored. To calculate the thickness of the EDL, the Debye length (see Subsection 6.1.3) was used. In the Eq. 6-3, the ionic strength (I) could be simply estimated as 1.6E-5*electrical conductivity (EC) with units of μS/cm. If EC=14.5 mS/cm, then the Debye length would be around 20 nm, which is two orders of magnitude smaller than the particle size. Suggesting that the effect of EDL can therefore be ignored. More details about the values of other parameters used in the equation are listed in Appendix I. For the other three parameters in Table 6-2, it will be explained with help from the numerical simulations. More analysis and discussion will therefore be presented in Chapter 7. In addition, error bars shown in the plot represent as the standard deviations of the bead-speed measurements under different particle sizes. Here, the number of particles measured in each case could be summarized as 8 beads for particle size of *Φ*1.54 μm, 20 beads for particle size of *Φ*2.88 μm, 23 beads for particle size of *Φ*4.95 μm, 7 beads for particle size of *Φ*7.79 μm, and 11 beads for particle size of *Φ*9.97 μm. In addition, some large standard deviations in the plot are due to the wide variations of the parameters a and b used to analyse the bead speed (see Eq. 6-8) during the curve fitting. As explained before, the wide variations arise from the nature of bead trajectories showing significant variations.

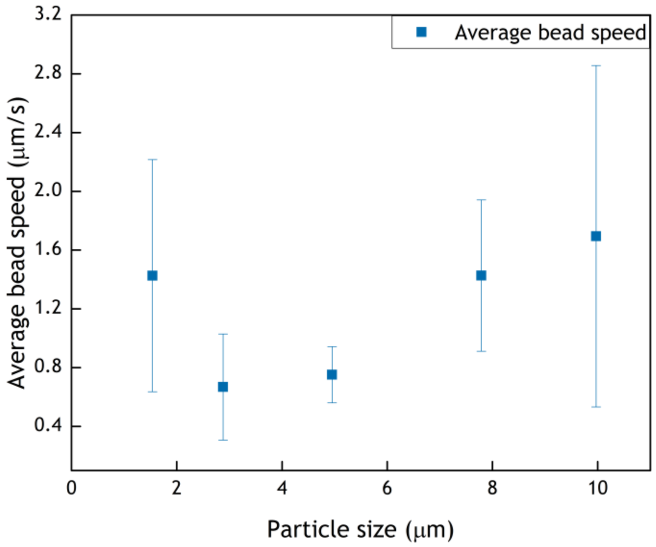

Fig. 6-17: Plot of average bead speed as a function of bead size at the distance from the beam centre of 75 μm under similar optical power absorptions.

Experiments with different samples	Optical power absorption (mW)	Averaged radius of SWNT cluster (μm)	Particle suspension position (μm)	Sample solution ingredient
Polystyrene beads with *Φ*1.54 μm	9.6	6.75	5.34	Bead stock solution : SWNT-RPMI 1640 (0.5 μL : 1 mL)
Polystyrene beads with other particle sizes	12	12.38	3.67-7.95	Same as above solution + 0.5% (w/w) SDS

Table 6-2: Experimental condition differences between the experiment with sample solution containing polystyrene beads with size of *Φ*1.54 μm, and the experiments with sample solutions containing polystyrene beads with sizes of *Φ*2.88, *Φ*4.95, *Φ*7.79 and *Φ*9.97 μm.

Effect of particle size on particle-stopping position

In addition, we also looked into the relation between the bead-stopping position and bead size. By checking the particle trajectories, it was found that the traces could be divided into two groups: trajectories with smooth turning corners (where the particle decelerated gradually) and trajectories with a sharp turning corner (where the particle came to a stop abruptly). In the former case, particles stopped by experiencing two balanced forces. In the latter case, particles were stopped by experiencing unspecific binding or encounter a physical obstruct, resulting particles stuck on the substrate. Fig. 6-18 (a) and (b) show example trajectories for the two cases. The plot of particle real stopping positions as a function of bead size is shown in Fig. 6-19. As shown in the graph, the particle-stopping position increases with bead size. Besides, the data from the two groups can be easily distinguished under the cases with larger bead size as they are separated by a blank gap, from which it can be concluded that the data for trajectories with smooth turning corners are 'more reliable' than those with sharp turning corners for showing where the forces balance, whereas the data from the latter group are more variable.

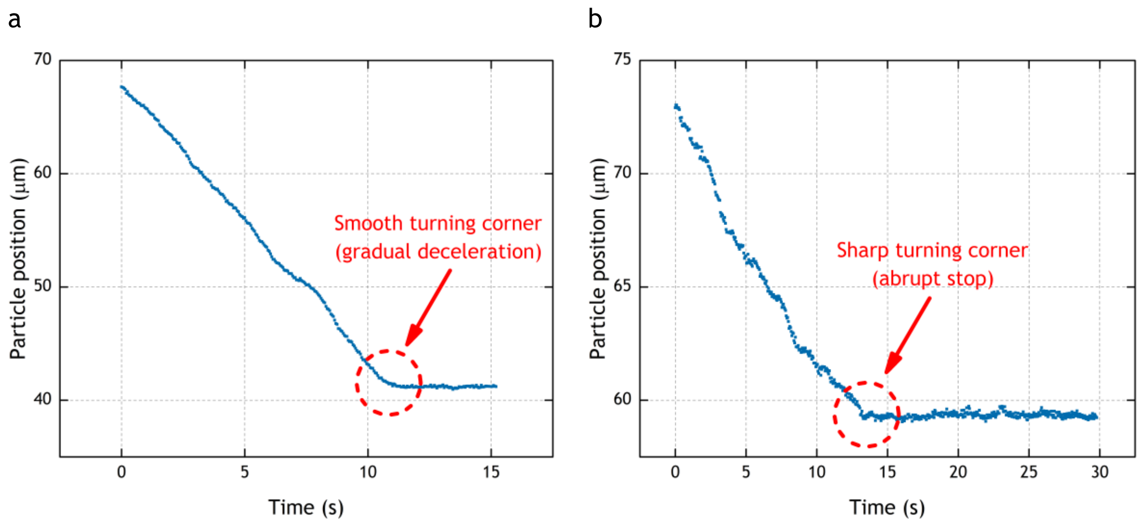

Fig. 6-18: Particle trajectory plots as a function of time with (a) smooth turning corner and (b) sharp turning corner.

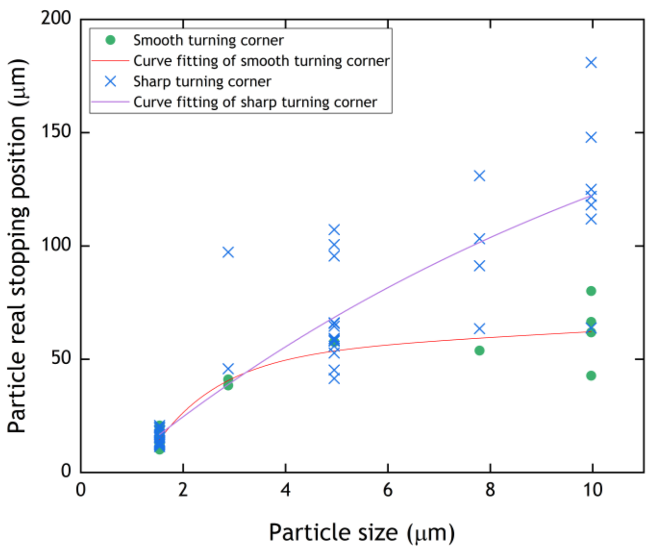

Fig. 6-19: Plot of particle real stopping position as a function of particle size based on the particle trajectories with smooth and sharp turning corner.

6.4.4 Biological sample studies

Effect of SWNT clusters on cell viability

So far, only polymer particles have been used as samples for the studies. It was important to assess the application of our device for biological samples. Therefore, a Jurkat cell line was used in the following experiment as Jurkat cell remain suspended and are easy for manipulating. Before the experiment, the influence of SWNT clusters on cells was investigated by cell viability test in SWNT cluster solution using 0.4% Trypan blue stain following the standard protocol described in Appendix II. The test was performed by adding the SWNT cluster solution into a culture flask containing cell samples, followed by transferring the flask back to the incubator. The numbers of dead cells and total cells were counted every 30 mins in the first 3 hours and then every hour for a further 2 hours. The results are plotted in Fig. 6-20. Almost 90% of cells are still alive after 5 hours, which indicates the cell viability is acceptable with our device using the SWNT cluster solution.

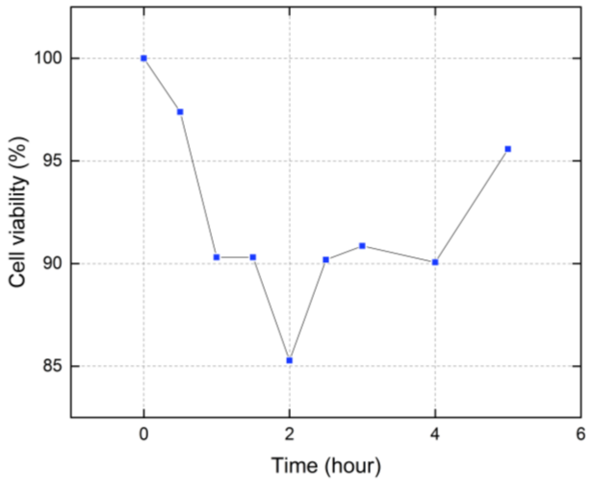

Fig. 6-20: Results of Jurkat cell viability test with the sample solution containing SWNT clusters and polystyrene microbeads.

Jurkat cell manipulation

The experimental system and conditions for the cell manipulation experiment were the same as for the previous experiment. The cell-SWNT suspension was prepared following the method described in Subsection 3.3.3. The laser was operated CW with a supply current of 650 mA. A normal microscope glass slide was used as the substrate for the sample device. This time, the sample device was simply placed on a heat sink. Fig. 6-21 (a) and (b) show the first and the last frame of the image stack. By comparing the two graphs, it can be clearly seen that cells accumulated around the cluster following the same behaviour as beads in the previous experiments, demonstrates that cells can be aggregated using our device. Note that beads were also added in the sample solution for indicator purpose only.

Further investigation on the temperatures that cells were exposed to within the ring region was undertaken. The temperatures were obtained from the numerical modeling (see Section 7.3) based on the cell positions measured in Fig. 6-21 (b). Eventually, the average temperature was 67 °C. Regarding the similar study reported by Song *et al.* [175], human prostate cancer cells were fated to undergo cell death at 51 °C after continuously heating for 5 mins. Therefore, in order to maintain a health biocompatible environment based on our technique, a lower optical power absorption by SWNT clusters needs to be considered, in which case the ambient temperature around the cluster should be kept below 51 °C.

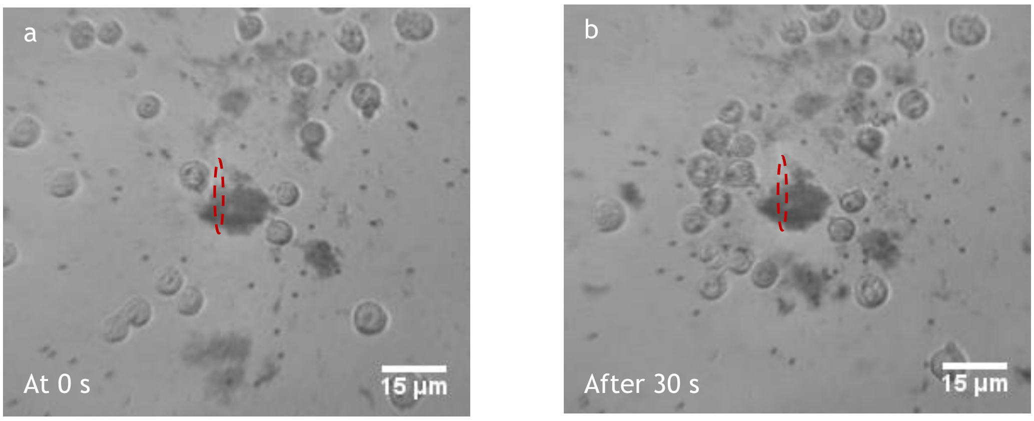

Fig. 6-21: Jurkat cell manipulation with SWNT cluster (a) at t=0 s, (b) at t=30 s. Laser spot size (highlighted by the red dashed ovals): Φ2.5 µm in the x-direction, Φ52.9 µm in the y-direction.

So far, regarding both microbeads and cells being manipulated successfully by our device, it can be concluded that we developed an alternative way to move particles by optical-thermophoretic tweezers with the feature of 'thermophobic' of thermophoresis. Compared to other tweezing techniques (such as optical tweezers, acoustic tweezers, etc.), our system using optical components with low numerical aperture (NA) and low optical power of the incident light, which is not harmful to the biological samples and does not require the complex and highly accurate aligned optical system. The sample device is cheap, easy to be fabricated and use, which does not require any patterning or fabrications on the substrate surface. The PDMS microfluidic channel is not necessarily needed, which saves time on fabricating the relative mould for the further steps in soft-lithography. Furthermore, the sample solution is simple and straightforward to be prepared. The work presented in this section is still in the early stage. It will become a useful and versatile tool for researches in bio-chemical, biology and biomedical fields by involving current techniques into the system. For instance, by using spatial light modulator (SLM), different light patterns (such as rings, parallel lines, etc.) can be constructed, which will be possible to trap and move single or multiple particles or biological molecules freely by following the movements of beam on a normal microscope slide with a thin carbon nanotube (CNT) sheet.

6.5 Microparticle manipulation under discontinuous illumination

After investigating several interesting phenomenon observed based on the sample containing the extra light energy absorbers under the CW laser-operation mode, we tested whether acoustic waves could be generated and could be strong enough to move particles by involving the CNTs as an absorber. Different to the experiments implemented in Chapter 4, instead of using continuous waves, it was intended to generate single ultrasound pulses by modulating the laser with different pulse widths under low modulation repetition rate. In the following sections, two groups of experiments were implemented based on the light pulses with short pulse widths (nanosecond scale) and long pulse widths (second scale). In each group, the laser was modulated using different methods. Interestingly, some different typical behaviours were observed and linked to the original positions of particles. The relative sample responses were analysed and summarised, which could support our understanding of the physical mechanisms of the experimental phenomena.

6.5.1 Experimental method

A colloidal mixture of SWNT clusters and polystyrene microbeads was used in all experiments. Similar to the methods introduced in Subsection 3.3.2, the SWNT conductive ink was dispersed into deionised water with 0.5% (w/w) SDS at ratio of 70 mg : 1 mL followed by vortex mixing. After that, the SWNT suspension was sonicated for 2 hours in order to form appropriate clusters. In the final step, the original polystyrene microbead stock solution with a bead size of *Φ*5 µm was suspended in the SWNT cluster suspension at the relevant dilution ratio of 5 µL : 1 mL followed by vortex mixing. In terms of the optical system setup, for the experiments with short pulse widths, the laser was modulated by a high power pulse generator (8114A, Keysight Technologies) with a modulation voltage of 45 Vpp and DC supply current of 200 mA, in order to obtain a deep modulation depth. The light pulse widths were varied from 200 ns - 1 µs with a fixed repetition rate of 2 Hz. For the experiments with long pulse widths, the laser was operated CW with a DC supply current of 650 mA. In order to achieve discontinuous illumination, a homemade optical shutter was used to open and block the beam manually. The light pulse width was controlled by adjusting the opening time of the shutter. Also, the 10x objective (NA = 0.25) was used to focus the laser beam on the clusters. For the camera settings, the frame rate was set as 400 fps. The sample device was fabricated by following the methods described in Subsection 3.2.3 with a silicon substrate.

Specifically, under the experiments with long pulse widths, three tests were implemented. In the first test, the clusters were illuminated by several light pulses with equal widths. In the second test, the laser beam was modulated with a series of different light pulse widths. Normally, four pulses were recorded in each video with pulse widths starting at 0.5 s, 0.7 s, 0.8 s and 1.1 s, respectively. In the final test, a single light pulse with a much longer pulse width was applied on the clusters. The recording time for each test was around 5-6 s.

6.5.2 Results and discussion

For the experiments with long pulse widths, the particle behaviours were the main phenomena that we focused on. During the tests, three typical particle responses were found and the related bead trajectories were analysed by the tracking software. The micrographs in Fig. 6-22 show the bead movements in one of the video frames within one of the illumination periods, and the trajectories relative to the beam centre are plotted as a function of recording time for each typical bead. As shown in the graphs, the particle behaviours can be differentiated based on the two position regions: the near region, where the initial positions of beads were close to the laser spot, and the far region, where the initial positions of beads were far away from the beam. In the near region, as shown in graph (a) and (b), the particle of interest moves towards the light spot in a step like movement once the optical shutter is opened. During the illumination period, the bead roughly stays at the same place rather than continuing to move further. Once the beam is blocked, the behaviour of the particle is very similar to when the beam is open except it tends to move back to the original position. Here, the red colour plot shown in graph (b) is a measure of laser light intensity in grey value, which is used to indicate the time points of the shutter being opened and closed. In contrast, in the far region, as shown in graph (c-f), instead of moving towards the beam, the bead moves away from the illumination area following a step like movement once the shutter is opened. During the illumination period, once it reaches the maximum displacement points, the bead changes direction immediately, and tends to move back and stay at its original position. When the beam is blocked, the behaviour of the particle is very similar to the above, except it moves towards the position where the light spot was and then moves back to the original position. Graph (g) and (h) show the trajectories of beads of interest in the two position regions for the case of single light pulse illumination. Again, the particle behaviours are very similar to those under the previous conditions. Here, the noise in the graphs is due to the system vibration and the small displacements measured.

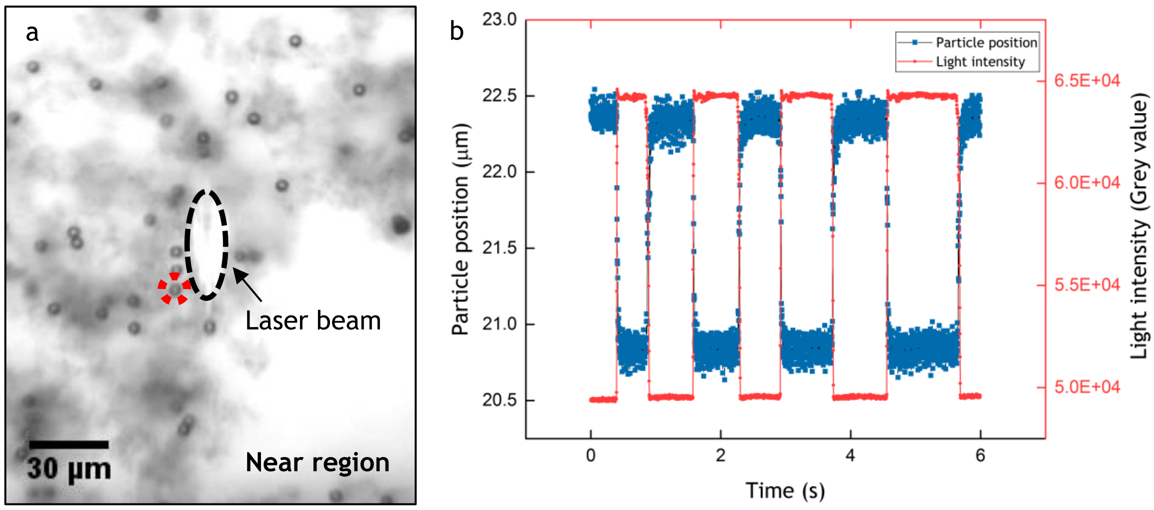

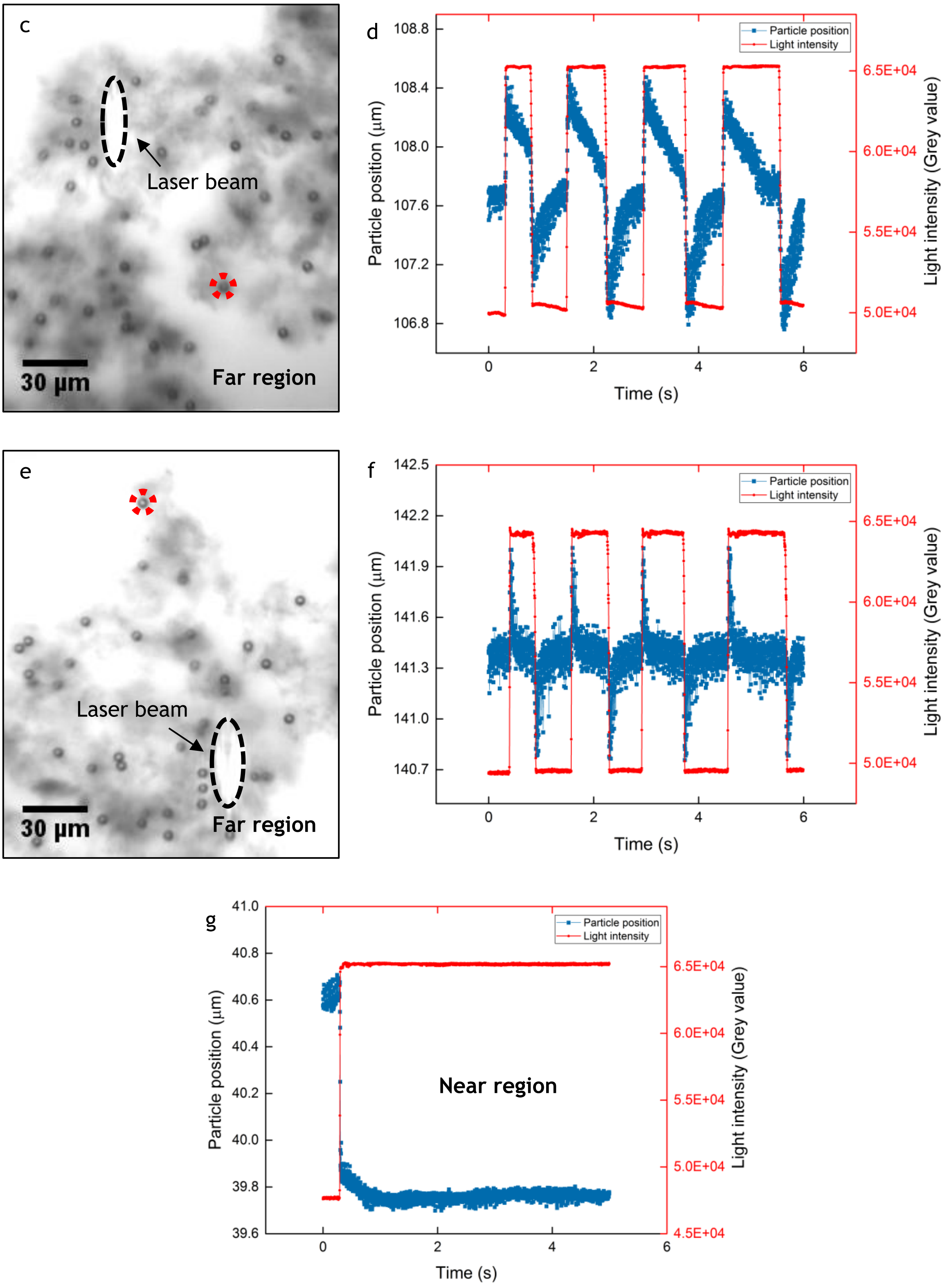
c
Laser beam
30 µm
Far region
d
Particle position
Light intensity
Particle position (µm)
Light intensity (Grey value)
Time (s)
108.8
108.4
108.0
107.6
107.2
106.8
6.5E+04
6.0E+04
5.5E+04
5.0E+04
0
2
4
6
e
Laser beam
30 µm
Far region
f
Particle position
Light intensity
Particle position (µm)
Light intensity (Grey value)
Time (s)
142.5
142.2
141.9
141.6
141.3
141.0
140.7
6.5E+04
6.0E+04
5.5E+04
5.0E+04
0
2
4
6
g
Particle position
Light intensity
Near region
Particle position (µm)
Light intensity (Grey value)
Time (s)
41.0
40.8
40.6
40.4
40.2
40.0
39.8
39.6
6.5E+04
6.0E+04
5.5E+04
5.0E+04
4.5E+04
0
2
4
6

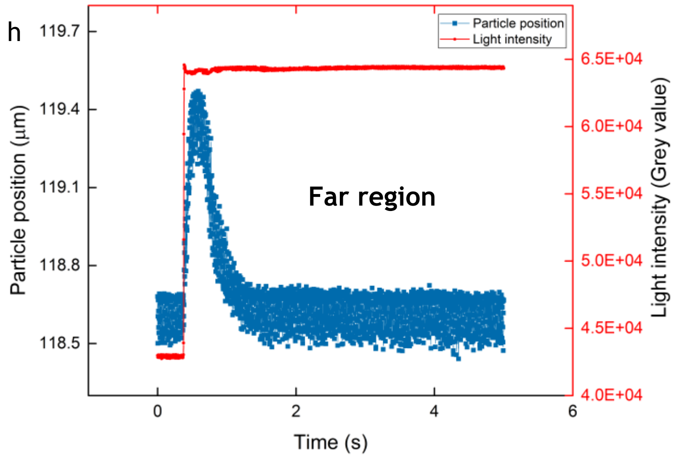

Fig. 6-22: The movement of the microbead of interest with SWNT clusters in one of the video frames, and multiple plots of corresponding bead trajectory and laser beam intensity as a function of time under the test based on different position region: (a-b) in the near region, (c-f) in the far region. Graphs (g) and (h) are similar plots using a single light pulse.

From the above interesting findings, we can explore the physical mechanisms of the phenomena. According to the discussions in Sections 6.3 and 6.4, it can be predicted that thermophoresis and thermal convection flow are generated with the similar experimental conditions. However, there was no convection flow seen in any experimental videos as almost all of beads were in contact with SWNT clusters, resulting in no free movement of beads in the liquid. Moreover, strong deformations of clusters within the illumination area were seen during the experiment. The beads not only moved towards the laser spot but moved out of focus as well, which we believe is the result of the clusters deforming in the vertical direction. Therefore, thermal expansion should be considered as well. According to the Newton's first law, a counterforce should also be involved, which should be an elastic force as the cluster deformations disappeared once the beam was blocked. Furthermore, the optical gradient force should be considered as well, as there is a possibility of particles being attracted by the force when they close to the beam.

We propose the following: in the near region, both the SWNT clusters and beads experienced an action force due to thermal expansion, Stokes's drag force and optical gradient force, which moved them towards the light spot, and a counterforce contributed by the elastic force and thermophoretic force, of which the schematics is shown in Fig. 6-23 (a). Due to the strong light absorption of the clusters, the action force was stronger than the counterforce once the shutter was opened. During the illumination period, the two forces were balanced and cancelled each other, which resulted in the particles remaining stationary. Interestingly, once the beam was blocked, the contributions of the thermophoretic force, Stokes's drag force, optical gradient force and thermal expansion could be ignored, which resulted in the elastic force being the only force applied to the samples. In the far region, the contribution of the optical gradient force could be ignored. This time, the action force was contributed by the thermophoretic force and thermal expansion, which pushed samples away from the beam. The counterforce was contributed by Stokes's drag force and the elastic force. The schematics of the two forces is shown in Fig. 6-23 (b). Regarding the magnitudes of thermal expansion and Stokes's drag force decreasing with distance, it was possible that the samples were partially moved towards the beam, whereas others were pushed away due to the thermophoretic force dominating. Once the shutter was opened, at first the action force dominates. With the fast response of the counterforce, it moved the samples back to the places around sample original positions where the two forces were balanced during the illumination period. Once the beam was blocked, due to the effect of elastic force, samples were moved towards the beam. Once the deformation happened again, the new elastic force was then created which prevented further deformation and tended to restore the system back to the static state.

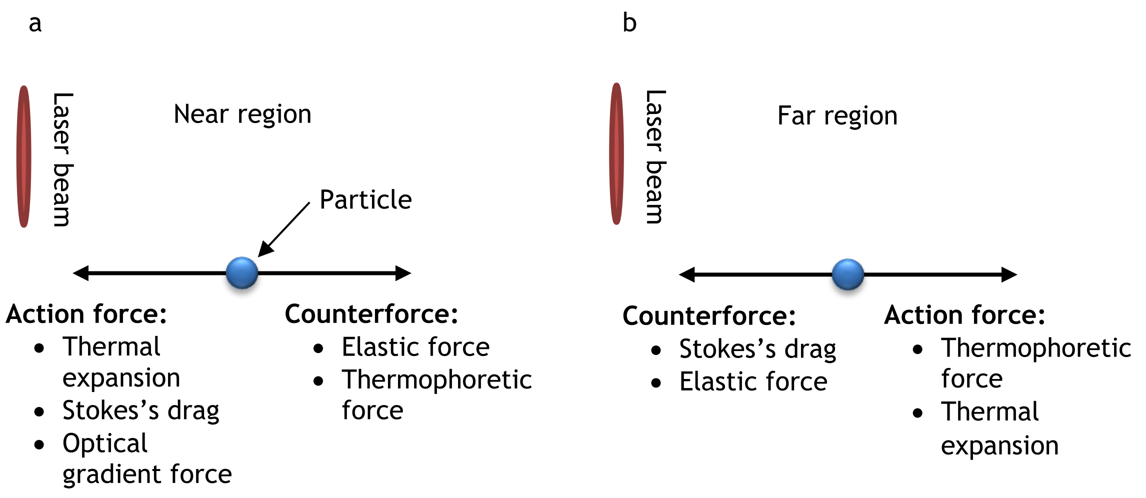

Fig. 6-23: The schematics of forces particles experiencing in different position regions: (a) near region and (b) far region.

Based on the particle trajectories shown in Fig. 6-22, our physical model can be considered as a mass-spring-damper system under overdamped situation. In this case, the displacement (x) of the object varies with time by following 2-term exponential expression, which can be written as [176]

$$x(t) = a_1 \cdot e^{-(\zeta+\sqrt{\zeta^2-1})\cdot\omega_n\cdot t} + a_2 \cdot e^{-(\zeta-\sqrt{\zeta^2-1})\cdot\omega_n\cdot t} \qquad \textbf{(Eq. 6-11)}$$

$$\zeta = \frac{c}{2m\omega_n} \text{ and } \omega_n = \sqrt{\frac{k}{m}}$$

where a_1 and a_2 are constants, ζ is the damping ratio, ω_n is the natural frequency of the system, c is the damping coefficient, m is the mass of the object and k is the spring constant. The Eq. 6-11 can be further simplified as

$$x(t) = r(t) = a \cdot \exp\left(b \cdot t\right) + c \cdot \exp\left(d \cdot t\right) + z \qquad \textbf{(Eq. 6-12)}$$

where $r(t)$ is the particle distance from the beam centre, t is time, a, b, c, d, z are the parameters. Here, parameters b and d determine the curvature of the trajectory. Parameters a and c determine the amplitude of the trajectory. Parameter z determines the offset position of the trajectory. Fig. 6-24 shows examples of the first term of Eq. 6-12 at different values of parameters a and b to demonstrate the relative effects on the data plot. It can be seen that when b varies from 0.1 to 40, the slope of the trajectory increases. When b becomes negative, the r value starts to decrease gradually rather than increase when it is positive.

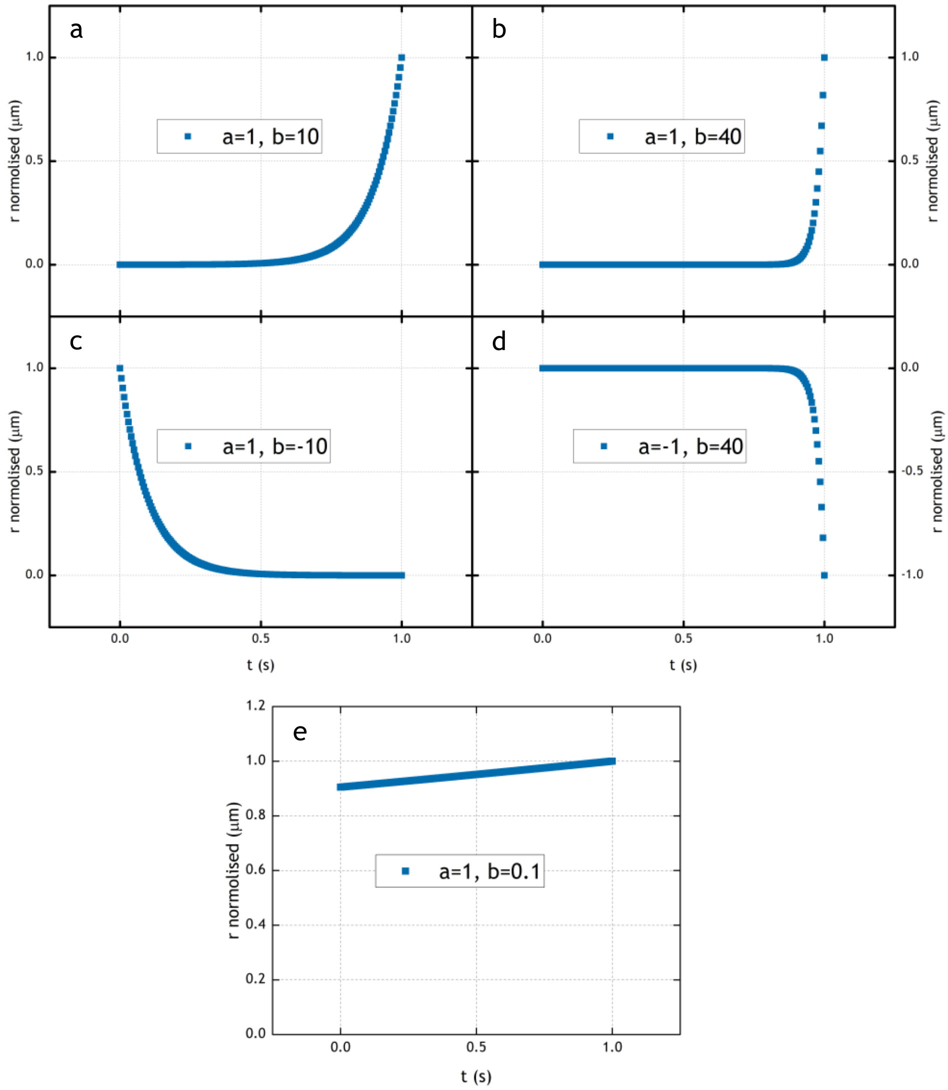

Fig. 6-24: Demonstrations of the effects of parameters a and b on the data plot for the first term of Eq. 6-12.

In order to further investigate the physical mechanisms, the particle trajectories within and outwith the illumination period (including the status changing points) were analysed by applying curve fitting using Eq. 6-12. To simplify the description, the illumination period will be called the “bright period”. In contrast, the period when the beam was blocked will be called the “dark period”. During the curve fitting, the time axis was adjusted to start at 0 s. Due to the large amount of data, only the longest bright period and the related dark period based on the test with different light pulse widths were analysed. After processing 440 trajectories in 12 videos, the values of the first four parameters were plotted as a function of distance from the beam centre based on the original bead positions. Fig. 6-25 shows plots of the parameters within the bright and the dark periods, respectively. As shown in both Fig. 6-25 (b) and (d), the values of the parameters within the two periods are similar, which suggests the parameters b and d are not affected by the change of situation. In contrast, for both Fig. 6-25 (a) and (c), almost symmetrical patterns are displayed. According to the four graphs, it can be concluded that the elastic force makes the main contribution to the experimental results.

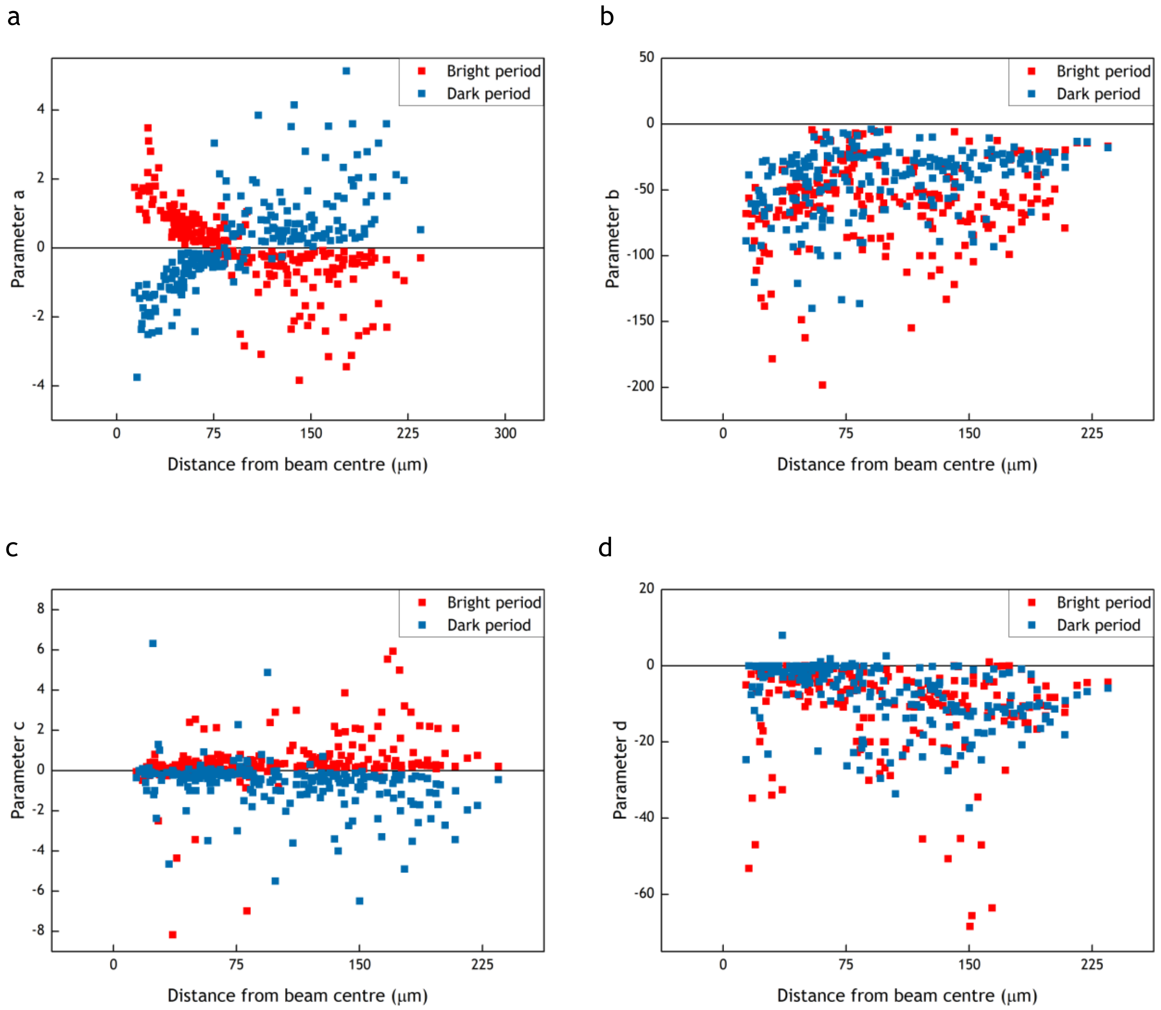

Fig. 6-25: Multiple plots of different parameters of fitted particle trajectories as a function of distance under the situations of the bright and the dark periods: (a) parameter a, (b) parameter b, (c) parameter c and (d) parameter d.

As we discussed before, the three typical particle behaviours could be grouped based on the near and the far regions. However, so far, the boundary between the two regions have not been accurately revealed. According to the previous conclusion, our understanding in the far region may be improved by defining the boundary. Therefore, in order to investigate this, all particle trajectories from the three experiments were plotted in one graph and the corresponding distance plots were analysed by the curve fitting. After looking into 571 trajectories in 43 videos, we found that the near region was restricted to an elongated area with position range between ±80 μm in the x-axis and ±70 μm in the y-axis. Here, the centre of the elongated area was the beam centre. According to the defined boundary, the first four parameters from all of the fitted trajectories were plotted as a function of distance based on the two regions separately, which are shown in Fig. 6-26. From the graphs, it can be seen that the values of parameter a decreases with distance within the near region. In the far region, the values tend to be more stable but smaller than those in the near region. It can be concluded that the elastic force in the far region is relatively weaker compared to the near region, which supports our physical model underpinning the motion of particles. In contrast, for the other graphs, there are no obvious differences between the two regions, which means the other parameters are not affected obviously by the distance.

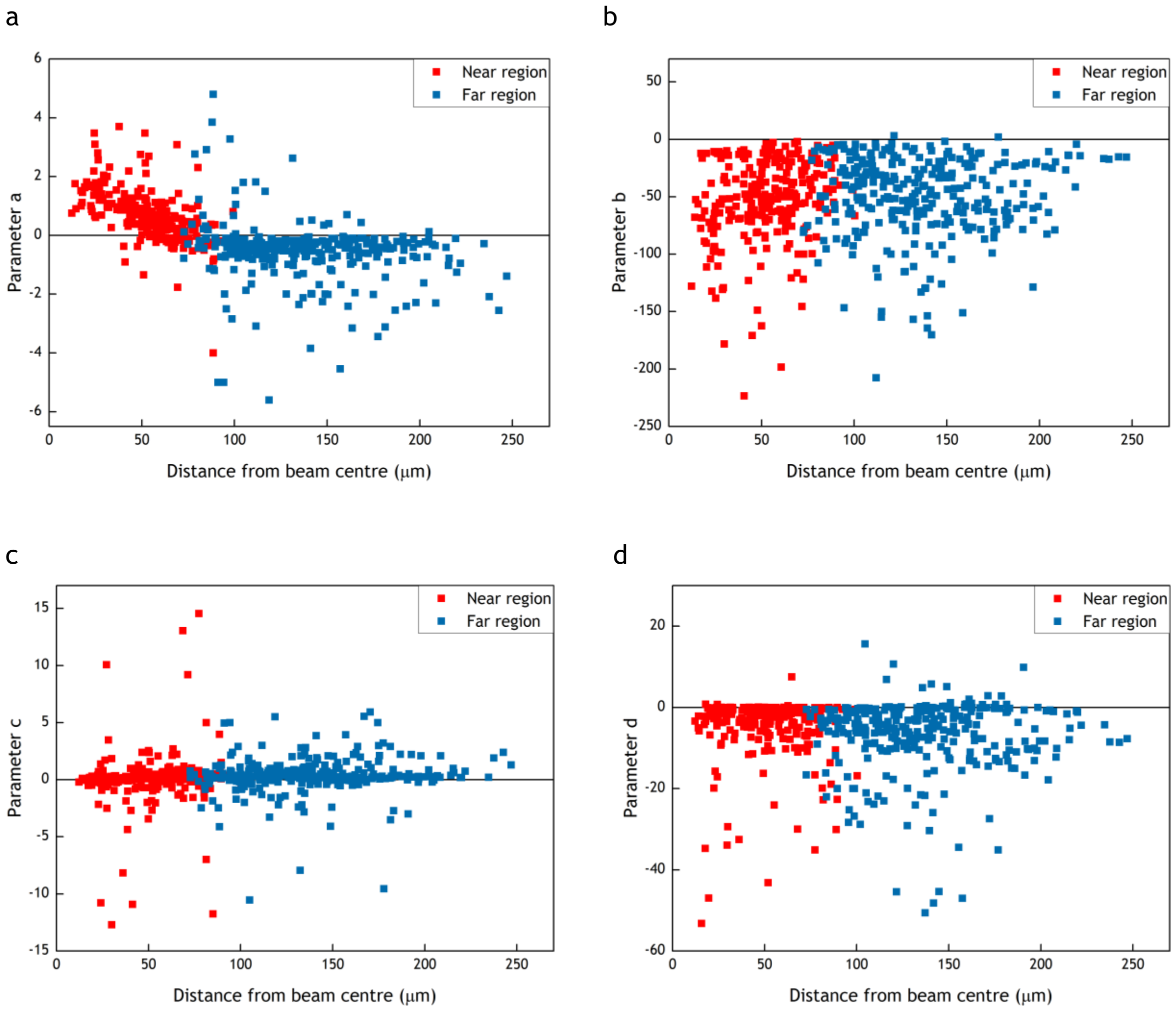

Fig. 6-26: Multiple plots of parameter values as a function of distance within the near and the far regions based on the fitted particle trajectories from three different tests: (a) parameter a, (b) parameter b, (c) parameter c and (d) parameter d.

For the experiments with short pulse widths (varying from 200 ns - 1 μs), there were no reactions observed on both of the particles and the clusters, which was unexpected. The thermal expansion of the clusters was also not observed. A potential cause is that the pulse width may have been too narrow which resulted in the clusters not absorbing enough energy to provide a response in such a short time period. Besides, according to the results in Subsection 6.4.3, the clusters were formed by low density SWNTs, which would also limit the energy absorption. Therefore, it may not be possible to generate acoustic pulses by using SWNT clusters based on our current methods and conditions.

6.6 Gas bubble generation and collection by laser heating

So far, the experimental phenomena that have been described in the previous sections are based on operation at nearly half of the maximum optical power. In order to investigate the maximum thermal expansion that could be obtained based on our experimental setup, it was necessary to implement tests with different incident optical powers (OP) up to full power. As for Subsection 6.4.1, the same sample mixture was used except the particle size was around 4.95 μm in diameter. The system setup and camera settings were also kept the same as previously. The sample device was fabricated based on the methods described in Subsection 3.2.3 with the substrate material of silicon. With full incident optical power illuminating the clusters, much stronger expansion effects were observed, which resulted from the formation of gas bubbles followed by explosions, catapulting particles away from the illumination region. Fig. 6-27 shows three images selected from the image stacks under the situations of before the laser beam moved onto the cluster, gas bubble generation during the illumination, and just before the explosion, respectively. By reducing the optical power, the explosions disappeared gradually but the formation of gas bubbles was still observed. When the OP was decreased to nearly half of the full power, in most cases, no gas bubbles were generated. Therefore, the maximum thermal expansion without affecting the particle manipulation could be obtained with optical power at the sample of 180 mW.

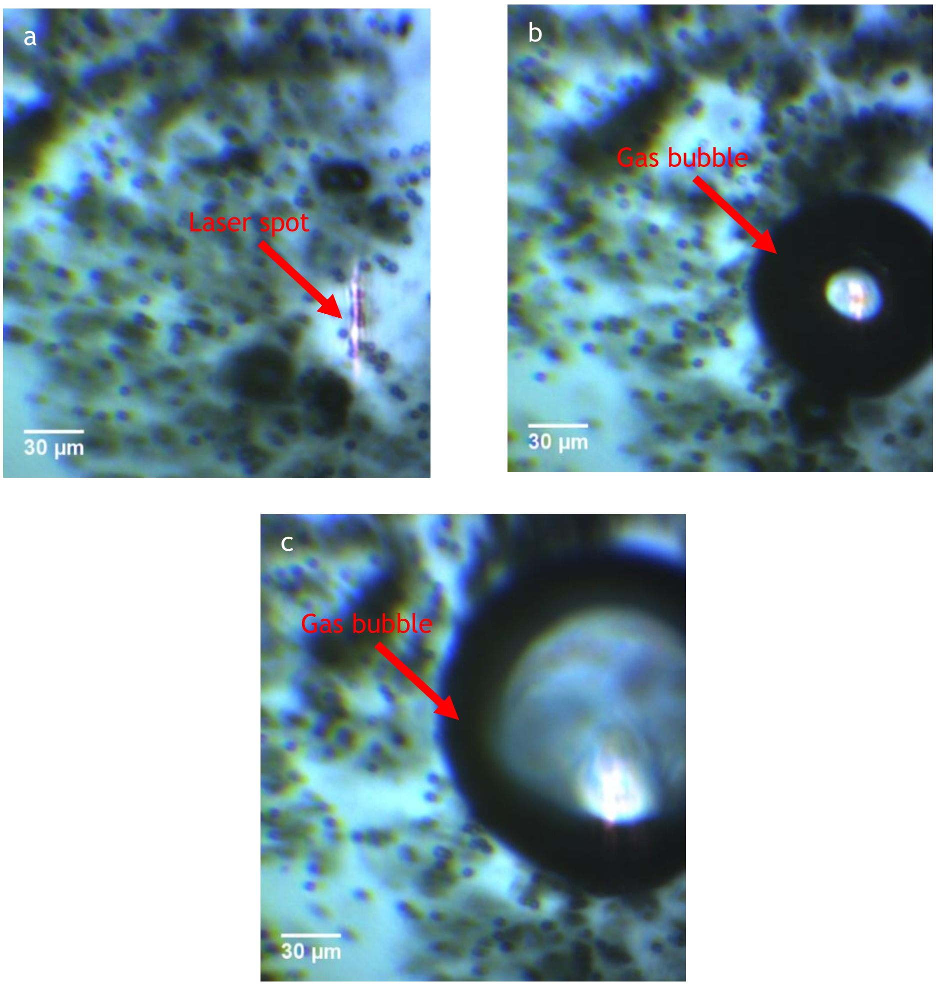

Fig. 6-27: Selected images from one of the image stacks for the experiment of gas bubble generation with a sample mixture of SWNT cluster and polystyrene bead (Φ4.95 μm), and full incident optical power under the situations of (a) before the laser beam moved onto the cluster; (b) gas bubble generation during the illumination; (c) the bubble just before the explosion.

Interestingly, regarding the strong reactions under full OP, similar phenomenon were reported in the literature published by a research group in Japan [177-179]. Instead of using carbon nanotubes, the Japanese group used a powder of *Bincho-tan* charcoal dispersed into a mixture of distilled water and alcohol. After laser illumination for 1 hour, the gas bubbles were collected by the water-displacement method. The chemical composition of the gas was analysed by quadrupole mass spectrometry, from which the main component was concluded to be hydrogen. Therefore, it would be interesting to try to collect and analyse the generated gas bubbles based on our experimental conditions, of which the more details were described and discussed in the following subsections.

6.6.1 Experimental methods

In this experiment, colloidal samples with different concentrations were prepared based on the methods mentioned in Subsection 3.3.2, except the SWNT conductive ink was dispersed into DI water containing 50% (w/w) ethanol with mixture ratios of 4 mg : 1 mL and 28 mg : 1 mL. The experimental setup is shown in Fig. 6-28. Similar to the literature, the gas bubbles were collected by the water-displacement method. A small glass beaker with more than half filled with colloidal solution was placed on a magnetic stirrer. A test tube filled with colloidal solution was inverted and fixed by a test tube clip. The opening of the tube was placed in the solution inside the beaker. The 10x objective (NA = 0.25) was then placed close to the beaker at a distance where the beam was focused inside the beaker but close to the sidewall. In order to collect the gas more efficiently, the test tube was placed next to the sidewall of the beaker and a stirrer bar was added into the beaker to prevent SWNT aggregation by mixing the sample and the solution continuously. A USB microscope was placed next to the objective to monitor the gas bubble generation. The laser was operated CW with full incident optical power at 1.1 A. During the tests, samples with different concentrations were illuminated by the laser beam for two and four hours, respectively. For the control sample, only DI water containing 50% (w/w) ethanol was illuminated by the laser under the same illumination periods.

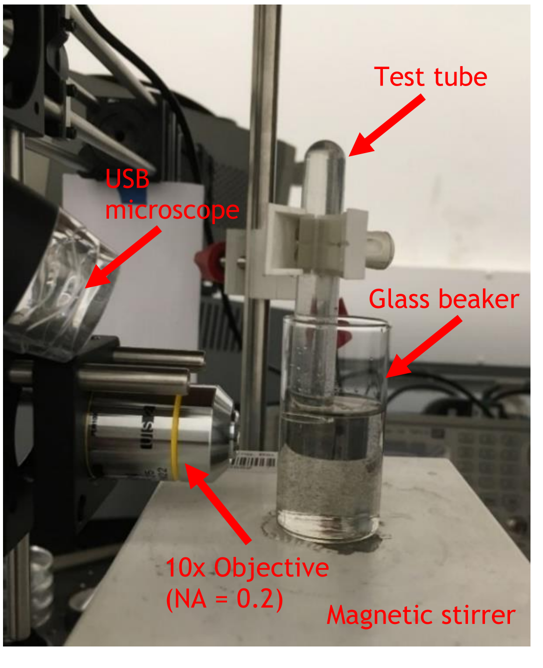

Fig. 6-28: The main part of experimental setup of gas bubble collection based on the water-displacement method.

6.6.2 Results and discussion

As the densities of gases are much lower than water, the generated gas bubbles should be expected to accumulate on the top of the inverted test tube. For the tests under two-hours of illumination, only two tiny gas bubbles were collected for the solution with a high concentration of SWNT clusters. No bubbles were seen for the sample with low concentration. For the control test, two smaller bubbles were collected compared to the test with high concentration sample. Fig. 6-29 shows the results under the test with the sample solution containing a high concentration of SWNT clusters. The collected gas bubbles are indicated by red arrows. Similar to the tests under two-hour illumination, for four-hour illumination, no bubbles were seen for the sample solution with a low concentration of SWNT clusters. However, for the high concentration solution, a bigger bubble was collected in the test tube compared to the situation before illumination. For the control test, once again two smaller bubbles could be seen under a 3x objective. Compared to the literature, only tiny amount of gas was collected under our tests, which was not enough for further chemical composition analysis. Potential reasons for not seeing more gas were that, firstly, there is a possibility that the generated gases dissolved into the solution before reaching the bottom of the tube; secondly, small gas molecules could penetrate into the glassware. Furthermore, it was hard to tell whether the generated gas bubbles were based on the chemical reaction between SWNT and solution or not, as bubbles were also collected under the control tests but with smaller sizes, indicating that some gas had dissolved into the solution before the tests. Therefore, we were unable to use the gas analysis method of quadrupole mass spectrometry. A more sensitive and simpler way to do the analysis would be to use chemical indicators, which will be implemented in the future.

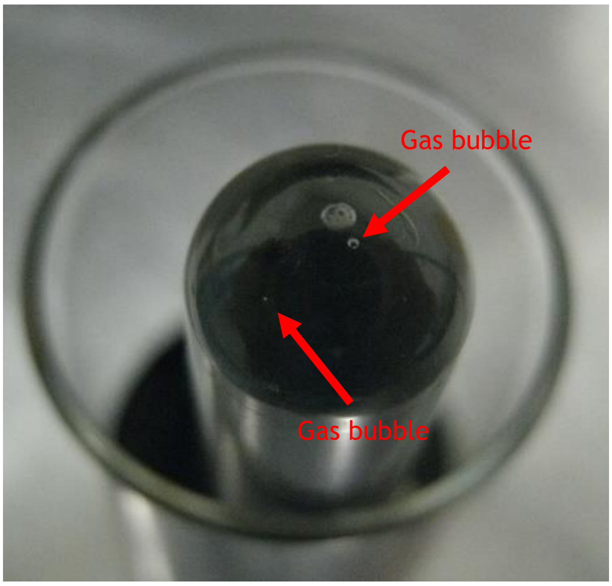

Fig. 6-29: Results of gas bubble collection based on the water-displacement method under the conditions of sample solution with high concentration of SWNT clusters and 2-hour full optical power illumination.

6.7 Summary

In this Chapter, microparticles and biological samples were manipulated successfully by either laser-induced optical forces or laser-induced thermal forces. Specifically, polystyrene beads with 20 μm diameter were trapped and moved by the CW laser beam using a silicon substrate under full optical power, due to the optical gradient force (see Section 6.2). In contrast, most of the smaller size beads (Φ4.95 μm) continuously moved away from the illumination region under continuous irradiation conditions, which indicated laser-induced thermophoresis dominating. The related thermophoretic mobility (D_T) was studied by comparing particle moving speeds for different materials and different incident optical powers. It was concluded that D_T increased for material with lower thermal conductivity. The thermophoretic velocity increased with incident optical power. Through introducing an extra light energy absorber – SWNT clusters into sample solution, the symmetrical thermal convection flows were observed under lower optical power (180 mW) and smaller particle size (Φ1.54 μm). In the control experiment, a ring shaped particle-stopping region around the beam was observed. However, the result was different from the one shown in Fig. 6-3 (c), which implied that D_T was also relevant to particle size. By replacing the substrate material with glass, a similar particle-stopping position region was observed, which supported the existence of thermophoresis and thermal convection flows. Beyond the particle-stopping region, the movements of particles were mainly determined by the strength of the fluid flow. The characteristics of the convection flow were studied by making a comparison of particle moving speeds for different optical power absorptions by clusters and different particle sizes. It was concluded that the flow speed was proportional to the energy absorption, and the particle moving speed increased with particle size, which indicated that the particle suspension height may have affected the moving speed as well. In terms of biological applications, Jurkat cells were manipulated successfully with similar behaviours to the microbeads. For better understanding the above experimental phenomenon, numerical modelling was undertaken as described in the next Chapter. Based on the modelling results, a clearer picture for each situation will be presented.

Next, SWNT clusters were illuminated by discontinuous laser beams. Instead of acoustic pulses being generated, three typical particle behaviours were observed based on the particle positions. By analysing particle trajectories within and outwith the illumination period using curve fitting, several physical mechanisms were considered. After examining the curve-fitting parameters with particle positions, one of the physical mechanisms (elastic force) was investigated, allowing us to describe the motion observed. In the final part of the Chapter, by increasing the incident optical power further, gas bubbles were generated followed by explosions. However, only small amount of gas was collected based on the water-displacement method. A proper chemical composition analysis will need to be implemented in the future.

Chapter 7

Simulation of laser-induced thermal forces

According to the studies in the last Chapter, the characteristics of the two physical phenomena, which were the laser-induced thermophoresis and the thermal convection flow, were discussed. In order to fully understand the physical mechanisms of the phenomena, it is appropriate to use the help of numerical simulations. In this Chapter, modelling of laser-induced thermal forces based on the silicon substrate and the glass substrate with SWNT clusters are presented. In terms of the distributions of the temperature, the temperature gradient and fluid flow, and the directions of the flow, the simulation results agree closely with the experimental results. In addition, the modelling based on the glass substrate was performed with different types of heat transfer as well, showing conduction was the main type of heat transfer. Furthermore, the relations between the flow speed and the absorbed optical power or the particle size were studied, showing the trends of the modelling results agreed with the experiment results. Moreover, the trend of the thermophoretic mobility with particle size was studied as well, which supported the predictions in Subsection 6.3.3. In summary, through combining experimental results and simulation results, a clear picture of the mechanisms will be obtained.

7.1 Theory

In this Section, some important definitions and equations used in the later sections are described.

7.1.1 Rayleigh number (Ra)

In fluid dynamics, the Rayleigh number (Ra) is a dimensionless number associated with natural convection, which determines whether heat transfer in a fluid is dominated by conduction or convection. When the Ra number is below a critical value, heat transfer in the fluid is conduction dominated, whereas if the Ra above the value, heat transfer is convection dominated. For water, the critical value is around 1700 [110]. Generally, the Ra number can be expressed as [110, 180-183]

$$Ra = \frac{g\beta\Delta TL^3}{\alpha\mu} \propto \frac{convection}{conduction} \quad \text{(Eq. 7-1)}$$

where β, α and μ are the coefficients of the thermal expansion, the thermal diffusivity and the kinematic viscosity of the fluid, respectively; g is the local gravitational acceleration; ΔT is the temperature difference across the medium; L is the characteristic length-scale of convection. Based on our experimental conditions (see Sections 6.3 and 6.4), the sample solutions were mainly water-based suspensions, which can be treated as water. The value of each parameters is summarized in Table 7-1.

β = 2.07E-4 /°C	g = 9.8 m/s^2	α = 0.142E-6 m^2/s
μ = 1.0034E-6 m^2/s	L = 1E-4 m	ΔT = 80 °C

Table 7-1: The defined values of parameters in Eq. 7-1 based on the experimental conditions in Sections 6.3 and 6.4.

Here, the value of L is determined by the thickness of the sample chamber, the value of ΔT is under the extreme case when the temperature reaches to the water boiling point. The initial temperature is considered as 20 °C. After calculation, the Ra number is around 1.14, which is much smaller than the critical value. Therefore, the heat transfer under our experimental conditions is conduction dominated.

7.2 Laser-induced thermal forces on a silicon substrate

In this Section, simulations based on the experiments of microbead manipulation with laser-induced thermal forces on a silicon substrate (see Section 6.3) are presented. According to our understandings, both laser-induced thermophoresis and thermal convection flow were generated under our experimental conditions. Regarding the further studies in Section 6.3, the characteristics of thermophoresis were revealed. However, no convection flow was observed, which indicates the much weaker convection currents being generated. Therefore, the following modelling will mainly focus on the situation of the fluid convection flow. Specifically, we modelled the distributions of the temperature and the temperature gradient within the liquid domain, the results agreed with the experimental observations. By modelling the flow velocity distribution, the weak flow was generated and the flow directions were very similar to the experimental phenomena after adding the extra light energy absorber into the sample solution. In addition, by comparing the thermophoretic velocity with the flow velocity, our understandings were supported. Furthermore, the effects of the air gap between the sample device and the heat sink were also studied.

7.2.1 Methods and parameter settings

In this work, 3D modelling under steady-state conditions was performed using COMSOL Multiphysics modelling software. The 3D geometric structure used to represent the sample device was created and is shown in Fig. 7-1. The structure was constructed from four parts: the silicon domain (representing the silicon substrate), the water domain (representing the closed sample chamber), the heat source domain (representing the central area of laser heating within the substrate) and the glass domain (representing the cover slide). Except for the heat source domain, the dimensions of the domains in the z-direction were set based on the real thicknesses of the device used in the experiments in Section 6.3. For more details of the dimension of the device, please refer to Subsection 3.2.3. The dimensions in x- and y-direction were set as 1 mm x 1 mm due to the limitations of the computer memory. Therefore, the total size of the structure (L x W x H) was 1 mm x 1 mm x 1.6 mm. For the heat source domain, the thickness was determined by the Beer-Lambert law, and the material was set as the same as silicon domain. At a wavelength of 808 nm, the absorption coefficient of silicon is around 945 cm^{-1} [184]. After passing through 50 μm of Si, the transmittance is around 0.01, which means the light is almost absorbed. Therefore, the thickness of the heat source domain was set as 50 μm. The dimensions of the domain in x- and y-direction were set based on the real beam size (referred to full width at half maximum (FWHM)) on the substrate, which were Φ2.5 μm and Φ52.9 μm, respectively. Moreover, most parts of the heat source domain were merged into the silicon domain; only the top surface was in the same plane as the top surface of the silicon domain.

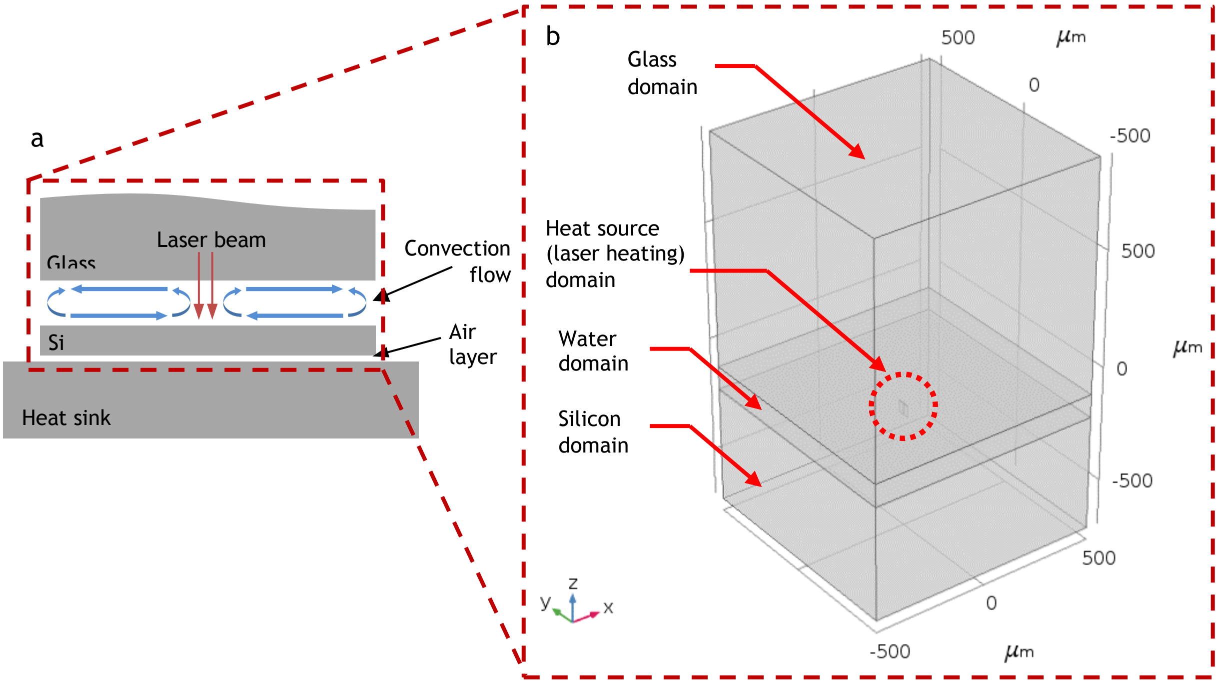

Fig. 7-1: Schematics of (a) the sample device configuration and (b) the 3D structure built in the simulation based on the real thickness of the sample device.

As described in Sections 6.1 and 6.3, the type of flow generated in the experiment should be Stokes flow in the form of natural convection. In order to model this kind of fluid flow under laser heating conditions, two physical models were chosen and coupled in the simulation: the heat transfer model and the laminar flow model. In the heat transfer model, the type for the water domain was set as fluid and the rest were set as solid. Heat transfer was calculated based on Eq. 5-1 in Section 5.1. The heat source domain was set to be a body heat source (Q_0) which could be expressed as

$$Q = Q_0 = \frac{P_0}{V} \qquad \textbf{(Eq. 7-2)}$$

where P_0 is the input power in Watt and V is the total volume of the selected domain. In our case, the input power should be the incident optical power. By considering the light energy lost during the beam passing through the cover slide and the water domain, P_0 can be calculated as follows:

$$P_0 = P \times T_g \times T_w \times (1 - R) \times (1 - T_{50}) \qquad \textbf{(Eq. 7-3)}$$

where P is the optical power before entering the device, T_g, T_w and T_{50} are the fraction of the light passing through the cover slide, the water domain and travelling 50 μm inside the substrate from the water-Si interface, respectively. *R* is the reflectance at the water-Si interface at wavelength of 808 nm. For the boundary conditions, a thin air layer was assumed to be present at the bottom surface of the silicon domain in order to simulate the poor heat conduction between the device and the heat sink in the real experimental setup. Later, in the next subsection, the effects of the thickness of the thin layer on the flow speed and the temperature gradient were investigated. The temperatures on the exterior boundaries of the layer were set as 20 DegC. In order to simulate natural convection cooling, a convective heat flux was present at the exterior surfaces of the glass and the silicon domains. Heat transfer by radiation between surfaces was neglected by default in the software, but this was only valid for surfaces with low emissivity (close to 0) [185]. After checking this parameter for each component of the device in the literature [186-189], it became apparent that it was necessary to consider the surface-to-surface radiation by adding the 'diffuse surface' boundary condition onto the water-Si interface, the water-glass interface, and the air-solid interface with the corresponding surface emissivity. In addition, the initial temperatures of all domains were set as 20 DegC.

In terms of the laminar flow model, it was considered only in the water domain. Again, according to Section 6.3, convection flow was generated by the internal density-dependent buoyancy force rather than external forces. Therefore, the incompressible flow and gravity options were selected. Here, the gravity feature would automatically add the fluid density-dependent volume force of buoyancy in the momentum equation in order to simulate the natural convection flow [190, 191]. The initial flow velocity was set to 0 to simulate the initial condition of the experiment. Therefore, based on above conditions, the fluid flow was analysed according to the Navier-Stokes equation

$$\begin{aligned} \rho(u \cdot \nabla)u &= \nabla \cdot \left[-pI + \mu\left(\nabla u + (\nabla u)^T\right)\right] + F \\ \rho\nabla \cdot (u) &= 0 \end{aligned} \qquad \text{(Eq. 7-4)}$$

where *p* is the pressure, *I* is the identity matrix, *μ* is the dynamic viscosity and *F* is the volumatic force. For the boundary conditions, the surfaces in contact with the water domain and the sidewalls of the domain were set as 'no slip', which means the flow velocity relative to the wall velocity is 0. Fig. 7-2 shows the main boundary conditions of the two physical models.

For the meshing, the heat source domain and the water domain were processed with ‘extra fine meshing’, the silicon domain was treated with ‘finer meshing’ and the glass domain was processed with ‘fine meshing’ due to the limitation of the computer memory size. The values of the main parameters used in the simulation are listed in Appendix IV.

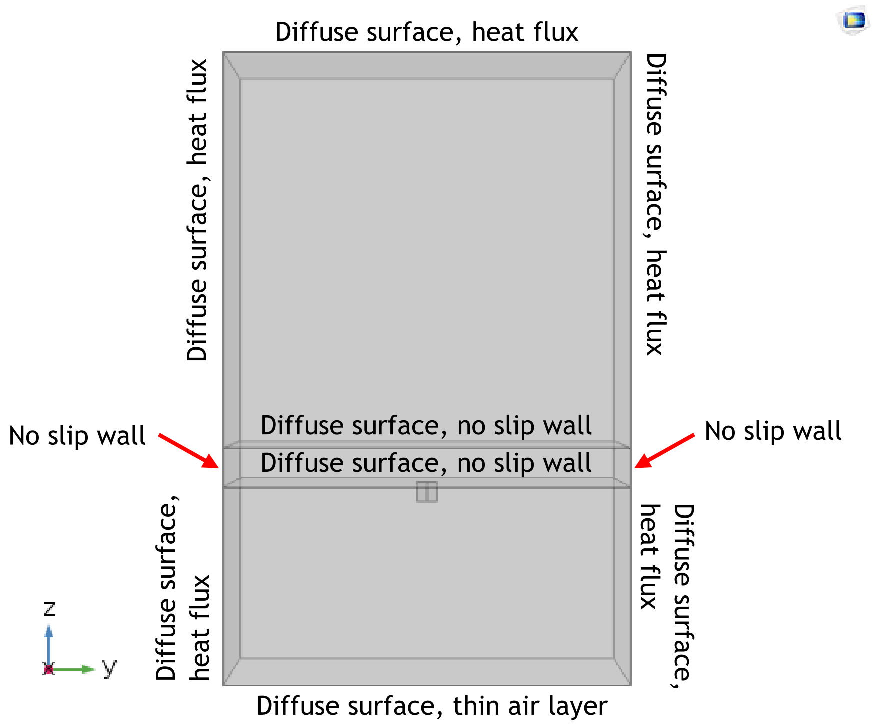

Fig. 7-2: Main boundary conditions of both the heat transfer model and the laminar flow model applied on the domains.

7.2.2 Results and discussion

As previously discussed, natural convection occurred due to the temperature gradient established in the fluid. Therefore, heat transfer inside the water domain was the first factor we examined. Fig. 7-3 displays the temperature distributions of the geometric structure with a thin air layer of 500 nm in y-z and x-z cross sections. As we expected, in the water domain, the temperature decreases with distance from the centre of the water-silicon interface in all three dimensions. The temperatures close to the interface in the central hot region of the domain are below but close to 40 DegC in both cross sections, which is consistent with the experiment as no air bubbles were seen during the experiment. Fig. 7-4 displays the corresponding temperature gradients. As can be seen from the graphs, similar to the temperature distribution, the temperature gradient also decreases with distance from the central hot region of the water domain in all three dimensions. Compared to the situations along the other boundaries, the temperature gradients along the water-silicon interface in the hot region of the domain are relatively higher in both cross sections, which is due to the different thermal conductivities of materials.

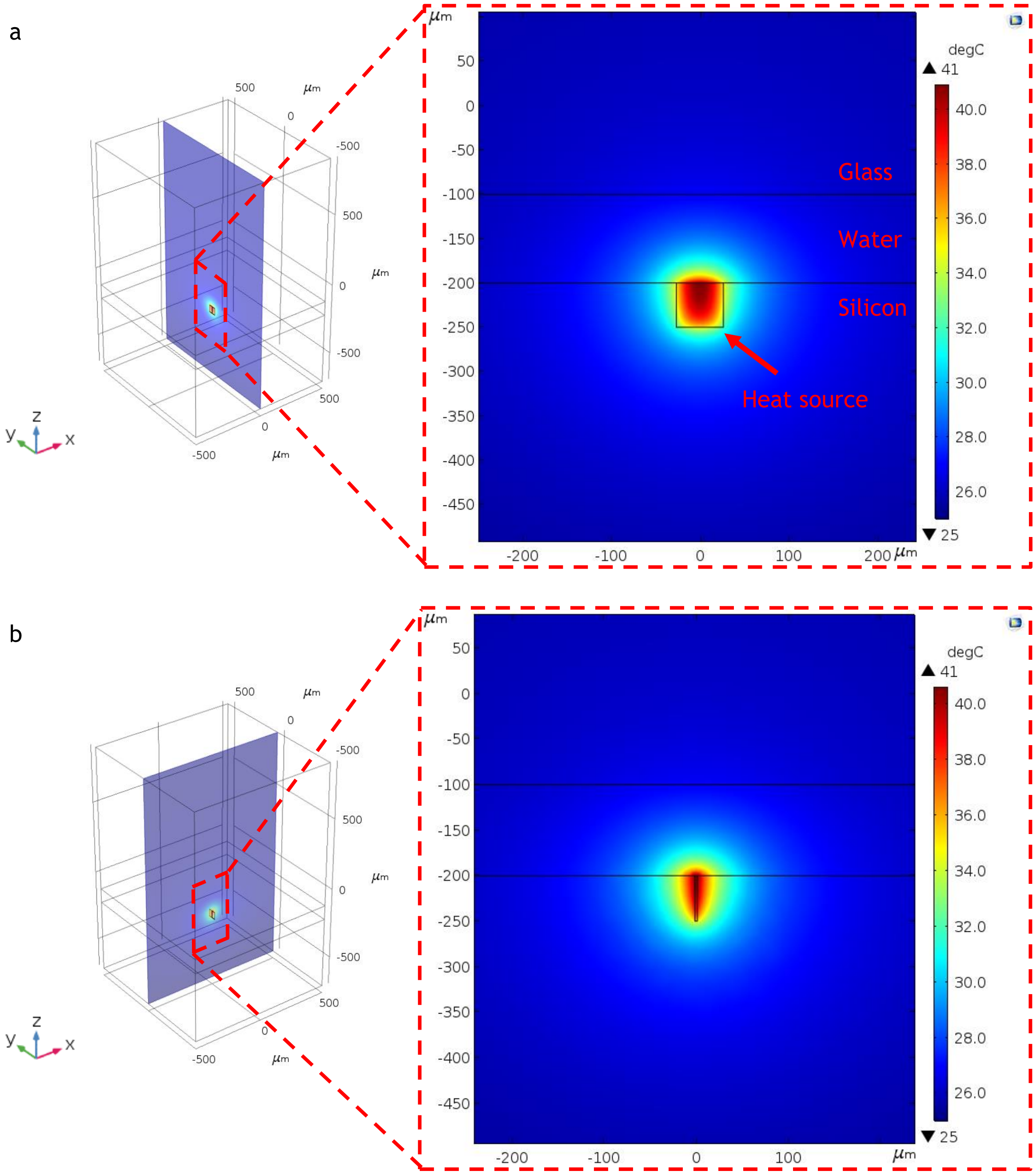

Fig. 7-3: Temperature distributions of the 3D structure with a thin air layer of 500 nm in (a) y-z cross section; (b) x-z cross section.

a

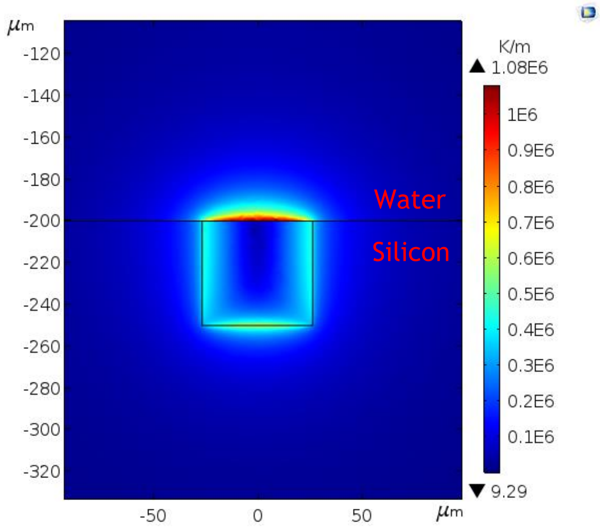

b

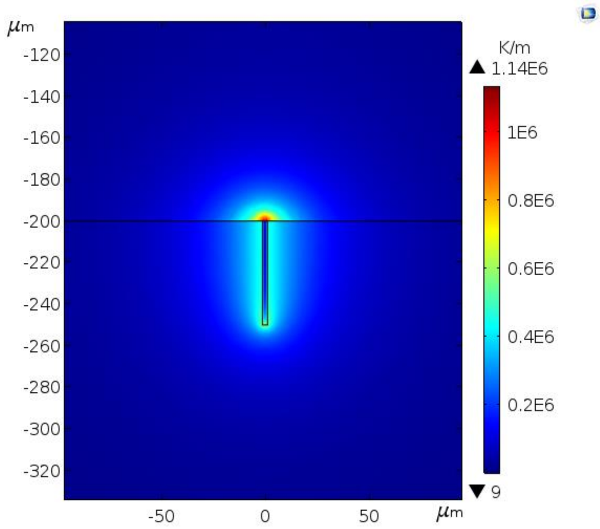

Fig. 7-4: Temperature gradients of the 3D structure with a thin air layer of 500 nm in (a) y-z cross section; (b) x-z cross section.

As described in Subsection 6.3.2, before adding the SWNT clusters into the sample solution, particles always moved away continuously from the beam and effects due to fluid convection flow were barely observable, implying the major force was due to thermophoresis. The existence of fluid flow inside the chamber under such conditions was modelled numerically. Fig. 7-5 shows the velocity magnitude distributions of the fluid flow, represented as a colour background, and the flow directions, highlighted by red arrows, inside the water domain in both y-z and x-z cross sections. It can be seen that fluid flows are present in all three dimensions. The fast flow region appears around the centroid of the domain with maximum speed of around 0.66 μm/s. Beyond this region, speeds are fastest close to both of the top and the bottom boundaries. The arrows show that a loop of fluid flow is generated. Flows close to the bottom boundary move parallel to the water-silicon interface towards the hot region. Once close to the laser spot, the flows are redirected upwards to the top boundary. As for the bottom boundary, flows close to the top boundary move parallel to the glass-water interface but away from the geometric centre of the domain. Once reaching the sidewall, flows are redirected down to the bottom boundary. Here, the simulated flow direction agrees well with the experimental phenomena described in Subsection 6.3.3. It also needs to be noted that the flow velocities are shown only in half of dimension of the domain as symmetrical patterns are obtained in the other part. In addition, the arrows only indicate flow direction and do not represent as the velocity strength.

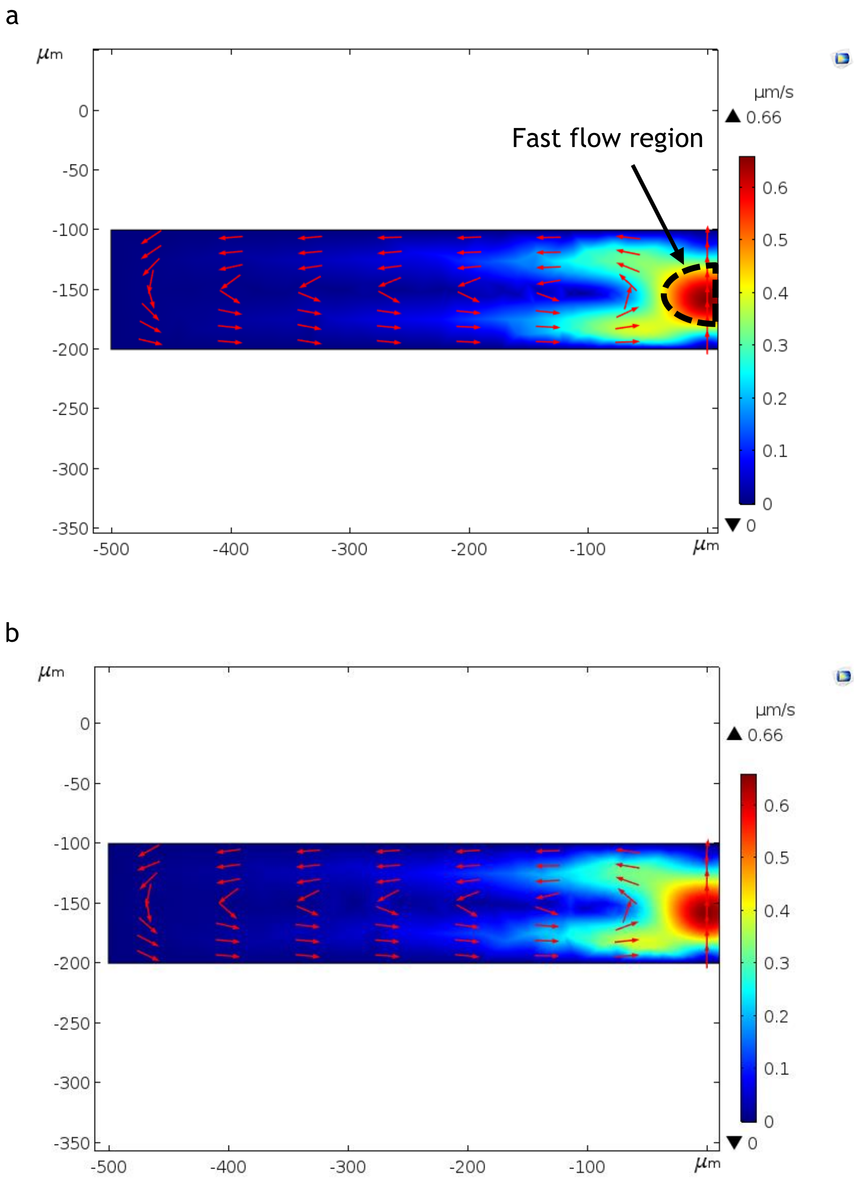

Fig. 7-5: Modelling results of fluid flow velocity distribution (shown as colour background) and direction (red arrows) within the water domain of the structure with a thin air layer of 500 nm in (a) y-z cross section and (b) x-z cross section.

So far, only fluid flow had been simulated and analysed. For thermophoresis, a limited physical model was available in the software, which could only be used to model thermophoresis in the gas condition. As described in Subsection 2.5.2, there is no general physical model of the phenomenon in liquid. However, the thermophoretic velocity had already been studied in the literature, which is dependent on both the thermophoretic mobility (D_T) and the temperature gradient established in the liquid. The temperature gradient had been modelled in the simulation. Therefore, it was possible to investigate the thermophoretic velocity based on our experimental conditions, if the thermophoretic mobility was known (see Eq. 2-9). Regarding the experimental results in Subsection 6.3.2, particles moved away from the hot region continuously without stopping, which indicated thermophoresis was dominant. Therefore, the particle speed should be the difference of the flow velocity and the thermophoretic velocity. Based on the particle trajectories shown in Fig. 6-4 (b), the average particle speed was obtained using the same analysis method described in Subsection 6.3.3. The average particle initial position and the average particle moving distance were obtained as well, which were used to create a 3D cut-line in the water domain. Based on the cut-line, the average flow velocity and the average temperature gradient could be easily calculated, from which the thermophoretic mobility was determined. The average D_T values were around 14.05 $\mu m^2/(s \cdot K)$ along the x-axis and 13.86 $\mu m^2/(s \cdot K)$ along the y-axis. Fig. 7-6 shows plots of the two velocities based on cut-lines from the edge of the heat source domain to the sidewalls of the water domain in the x- and y-directions. The vertical positions of the cut-lines were determined from the real measurement of the particle suspension position based on polystyrene beads with 4.95 µm diameter, which will be presented in the next Section. As shown in the plots, the thermophoretic speeds in both cases are always higher than the flow speed up to 250 µm away from the heat source domain, which agrees well with the experimental observations. In addition, the thermophoretic speed varied much faster with distance in the first 40 µm, being almost comparable to the flow speed. Therefore, based on the experimental observations (see Subsection 6.3.2) and the modelling results, it can be concluded that the particle movements are mainly determined by the thermophoresis, which supported our conclusions in Subsection 6.3.3.

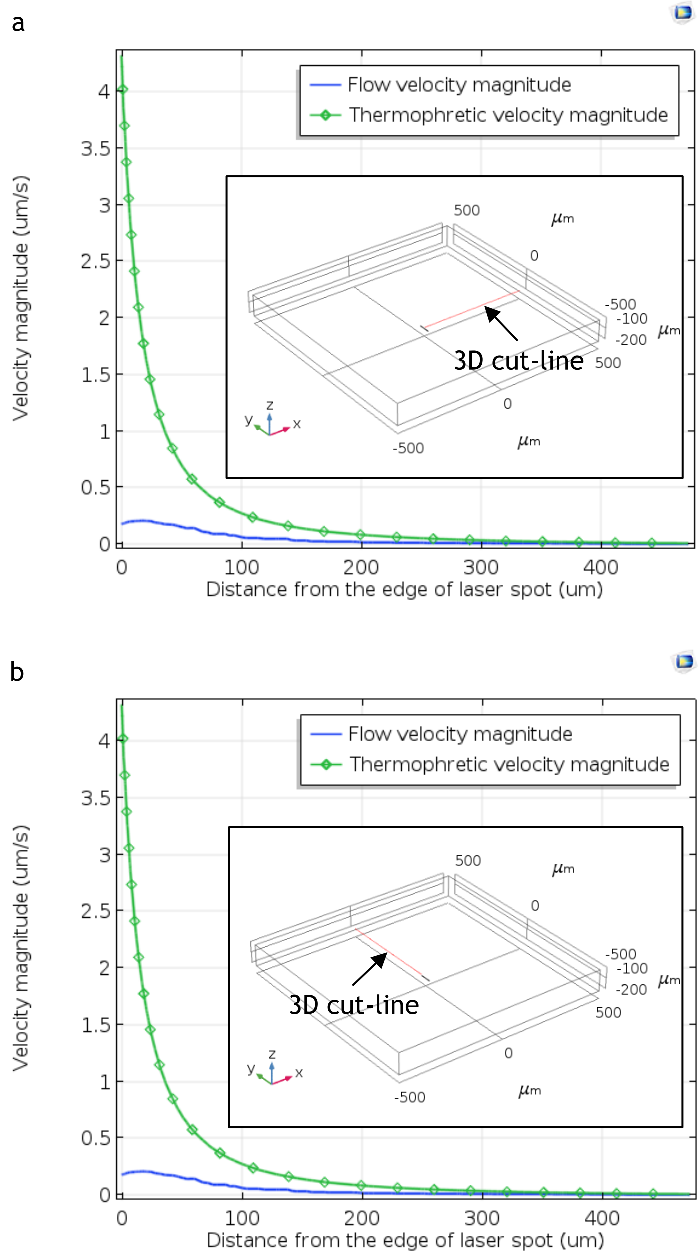

Fig. 7-6: Plots of the flow speed and the thermophoretic speed based on a 3D cut-line (shown in red) from the edge of the light spot to the sidewall of the water domain along (a) the x-axis and (b) the y-axis.

Furthermore, the effect of the thickness of the thin air layer present at the bottom of the silicon domain was also investigated. As described in the previous subsection, the purpose of this layer was to simulate the poor heat conduction between the sample device and the heat sink. In this study, five layer thicknesses were chosen, 0 μm, 0.5 μm, 1 μm, 5 μm and 10 μm. Fig. 7-7 (a) and (b) show plots of flow speed as a function of position relative to the edge of the heat source domain along the two axes for different layer thicknesses. Similarly, Fig. 7-7 (c) and (d) show plots of temperature gradient under the same conditions. Here, the plots are based on the same cut-lines used in Fig. 7-6. As can be seen from the graphs, the thickness of the thin layer has almost no effect on the flow speed along either axes. In addition, as the distances reduced, the speed increases initially. As the heat source domain is approached, the speed reaches maxima then decreases shortly, which is caused by the 'no slip' boundary condition imposed on the top surface of the heat source domain. Furthermore, by comparing Fig. 7-7 (a) and (b) with Fig. 6-5 (f), it can be seen that the flow speeds are at least 4.5 times lower than the measured particle speeds. As reported in Subsection 6.3.3, convection flow was barely observed during the experiment, because convection was relatively weaker compared to thermophoresis and gravity effects. Temperature gradient within the distance range of the first 50 μm showing slight differences along the two axes. Beyond that point, the differences become more obvious. Besides, the temperature gradients at the edges of the heat source domain are different, which could be caused by the shape of the domain. Here, the edges of the domain are represented as the cases with distance of 0 μm in the plots.

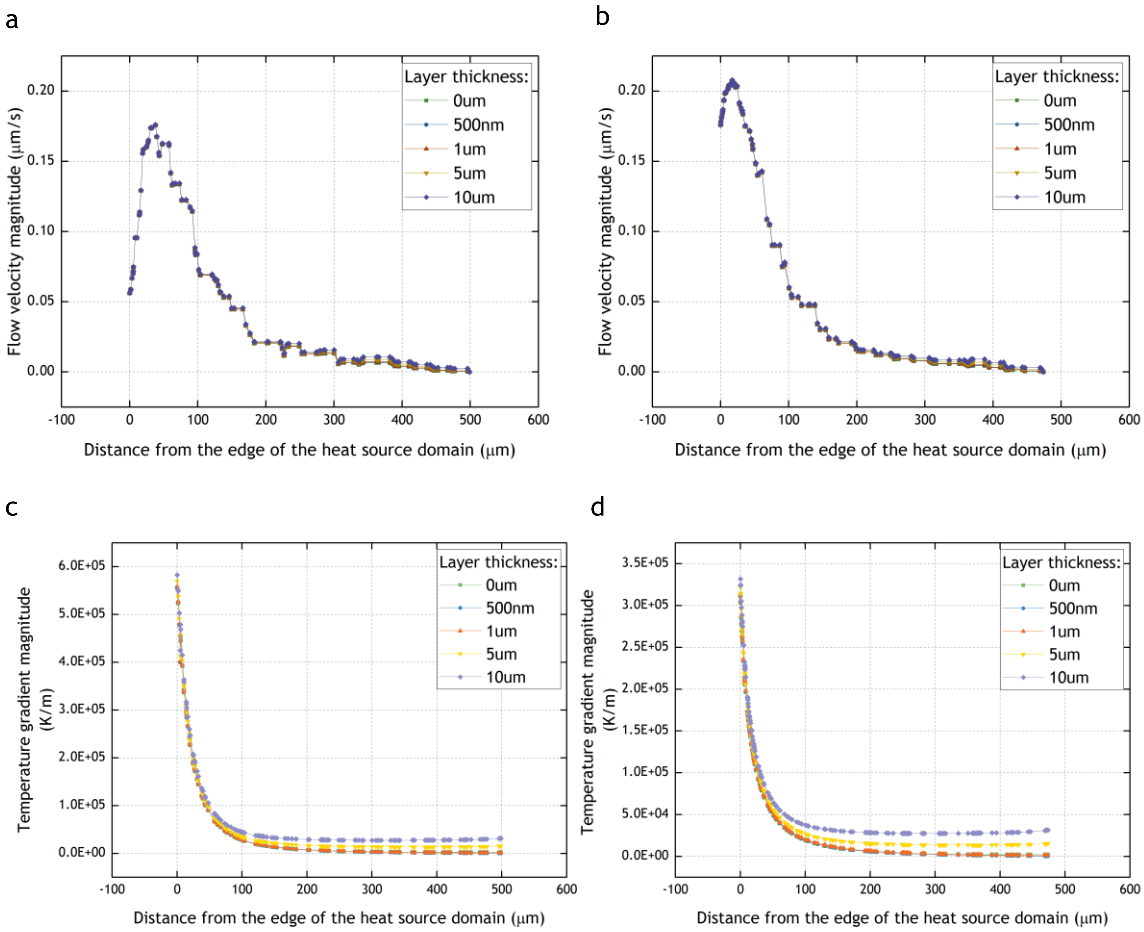

Fig. 7-7: Plots of the flow speed and the temperature gradient for different air layer thicknesses based on the same cut-lines used in Fig. 7-6 along the x-axis (a & c) and the y-axis (b & d).

7.3 Laser-induced thermal forces on a glass substrate

In this Section, simulations of microbead manipulation with laser-induced thermal forces on a glass substrate are reported (see Section 6.4). By modelling different types of heat transfer, we concluded the heat transfer in our experiments was conduction dominated, which providing more clues about the laser-induced thermal forces. By looking into the relationship between the flow velocity and the input energy or the particle position, the conclusions from Subsection 6.4.3 were supported. In addition, the relationship between thermophoretic mobility and particle size was also revealed.

7.3.1 Methods and parameter settings

Similar to Section 7.2, 3D modelling under steady-state condition was performed using COMSOL software. To simulate the experiment in Subsection 6.4.1, a 3D geometric structure containing four domains was built. Fig. 7-8 shows the structure with the related domains. The dimensions of the water domain and the cover slide domain were the same as previous work. However, the silicon domain was replaced by a glass substrate domain with the same dimension as the cover slide domain. The heat source domain now associated with SWNTs, was moved into the water domain with its bottom sitting on the top surface of the substrate domain. In order to make a realistic model, the dimensions of the heat source, which is the SWNT cluster in this work, in the real experiment were measured by the following two independent experiments: the thickness and the 2D dimension tests of SWNT clusters. For the thickness test, the measurement was performed using a commercial microscope with a 10x objective (NA = 0.3, UPlanFL N, Olympus). By focusing on the top and the bottom surfaces of the clusters, the thickness could be obtained by looking at the vertical position differences of the two optical planes. The sample solution was prepared following the method described in Subsection 3.3.2, and then injected into the sample device by pipetting. The test was implemented 10 times with different clusters each time. Eventually, the average thickness was found to be 31±15 μm. For the 2D dimension test, the distance between the cluster edge and its geometric centre was measured by the particle tracking software based on the videos recorded during the experiments in Subsection 6.4.3. During the test, 8 edge points were chosen on each cluster and 9 videos were analysed in total. Due to the fact that the shapes of clusters in most videos were elliptical or nearly round, a cylinder was used in the heat source domain to represent the cluster in the simulation. The radius of the cylinder was the average distance measured from the videos, which was 12.4±3.5 μm. Here, the 8 edge points were the points of intersections of the 4 geometric central lines, which divided the whole cluster into 8 equal parts based on the angle, and the cluster edge.

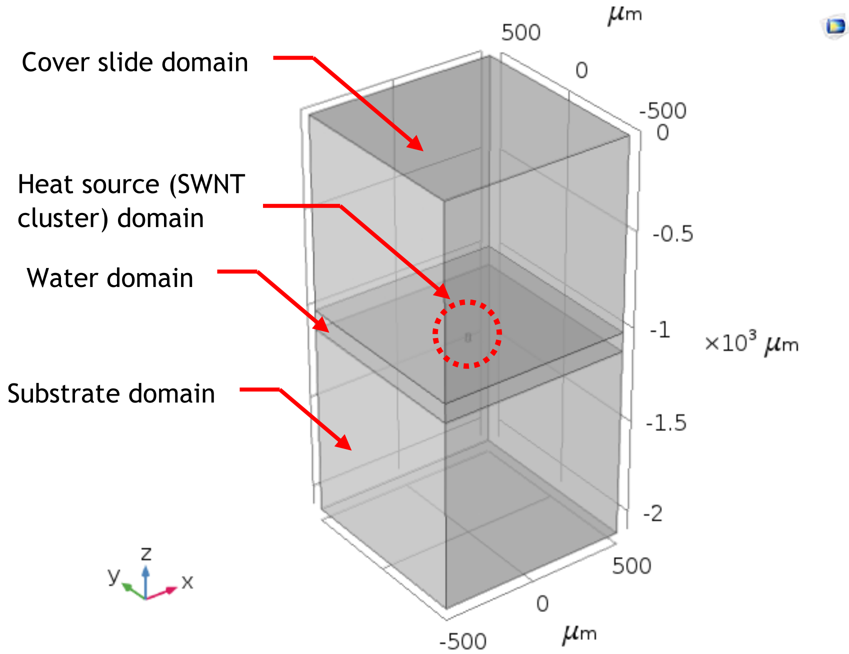

Fig. 7-8: Schematic of the 3D structure built in the simulation based on the real thickness of the sample device.

As in the previous Section, the laser-induced thermal convection flow was modelled by coupling two physical models: the heat transfer model and the laminar flow model. For the heat transfer model, the heat transfer function, the initial values, and almost all of the domain and boundary condition settings were kept the same as previously except the input power (P_0) of the heat source domain was based on the real measurement results reported in Subsection 6.4.3, which was around 10 mW. Here, the heat source (SWNT cluster) domain was characterised as body heat source because of the conclusion from Fig. 6-11 (a), which stated that the cluster could be treated as bulk heat source after studying the relation between the particle-stopping positions and the edges of the corresponding clusters. The thin air layer added to the substrate bottom previously was removed. Instead, heat radiation into the air from the bottom was modelled. Moreover, a thin water layer with thickness of 500 nm was added between the heat source domain and the substrate domain in order to model the real liquid gap along the interface of the two materials and the poor heat conduction under real experimental conditions.

For the laminar flow model, the version of Navier-Stokes equation, the initial values, and almost all of the domain and the boundary condition settings were also kept the same as previously except all of the surfaces of the heat source domain in contact with water were set as ‘no slip’. Fig. 7-9 shows the main boundary conditions of the two physical models added onto the domains.

For the meshing, only the heat source domain was processed with ‘extra fine meshing’, and the rest were treated with ‘finer meshing’ due to the limitation of the computer memory size. The values of the main parameters used in the simulation are listed in Appendix V.

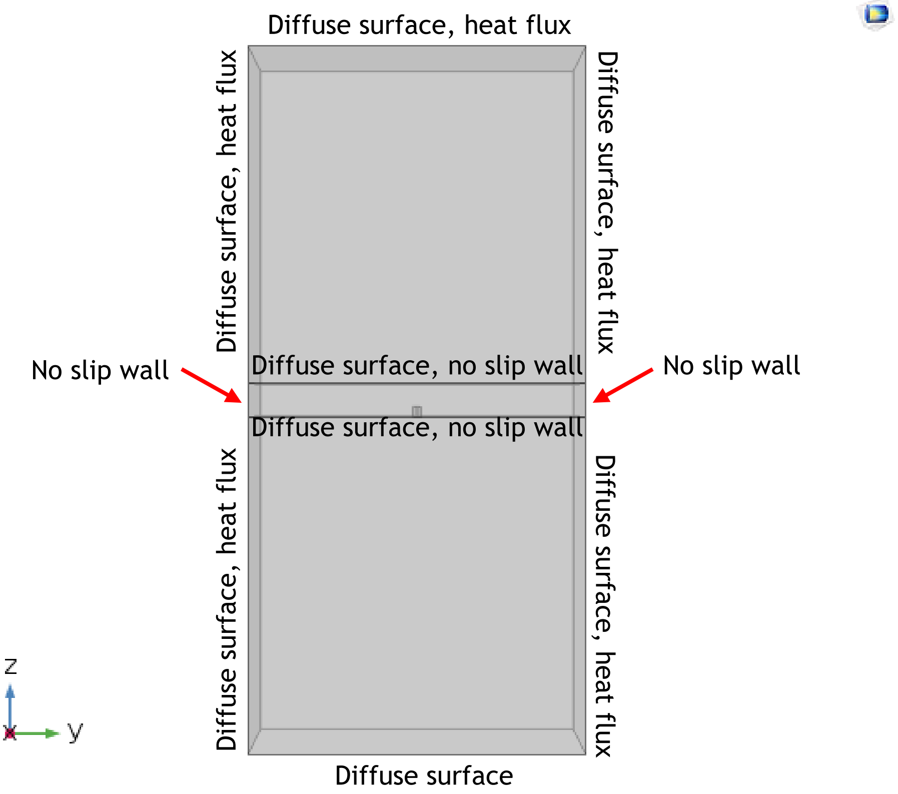

Fig. 7-9: Main boundary conditions of both the heat transfer model and the laminar flow model applied on the domains.

7.3.2 Results and discussion

According to the simulation settings in both Subsections 7.2.1 and 7.3.1, the simulation results inside the water domain resulted from combined effects of thermal convection and conduction, which limited our view of understanding the physical mechanisms of the experimental phenomena. It would be better if the modelling could be performed based on single type of heat transfer, which could probably provide more information to improve our current understandings. The following part presents the modelling results based on conduction only and the combined effects, respectively.

In order to perform the modelling under conduction only, in the physical model settings of the software, the types of all domains must be set as solid with the heat transfer model being activated only. Fig. 7-10 displays the temperature distributions within the structure under the different types of heat transfer in x-z cross section. There are no obvious differences in temperature distribution outside the heat source domain between the two cases, which indicates that the heat transfer is mainly in the form of conduction, and convection does not transfer much heat within the water domain. As a sense check, the Rayleigh number was another factor that we looked into. In Subsection 7.1.1, the Rayleigh number under our experimental conditions was found to be around 1.14, which is much smaller than the critical value of 1700. The confirming conduction should be dominant. The situations of heat transfer based on our experimental conditions can be concluded that the light energy was converted into heat due to the SWNT cluster absorbing the beam. The heat was then mainly transferred into the fluid field through conduction, resulting in a temperature gradient being established inside the chamber. Due to the temperature distribution, the fluid density varied in different areas, which caused a buoyancy force to be generated giving rise to natural convection flow. The laser-induced thermal conviction was not responsible for significant heat transfer.

As before, the temperature decreases with distance from the heat source (SWNT cluster) domain in all three dimensions. The temperatures inside the liquid around the cluster domain close to 100 DegC, which agrees with the real experiments. In some experiments, a few air bubbles were seen when the laser beam illuminated clusters with a similar shape and thickness to the experiments in Section 6.4, which means the temperatures around the clusters in the other experiments could be expected to be very close to the water boiling point.

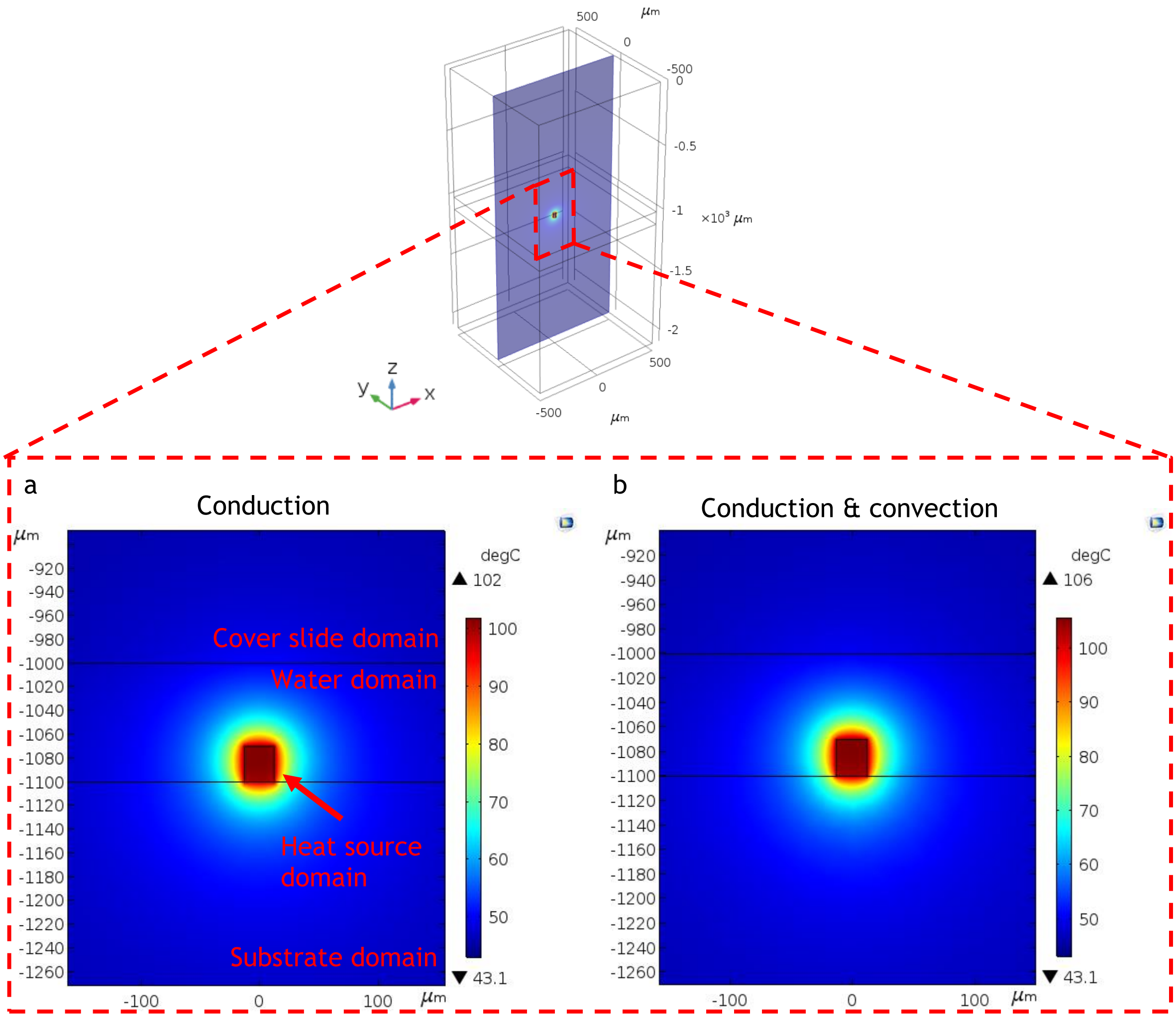

Fig. 7-10: Temperature distributions within the structure in x-z cross section under different types of heat transfer: (a) conduction, (b) conduction & convection. (Size of heat source domain (R x H): 12.5 µm x 30 µm)

It is also necessary to check the temperature gradient and the fluid flow under the steady-state condition. Fig. 7-11 shows the modelling results in the water domain in x-z cross section of the structure. As shown in Fig. 7-11 (a), the temperature gradient decreases with distance from the edges of the heat source domain in all three dimensions. Interestingly, the temperature gradients along the edges of the top surface and the bottom surface of the cluster domain are higher than for other boundaries between the domain and the water domain or the substrate domain. For the fluid flow shown in Fig. 7-11 (b - e), convection currents are generated in all three dimensions as we expected. The fast flow region (illustrated in Fig. 7-11 (c)) is shifted from the geometric centre of the water domain to the adjacent top surface edge of the cluster domain compared to Fig. 7-5, and the maximum speed is around 4.5 µm/s. Beyond this region, the flow speeds close to both the top and the bottom boundaries of the water domain decrease gradually (illustrated in Fig. 7-11 (c)), whereas the speeds decrease much faster in the vertical central area (illustrated in Fig. 7-11 (d)). Similar to Fig. 7-5, a loop of fluid flow is also created as illustrated by the red arrows, which also agrees well with the experimental phenomena described in Subsection 6.3.3. Moreover, only half of the domain is shown in the Figure due to symmetry. Fig. 7-11 (e) shows the flow directions from the top view of the substrate domain based on a xy-plane that is slightly above the substrate surface due to the presence of a boundary layer. Obviously, symmetrical convection flows are formed in all three dimensions.

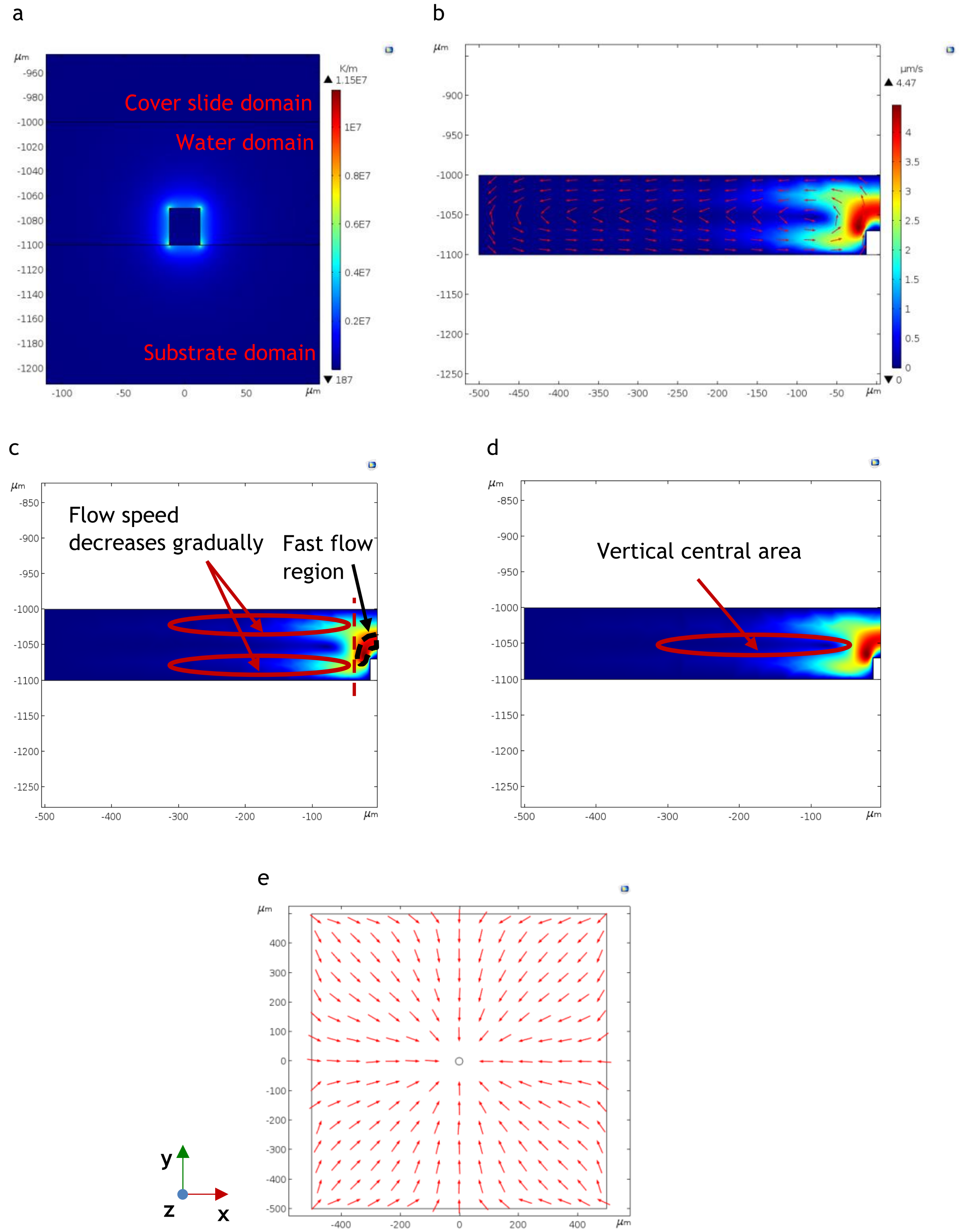

Fig. 7-11: (a) Modelling results of temperature gradient distributions in x-z cross section of the structure; (b - d) Modelling results of fluid flow velocity distributions (shown as colour background) and directions (red arrows) in x-z cross section of the water domain; (e) Modelling results of the directions of fluid flows based on a xy-plane close to the substrate viewed from the top.

According to Fig. 6-16 in Subsection 6.4.3, the average particle speed was plotted as a function of absorbed optical power at a position 75 µm away from the beam centre. By checking the experimental videos, it was verified that all particles of interest at that position moved towards the clusters. Therefore, it was concluded that the particle movements were mainly determined by the fluid convection flow at that position. Further, from the trend in Fig. 6-16, the flow speed was proportional to the absorbed optical power. The simulation was also performed with different input powers (P_0) of 1 mW, 5 mW, 10 mW, 15 mW and 20 mW. Fig. 7-12 displays the flow speed and the temperature gradient as a function of input power at points with x equals 75 µm, y equals 0 µm, and different heights above from the substrate in the z-axis. As shown in Fig. 7-12 (a), for a constant height, the flow speed is proportional to the input power, which agrees with the experimental results. Similarly, at the same input power, the flow speeds increase with height as well. Fig. 7-12 (b) shows the temperature gradient is also proportional to the input power with the same height. However, at lower input power (<10 mW), there are less obvious variations of the temperature gradients at different heights.

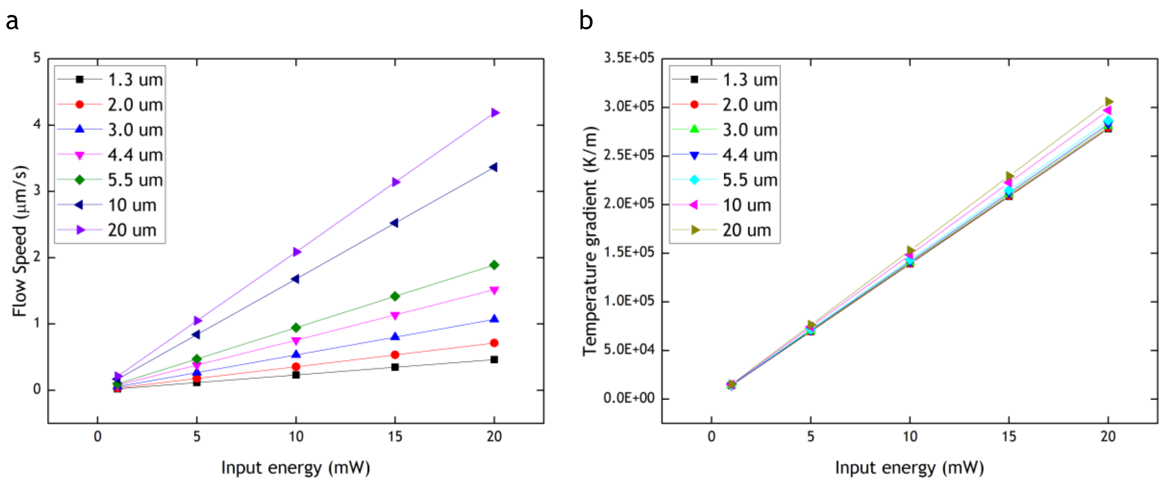

Fig. 7-12: Multiple modelling plots of (a) the fluid flow speed and (b) the temperature gradient as a function of the absorbed/input power (P_0) based on the points with same horizontal distances (75 µm) from the vertical geometric central line of the structure but different heights above the substrate domain.

The relation between the particle moving speed and the particle size was investigated in Subsection 6.4.3 with the result summarized in Fig. 6-17. From the Figure, it can be concluded that the particle moving speed increases with particle size except in the case of the smallest particle size. In order to explain the difference, four potential factors are listed in Table 6-2. The effect of the ionic strengths of the sample solutions has already been discussed. For the other three factors, the numerical model will be used to continue the analyses.

We have already shown optical power absorption exhibits a proportional trend (Fig. 7-12 (a)). Therefore, power absorption cannot explain the difference in Fig. 6-17. However, the particle speed varies with height above the substrate. Thus, another factor that may be responsible is the particle vertical suspension position in the sample chamber. In order to measure the vertical positions of particles with five different sizes, a 40x objective (NA = 0.75) was used to image the particles. A thin cover slip with thickness of 110 μm was used as the cover slide of the sample device because of the short working distance of the objective. The vertical positions of the particles were obtained by measuring the height differences between the geometric central points of the particle bodies and the top surface of the substrate by varying the position of the focal plane. Ten measurements were implemented for each particle size. The average particle vertical positions were plotted as a function of particle size, and are shown in Fig. 7-13 (a). It can be seen that the particle vertical suspension position increases with the particle size except for the case of the smallest particles, for which the position is the highest of the first three particle sizes. Here, the standard deviations of the measurements are represented as error bars shown in the plot. Some large errors in the plot may be due to the low image contrast and optical resolution of the system, which affects the accuracy of the measurements. Based on the measurement results, the true particle position for each bead size can be determined and is illustrated in Fig. 7-13 (b). Fig. 7-13 (c) displays the flow speed as a function of particle size at the corresponding suspension position. The trend of the plot is similar to the results measured from the real experiments shown in Fig. 6-17.

To investigate the effect of the SWNT cluster size, the radiuses of the clusters used in the experiments were measured using the same methods described in the last Subsection. Referring to Table 6-2, for the case of a particle size of Φ1.54 μm, the radius of the heat source domain was set as 6.5 μm, whereas it was around 12.5 μm for the other cases. Using these two values, simulations were performed separately with the same input power of 10 mW. Fig. 7-13 (c) displays the flow speed for different cluster sizes. The flow speeds with a small-size heat source are faster than those with a larger heat source except for the largest particles, in which the two data points are nearly overlapped. Therefore, it is concluded that the smallest beads move faster than larger particles because of the contributions of the particle vertical suspension position and the cluster size.

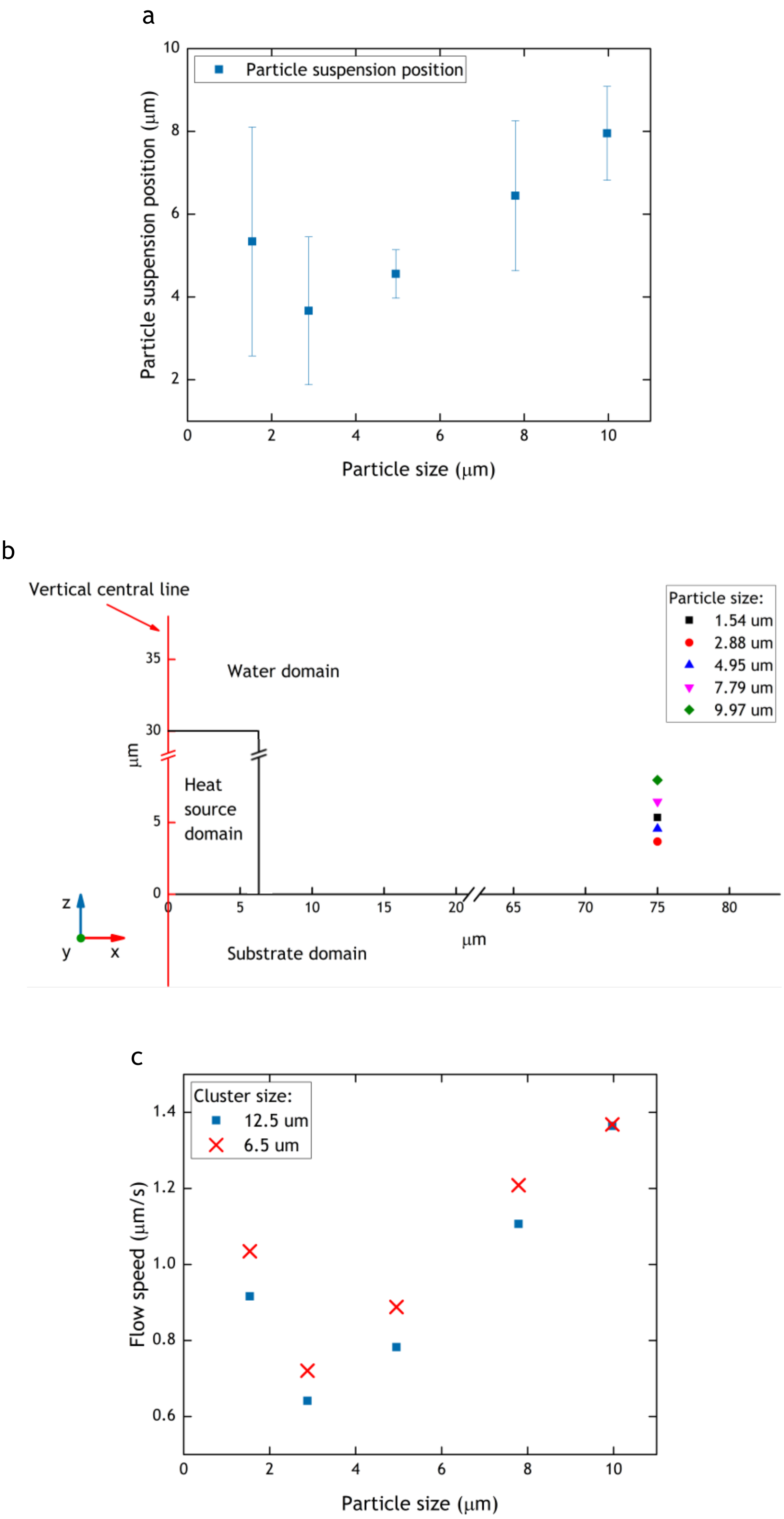

Fig. 7-13: (a) Plot of average particle suspension position in the vertical direction as a function of particle size; (b) schematic of real particle suspension plots with different particle sizes; (c) modelling results of flow speed as a function of the particle size based on the real particle suspension positions with different SWNT cluster sizes and the same optical power absorption (10 mW).

According to the trend in Fig. 6-19, the particle-stopping position increases with particle size. Here, the particles stopped moving when they experienced two balanced forces that could also be considered as two different velocities with the same magnitude but opposite directions. The fluid flow speeds and the temperature gradients can be obtained from the simulation. Therefore, it should be possible to investigate the relation between the thermophoretic mobility (D_T) and particle size. In order to identify the stopping positions for each bead size in Fig. 6-19, the average stopping positions in xy-plane were calculated from the experimental data based on the group of particle trajectories with smooth turning corners and some data, which also fell in the same distance range as the former group, from the group with sharp turning corners. The stopping positions in the vertical direction were determined based on measurements shown in Fig. 7-13 (b). According to the relation between the thermophoretic velocity and D_T (see Eq. 2-9), a plot of the thermophoretic mobility as a function of particle size with the corresponding cluster size based on the real measurements is displayed in Fig. 7-14. From the plot, it can be seen that D_T increases with particle size, following a nearly linear trend, which agrees with similar findings reported in the literature [31, 116, 172]. Here, the simulations were all performed with an input power of 10 mW.

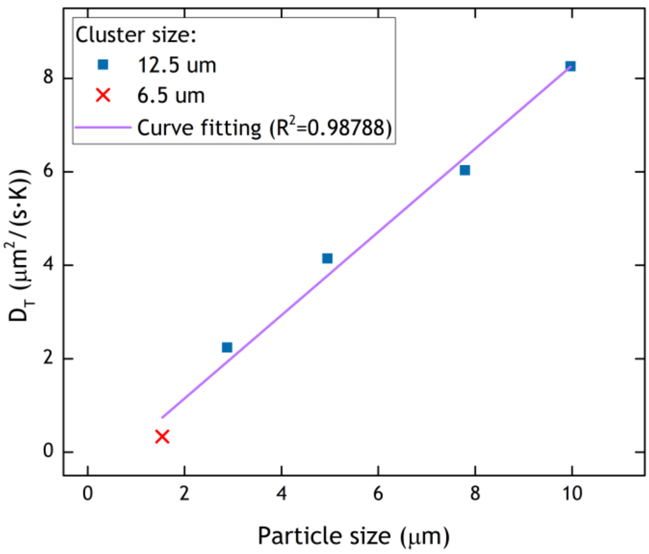

Fig. 7-14: Simulation of the thermophoretic mobility (D_T) as a function of particle size for the same optical power absorption (10 mW) based on the average particle-stopping positions measured from real experiments.

7.4 Summary

In this Chapter, numerical modelling of the experiments (Sections 6.3 and 6.4) reported in the last Chapter was performed. For a silicon substrate, by modelling the distributions of the temperature, the temperature gradient and the fluid flow, it could be confirmed that a weak symmetrical laser-induced natural convection flows were formed. By comparing the flow speed with the thermophoretic speed, the latter was always higher, which supports the hypothesis that thermophoresis is the main force contributing to the continuous movement of particles away from the hot region. For a glass substrate with the SWNT absorber, conduction was responsible for heat transfer under our experimental conditions rather than the convection current. Compared to the silicon substrate, a stronger fluid flow was generated, which supports the conclusion that the convection flow is the main force that pushed particle towards the laser beam beyond the particle-stopping region. In addition, by modelling the flow speed at different absorption powers, the simulation results agreed well with the real measurements. After taking account of the vertical positions of the particles, the simulated results of the flow speed as a function of particle size also agreed well with experimental results. The relation between the thermophoretic mobility and the particle size was derived showing a nearly linear trend, which supported the predictions in the last Chapter.

In summary, when the focused laser beam illuminates the absorbing substrate or the SWNT cluster, the light energy is absorbed and converted into heat. The heat then establishes a temperature gradient inside the chamber. Due to the temperature distribution, the fluid density varies in different areas, resulting in a buoyancy force. The areas with low densities move from high temperature regions to low temperature regions. In contrast, the areas with high densities would move in the opposite direction due to gravity. Therefore, a natural convection flow is established. Despite the presence of convection, at the low Rayleigh number operating here, heat transfer is thermal conduction dominated. Because of the temperature gradient, thermophoresis is also present. The particles inside the fluid chamber mainly experience two forces: the Stokes's drag force, which drags particles towards the optical beam, and the thermophoretic force, which pushes particles away from the hot region. The particle trajectories result from the action of the two forces.

Chapter 8

Conclusion and future directions

In this thesis, microparticle manipulation using CW and modulated diode laser has been explored and discussed. The work presented focuses on two different physical phenomena: particle manipulation by laser ultrasonics and particle manipulation by laser-induced thermal forces. This chapter summarizes the findings obtained during the research and related analysis for the physics, leading to suggestions for several potential improvements to address the limitations of our current experimental system and for an improved physical understanding of the observed phenomena.

8.1 Laser-induced SAWs detection

8.1.1 Conclusion

In the field of laser ultrasonics, it was planned to use SAWs generated by an array of diode lasers to achieve acoustic tweezing. First of all, it was necessary to assess whether the intensity of the surface waves induced by single modulated diode laser was sufficient to move particles. As described in Chapter 4, different methods and techniques were applied to both SAW generation and detection. Regarding the inspiration from the literature, it was attempted to identify SAWs by visualising the particle movements in both a single droplet and a thin fluidic chamber, and by detecting the temperature variations on the surface of the substrate based on the thermal imaging technique. However, none of the expected results was obtained from any of them when using the SAW generation methods of single spot and single line illumination. This indicates any generated waves were too weak to move particles. Therefore, our system was improved by increasing the modulation depth of the laser beam and increasing the optical intensity in the illumination region, and using approaches with higher sensitivities, namely a fibre-optic hydrophone, laser Doppler vibrometer and slanted IDT, for the detection. Meanwhile, the waves were generated by either single spot or multi-line array illumination. However, due to the physical limitations and the large noise level from the system, no obvious signals were detected. Regarding the literature, using similar experimental setups and conditions, generated SAWs were measured to be in femtometre range, which was 3 orders of magnitude smaller than the minimum displacement that could be detected by our current equipment.

The factors that affected the amplitude of the SAWs were further investigated by numerical modelling. As concluded in Chapter 5, the time constant of heat dissipation and the related deformability of the silicon substrate were predicted to be sufficient at a low light modulation repetition rate of 1 kHz. By introducing a metal thin layer on the substrate and increasing the optical intensity within the illumination region, the amplitude of the surface displacement was enhanced significantly. However, the value decreased greatly with frequency. At a frequency of 25 MHz, the model showed the amplitude of the surface displacement was reduced to 3 fm with a Mo layer, which was 5 orders of magnitude smaller than that at 1 kHz. Therefore, it could be concluded that the SAWs were generated under our experimental conditions. However, they were too weak to be detected by our current detection system.

8.1.2 Future directions

In order to achieve particle manipulation with SAWs induced by a modulated diode laser, two directions were considered to enhance the generated waves, increasing further the optical intensity in the illumination area, and increasing the modulation depth of the laser beam.

For the first direction, the solution can be achieved either by further reducing the size of illumination region through adjusting the optical system, such as using a higher magnification objective with a large numerical aperture (NA), or by further increasing the incident optical power. However, measurement of the optical power in the current incident beam showed that nearly 60% of the optical power is lost when travelling through the optical path to the sample surface. Therefore, it is necessary to improve the laser system setup by fibre-coupled laser diode. For instance, the one found in the market can delivery 10 W laser beam at wavelength of 975 nm. Alternatively, the optical power can be enhanced by using another laser diode with higher power. Furthermore, an optical amplifier could be used to increase the incident beam power at certain wavelengths.

For the second direction, the approach was to modify the LD modulation circuit. Due to the circuit board being designed and fabricated based on the surface-mount technology (SMT), the whole PCB probably needs to be redesigned and remanufactured in order to fit the new surface-mount device (SMD). Alternatively, by increasing the light absorption, the modulation depth can be deepened as well, which can be achieved using an incident beam with shorter wavelength.

In terms of SAW detection, the SNR can be increased by shortening the distance between the generation and the detection region using a fibre-optic interferometer, where it is easy to place the sensor head close to the light spot due to the small physical size. Furthermore, a homebuilt interferometer that shares the same objective would be an alternative way to detect sound waves.

If SAWs with sufficient amplitude can be generated by the above solutions, the next step will be 1D particle manipulation. The experiment could be undertaken by diverting particles with different sizes into different outlets in a microfluidic channel. A PDMS (polydimethylsiloxane) channel with two inlets and two outlets will be designed and fabricated, as shown in Fig. 8-1. Sample solution containing microparticles will be injected into the channel at an appropriate flow rate through the inlet A. The inlet B will be injected with DI water at relatively higher flow rate to create a sheath flow inside the channel. The sample flow direction is controlled by the sheath flow to ensure all particles will leave from outlet A. Here, both flows are controlled in the laminar flow region. When acoustic field is applied inside the channel, particles with large size will experience stronger acoustic radiation force (see Subsection 2.3.3), resulting in large particles move faster than small particles. Eventually, the large particles are pushed into the sheath flow region and leave from outlet B. Therefore, the particle separation is achieved. Please note that the small particles may be diverted into the sheath flow as well. However, it will take longer time for them travelling into the sheath flow. If the generated SAWs are even stronger, we also can place a glass capillary with proper dimension into the stream of the waves. The waves will penetrate into the capillary and then create standing acoustic waves, which will concentrate particles into a single line, inside the channel.

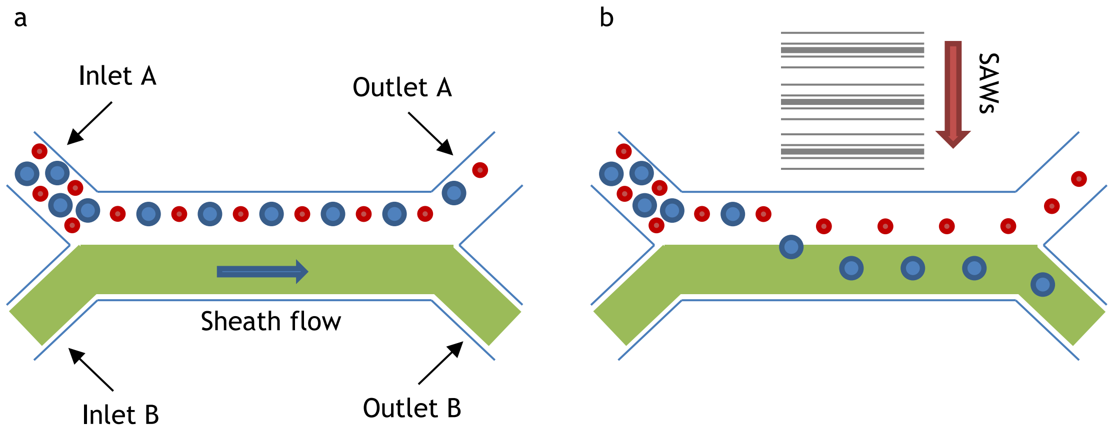

Fig. 8-1: Schematics of particle separation using laser-induced SAWs. (a) SAWs is turned off; (b) SAWs is turned on.

8.2 Microparticle manipulation by laser-induced thermal forces

8.2.1 Conclusion

In the field of laser-induced thermal forces, microparticles and biological samples were manipulated successfully in a thin fluidic chamber by the combination effect of different laser-induced thermal forces. With further investigations and relative numerical modelling, an explanation of the observed physical phenomena was put forward. As reported in Chapter 6, most of smaller beads, with Φ4.95 μm, continuously moved away from the illumination region on the silicon substrate under continuous irradiation conditions, which indicated that laser-induced thermophoresis dominated. By comparing particle-moving speeds using different materials and different incident optical powers, it was concluded that the thermophoretic mobility (D_T) increased with lower thermal conductivity of the particle, and the thermophoretic velocity increased with incident optical power. By introducing an extra light energy absorber – SWNT clusters into the sample solution, symmetrical thermal convection flows were observed, which indicated the existence of a thermal convection flow. By replacing the silicon substrate with glass, a ring shaped particle-stopping region around the beam was observed, which indicated that, for beyond the particle-stopping region, the particle movements were dominated by Stokes's drag forces arising from the convection flow, whereas for particles close to the beam, the movements were dominated by thermophretic forces arising from thermophoresis. The particle-stopping region was formed due to the two forces being balanced. By comparing the particle-moving speeds for different optical power absorptions by clusters and for different particle sizes, the characteristics of the convection flow were studied. This can be summarized as the flow speed was proportional to the energy absorption, and the particle moving speed increased with particle size, which indicated that the particle suspension height may have affected the flow speed as well. Furthermore, biological cells were manipulated successfully by our device that has good biocompatibility, which indicate this technique would be an alternative and useful tool for particle manipulation and studies in the life science field.

For better understanding of the experiments, numerical modelling was undertaken. As concluded in Chapter 7, when modelling the device using the silicon substrate without a light absorber, symmetrical convection flows arising from laser heating were formed, which could be clearly seen when a light absorber was introduced into the solution. However, the flow speed was relatively weak compared to the thermophoretic speed, which proved the particle movements were dominated by thermophoresis. When modelling the glass slide with the light absorber, by comparing temperature distributions for different types of heat transfer, the results showed heat was mainly transferred in the form of conduction within the device. By looking into the flow speed at different light powers, and for different particle sizes with related suspension heights, the simulation showed the same trend as the results from real measurements. In particular, the thermophoretic mobility shows a nearly linear increase with particle size. Therefore, it can be concluded that the dominant forces particles experienced are the Stokes's drag associated with natural convection flow and the thermophoretic force arising from the temperature gradient established by laser heating. Heat flow was always dominated by conduction at the low Reynolds number operating here. The natural convection flow was formed due to the temperature distribution established by conduction.

8.2.2 Future directions

The work presented in the thesis points in many exciting directions. In terms of further research and improvements, during the experiments, we found that it was impossible to control the size and the thickness of the SWNT clusters accurately based on the current preparation procedure, which made it difficult to reproduce the same experimental conditions. Therefore, it would be worthwhile using a CNT thin sheet fabricated based on CNT forests synthesized by the chemical vapour deposition growth [192], filtration of CNT suspension [193] or under an electric field [194]. In addition, experiments for moving different types of biological samples (such as DNA, red blood cells, etc.) can be implemented, in order to assess the performance and potential limitations of our device.

In terms of particle separation, as concluded in the previous section, D_T increases as the thermal conductivity decreases. It is therefore possible to separate particles with same size but different materials, where several concentric ring-shaped regions would be formed with particles with lowest thermal conductivity at the exterior ring and particles with highest thermal conductivity at the innermost ring. Particles with different sizes can also be separated by our device. Although both thermophoretic velocity and flow velocity increase with particle size, the rate of change of D_T is higher than that of flow velocity, which can be seen by comparing the results shown in Fig. 6-17 and Fig. 7-14, indicating several concentric particle-stopping regions are formed. Particles of different sizes will therefore stop at different distances from the laser beam, forming rings with the largest particles in the outermost ring. In terms of particle trapping and manipulation, once adding CNT thin sheet into sample solution, a spatial light modulator (SLM) could be used for structuring the incident beam with different patterns (such as rings, parallel lines, etc.), which could lead to a device capable of performing single cell trapping or patterning bio-chemical samples.

8.3 General conclusion

In conclusion, although the SAWs generated by our modulated diode laser were not strong enough to move microparticles, it is still possible to achieve the goal by using alternative approach. We have shown both microbeads and cells could be manipulated by our optical-thermophoretic tweezers, demonstrating we have developed an alternative way for moving particles with laser powers of up to 200 mW. With further improvements in the device and the system, the approach will become a useful and versatile tool for research in the bio-chemical, biology and biomedical fields, particularly for studies requiring an analysis tool that is not harmful to biological samples. Moreover, the system is easy to set up and operate, cheap and disposable, biocompatible and with the flexibility to trap and manipulate single or multiple particles.

Appendix I

Debye length

According to the experimental conditions in Subsection 6.4.3, the values of parameters used in Eq. 6-3 are listed in the following table, in order to calculate the thickness of the electrical double layer (EDL).

Dielectric constant of solvent (water at 20 DegC), ε_r	80.1
Permittivity of free space, ε_0	8.854E-12 $F \cdot m^{-1}$
Boltzmann constant, k_B	1.381E-23 $J \cdot K^{-1}$
Absolute temperature, T	293 K
Avogadro number, N_A	6.022E23 mol^{-1}
Elementary charge, e	1.602E-19 C

Appendix II

Trypan Blue protocol

The cell viability can be accurately determined by the following procedure. Cell viability is calculated as the number of viable cells divided by the total number of cells within the grids on the hemocytometer. If cells are dyed by trypan blue, they are considered non-viable.

I. Clean and sterilize the hemocytometer with 70% ethanol. Then dry it with lint free tissue.

II. Prepare a 0.4% solution of trypan blue in buffered isotonic salt solution, pH 7.2 to 7.3 (i.e., phosphate-buffered saline).

III. Add 0.1 mL of trypan blue stock solution to 0.1 mL of cell solution.

IV. Load the solution from Step III in to the hemacytometer and examine immediately under a microscope at low magnification.

V. Count the number of blue staining cells and the number of total cells. Cell viability should be at least 95% for healthy log-phase cultures.

% viable cells = [1.00 – (Number of blue cells ÷ Number of total cells)] × 100

Appendix III

Main parameter settings in modelling of laser-induced SAWs on a silicon substrate

For heat source settings		**For silicon domain**	
Average power of laser beam, Q_0	269 mW	Heat capacity, C_p	700 J/(kg·K)
Reflectance of silicon, R_c	0.32876	Density, ρ	2329 kg/m^3
Absorption coefficient of silicon, A_c	928 1/cm	Thermal conductivity, k	130 W/(m·K)
Standard deviations of the Gaussian beam in the x-direction, σ_x	6.15E-5 m	Young's modulus, E	1.70E11 Pa
Standard deviations of the Gaussian beam in the y-direction, σ_y	1.25E-3 m	Poisson's ratio, nu	0.28

For silicon domain boundaries	
Surface emissivity, ε_{Si}	0.66
Constant temperature, T_0	293.15 K

For mesh size	
Silicon domain	7 μm – 700 μm

Appendix IV

Main parameter settings in modelling of laser-induced thermal forces on a silicon substrate

For heat source domain		**For glass domain**	
Transmittance after cover slide, T_g	0.92	Heat capacity, C_p	703 J/(kg·K)
Transmittance after water domain, T_w	0.9954	Density, ρ	2203 kg/m^3
Transmittance after 50 μm in substrate, T_{50}	0.0088495	Thermal conductivity, k	1.38 W/(m·K)
Reflectance at the water-Si interface, R	0.2211		
Incident optical power, P	378 mW		

For silicon domain		**For boundary settings**	
Heat capacity, C_p	700 J/(kg·K)	Surface emissivity of water domain, ε_{water}	0.96
Density, ρ	2329 kg/m^3	Surface emissivity of glass domain, ε_{glass}	0.92
Thermal conductivity, k	130 W/(m·K)	Surface emissivity of silicon domain, ε_{Si}	0.66

For mesh size	
Water and heat source domains	2.4 μm – 56 μm
Glass domain	16 μm – 128 μm
Silicon domain	6.4 μm – 88 μm

Appendix V

Main parameter settings in modelling of laser-induced thermal forces on a glass substrate

For cover slide and substrate domain		For boundary settings	
Heat capacity, C_p	703 J/(kg·K)	Surface emissivity of water domain, ε_{water}	0.96
Density, ρ	2203 kg/m^3	Surface emissivity of glass domain, ε_{glass}	0.92
Thermal conductivity, k	1.38 W/(m·K)	Surface emissivity of heat source domain, ε_{SWNT}	0.98

For heat source domain	
Heat capacity, C_p	9.3E4 J/(kg·K)
Density, ρ	100 kg/m^3
Thermal conductivity, k	35 W/(m·K)
Input energy, P_0	1 mW, 5 mW, 10 mW, 15 mW & 20 mW

For mesh size	
Water domain	4 μm – 37 μm
Heat source domain	3.15 μm – 73.5 μm
Cover slide and substrate domains	8.4 μm – 116 μm

References

[1] D. Li, *Electrokinetics in microfluidics*. Elsevier, 2004.

[2] H. A. Pohl, "The motion and precipitation of suspensoids in divergent electric fields," *Journal of Applied Physics,* vol. 22, no. 7, pp. 869-871, 1951.

[3] A. Ashkin, J. M. Dziedzic, J. Bjorkholm, and S. Chu, "Observation of a single-beam gradient force optical trap for dielectric particles," *Optics letters,* vol. 11, no. 5, pp. 288-290, 1986.

[4] J. K. Valley, A. Jamshidi, A. T. Ohta, H.-Y. Hsu, and M. C. Wu, "Operational regimes and physics present in optoelectronic tweezers," *Journal of Microelectromechanical Systems,* vol. 17, no. 2, pp. 342-350, 2008.

[5] M. Yamada and M. Seki, "Hydrodynamic filtration for on-chip particle concentration and classification utilizing microfluidics," *Lab on a Chip,* vol. 5, no. 11, pp. 1233-1239, 2005.

[6] G. P. Hatch and R. E. Stelter, "Magnetic design considerations for devices and particles used for biological high-gradient magnetic separation (HGMS) systems," *Journal of Magnetism and Magnetic Materials,* vol. 225, no. 1-2, pp. 262-276, 2001.

[7] J. Shi, D. Ahmed, X. Mao, S. C. Lin, A. Lawit, and T. J. Huang, "Acoustic tweezers: patterning cells and microparticles using standing surface acoustic waves (SSAW)," *Lab Chip,* vol. 9, no. 20, pp. 2890-5, Oct 21 2009.

[8] X. Ding, J. Shi, S.-C. S. Lin, S. Yazdi, B. Kiraly, and T. J. Huang, "Tunable patterning of microparticles and cells using standing surface acoustic waves," *Lab on a chip,* vol. 12, no. 14, pp. 2491-2497, 2012.

[9] J. Nam, H. Lim, D. Kim, and S. Shin, "Separation of platelets from whole blood using standing surface acoustic waves in a microchannel," *Lab Chip,* vol. 11, no. 19, pp. 3361-4, Oct 7 2011.

[10] J. E. Molloy and M. J. Padgett, "Lights, action: optical tweezers," *Contemporary physics,* vol. 43, no. 4, pp. 241-258, 2002.

[11] A. Ashkin, "Optical trapping and manipulation of neutral particles using lasers," *Optics and Photonics News,* vol. 10, no. 5, p. 41, 1999.

[12] X. Zhu, H. Yi, and Z. Ni, "Frequency-dependent behaviors of individual microscopic particles in an optically induced dielectrophoresis device," *Biomicrofluidics,* vol. 4, no. 1, p. 013202, 2010.

[13] S. Lee, H. J. Park, J. S. Yoon, and K. H. Kang, "Optoelectrofluidic field separation based on light-intensity gradients," *Biomicrofluidics,* vol. 4, no. 3, p. 034102, 2010.

[14] W.-Y. Lin, Y.-H. Lin, and G.-B. Lee, "Separation of micro-particles utilizing spatial difference of optically induced dielectrophoretic forces," *Microfluidics and Nanofluidics,* vol. 8, no. 2, pp. 217-229, 2010.

[15] J. Shi, X. Mao, D. Ahmed, A. Colletti, and T. J. Huang, "Focusing microparticles in a microfluidic channel with standing surface acoustic waves (SSAW)," *Lab on a Chip,* vol. 8, no. 2, pp. 221-223, 2008.

[16] H. Lee, A. Purdon, and R. Westervelt, "Manipulation of biological cells using a microelectromagnet matrix," *Applied physics letters,* vol. 85, no. 6, pp. 1063-1065, 2004.

[17] M. Zborowski, P. S. Malchesky, T.-F. Jan, and G. S. Hall, "Quantitative separation of bacteria in saline solution using lanthanide Er (III) and a magnetic field," *Microbiology,* vol. 138, no. 1, pp. 63-68, 1992.

[18] A. Khademhosseini, M. H. May, and M. V. Sefton, "Conformal coating of mammalian cells immobilized onto magnetically driven beads," *Tissue engineering,* vol. 11, no. 11-12, pp. 1797-1806, 2005.

[19] S. Li *et al.*, "Standing surface acoustic wave (SSAW)-based cell washing," *Lab Chip,* vol. 15, no. 1, pp. 331-8, Jan 7 2015.

[20] A. A. Kolomenskii, H. Schuessler, V. Mikhalevich, and A. Maznev, "Interaction of laser-generated surface acoustic pulses with fine particles: Surface cleaning and adhesion studies," *Journal of applied physics,* vol. 84, no. 5, pp. 2404-2410, 1998.

[21] A. A. Kolomenskii and A. Maznev, "Propagation of laser-generated surface acoustic waves visualized by shake-off of fine particles," *Journal of applied physics,* vol. 77, no. 11, pp. 6052-6054, 1995.

[22] M. Braibanti, D. Vigolo, and R. Piazza, "Does thermophoretic mobility depend on particle size?," *Physical review letters,* vol. 100, no. 10, p. 108303, 2008.

[23] S. Iacopini, R. Rusconi, and R. Piazza, "The “macromolecular tourist": Universal temperature dependenceof thermal diffusion in aqueous colloidal suspensions," *The European Physical Journal E,* journal article vol. 19, no. 1, pp. 59-67, January 01 2006.

[24] P. M. Shiundu, P. S. Williams, and J. C. Giddings, "Magnitude and direction of thermal diffusion of colloidal particles measured by thermal field-flow fractionation," *Journal of colloid and interface science,* vol. 266, no. 2, pp. 366-376, 2003.

[25] S. A. Putnam, D. G. Cahill, and G. C. L. Wong, "Temperature Dependence of Thermodiffusion in Aqueous Suspensions of Charged Nanoparticles," *Langmuir,* vol. 23, no. 18, pp. 9221-9228, 2007/08/01 2007.

[26] R. Sugaya, B. A. Wolf, and R. Kita, "Thermal Diffusion of Dextran in Aqueous Solutions in the Absence and the Presence of Urea," *Biomacromolecules,* vol. 7, no. 2, pp. 435-440, 2006/02/01 2006.

[27] R. Kita, G. Kircher, and S. Wiegand, "Thermally induced sign change of Soret coefficient for dilute and semidilute solutions of poly (N-isopropylacrylamide) in ethanol," *The Journal of chemical physics,* vol. 121, no. 18, pp. 9140-9146, 2004.

[28] D. Vigolo, S. Buzzaccaro, and R. Piazza, "Thermophoresis and thermoelectricity in surfactant solutions," *Langmuir,* vol. 26, no. 11, pp. 7792-7801, 2010.

[29] R. Piazza, "Thermophoresis: moving particles with thermal gradients," *Soft Matter,* vol. 4, no. 9, pp. 1740-1744, 2008.

[30] S. A. Putnam and D. G. Cahill, "Transport of nanoscale latex spheres in a temperature gradient," *Langmuir,* vol. 21, no. 12, pp. 5317-5323, 2005.

[31] S. Duhr and D. Braun, "Why molecules move along a temperature gradient," *Proceedings of the National Academy of Sciences,* vol. 103, no. 52, pp. 19678-19682, 2006.

[32] L. Lin, X. Peng, Z. Mao, X. Wei, C. Xie, and Y. Zheng, "Interfacial-entropy-driven thermophoretic tweezers," *Lab on a Chip,* vol. 17, no. 18, pp. 3061-3070, 2017.

[33] E. Flores-Flores *et al.*, "Trapping and manipulation of microparticles using laser-induced convection currents and photophoresis," *Biomedical optics express,* vol. 6, no. 10, pp. 4079-4087, 2015.

[34] T. Murray, O. Balogun, and N. Pratt, "High Frequency Laser Based Acoustic Microscopy Using a CW Generation Source," in *16th World Conference on Nondestructive Testing, Montreal, Canada*, 2004: Citeseer.

[35] T. Murray and O. Balogun, "High-sensitivity laser-based acoustic microscopy using a modulated excitation source," *Applied Physics Letters,* vol. 85, no. 14, pp. 2974-2976, 2004.

[36] S. Pierce, B. Culshaw, and Q. Shan, "Laser generation of ultrasound using a modulated continuous wave laser diode," *Applied Physics Letters,* vol. 72, no. 9, pp. 1030-1032, 1998.

[37] H. Takamatsu, Y. Nishimoto, and Y. Nakai, "Photodisplacement measurement by interferometric laser probe," *Japanese Journal of Applied Physics,* vol. 29, no. 12R, p. 2847, 1990.

[38] D. Braun and A. Libchaber, "Trapping of DNA by thermophoretic depletion and convection," *Physical review letters,* vol. 89, no. 18, p. 188103, 2002.

[39] S. Duhr, S. Arduini, and D. Braun, "Thermophoresis of DNA determined by microfluidic fluorescence," *The European Physical Journal E,* vol. 15, no. 3, pp. 277-286, 2004.

[40] S. Duhr and D. Braun, "Optothermal molecule trapping by opposing fluid flow with thermophoretic drift," *Physical review letters,* vol. 97, no. 3, p. 038103, 2006.

[41] V. Garcés-Chávez, R. Quidant, P. Reece, G. Badenes, L. Torner, and K. Dholakia, "Extended organization of colloidal microparticles by surface plasmon polariton excitation," *Physical Review B,* vol. 73, no. 8, p. 085417, 2006.

[42] R. Ellwood, "The effect of microstructure and fatigue on the acoustoelastic response of aerospace materials," Ph.D. thesis, Department of Electrical and Electronic Engineering, University of Nottingham, Nottingham, 2012.

[43] K. Länge, B. E. Rapp, and M. Rapp, "Surface acoustic wave biosensors: a review," *Analytical and bioanalytical chemistry,* vol. 391, no. 5, pp. 1509-1519, 2008.

[44] G. Hübschen, I. Altpeter, R. Tschuncky, and H.-G. Herrmann, *Materials characterization using Nondestructive Evaluation (NDE) methods*. Woodhead Publishing, 2016.

[45] D. Cook and Y. Berthelot, "Detection of small surface-breaking fatigue cracks in steel using scattering of Rayleigh waves," *NDT & E International,* vol. 34, no. 7, pp. 483-492, 2001.

[46] Q. Shan and R. Dewhurst, "Surface-breaking fatigue crack detection using laser ultrasound," *Applied Physics Letters,* vol. 62, no. 21, pp. 2649-2651, 1993.

[47] M. G. Somekh, M. Liu, H. P. Ho, and C. W. See, "An accurate non-contacting laser based system for surface wave velocity measurement," *Measurement Science and Technology,* vol. 6, no. 9, p. 1329, 1995.

[48] G. Gerhart, "Rayleigh wave velocity for a stress-induced slightly anisotropic solid," *The Journal of the Acoustical Society of America,* vol. 60, no. 5, pp. 1085-1088, 1976.

[49] M. Duqennoy, M. Ouaftouh, and M. Ourak, "Determination of stresses in aluminium alloy using optical detection of Rayleigh waves," *Ultrasonics,* vol. 37, no. 5, pp. 365-372, 1999.

[50] B. Mi, J. E. Michaels, and T. E. Michaels, "An ultrasonic method for dynamic monitoring of fatigue crack initiation and growth," *The Journal of the Acoustical Society of America,* vol. 119, no. 1, pp. 74-85, 2006.

[51] P. Warren, C. Pecorari, O. Kolosov, S. Roberts, and G. Briggs, "Characterization of surface damage via surface acoustic waves," *Nanotechnology,* vol. 7, no. 3, p. 295, 1996.

[52] I. Pape *et al.*, "Evaluation of polishing damage in alumina," *Philosophical Magazine A*, vol. 80, no. 8, pp. 1913-1934, 2000.

[53] S. D. Sharples, M. Clark, and M. G. Somekh, "Fast noncontact imaging of material microstructure using local surface acoustic wave velocity mapping," in *IEEE International Ultrasonics Symposium, vols*, 2005, pp. 1-4.

[54] M. Clark, S. Sharples, and M. Somekh, "Non-contact acoustic microscopy," *Measurement Science and Technology*, vol. 11, no. 12, p. 1792, 2000.

[55] M. Clark, S. D. Sharples, and M. G. Somekh, "Fast, all-optical Rayleigh wave microscope: Imaging on isotropic and anisotropic materials," *Ultrasonics, Ferroelectrics, and Frequency Control, IEEE Transactions on*, vol. 47, no. 1, pp. 65-74, 2000.

[56] W. Li, S. D. Sharples, M. Clark, and M. G. Somekh, "Frequency spectrum spatially resolved acoustic spectroscopy for microstructure imaging," in *Ultrasonics Symposium (IUS), 2009 IEEE International*, 2009, pp. 791-794: IEEE.

[57] B. Jakoby and M. J. Vellekoop, "Properties of Love waves: applications in sensors," *Smart materials and structures*, vol. 6, no. 6, p. 668, 1997.

[58] C. J. Ammon. *Seismic Waves and Earth's Interior*. Available: http://eqseis.geosc.psu.edu/~cammon/HTML/Classes/IntroQuakes/Notes/waves_and_interior.html

[59] J. Du, G. Harding, J. A. Ogilvy, P. Dencher, and M. Lake, "A study of Love-wave acoustic sensors," *Sensors and Actuators A: Physical*, vol. 56, no. 3, pp. 211-219, 1996.

[60] T. Hayashi and K. Kawashima, "Multiple reflections of Lamb waves at a delamination," *Ultrasonics*, vol. 40, no. 1, pp. 193-197, 2002.

[61] J. Tian, U. Gabbert, H. Berger, and X. Su, *Lamb wave interaction with delaminations in CFRP laminates*. Univ., Fak. für Maschinenbau, 2001.

[62] W. Staszewski, B. Lee, and R. Traynor, "Fatigue crack detection in metallic structures with Lamb waves and 3D laser vibrometry," *Measurement Science and Technology*, vol. 18, no. 3, p. 727, 2007.

[63] S. Grondel, C. Delebarre, J. Assaad, J.-P. Dupuis, and L. Reithler, "Fatigue crack monitoring of riveted aluminium strap joints by Lamb wave analysis and acoustic emission measurement techniques," *Ndt & E International*, vol. 35, no. 3, pp. 137-146, 2002.

[64] C. B. Scruby and L. E. Drain, *Laser ultrasonics techniques and applications*. CRC Press, 1990.

[65] J. Padilla-Martinez, C. Berrospe-Rodriguez, G. Aguilar, J. Ramirez-San-Juan, and R. Ramos-Garcia, "Optic cavitation with CW lasers: A review," *Physics of Fluids*, vol. 26, no. 12, p. 122007, 2014.

[66] H. W. Baac *et al.*, "Carbon-nanotube optoacoustic lens for focused ultrasound generation and high-precision targeted therapy," *Scientific reports*, vol. 2, p. 989, 2012.

[67] T.-T. Wu and Y.-H. Liu, "Inverse determinations of thickness and elastic properties of a bonding layer using laser-generated surface waves," *Ultrasonics*, vol. 37, no. 1, pp. 23-30, 1999.

[68] A. Lomonosov, V. Mikhalevich, P. Hess, E. Y. Knight, M. Hamilton, and E. Zabolotskaya, "Laser-generated nonlinear Rayleigh waves with shocks," *The Journal of the Acoustical Society of America*, vol. 105, no. 4, pp. 2093-2096, 1999.

[69] A. Aindow, R. Dewhurst, and S. Palmer, "Laser-generation of directional surface acoustic wave pulses in metals," *Optics communications*, vol. 42, no. 2, pp. 116-120, 1982.

[70] A. Murfin, R. Soden, D. Hatrick, and R. J. Dewhurst, "Laser-ultrasound detection systems: a comparative study with Rayleigh waves," *Measurement Science and Technology,* vol. 11, no. 8, p. 1208, 2000.

[71] H. Coufal, R. Grygier, P. Hess, and A. Neubrand, "Broadband detection of laser-excited surface acoustic waves by a novel transducer employing ferroelectric polymers," *The Journal of the Acoustical Society of America,* vol. 92, no. 5, pp. 2980-2983, 1992.

[72] A. Neubrand and P. Hess, "Laser generation and detection of surface acoustic waves: Elastic properties of surface layers," *Journal of Applied Physics,* vol. 71, no. 1, pp. 227-238, 1992.

[73] P. Doyle and C. Scala, "Near-field ultrasonic Rayleigh waves from a laser line source," *Ultrasonics,* vol. 34, no. 1, pp. 1-8, 1996.

[74] J. Huang, S. Krishnaswamy, and J. D. Achenbach, "Laser generation of narrow-band surface waves," *The Journal of the Acoustical Society of America,* vol. 92, no. 5, pp. 2527-2531, 1992.

[75] F. L. Di Scalea, T. P. Berndt, J. B. Spicer, and B. B. Djordjevic, "Remote laser generation of narrow-band surface waves through optical fibers," *Ultrasonics, Ferroelectrics, and Frequency Control, IEEE Transactions on,* vol. 46, no. 6, pp. 1551-1557, 1999.

[76] A. McKie, J. Wagner, J. Spicer, and C. Penney, "Laser generation of narrow-band and directed ultrasound," *Ultrasonics,* vol. 27, no. 6, pp. 323-330, 1989.

[77] S. Kenderian, B. B. Djordjevic, and R. E. Green Jr, "Narrow band laser-generated surface acoustic waves using a formed source in the ablative regime," *The Journal of the Acoustical Society of America,* vol. 113, no. 1, pp. 261-266, 2003.

[78] A. Maznev, A. Mazurenko, L. Zhuoyun, and M. Gostein, "Laser-based surface acoustic wave spectrometer for industrial applications," *Review of scientific instruments,* vol. 74, no. 1, pp. 667-669, 2003.

[79] A. Harata, H. Nishimura, and T. Sawada, "Laser-induced surface acoustic waves and photothermal surface gratings generated by crossing two pulsed laser beams," *Applied physics letters,* vol. 57, no. 2, pp. 132-134, 1990.

[80] C. Edwards, A. Bushell, S. B. Palmer, and H. Nakano, "Laser interference grating for surface wave generation," *Nondestructive Testing and Evaluation,* vol. 10, no. 1, pp. 15-23, 1992.

[81] H. Nishino, Y. Tsukahara, Y. Nagata, T. Koda, and K. Yamanaka, "Excitation of high frequency surface acoustic waves by phase velocity scanning of a laser interference fringe," *Applied physics letters,* vol. 62, no. 17, pp. 2036-2038, 1993.

[82] T. Murray, J. Deaton, and J. Wagner, "Experimental evaluation of enhanced generation of ultrasonic waves using an array of laser sources," *Ultrasonics,* vol. 34, no. 1, pp. 69-77, 1996.

[83] T. Stratoudaki, M. Clark, and M. G. Somekh, "Novel optical transducers for non-linear ultrasonic applications," in *Proceedings of ECNDT*, 2006.

[84] T. Stratoudaki, J. A. Hernandez, M. Clark, and M. G. Somekh, "Cheap optical transducers (CHOTs) for narrowband ultrasonic applications," *Measurement Science and Technology,* vol. 18, no. 3, pp. 843-851, 2007.

[85] I. J. Collison, T. Stratoudaki, M. Clark, and M. G. Somekh, "Measurement of elastic nonlinearity using remote laser ultrasonics and CHeap Optical Transducers and dual frequency surface acoustic waves," *Ultrasonics,* vol. 48, no. 6-7, pp. 471-7, Nov 2008.

[86] O. Manneberg, B. Vanherberghen, B. Onfelt, and M. Wiklund, "Flow-free transport of cells in microchannels by frequency-modulated ultrasound," *Lab Chip,* vol. 9, no. 6, pp. 833-7, Mar 21 2009.

[87] M. Wiklund, C. Gunther, R. Lemor, M. Jager, G. Fuhr, and H. M. Hertz, "Ultrasonic standing wave manipulation technology integrated into a dielectrophoretic chip," *Lab Chip,* vol. 6, no. 12, pp. 1537-44, Dec 2006.

[88] B. Vanherberghen *et al.*, "Ultrasound-controlled cell aggregation in a multi-well chip," *Lab Chip,* vol. 10, no. 20, pp. 2727-32, Oct 21 2010.

[89] A. Nilsson, F. Petersson, H. Jonsson, and T. Laurell, "Acoustic control of suspended particles in micro fluidic chips," *Lab Chip,* vol. 4, no. 2, pp. 131-5, Apr 2004.

[90] F. Petersson, A. Nilsson, H. Jönsson, and T. Laurell, "Carrier medium exchange through ultrasonic particle switching in microfluidic channels," *Analytical chemistry,* vol. 77, no. 5, pp. 1216-1221, 2005.

[91] F. Petersson, L. Åberg, A.-M. Swärd-Nilsson, and T. Laurell, "Free flow acoustophoresis: microfluidic-based mode of particle and cell separation," *Analytical chemistry,* vol. 79, no. 14, pp. 5117-5123, 2007.

[92] F. Petersson, A. Nilsson, C. Holm, H. Jonsson, and T. Laurell, "Separation of lipids from blood utilizing ultrasonic standing waves in microfluidic channels," *Analyst,* vol. 129, no. 10, pp. 938-43, Oct 2004.

[93] J. Shi, H. Huang, Z. Stratton, Y. Huang, and T. J. Huang, "Continuous particle separation in a microfluidic channel via standing surface acoustic waves (SSAW)," *Lab Chip,* vol. 9, no. 23, pp. 3354-9, Dec 7 2009.

[94] J. Shi *et al.*, "Three-dimensional continuous particle focusing in a microfluidic channel via standing surface acoustic waves (SSAW)," *Lab Chip,* vol. 11, no. 14, pp. 2319-24, Jul 21 2011.

[95] S. Tyagi and V. G. Mahesh, "Saw And Interdigital Transducers," *International Journal of Scientific and Engineering Research,* vol. 3, no. 12, pp. 1141-1144, 2012.

[96] X. Ding *et al.*, "Standing surface acoustic wave (SSAW) based multichannel cell sorting," *Lab on a chip,* vol. 12, no. 21, pp. 4228-4231, 2012.

[97] J. Nam, Y. Lee, and S. Shin, "Size-dependent microparticles separation through standing surface acoustic waves," *Microfluidics and Nanofluidics,* vol. 11, no. 3, pp. 317-326, 2011.

[98] J. Nam, H. Lim, C. Kim, J. Yoon Kang, and S. Shin, "Density-dependent separation of encapsulated cells in a microfluidic channel by using a standing surface acoustic wave," *Biomicrofluidics,* vol. 6, no. 2, pp. 24120-2412010, Jun 2012.

[99] X. Ding *et al.*, "Cell separation using tilted-angle standing surface acoustic waves," *Proceedings of the National Academy of Sciences,* vol. 111, no. 36, pp. 12992-12997, 2014.

[100] S. Li *et al.*, "An on-chip, multichannel droplet sorter using standing surface acoustic waves," *Anal Chem,* vol. 85, no. 11, pp. 5468-74, Jun 4 2013.

[101] C. Witte, "Micromanipulation in microfluidics using optoelectronic and acoustic tweezing," Ph.D. thesis, University of Glasgow, 2015.

[102] S. Li *et al.*, "Standing surface acoustic wave based cell coculture," *Anal Chem,* vol. 86, no. 19, pp. 9853-9, Oct 7 2014.

[103] S. Toru, M. Frénéa-Robin, N. Haddour, and F. Buret, "Tunable and label-free bacteria alignment using standing surface acoustic waves," in *Engineering in Medicine and Biology Society (EMBC), 2012 Annual International Conference of the IEEE*, 2012, pp. 4998-5001: IEEE.

[104] F. M. Phillips and M. C. Castro, "5.15 - Groundwater Dating and Residence-time Measurements," in *Treatise on Geochemistry*, H. D. Holland and K. K. Turekian, Eds. Oxford: Pergamon, 2003, pp. 451-497.

[105] D. Bennett. (2017). *The Difference between Convection & Advection Heat Transfers*. Available: https://sciencing.com/difference-convection-advection-heat-transfers-8479535.html

[106] *CONVECTION*. Available: http://www.scienceclarified.com/everyday/Real-Life-Chemistry-Vol-7/Convection.html

[107] D. Annaratone, *Engineering Heat Transfer*. Springer, 2010.

[108] T. Henderson. (1996-2018). *Methods of Heat Transfer*. Available: http://www.physicsclassroom.com/class/thermalP/Lesson-1/Methods-of-Heat-Transfer

[109] E. L. Koschmieder, *Bénard cells and Taylor vortices*. Cambridge University Press, 1993.

[110] A. V. Getling, *Rayleigh-B nard Convection: Structures and Dynamics*. World Scientific, 1998.

[111] A. S. Engineering. *Thermophoresis*. Available: https://aerosol.ees.ufl.edu/Thermophoresis/section01.html

[112] D. Bedeaux, S. Kjelstrup, and J. Sengers, *Experimental Thermodynamics Volume X: Non-equilibrium Thermodynamics with Applications*. Royal Society of Chemistry, 2015.

[113] A. Parola and R. Piazza, "Particle thermophoresis in liquids," *The European Physical Journal E*, vol. 15, no. 3, pp. 255-263, 2004.

[114] R. Piazza and A. Parola, "Thermophoresis in colloidal suspensions," *Journal of Physics: Condensed Matter*, vol. 20, no. 15, p. 153102, 2008.

[115] D. Vigolo, R. Rusconi, H. A. Stone, and R. Piazza, "Thermophoresis: microfluidics characterization and separation," *Soft Matter*, vol. 6, no. 15, pp. 3489-3493, 2010.

[116] S. Duhr and D. Braun, "Thermophoretic depletion follows Boltzmann distribution," *Physical review letters*, vol. 96, no. 16, p. 168301, 2006.

[117] S.R. De Groot and P. Mazur, *Non-equilibrium thermodynamics*. Netherlands: Noth-Holland Publishing Co., Amsterdam, 1962.

[118] D. D. Fitts, *Nonequilibrium thermodynamics: a phenomenological theory of irreversible processes in fluid systems*. McGraw-Hill New York, 1962.

[119] Y. Lamhot, A. Barak, O. Peleg, and M. Segev, "Self-trapping of optical beams through thermophoresis," *Physical review letters*, vol. 105, no. 16, p. 163906, 2010.

[120] K. Morozov, "FLUIDS-Thermal diffusion in disperse systems," *Journal of Experimental and Theoretical Physics*, vol. 88, no. 5, pp. 944-946, 1999.

[121] S. N. Rasuli and R. Golestanian, "Soret motion of a charged spherical colloid," *Physical review letters*, vol. 101, no. 10, p. 108301, 2008.

[122] A. Würger, "Thermal non-equilibrium transport in colloids," *Reports on Progress in Physics*, vol. 73, no. 12, p. 126601, 2010.

[123] A. Würger, "Transport in charged colloids driven by thermoelectricity," *Physical review letters*, vol. 101, no. 10, p. 108302, 2008.

[124] G. Guthrie Jr, J. N. Wilson, and V. Schomaker, "Theory of the thermal diffusion of electrolytes in a Clusius column," *The Journal of Chemical Physics*, vol. 17, no. 3, pp. 310-313, 1949.

[125] P. O. Staffeld and J. A. Quinn, "Diffusion-induced banding of colloid particles via diffusiophoresis: 2. Non-electrolytes," *Journal of colloid and interface science*, vol. 130, no. 1, pp. 88-100, 1989.

[126] H.-R. Jiang, H. Wada, N. Yoshinaga, and M. Sano, "Manipulation of colloids by a nonequilibrium depletion force in a temperature gradient," *Physical review letters,* vol. 102, no. 20, p. 208301, 2009.

[127] Y. Zhou, C. Yang, and Y. C. Lam, "Experimental Methods of Thermophoresis in Liquids," *Encyclopedia of Microfluidics and Nanofluidics,* pp. 1-11, 2013.

[128] Y. Zhao, C. Zhao, J. He, Y. Zhou, and C. Yang, "Collective effects on thermophoresis of colloids: a microfluidic study within the framework of DLVO theory," *Soft Matter,* vol. 9, no. 32, pp. 7726-7734, 2013.

[129] A. Macleod, "Optical Absorption | Part 1," in *SVC Bulletin 2013 Technical Conference Review*, 2013, pp. 24-31: Society of Vacuum Coaters (SVC™).

[130] H. A. Macleod and H. A. Macleod, *Thin-film optical filters*. CRC press, 2010.

[131] G. Cox, *Optical imaging techniques in cell biology*. CRC Press, 2012.

[132] *Reflected Light Microscopy*. Available: http://zeiss-campus.magnet.fsu.edu/articles/basics/reflected.html

[133] A. H. Jeorrett *et al.*, "Optoelectronic tweezers system for single cell manipulation and fluorescence imaging of live immune cells," *Optics express,* vol. 22, no. 2, pp. 1372-1380, 2014.

[134] M.-C. Tien, A. T. Ohta, K. Yu, S. L. Neale, and M. C. Wu, "Heterogeneous integration of InGaAsP microdisk laser on a silicon platform using optofluidic assembly," *Applied Physics A,* vol. 95, no. 4, pp. 967-972, 2009.

[135] H. Li, J. R. Friend, and L. Y. Yeo, "Microfluidic colloidal island formation and erasure induced by surface acoustic wave radiation," *Physical review letters,* vol. 101, no. 8, p. 084502, 2008.

[136] X. Du *et al.*, "Surface acoustic wave induced streaming and pumping in 128 Y-cut LiNbO3 for microfluidic applications," *Journal of Micromechanics and Microengineering,* vol. 19, no. 3, p. 035016, 2009.

[137] H. Li, J. R. Friend, and L. Y. Yeo, "Surface acoustic wave concentration of particle and bioparticle suspensions," *Biomedical microdevices,* vol. 9, no. 5, pp. 647-656, 2007.

[138] R. Wilson, J. Reboud, Y. Bourquin, S. L. Neale, Y. Zhang, and J. M. Cooper, "Phononic crystal structures for acoustically driven microfluidic manipulations," *Lab on a Chip,* vol. 11, no. 2, pp. 323-328, 2011.

[139] P. R. Rogers, J. R. Friend, and L. Y. Yeo, "Exploitation of surface acoustic waves to drive size-dependent microparticle concentration within a droplet," *Lab on a Chip,* vol. 10, no. 21, pp. 2979-2985, 2010.

[140] Z. v. Guttenberg *et al.*, "Flow profiling of a surface-acoustic-wave nanopump," *Physical Review E,* vol. 70, no. 5, p. 056311, 2004.

[141] T. Franke, A. R. Abate, D. A. Weitz, and A. Wixforth, "Surface acoustic wave (SAW) directed droplet flow in microfluidics for PDMS devices," *Lab on a Chip,* vol. 9, no. 18, pp. 2625-2627, 2009.

[142] T. Franke, S. Braunmüller, L. Schmid, A. Wixforth, and D. Weitz, "Surface acoustic wave actuated cell sorting (SAWACS)," *Lab on a Chip,* vol. 10, no. 6, pp. 789-794, 2010.

[143] C. Witte, J. Reboud, R. Wilson, J. Cooper, and S. Neale, "Microfluidic resonant cavities enable acoustophoresis on a disposable superstrate," *Lab on a Chip,* vol. 14, no. 21, pp. 4277-4283, 2014.

[144] D. Fitzpatrick, *Analog Design and Simulation Using OrCAD Capture and PSpice*. Elsevier, 2012.

[145] M. H. Rashid, *SPICE for Circuits and Electronics Using PSpice*. Prentice Hall, 1995.

[146] P. W. Tuinenga, *Spice: A Guide to Circuit Simulation and Analysis Using PSpice*. Prentice Hall, 1995.

[147] *Photodiode Tutorial*. Available: https://www.thorlabs.com/tutorials.cfm?tabID=31760

[148] P. C. Beard, A. M. Hurrell, and T. N. Mills, "Characterization of a polymer film optical fiber hydrophone for use in the range 1 to 20 MHz: A comparison with PVDF needle and membrane hydrophones," *Ultrasonics, Ferroelectrics, and Frequency Control, IEEE Transactions on,* vol. 47, no. 1, pp. 256-264, 2000.

[149] P. Morris, A. Hurrell, and P. Beard, "Development of a 50MHz Fabry-Perot type fibre-optic hydrophone for the characterisation of medical ultrasound fields," 2006.

[150] B. Cox, E. Zhang, J. Laufer, and P. Beard, "Fabry Perot polymer film fibre-optic hydrophones and arrays for ultrasound field characterisation," in *Journal of Physics: Conference Series*, 2004, vol. 1, no. 1, p. 32: IOP Publishing.

[151] P. Morris, A. Hurrell, A. Shaw, E. Zhang, and P. Beard, "A Fabry–Pérot fiber-optic ultrasonic hydrophone for the simultaneous measurement of temperature and acoustic pressure," *The Journal of the Acoustical Society of America,* vol. 125, no. 6, pp. 3611-3622, 2009.

[152] P. Beard and T. Mills, "Miniature optical fibre ultrasonic hydrophone using a Fabry-Perot polymer film interferometer," *Electronics Letters,* vol. 33, no. 9, pp. 801-802, 1997.

[153] "User Manual," in *Fiber-coupled Vibrometer Sensor Head OFV-534*, ed: Polytec GmbH.

[154] "2.4.1 The speed and attenuation of sound," Tables of Physical & Chemical Constants (16th edition 1995)Version 1.0 ed.: Kaye & Laby Online, 2005. [Online]. Available: http://www.kayelaby.npl.co.uk/.

[155] J. Mazumder and W. Steen, "Heat transfer model for CW laser material processing," *Journal of Applied Physics,* vol. 51, no. 2, pp. 941-947, 1980.

[156] J. Moody and R. Hendel, "Temperature profiles induced by a scanning cw laser beam," *Journal of Applied Physics,* vol. 53, no. 6, pp. 4364-4371, 1982.

[157] K. J. Suthar, J. Patten, L. Dong, and H. Abdel-Aal, "Estimation of temperature distribution in silicon during micro laser assisted machining," in *ASME 2008 International Manufacturing Science and Engineering Conference collocated with the 3rd JSME/ASME International Conference on Materials and Processing*, 2008, pp. 301-309: American Society of Mechanical Engineers.

[158] S. T. Yang *et al.*, "Comparing the use of mid-infrared versus far-infrared lasers for mitigating damage growth on fused silica," *Applied Optics,* vol. 49, no. 14, pp. 2606-2616, 2010.

[159] M. N. Polyanskiy. *Refractive index database*. Available: https://refractiveindex.info

[160] G. R. Center, "Reynolds number," ed: NASA.

[161] G. Falkovich, "Fluid Mechanics," *Fluid Mechanics, by Gregory Falkovich, Cambridge, UK: Cambridge University Press, 2011,* 2011.

[162] A. Sommerfeld, "Ein beitrag zur hydrodynamischen erklaerung der turbulenten fluessigkeitsbewegungen," *Atti del,* vol. 4, pp. 116-124, 1908.

[163] G. K. Batchelor, *An introduction to fluid dynamics*. Cambridge university press, 2000.

[164] S. Kim and S. J. Karrila, *Microhydrodynamics: principles and selected applications*. Courier Corporation, 2013.

[165] B. J. Kirby, *Micro-and nanoscale fluid mechanics: transport in microfluidic devices*. Cambridge university press, 2010.

[166] J. O. M. Bockris and S. U. Khan, *Surface electrochemistry: a molecular level approach*. Springer Science & Business Media, 2013.

[167] P. Ghosh, "Electrostatic Double Layer Force: Part II." Department of Chemical Engineering

IIT Guwahati, Guwahati

[168] M. Nakamura, N. Sato, N. Hoshi, and O. Sakata, "Outer Helmholtz plane of the electrical double layer formed at the solid electrode-liquid interface," *ChemPhysChem,* vol. 12, no. 8, pp. 1430-1434, 2011.

[169] Z. Stojek, "The electrical double layer and its structure," in *Electroanalytical methods*: Springer, 2010, pp. 3-9.

[170] M. E. Schimpf and S. N. Semenov, "Mechanism of polymer thermophoresis in nonaqueous solvents," *The Journal of Physical Chemistry B,* vol. 104, no. 42, pp. 9935-9942, 2000.

[171] H. Brenner, "Navier–Stokes revisited," *Physica A: Statistical Mechanics and its Applications,* vol. 349, no. 1-2, pp. 60-132, 2005.

[172] R. T. Schermer, C. C. Olson, J. P. Coleman, and F. Bucholtz, "Laser-induced thermophoresis of individual particles in a viscous liquid," *Optics express,* vol. 19, no. 11, pp. 10571-10586, 2011.

[173] L. M. Jiji and SpringerLink, *Heat conduction*, 3rd ed. (no. Book, Whole). London;Berlin;: Springer, 2009.

[174] K. A. Eslahian, A. Majee, M. Maskos, and A. Würger, "Specific salt effects on thermophoresis of charged colloids," *Soft Matter,* vol. 10, no. 12, pp. 1931-1936, 2014.

[175] A. S. Song, A. M. Najjar, and K. R. Diller, "Thermally Induced Apoptosis, Necrosis, and Heat Shock Protein Expression in Three-Dimensional Culture," *Journal of biomechanical engineering,* vol. 136, no. 7, p. 071006, 2014.

[176] D. J. Inman, *Engineering Vibration*. Prentice Hall, 2001.

[177] I. Akimoto, K. Maeda, and N. Ozaki, "Hydrogen generation by laser irradiation of carbon powder in water," *The Journal of Physical Chemistry C,* vol. 117, no. 36, pp. 18281-18285, 2013.

[178] I. Akimoto, S. Yamamoto, and K. Maeda, "White-light emission from solid carbon in aqueous solution during hydrogen generation induced by nanosecond laser pulse irradiation," *Applied Physics A,* vol. 122, no. 7, p. 675, 2016.

[179] K. Maeda, N. Ozaki, and I. Akimoto, "Alcohol additive effect in hydrogen generation from water with carbon by photochemical reaction," *Japanese Journal of Applied Physics,* vol. 53, no. 5S1, p. 05FZ03, 2014.

[180] R. B. Bird, W. E. Stewart, and E. N. Lightfoot, "Transport Phenomena; 2001 John Wiley and Sons," ed: New York, 2002.

[181] S. Chandrasekhar, "Hydrodynamic and Hydromagnetic Stability (London: Oxford University) 429 Chap," ed: VIII, 1961.

[182] M. Favre-Marinet and S. Tardu, *Convective Heat Transfer: Solved Problems*. John Wiley & Sons, 2013.

[183] R. Sinnot, *Coulson & Richardson's chemical engineering*. Pergamon, 1993.

[184] M. A. Green and M. J. Keevers, "Optical properties of intrinsic silicon at 300 K," *Progress in Photovoltaics: Research and Applications,* vol. 3, no. 3, pp. 189-192, 1995.

[185] *Online tutorial: Electronic Chip Cooling (Application ID: 47721)*. Available:

https://www.comsol.com/model/download/381171/models.heat.chip_cooling.pdf
[186] K. Mizuno *et al.*, "A black body absorber from vertically aligned single-walled carbon nanotubes," *Proceedings of the National Academy of Sciences,* vol. 106, no. 15, pp. 6044-6047, 2009.
[187] S. M. Jung, C. J. Park, H. Jeong, and M. W. Shin, "Effect of number of laser pulses on p+/n silicon ultra-shallow junction formation during non-melt ultra-violet laser thermal annealing," *Materials Science in Semiconductor Processing,* vol. 60, pp. 34-39, 2017.
[188] D. J. Lim, H. Ki, and J. Mazumder, "Mass removal modes in the laser ablation of silicon by a Q-switched diode-pumped solid-state laser (DPSSL)," *Journal of Physics D: Applied Physics,* vol. 39, no. 12, p. 2624, 2006.
[189] F. Corporation. (2013). *Emissivity values of common materials*. Available: http://support.fluke.com/find-sales/Download/Asset/3038318_6251_ENG_C_W.PDF
[190] B. Carasi. (2016). *Compressibility Options and Buoyancy Forces for Flow Simulations*. Available: https://www.comsol.com/blogs/compressibility-options-and-buoyancy-forces-for-flow-simulations/
[191] E. Fontes. (2016). *Introduction to Modeling Natural Convection in COMSOL Multiphysics®*. Available: https://www.comsol.com/blogs/introduction-to-modeling-natural-convection-in-comsol-multiphysics/
[192] M. Zhang *et al.*, "Strong, transparent, multifunctional, carbon nanotube sheets," *Science,* vol. 309, no. 5738, pp. 1215-1219, 2005.
[193] S. Lu and B. Panchapakesan, "Photoconductivity in single wall carbon nanotube sheets," *Nanotechnology,* vol. 17, no. 8, p. 1843, 2006.
[194] Y. H. Kim and E. Y. Jang, "Carbon nanotube sheet," ed: Google Patents, 2012.